5-6-2017

Experimental Evaluation Of A Precast Concrete Beam-To-Column Prototype Design Under A Column Removal Scenario

Jorge Omar Torres Alamo

Experimental evaluation of a precast concrete beam-to-column prototype design under a column removal scenario

By

Jorge O. Torres-Alamo

A Thesis
Submitted to the Faculty of
Mississippi State University
in Partial Fulfillment of the Requirements
for the Degree of Master of Science
in Civil Engineering (Structures)
in the Department of Civil and Environmental Engineering

Mississippi State, Mississippi

May 2017

Experimental evaluation of a precast concrete beam-to-column prototype design under a column removal scenario

By

Jorge O. Torres-Alamo

Approved:

_____

Philip M. Gullett
(Major Professor)

_____

Stanley C. Woodson
(Minor Professor)

_____

Seamus F. Freyne
(Committee Member)

_____

James L. Martin
(Graduate Coordinator)

_____

Jason M. Keith
Dean
Bagley College of Engineering

Name: Jorge O. Torres-Alamo

Date of Degree: May 5, 2017

Institution: Mississippi State University

Major Field: Civil Engineering (Structures)

Major Professor: Dr. Phillip M. Gullett

Title of Study: Experimental evaluation of a precast concrete beam-to-column prototype design under a column removal scenario

Pages in Study: 215

Candidate for Degree of Master of Science

Precast concrete multistory buildings are used in an attempt to optimize the available construction space and reduce costs. However, little is known about predicting their capacity in a brittle response mode due to the sudden loss of a critical element that could induce a Progressive Collapse Scenario. Therefore, the National Institute for Standards and Technology (NIST) developed an explicit approach in the design of precast concrete systems that is intended to mitigate a progressive collapse by enhancing the rotational capacity of joints and the robustness of the structural system.

A full-scale experiment was conducted to investigate the structural performance of a prototype design under a column-removal scenario. The test assembly frame, consisting of three columns and two beams, was subjected to a displacement controlled vertical force acting at the center to characterize the failure modes and collapse mechanisms. Brittle-failures of critical structural elements were observed and significantly impacted the performance.

DEDICATION

I dedicate my thesis work to my beloved family. To my precious wife Natalie, without whose caring support and understanding it would not have been possible, to my twin boys Sebastian and Alejandro, and to my little princess Gabriella. Kids, you are my inspiration and strength to purse a better future for all of us. I also would like to give a special feeling of gratitude to my loving parents, Jorge L. and Maria C., whose words of encouragement and push for tenacity ring in my ears.

ACKNOWLEDGEMENTS

The author expresses his sincere gratitude to the many people without whose selfless assistance this thesis could have materialized. First, sincere thanks are due to Dr. Stanley C. Woodson, my associated committee chairman, for his magnanimity in expending time and effort to guide and assist me throughout the intricacies of the graduate program and the thesis process. Expressed appreciation is also due to the other members of my thesis committee, namely, Drs. Philip M. Gullett and Seamus Freyne, for the invaluable aid and direction provided by them. The author would also like to thank Drs. H. S. Lew and Joseph Main of NIST for allowing ERDC to conduct the full-scale field experiment. Finally, the author would like to thank Dr. Mila Kennett of the Department of Homeland Security for sponsoring the execution of the full-scale experiment at ERDC.

TABLE OF CONTENTS

DEDICATION ii

ACKNOWLEDGEMENTS iii

LIST OF TABLES viii

LIST OF FIGURES ix

NOMENCLATURE xvii

UNIT CONVERSION FACTORS xx

CHAPTER

I. INTRODUCTION AND BACKGROUND 1

1.1 Introduction 1
1.2 Background 2
1.3 Definition of progressive collapse 6
1.4 Design approaches 7
1.5 Incorporation into design guides and codes 8
1.6 Previous research 13
1.7 Research objectives 19
1.8 Scope of study 19

II. STRUCTURAL DETAILS OF PROTOTPYE BUILDING AND TEST SPECIMEN 20

2.1 Prototype building general details 20
2.2 Design of moment resistance frame 22
2.3 Design and dimensions of the OMRF test specimen 24
2.3.1 Design of spandrel beams 25
2.3.2 Design of columns 28
2.3.3 Design of beam-to-column moment connection 30

III. EXPERIMENTAL PROCEDURES 32

3.1 Materials 32
3.1.1 Concrete 32

3.1.2 Steel reinforcement and steel components 32
3.1.3 Material tests 33
3.1.3.1 Concrete mechanical properties 33
3.1.3.2 Steel reinforcement mechanical properties 34
3.2 Fabrication of test specimen 35
3.2.1 Forming of precast structural elements 35
3.2.2 Fabricating and placing the reinforcement and steel components 36
3.2.2.1 Placing of spandrel beam reinforcement and steel components 36
3.2.2.2 Column reinforcement and steel components 38
3.2.3 Concrete placement in structural elements 39
3.2.4 Assembly of the OMRF test specimen 42
3.3 Testing procedure 45
3.3.1 Reaction structure and loading device 45
3.4 Test measurements and instrumentation 51
3.4.1 Pseudo-static response channels 52
3.4.1.1 Load cell and differential pressure gauge measurements 52
3.4.1.2 Displacement and deflection measurements 53
3.4.1.3 Inclinometers 54
3.4.1.4 Strain measurements 55
3.4.1.4.1 Internal strain gauges 55
3.4.1.4.2 External strain gauges 59
3.4.1.5 Tension in torsion bars 60
3.4.2 High-frequency response channels 61
3.4.2.1 Acoustic emission sensors 62
3.4.2.2 Accelerometers 64
3.4.3 Photography 65
3.5 Experiment loading procedure 65

IV. EXPERIMENTAL RESULTS 68

4.1 Overview 68
4.2 OMRF overall structural performance 69
4.3 Posttest structural damage observations 73
4.3.1 Posttest damage of columns 74
4.3.1.1 Left (east) end-column posttest damage 74
4.3.1.2 Unsupported center column/stud posttest damage 76
4.3.1.3 Right (west) end-column posttest damage 77
4.3.2 Spandrel beams posttest damage 80
4.3.3 Steel link plates posttest damage 85
4.4 Loading characteristics and measurements 85
4.4.1 Experiment data records 87
4.4.1.1 Pseudo-static measurements 87
4.4.1.1.1 Load measurements 87
4.4.1.1.2 Displacement measurements 88

4.4.1.1.3 Inclinometers measurements 89
4.4.1.1.4 Strain measurements....89
4.4.1.1.5 Torsion load cells 90
4.4.1.2 High-frequency measurements....91

V. DISCUSSION AND EVALUATION OF RESULTS 93

5.1 Structural responses and observed failure modes....93
5.1.1 Forensic examination of response zone I 98
5.1.2 Forensic examination of response zone II 100
5.1.3 Forensic examination of response zone III....102
5.1.4 Forensic examination of response zone IV 107
5.1.5 Forensic examination of response zone V....113
5.2 Performance of beam-to-column connection prototype design....121
5.2.1 Bottom-center anchor bars 122
5.2.2 Steel link plates....140
5.2.2.1 Steel link plate at location 1 142
5.2.2.2 Steel link plate at location 2 143
5.2.2.3 Steel link plate at location 3 144
5.2.2.4 Steel link plate at location 4 146
5.2.2.5 Steel link plate at location 5 147
5.2.2.6 Steel link plate at location 6 148
5.2.2.7 Steel link plates at location 7 and 8 149
5.3 Development of arching action 150
5.4 Summary of observations 152

VI. SUMMARY, CONCLUSIONS, AND RECOMMENDATIONS 155

6.1 Summary....155
6.2 Conclusions 157
6.3 Recommendations 158

REFERENCES 161

APPENDIX

A. DATA RECORDS....165

A.1 Instrumentation matrixes 166
A.2 Experiment pseudo-static response data records (40 Hz)....170
A.3 Experiment high-frequency response data records (2 MHz)....186

B. MATERIAL PROPERTY STUDY 189

B.1 Concrete material property study 190
B.2 Reinforcement A706 Samples Tensile Test Data....191

C. OMRF TEST SPECIMEN: FABRICATION DRAWINGS 196

D. EXPERIMENT PROCEDURE 211

D.1 Experimental Testing Procedure 212
D.2 Test safety procedures 214

LIST OF TABLES

3.1 Tensile strength values of reinforcement bars in test specimen – ASTM E8 35

3.2 Instrumentation plan matrix 51

3.3 High-speed (2 MHz) channel matrix 62

4.1 Description of the experiment displacement-controlled loading scenario 86

4.2 Seven most significant acoustic emission response transient events 92

5.1 Incidents linked to structural responses observed throughout the experiment 96

5.2 Three most significant acoustic emission response transient events and the related incident 96

5.3 Associated stress to experimental strain readings per incidents 133

5.4 Associated sectional moment obtained using experimental strain readings per incidents 134

A.1 Pseudo-static response instrumentation legend 166

A.2 High-frequency response instrumentation legend 169

B.1 28-Day compressive strength sampling test result 190

B.2 28-Day splitting tensile strength sampling test result 191

B.3 Rebar samples sent to Boycote for tensile test – ASTM E8 192

D.1 SDC-B Experiment Procedure 213

LIST OF FIGURES

1.1 Ronan Point partial collapse: a gas explosion on the 18th floor resulted in a "progressive" collapse (MacLeod, 2005) 3

1.2 Side view of Ronan Point Apartments design of joint (Figueroa, 2014)....6

1.3 Side of Khobar building facing the explosive (KTBD, 1996)....11

1.4 Khobar Towers connection at floor plank and wall intersection (Ellingwood et al., 2007)....12

1.5 PCI typical spandrel beam-to-column connection (PCI, 2010)....16

1.6 On-site typical beam-to-column connection layout (Chahal, 2016) 16

2.1 SDC-B Prototype building (Main et al., 2015)....21

2.2 Illustration of perimeter moment frame showing link-plate connections and placement of spandrel beams within pockets in the columns (Main et al., 2015)....23

2.3 OMRF test specimen design details (Main et al., 2015) 25

2.4 OMRF typical layout of the spandrel beams....27

2.5 Welding details on M6 and M7 beam embedded angles....27

2.6 Test specimen design of end-columns....28

2.7 Test specimen design of center column/stud....29

2.8 Test specimen connection details (Main et al., 2015) 31

3.1 Torsion rods across beam and column, and bearing pad at location #8 33

3.2 Spandrel beams reinforcement details....36

3.3 Concrete placement in OMRF's spandrel beam....41

3.4 Concrete placement in OMRF's center column/stud 41

3.5 Welding of end-columns to reaction structure's footing 43

3.6 Assembly of unsupported center column 43

3.7 Assembly of spandrel beams into the moment frame 44

3.8 OMRF's setup in ERDC reaction structure 46

3.9 ERDC's 600-kip (267-kN) hydraulic ram 47

3.10 Ram steel plate and rail columns of reaction structure 48

3.11 Roller-bearing supports in ram steel plate 48

3.12 Reaction structure horizontal restraints at center column/stud: (a) front face, (b) back face 49

3.13 Reaction structure restraint short beams 50

3.14 OMRF's idealized boundary conditions: (a) front view, (b) top view 50

3.15 Load Cell (400-kip) (1779-kN) and differential pressure sensor 53

3.16 Location of displacement gauges in the test specimen 54

3.17 Location of inclinometers gauges in the test specimen 55

3.18 Beam-L – Internal strain gauges on steel anchor bars at M6 and M7 plates 57

3.19 Beam-L – Internal strain gauges at mid span of long anchor bars 57

3.20 Beam-R – strain gauges on steel anchor bars at M6 and M7 plates 58

3.21 Beam-R –strain gauges at mid span of #10 (#32) flexural bars 58

3.22 Location of strain gauges on link steel plates and upper brace steel beam 60

3.23 Location of the torsion doughnuts load cells 61

3.24 Score Dunegan SE900-MWB calibration curve (Score Atlanta Inc., 2012) 63

3.25 Acoustic emission sensor (Score Atlanta Inc., 2012) 64

3.26 Location of acoustic emission sensors at bottom M8 plate in center column 64

3.27 Location of accelerometers at bottom centerline of spandrel beam 65

4.1 Applied load vs. vertical center displacement of OMRF 69

4.2 Elevation view, development of the first observed cracks in the beams near the top of the center column/stud, at Δ of 0.38 in. (9.6 mm).....70

4.3 Elevation views, development of the first observed cracks in the end-columns at Δ of 1.8 in. (45.7 mm).....72

4.4 Elevation views, development of the first observed crack in center column at Δ of 2.1 in. (52.7 mm) 72

4.5 Pretest vs. posttest views of the OMRF test specimen.....73

4.6 Elevation views, posttest damage of left (east) end-column 75

4.7 Elevation view, posttest damage of bottom of left (east) end-column 75

4.8 Elevation views, detachment of the upper M8 plate in the left (east) end-column 76

4.9 Elevation view, posttest condition of the center column/stud.....77

4.10 Elevation views, posttest damage of right (west) end-column.....79

4.11 Elevation view, posttest damage of bottom of the right (west) end-column 79

4.12 Elevation views, detachment of the upper M8 plate in the right (west) end-column 80

4.13 Elevation view, posttest damage of the spandrel beams near the top of the center column/stud.....81

4.14 Side view, posttest damage of the bottoms of the spandrel beams near the center column/stud.....82

4.15 Elevation views, posttest damage of spandrel beams near the end-columns.....82

4.16 Elevation view, posttest damage of the spandrel beam at the bottom connections to the center column 84

4.17 Fractured anchor bars of M7 angle plate in Beam-L (elevation view).....84

4.18 Load cell vs. MTS ram internal differential pressure sensor correlation.....88

5.1 Applied load and center vertical displacement vs. time with AE event marks 95

5.2 Elevation view of OMRF test specimen, damage per response zones 97

5.3 Elevation view, response zone I – incident (a): first observed concrete cracks on the test specimen at the center, 63 kips (280 kN) 99

5.4 Top view of link plate connection showing (Main et al., 2015) 99

5.5 Elevation view, response zone II – incident (b): end-columns first concrete cracks at 114 kips (507 kN) 102

5.6 Location of M7 anchor bars 103

5.7 Elevation view, response zone III – incident (e): concrete crack growth around top M8 plate at left (east) end-column, initiation of bearing of beams to columns 105

5.8 Elevation view, response zone III – incident (f): initial bearing of beams against columns. 107

5.9 Development of concrete cracks around the upper M8 plate in left (east) end-column; detachment of M8 107

5.10 Elevation view, response zone IV – incidents (g), (h) and (i): concrete spalling due to arching and rupture of the upper M7 anchorage bar 109

5.11 Different angles showing the location of fracture of the M7 anchor bars embedded in Beam-L near the center column 113

5.12 Elevation view, response zone V – incident (j): fracture of lower torsion bar in right end-column 114

5.13 Elevation view, response zone V – incident (k): fracture of lower torsion bar in left end-column, and cracking around top M8 plate in right (west) end-column 116

5.14 Elevation view, posttest damage to the left (east) end-column 117

5.15 Elevation view, response zone V – incident (l): detachment of the upper M8 plate embedded in the right (west) end-column 119

5.16 Response zone V – incident (l): detachment of the upper M8 in the right (west) end-column 119

5.17 Elevation view, posttest damage to the right (west) end-column 120

5.18 Elevation view of simplified-frame of the OMRF test specimen.....123
5.19 Stress block of simplified OMRF test specimen 125
5.20 A706 material sample data and curve fit to determine *fs* 127
5.21 Close-up view of the fractured profile of both failed M7 anchor bars.....136
5.22 Component test setup for welded anchor bar (Main et al., 2015) 139
5.23 Results of welded anchor bar component test (Main et al., 2015) 139
5.24 Vertical displacement measurements by incidents.....141
5.25 Close up view to posttest damage steel link plate #1 143
5.26 Close up view to posttest damage steel link plate #2 144
5.27 Close up view to posttest damage steel link plate #3 145
5.28 Close up view to posttest damage of steel link plate #4.....146
5.29 Close-up view to posttest damage steel link plate #5.....147
5.30 Close-up view to posttest damage steel link plate #6.....148
5.31 Close up view to posttest damage steel link plate #7 150
5.32 Close up view to posttest damage steel link plate #8 150
A.1 Beam vertical displacements from gauges D–83, D-85, D-86, and D-88.....170
A.2 Horizontal displacement of end-columns (LVDTs 81 and 90) 170
A.3 Beam endpoint rotations.....171
A.4 Strains in top anchor bars in M6 embedded angle 171
A.5 Strains in top anchor bars in M7 embedded angle 172
A.6 trains in outer-most top bars at mid-span 172
A.7 Strains in outer-most bottom bars at mid-span.....173
A.8 Strains in steel link plate #1, left (east) end-column, Beam-L 173
A.9 Strains in steel link plate #2, center column, Beam-L.....174

A.10 Strains in steel link plate #3, center column, Beam-L 174

A.11 Strains in steel link plate #4, center column, Beam-R 175

A.12 Strains in steel link #5, right (west) end-column, Beam-R 175

A.13 Strains in steel link plate #6, center column, Beam-R 176

A.14 Strains in steel link #7, left (east) end-column, Beam-L 176

A.15 Strains in steel link #8, right (west) end-column, Beam-R 177

A.16 Strains in top lateral restraint steel beam 177

A.17 Load cells on torsion rods bottom center column 178

A.18 Response zone I – load and displacement vs. time, incident (a): load vs. displacement, first cracks observed at 63.2 kips (281 kN) 178

A.19 Response zone I - incident (a): drop in load, increment in strain in steel link plates #2-(a), and #4-(b) 179

A.20 Response zone II – load and displacement vs. time, incident (b): first cracks observed in end-columns 179

A.21 Response zone II – Incident (b): (a) drop in load, increment in end-column horizontal displacement; (b) drop in load, increment in strain in steel link Plates #7 and #8 180

A.22 Response zone III: load and displacement vs. time, yielding of M7 bottom bar at incident (c), initial peak load at incident (d), cracking around left-top M8 plate at incident (e), and detachment of M8 plate at incident (f) 180

A.23 Response zone (III) – incident (c): strain in center-top M7 anchor bars 181

A.24 LVDTs horizontal displacement measurements vs. time 181

A.25 Response zone III – incidents (e) and (f): drop in torsion load at (T2) 182

A.26 Response zone III – incidents (e) and (f): steel link plate #1 182

A.27 Response zone IV: load and displacement vs. time, development of arching action at incident (g), concrete scabbing at the bottom corners of beams towards the center at incident (h), and brittle failure of top M7 anchor bar at incident (i) 183

A.28 Response zone IV – incidents (g) and (h) 183

A.29 Response zone IV – incident (h): drop in torsion load at (T2) 184

A.30 Response Zone IV – incident (h): Beam-L M7, strain vs. time 184

A.31 Response zone V: load and displacement vs. time, torsion bars ejected at incidents (j) and (k), detachment of top M8 plate on right (west) end-column at incident (l) 185

A.32 Transient event (185): (a) acceleration, AE vs. time (100 msec.); (b) acceleration (Beam-L), AE vs. time (15 msec) 186

A.33 Transient event (194): acoustic emission activity at 216.15 min. of testing, (a) 100 msec, (b) 50 msec 186

A.34 Transient event (194): acceleration activity at 216.15 min. of testing, (a) 100 msec, (b) 20 msec 187

A.35 Transient event (194): strain activity at 216.15 min. of testing, (a) 100 msec, (b) 30 msec 187

A.36 Transient event (195): acoustic emission activity at 276.53 min. of testing, (a) 100 msec, (b) 55 msec 188

A.37 Transient event (195): accelerometer, activity at 276.53 min. of testing, (a) 100 msec, (b) 20 msec 188

B.1 Tensile test A706 - #10 bar, sample #227, strain vs. load graph 193

B.2 Tensile test A706 - #10 bar, sample #228, strain vs. load graph 193

B.3 Tensile test A706 - #8 bar, sample #231, strain vs. load graph 194

B.4 Tensile test A706 - #8 bar, sample #232, strain vs. load graph 194

B.5 Tensile test A706 - #4 bar, sample #222, strain vs. load graph 195

B.6 Tensile test A706 - #4 bar, sample #223, strain vs. load graph 195

C.1 Overview of instrumentation layout of SDC-B 197

C.2 Section A-A of SDC-B overview layout 197

C.3 Section B-B of SDC-B overview layout 198

C.4 Section B'-B' of SDC-B overview layout 199

C.5 C-C and C'-C' of SDC-B overview layout 200

C.6 Section D-D of SCD-B overview layout 201
C.7 Section E-E of SDC-B overview layout 202
C.8 Section F-F of SDC-B overview layout 203
C.9 Section G-G of SDC-B overview layout 204
C.10 Section H-H of SDC-B overview layout 204
C.11 Section G'-G' of SDC-B overview layout 205
C.12 Section H'-H' of SDC-B overview layout 206
C.13 Section I-I of SDC-B overview layout 207
C.14 Section I-I' of SDC-B overview layout 208
C.15 Section J-J of SDC-B overview layout 209
C.16 Section K-K of SDC-B overview layout 210

NOMENCLATURE

g	Acceleration
AE	Acoustic Emission
ACI	American Concrete Institute
ASCE	American Society of Civil Engineers
ASTM	American Standards for Testing and Materials
AWS	American Welding Society
Δu	Average center column displacement at the ultimate load
Δ	Average center column vertical displacement
BSSC	Building Seismic Safety Council
cm	Centimeter
Θ_u	Chord rotation at the ultimate load
r	Coefficient of Correlation
^{o}	Degrees
DoD	Department of Defense
DHS	Department of Homeland Security
ft	Feet
ε_f	Fracture Strain
GSA	General Service Administration
Hz	Hertz

in.	Inches
kN	Kilonewtons
kN/m^2	Kilonewtons per-square-meter
kPa	Kilopascal
MHz	Megahertz
MPa	Megapascals
m	Meter
mm	Millimeters
msec	Milliseconds
min.	Minutes
NEHRP	National Earthquake Hazards Reduction Program
NIST	National Institute for Standard and Technology
N	Newtons
ε_{tf}	Nominal Fracture Strain
ε_{tu}	Nominal Ultimate Strain
kip	One-thousand pounds
ksi	One-thousand pounds per-square-inch
OMF	Ordinary Moment Frame
Pa	Pascals
%	Percentage
lb	Pounds
psf	Pounds per-square-feet
psi	Pounds-per-square inch

PCI	Precast Concrete Institute
rad	Radians
SDC	Seismic Design Category
SFM	Special Moment Frame
m^2	Square meter
ERDC	U.S. Army Engineer Research and Development Center
ε_u	Ultimate Strain
UHPC	Ultra-High-Performance-Concrete
UFC	Unified Facilities Criteria
U.K.	United Kingdom
U.S.	United States
V	Volts
fy	Yield Strength

UNIT CONVERSION FACTORS

Multiply	By	To Obtain
cubic feet	0.02831685	cubic meters
cubic inches	1.6387064 E-05	cubic meters
degrees (angle)	0.01745329	radians
feet	0.3048	meters
inches	0.0254	meters
pounds (force)	4.448222	newtons
pounds (force) per square foot	47.88026	pascals
pounds (force) per square inch	6.894757	kilopascals
pounds (mass)	0.45359237	kilograms
pounds (mass) per cubic foot	16.01846	kilograms per cubic meter
pounds (mass) per cubic inch	2.757990 E+04	kilograms per cubic meter
pounds (mass) per square foot	4.882428	kilograms per square meter
square feet	0.09290304	square meters
square inches	6.4516 E-04	square meters

CHAPTER I

INTRODUCTION AND BACKGROUND

1.1 Introduction

The use of precast concrete members for the construction of multistory buildings has become increasingly popular during past decades. Today, engineers and architects have adopted this ancient Roman construction design method to minimize time and costs and optimize the use of available construction space. While conventional cast-in-place concrete is poured into site-specific forms and cured on site. Precast concrete is cast off-site in reusable molds or formworks, cured in a controlled environment, transported to the construction site, lifted into place, and connected by bolts, pins, or welds.

The increasing popularity in the use of precast concrete is due to its multiple construction advantages, such as rapid on-site assembly, improved quality control, reduced dependency on weather factors, etc. However, precast concrete poses a different set of challenges for designers. In particular, the understanding of the behavior of connections is critical to the success of the precast concrete assembly because it will affect load distribution, strength, stability, rotational capacity, and constructability of the global structure. The criticality of understanding the behavior of these connections is due to the potential for catastrophic consequences of one of these connection details failing without warning when subjected to abnormal loads.

Since World War I, many multi-story buildings around the world have been subjected to abnormal loads, and the vulnerability of critical structural elements under abnormal loads is a major concern for today's structural engineering community. Most buildings in the United States of America (U.S.) are not designed for severe loading conditions, such as gas explosions, bomb explosions, vehicular collisions, aircraft collisions. Thus, when buildings are subjected to these abnormal loads, they may sustain extensive damage (Somes, 1973; Burnett, 1975). In many cases, a localize impact or blast causes the failure of one or more critical structural members (e.g., columns) inducing the structure into a chain reaction of failure by exceeding the capacity of the undamaged elements as a result of the local failure. This chain of failures typically leads to the partial or total collapse of the structure. Because of this type of failure, a greater concern has arisen regarding the vulnerability of precast concrete structures due to the natural brittle behavior at the connections. An unforeseen event that causes the failure of a critical element in a precast concrete structure could result in a catastrophe due to the lack of rotational capacity at the joints and robustness.

The study reported herein discuss the experimental evaluation of a prototype beam-to-column connection design intended to mitigate a progressive collapse in precast concrete structures by enhancing the rotational capacity of joints and the robustness of the structural system.

1.2 Background

A good example of this is the partial collapse of the Ronan Point Tower block in London, United Kingdom (U.K.), a 22-story precast concrete building. On the morning of May 16, 1968, a gas explosion blew out a load bearing wall on the 18th floor of the

Ronan Point Tower. The loss of an exterior wall triggered the collapse of the floors above (Figure 1.1).

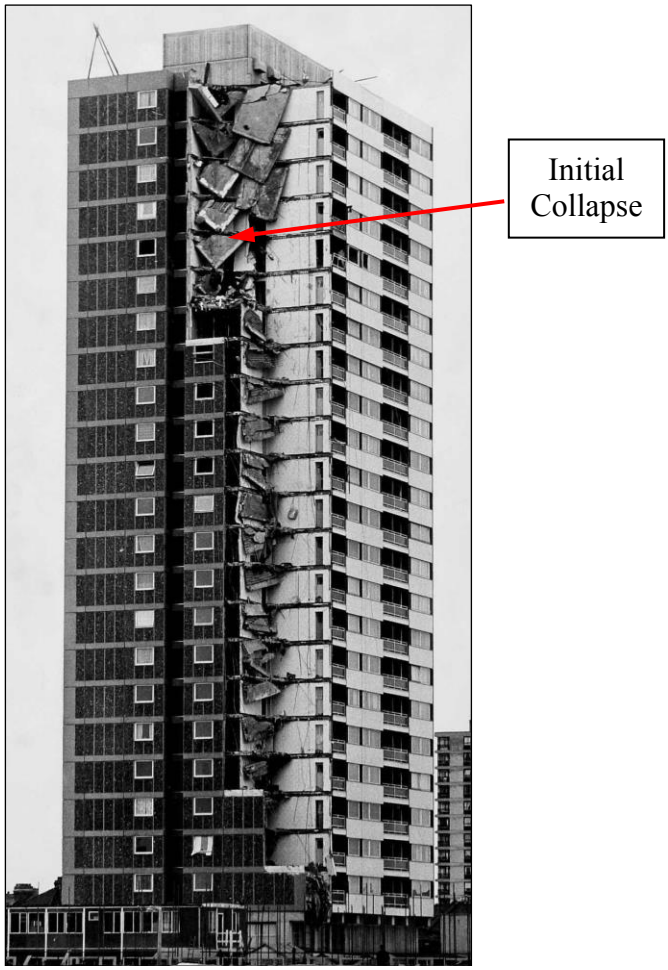

Figure 1.1 Ronan Point partial collapse: a gas explosion on the 18th floor resulted in a "progressive" collapse (MacLeod, 2005)

The dynamic loading imparted by the falling debris triggered the "progressive collapse" of the seventeenth floor and below. The southeast corner of the building collapsed to the ground (Ellingwood et al., 2007). The collapse destroyed the living room

portions of the apartments, leaving intact the bedrooms, except for floors numbered seventeen through twenty-two (Figure 1.1) (Ellingwood et al., 2007). Four people were killed and seventeen were injured.

British forensic investigators attributed the partial collapse of the Ronan Point building to its lack of structural integrity. They identified multiple flaws in both the design and construction that contributed to its partial collapse. They concluded:

1. the existing building codes were inadequate for ensuring the safety and integrity of high-rise precast concrete apartment buildings (Pearson and Delatte, 2005);
2. the Larsen-Nielson building system followed in the design of the Ronan Point Tower was intended for 6-story-high buildings, not 22-story; and
3. when the structure was dismantled, appallingly poor workmanship was found at the critical connections between the panels (Pearson and Delatte, 2005).

Ronan Point designers followed the Larsen–Nielson system in the design of the precast structure. This building technique was developed in Denmark in 1948, and it encompassed the patterns for the panels and joints, the method of panel assembly, and the methods of production of the panels. In this type of structural system, each floor is intended to be supported by the load bearing walls directly beneath it. Gravity-load transfer occurred only through these load-bearing walls. The walls and floor system shall fit together in slots. These joints shall then be bolted together and filled with dry pack mortar to secure the connections (Figure 1.2). However, no structural frame is included, forcing the connections to rely, in large part, on friction (Highrise Fire, 2016).

When Ronan Point forensic investigators began to dismantle the structure, they discovered that not only the Larsen-Nielson system was extended beyond its safety point, but also that the connection details were not followed as recommended in the system. Some of the joints were not screwed tightly, and ties were not attached. Even more, voids

filled with garbage were found in place of the appropriate construction material designated in construction documents (Figueroa, 2014). Figure 1.2 illustrates a Ronan Point's typical connection detail between the precast slab and the precast flank (bearing) wall. Figure 1.2(a) illustrates the original design detail and Figure 1.2(b) the as-built (Figueroa, 2014).

However, in spite of the fact that the connection design details were under designed and not constructed as specified, the structural engineering community believes that the assembly still would have failed since there was no redundancy or alternate load path for the redistribution of forces along the connection details at the onset of the loss of a bearing wall. Therefore, as the exterior wall of the 18th floor apartment was destroyed, the exterior walls of the upper floors were unsupported and immediately collapsed. The impact loading of the falling debris on the seventeenth floor was sufficient to exceed the capacity of the bearing wall and flank connection detail. Consequently, the loading triggered the sequential failure of the lower 16 floors (Ellingwood et al., 2007). In essence, the Ronan Point precast building was like a "house of cards" with no redundancy for load redistribution in the event of a local failure of a critical element such as a beam, column, or joint.

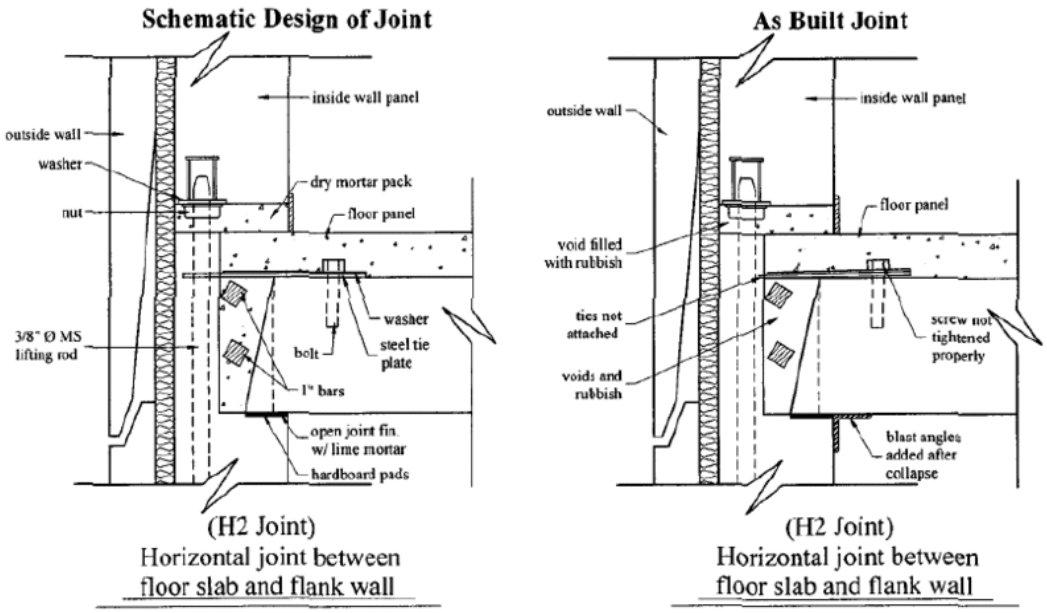

(a) Schematic design of joint (b) As-built joint

Figure 1.2 Side view of Ronan Point Apartments design of joint (Figueroa, 2014)

1.3 Definition of progressive collapse

The brittleness at the connection exhibited during the partial collapse of the Ronan Point Apartments revolutionized the structural engineering community and raised deep concerns regarding the reliability of precast structures. It also, highlighted the importance of designing more robust structures capable of resisting damage under extreme loads. In fact, the term “progressive collapse” was first used by the British forensic investigators to explain the disproportionate collapse of the Ronan Point apartment building in 1968. Although the entire building did not collapse, the extent of failure was disproportionate to the initial damage. For these reasons, it is considered the first documented progressive collapse event in history. Since then, this term has been

used to describe the spread of an initial localized failure into a chain reaction that leads to partial or total collapse of a building.

Currently, there is no unique universal definition of what constitutes a progressive collapse. However, the fundamental characteristic of progressive collapse is that the final state of failure is disproportionately greater than the failure that initiated the collapse (Ellingwood et al., 2007). The American Society of Civil Engineers (ASCE) first defined the term progressive collapse in ASCE Standard 7-05 as "the spread of local damage, from an initiating event, from element to element resulting, eventually, in the collapse of an entire structure or a disproportionately large part of it; also known as disproportionate collapse" (ASCE, 2005).

1.4 Design approaches

The Ronan Point collapse provided an impetus to the world structural engineering community to examine the British assessment and conduct extensive research to develop and experimentally investigate alternate connection design approaches. These design approaches could potentially improve the rotational capacity of precast concrete connection details by adding ductility, increasing structural stability, increasing moment resistance, and enhancing its ability to redistribute load. Such improvements could decrease the potential of the assembly to undergo a progressive collapse scenario initiated by a local brittle failure of a critical structural member. In summary, the structural engineering community seems to converge on three main approaches divided into two major categories, i.e., direct and indirect design. The alternatives are summarized and detailed below.

1. Tie force method: an indirect design approach – resistance to progressive collapse is considered indirectly through provision of minimum levels of strength, continuity, and ductility through the whole structure by application of ties.

2. Alternative load path method: a direct design approach – presumes that a critical element is removed from the structure as a result of an abnormal loading. Resistance to progressive collapse is provided by enabling the structure to redistribute all loads to the remaining undamaged structural elements. The selection of the critical elements will play a major role in the success of this approach. This method implies the following: (1) the element in which the damage occurred must be bridged by an alternative load-bearing system, and (2) the system as a whole must be stable after the local damage.

3. Specific load method: a direct design approach – resistance to progressive collapse is provided by enhancing the design of all critical load-bearing members to be resistant to a specified design value of abnormal load.

1.5 Incorporation into design guides and codes

Designing structures to fully prevent the occurrence of progressive collapse for all threats is not feasible; however, a combination of these approaches could prevent major disasters and save human lives. Since the 1980s, as a result of multiple studies scoped to develop design approaches to prevent progressive collapse, the engineering communities in the U.S. have incorporated additional guidance into four of their design codes for precast concrete structures: (1) American Concrete Institute (ACI) - 318 (ACI318-08, 2008), (2) ASCE 7-10 (ASCE 7-10, 2010), (3) U.S. General Service Administration (GSA) Federal Facilities guidelines (GSA, Progressive Collapse Analysis and Design for New Federal Buildings and Major Modernization Projects, 2013), (GSA, 2013); and (4) Department of Defense (DoD) Unified Facilities Criteria (UFC)-4-023-03, (DoD 2005).

Progressive collapse is not explicitly addressed in the ACI-318 Code. However, ACI-318 Section 7.13 stipulates requirements of structural integrity in order to improve

redundancy and ductility in structures so that, in the event of damage to a major supporting element or an abnormal loading event, the resulting damage may be confined to a relatively small area, and the structure will have a better chance to maintain overall stability (ACI318-08, 2008). For example, according to the ACI Code, precast concrete member tension ties shall be provided in the transverse, longitudinal, and vertical directions and around the perimeter of the structure to effectively tie elements together.

The ASCE 7-10 does not provide specific requirements for progressive collapse; however, it recommends minimum strength criteria that will provide structural integrity for normal service and robustness against unforeseen events that may occur throughout the life of the structure. The ASCE 7-10 also discusses in its Commentary two alternative design approaches to resist progressive collapse. The first method is an indirect design approach that provides minimum levels of strength, redundancy, continuity, and ductility (e.g., tie force). The other alternative is called direct design and involves approaches such as the alternate path method and the specific local resistance method.

On the other hand, the GSA Federal Facilities Guidelines are intended to bring a consistent level of protection in the application of progressive collapse design to Federal facilities and to bring alignment with the suite of security standards issued by the Interagency Security Committee (ISC) and the GSA in their philosophy, decision-making methodology, and application (GSA, 2013). Its design procedure aims to reduce the potential for progressive collapse through the alternate path method and by providing a redundant and balanced structural system.

And last but not least, the UFC-4-023-03 provides design requirements to resist progressive collapse. These design requirements are specified depending on the

occupancy category (OC) of the structure. The OC level can be considered as a measure of the consequences of a progressive collapse event and is based on two main factors, level of occupancy and building function or criticality (DoD, 2005). The UFC-4-023-03 design approaches employ tie forces, alternate path method, and enhanced local resistance.

The attack on Khobar Towers in 1996 is probably the most significant event in history that strengthens the belief of enforcing the use of progressive collapse mitigation techniques worldwide. On June 25, 1996, an eight-story precast concrete building in Al-Khobar near Dhahran, Saudi Arabia, was extensively damaged when a large vehicle carrying a bomb was detonated near the structure. In fact, other similar buildings in the vicinity were also damaged by this unforeseen terrorist attack. The explosion, which created a crater 55 ft (17 m) in diameter and 16 ft (5 m) deep, destroyed the facing front wall of the closest building and damaged interior floors and wall components (Figure 1.3) (KTBD, 1996).

Figure 1.3 Side of Khobar building facing the explosive (KTBD, 1996)

The main structural difference between Khobar Towers and Ronan Point Tower was the incorporation of mitigation techniques into the design of Khobar Towers. These apartment complexes in Khobar, Saudi Arabia, were designed using the British concrete design code (CP 110, 1976). This code included a prescriptive approach for collapse prevention and required ductile detailing and effective ties forces. In the system implemented in these buildings, the precast floor planks were cast with castellated edges that featured loops of reinforcing steel extending from the slabs' ends into what would be the gap between adjacent slabs' ends (Figure 1.4a). Similarly, joints between wall elements were constructed with protruding loops that were threaded with steel bars. The bars from one level to the next were connected with nuts inside connecting brackets (Figure 1.4b) (Ellingwood et al., 2007).

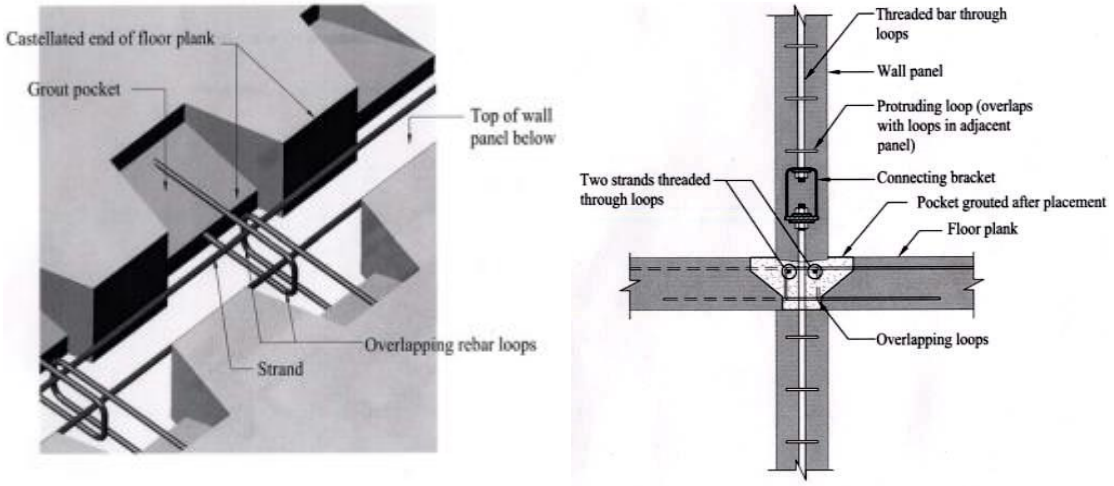

(a) Typical floor plank connection of Khobar Towers

(b) Connection at floor plank and wall intersection in Khobar Towers

Figure 1.4 Khobar Towers connection at floor plank and wall intersection (Ellingwood et al., 2007)

Khobar Tower collapse was limited to the front wall and some slabs of the outer bay of the closest building. Even though the exterior shear wall was removed by the blast for essentially the full length of the building, collapse did not progress beyond areas of first damage (Ellingwood et al., 2007). In fact, an investigation of the damage to Khobar Towers revealed that the precast concrete system used for these buildings had sufficient ductility to resist the extraordinary assault (Ellingwood et al., 2007). Floor slabs spanned parallel to the shear wall that was removed by the blast, limiting the damage induced by the removal of the front wall. Even though walls parallel to the blast propagation and interior walls facing the blast were extensively damaged, they continued to support vertical load. The precast elements themselves generally were detailed with sufficient ductility to retain integrity even after they were seriously damaged. In addition, the interlocked connections between floor slabs in adjacent bays and between slabs and wall

elements mostly survived the blast, resisting the potential for the building to collapse as a "house of cards" (Ellingwood et al., 2007).

1.6 Previous research

Chapter 9 in Elliott and Jolly (2013) presents a summary of design approaches for disproportionate collapse mitigation with application to multi-story precast concrete structures. One such approach is the previously defined tie force method. As summarized by Elliott and Jolly (2013), several experimental studies investigated the effectiveness of tie forces in precast concrete floor slabs for redistributing loads through catenary action (e.g., Regan, 1974; Schultz et al., 1978; Engström, 1990). Recently, Nimse et al. (2014, 2015) tested one-third-scale precast concrete frame assemblies under a column removal scenario and compared the performance of monolithic connections, cast-in-place ("wet") connections, and field-bolted ("dry") connections. From the results of the study, it was concluded that precast connections could be used as replacements of monolithic connections since they are more ductile and resist higher maximum loads compared to monolithic connections (Nimse et al., 2014).

Furthermore, Kang and Tan (2015) performed testing of half-scale precast concrete frame assemblies with cast-in-place connections under simulated column removal. Kang and Tan (2015) then compared the performance of specimens with different reinforcement details in the joints. Test results showed that significant compressive arch action and catenary action developed in the beams under column removal scenarios with pull-out failure of the bottom beam reinforcement in the joint. The enhancement of compressive arch action and catenary action to structural resistance greatly depends on joint detailing and beam reinforcement ratio (Kang and Tan, 2015).

At the same time, Tohidi et al. (2014) conducted research to develop an improved tie force methodology to prevent progressive collapse in the design of precast concrete cross wall structures. Particularly, Tohidi et al. (2014) gave attention to the post-bond failure behavior of tie strands in the floor-to-floor joints. The results were evaluated to determine the adequacy of current tie force methods as recommended by most codes of practice (Tohidi, 2014). Tohidi et al. (2014) concluded that it is the ductility rather than the tie strength that should be considered in the progressive collapse design.

The tie force method can be considered an overly simplified method; it's suitable for hand calculations, and its results are only approximations. However, this approach does not consider the ductility of the ties and thus does not ensure that the loads can actually be redistributed as large deformations develop following a local failure. On the other hand, the alternative load path method does consider the ductility of the ties, but it requires structural analysis to demonstrate explicitly the adequacy of the structural system to redistribute loads following a local failure. Recently, this direct approach (alternate path method) has become more popular in the construction industry; however, this approach requires characterization of the nonlinear behavior and ductility of structural components and connections, which can involve mechanisms such as arching action and catenary action. Experimental data from structural assemblies and systems under local failure scenarios, such as column removal, are indispensable in characterizing the complex nonlinear behaviors whereby alternative load paths can be developed.

Therefore, the National Institute of Standards and Technology (NIST) is conducting a comprehensive analytical and experimental research program to study the vulnerability of multi-story structures to undergo progressive collapse behavior. Also,

NIST is designing and testing new alternative path strategies intended to resist progressive collapse. As part of this research, ten-story prototype buildings have been designed with various structural systems, including steel frame, cast-in place concrete frame, and precast concrete frame buildings. Moment-frame assemblies representing portions of these structural systems have been tested at full scale under simulated column removal. Sadek et al. (2010) described testing and analysis of steel moment-frame assemblies, and Lew et al. (2011) described testing and analysis of cast-in-place concrete moment-frame assemblies. However, experimental data on the progressive collapse resistance of precast concrete structures have been quite limited. In particular, vulnerability studies of deeper spandrel beams to collapse after the removal of an exterior column are needed.

Typical PCI spandrel beam-to-column connection details are shown in Figure 1.5 and Figure 1.6. These connection details are typically designed in accordance with the National Earthquake Hazards Reduction Program (NEHRP) Recommended Seismic Provisions to sustain earthquake loading cycles. Since 1985, the Building Seismic Safety Council (BSSC) develops and the Federal Emergency Management Agency publishes at a regular interval the NEHRP Recommended Seismic Provisions for New Buildings and Other Structures, hereafter referred to as "Provisions." The Provisions serve as a resource used by the codes and standards development organizations as they formulate sound seismic-resistant design and construction requirements.

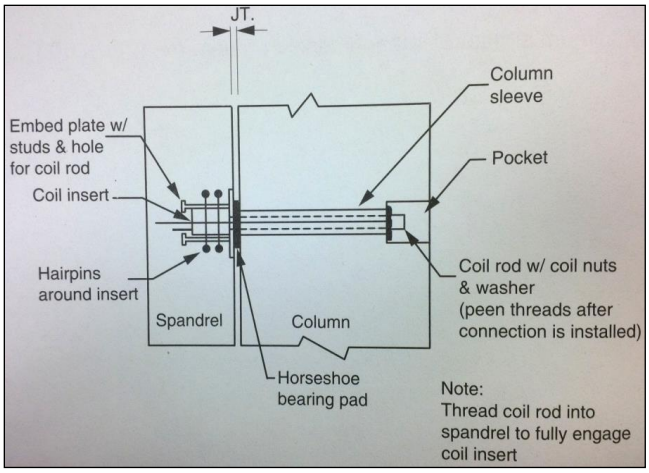

Figure 1.5 PCI typical spandrel beam-to-column connection (PCI, 2010)

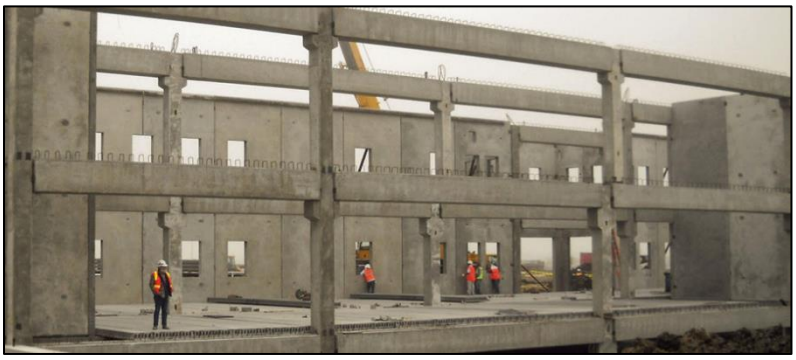

Figure 1.6 On-site typical beam-to-column connection layout (Chahal, 2016)

The Provisions recognize that, independent of the quality of their design and construction, not all buildings pose the same seismic risk. It uses the Seismic Design Category (SDC) concept to categorize structures according to the seismic risk of each region. Today, engineers and architects in the U.S. are required by law to design precast concrete structures for seismic loads utilizing Moment Resisting Frames (MRFs), rectilinear assemblages of beams and columns with the beams rigidly connected to the

columns by ductile joints to support gravity loads. MRFs also provide resistance to lateral load primarily by flexural action of members and may be classified as one of the followings types:

1. Special Moment Resisting Frames (SMRFs)
2. Intermediate Moment Resisting Frames (IMRFs)
3. Ordinary Moment Resisting Frames (OMRFs).

The level of seismic detailing in the design of the joints is driven by the SDC region. The framing systems, IMRF and SMRF, require special detailing to provide ductile behavior conforming to the Provisions, but the OMRF does not. In the Provisions, the resistance to lateral forces is provided primarily by rigid frame action, i.e., by the development of bending moment and shear force in the frame members and joints. By virtue of the rigid beam-column connections, a MRF cannot displace laterally without bending the beams or columns depending on the geometry of the connection. Therefore, the bending rigidity and strength of the frame members is the primary source of lateral stiffness and strength for the entire frame. However, despite these requirements, little is known about predicting or improving the ability of a precast concrete system to redistribute load at the time that a critical column fails or is destroyed by abnormal loads, which may lead to a progressive collapse scenario.

According to the Precast Concrete Institute (PCI 7th Edition, 2010), connections developing frame action must be designed for appropriate moment and shear transfer capabilities when lateral stability of precast concrete structures is achieved by frame action or by a combination of shear wall and frame action. The tension forces for the moment resistance within a connection can be resisted by various types of cast-in

embedments, such as headed studs and deformed bar anchors. These inserts must be properly anchored to preclude failure of the concrete and ensure a ductile mode of failure. (PCI 7th Edition, 2010) However, in the event of a sudden loss of a critical element, e.g., a column, a higher degree of moment resistance and ductility is required to provide the structural stability for the precast system.

Therefore, PCI, NIST, and the DHS tasked the U.S. Army Engineer Research and Development Center (ERDC) to conduct a full-scale experiment to evaluate the performance of an alternate beam-to-column prototype connection design that is intended to enhance the rotational capacity of the joints and increase ductility to the assembly by enabling the moment frame to redistribute load to the undamaged structural members in the event of a loss of a critical member, e.g., a column. The proposed connection detail applied in the experiment is illustrated in PCI 7th Edition, Example 6.13.7 (PCI 7th Edition, 2010). This PCI-proposed connection design has OMRF connections formed by fillet-welding steel link plates between embedded plates in the columns bonded to the concrete by headed studs. Also, steel link plates are fillet-welded to embedded angles bonded to the concrete by deformable anchor bars.

The novelty of this research relies on the experimental evaluation of the proposed beam-to-column connection detail for spandrel beams illustrated in the PCI 7th Edition, Example 6.13.7 (PCI 7th Edition, 2010) to determine its adequacy to resist progressive collapse by empowering the assembly to redistribute loads to the undamaged structural elements after the sudden loss of a critical column.

1.7 Research objectives

The objectives of this research project were to:

1. Evaluate the structural performance of a prototype moment-frame assembly, based on the PCI connection detail discussed above, by examining the adequacy of the proposed moment-resistant beam-to-column connection design to carry or redistribute loads along the assembly under a column removal scenario.

2. Determine the failure modes and quantify the large deflection behavior and joint rotational capacity of the assembly under a column removal scenario.

3. Provide experimental data critical for the validation and calibration of high-fidelity computational models developed by NIST.

1.8 Scope of study

The study reported herein included full-scale testing and evaluation of a precast concrete moment-frame assembly that represented exterior portions of the third-floor framing of a prototype ten-story building. The test specimen consisted of two fixed-end columns, two spandrel beams, and an unsupported column at the center. A moment-resistant beam-to-column connection, designed as part of an OMRF in an SDC-B zone, was incorporated into the system. The specimen was subjected to a monotonically increasing vertical displacement-controlled force over the unsupported center column to observe its behavior under a simulated column removal scenario. The test was continued beyond the ultimate capacity of the assembly in order to determine the failure modes and collapse mechanisms that developed. Active instrumentation was installed on the specimens and monitored throughout the test to investigate structural response during experiment execution. The data collected from this experiment will also be utilize to validate or lead to improvements of the current proposed connection design as well as improve the current design guidance to prevent progressive collapse.

CHAPTER II

STRUCTURAL DETAILS OF PROTOTPYE BUILDING AND TEST SPECIMEN

2.1 Prototype building general details

The building prototype has perimeter OMRFs designed to resist lateral loads while the interior framing is designed for gravity loads only. Perimeter OMRFs consist of spandrel beams connected to columns by steel link plates welded to embedded plates and angles. The interior gravity framing consists of simply-supported inverted T beams spanning between columns in the east-west direction. The floor system consists of cambered double T members spanning in the north-south direction with a concrete topping that varies in thickness.

NIST and Metromont Inc. along with a panel of practicing structural engineers across the U.S. developed the overall configuration and dimensions of the prototype ten-story building for office occupancy. An alternative design incorporating ductile moment-resistant beam-to-column connections was incorporated into the prototype's OMRF's for examining the effectiveness of the approach and detailing in resisting progressive collapse. A square plan layout was chosen for this prototype building, as shown in Figure 2.1(a), with plan dimensions of 150 ft (45.7 m) by 150 ft (45.7 m). As shown in Figure 2.1(b), the height of the first story is 15 ft (4.6 m), and the height of each upper story is 13 ft (4.0 m). (Kim et al., 2009)

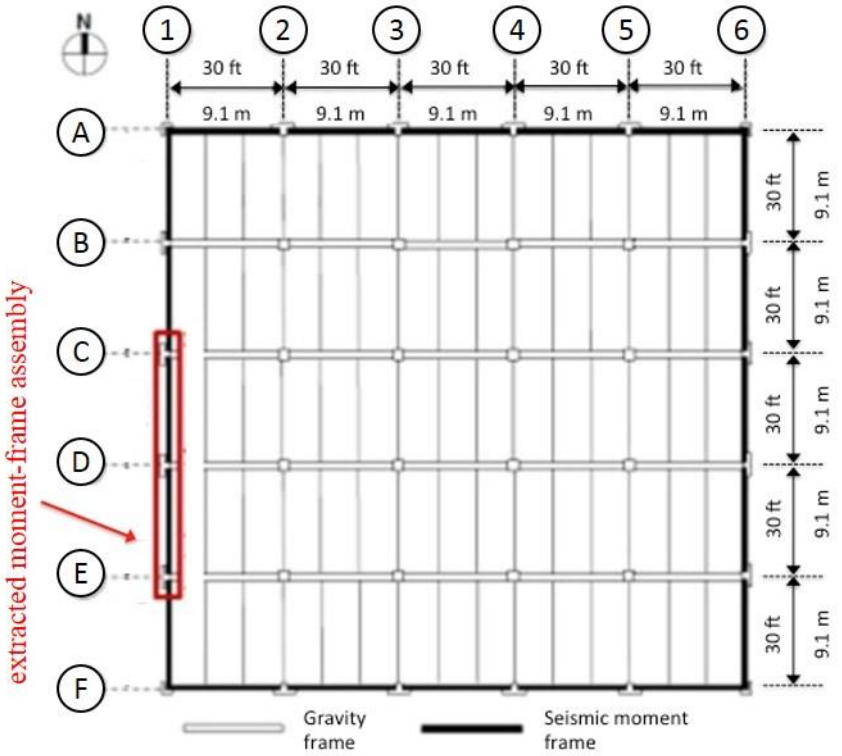

(a) Plan layout

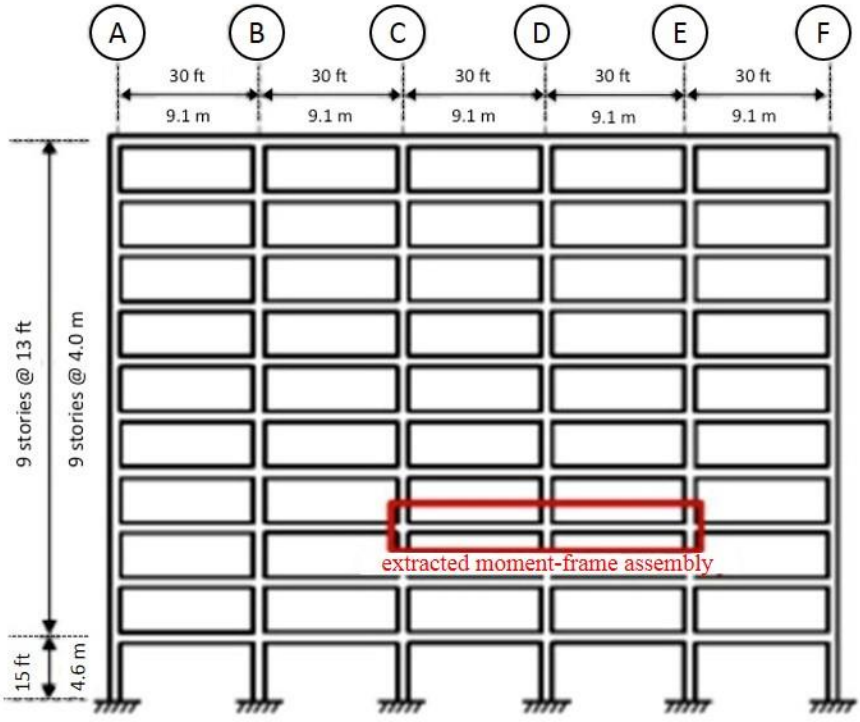

(b) Elevation view

Figure 2.1 SDC-B Prototype building (Main et al., 2015)

The loads to the structure were determined in accordance with ASCE 7-05 (ASCE 2005) for an occupancy category II. A superimposed dead load of 0.069 psi (0.48 kN/m^2) was considered in addition to the self-weight of the structure. Typical floors were designed for a live load of 0.69 psi (4.79 kN/m^2), which was reduced in accordance with section 4.8 of ASCE 7-05. The roof was designed for a live load of 0.17 psi (1.20 kN/m^2). Seismic design of the OMRF building was based on a location in Atlanta, GA, on Site Class C. The design of the structural members was based on the requirements of the ACI 318-05 code (ACI 318-05). Both the precast structural members and the concrete topping were designed using normal-weight concrete with a specific weight of 150 lbf/ft^3 (23.6 kN/m^3). A compressive strength of 6,000 psi (41.4 MPa) was specified for the precast structural members, and a compressive strength of 4,000 psi (27.6 MPa) was specified for the concrete topping. A minimum yield strength, denoted as *fy*, equal to 60 ksi (414 MPa) was specified for the reinforcing bars (Main et al., 2015).

2.2 Design of moment resistance frame

The prototype building's exterior framing consisted of columns and spandrel beams and was designed to provide the lateral load resisting system for the building. Figure 2.2 shows the structural concept for the moment connections. The spandrel beams are placed inside pockets in the exterior columns, and moment connections are established by welding steel link plates to the separate steel angles embedded in the beams and the columns. The steel column plates are embedded in the column concrete. The moment in the beam is transferred to the column by the coupling forces generated in the top and bottom steel link plates.

Anchorage reinforcing bars in the spandrel beams are welded to the steel angles embedded at the top and bottom of the beams. Class B splices are provided between the anchorage bars and the beam flexural reinforcement to maintain continuity of the beam reinforcement through the connection, as required for precast concrete by Section 21.6.2 of ACI 318-05.

The frame clear span-to-depth ratio is 2.3 for the spandrel beams, which indicates the beams should be considered “deep” beams as defined by Section 10.7.1 of ACI 318-05. Further details on the prototype moment-frame assemblies considered in this study, including the member dimensions and reinforcement details, are provided by Main et al. (2015) and presented herein as appropriate.

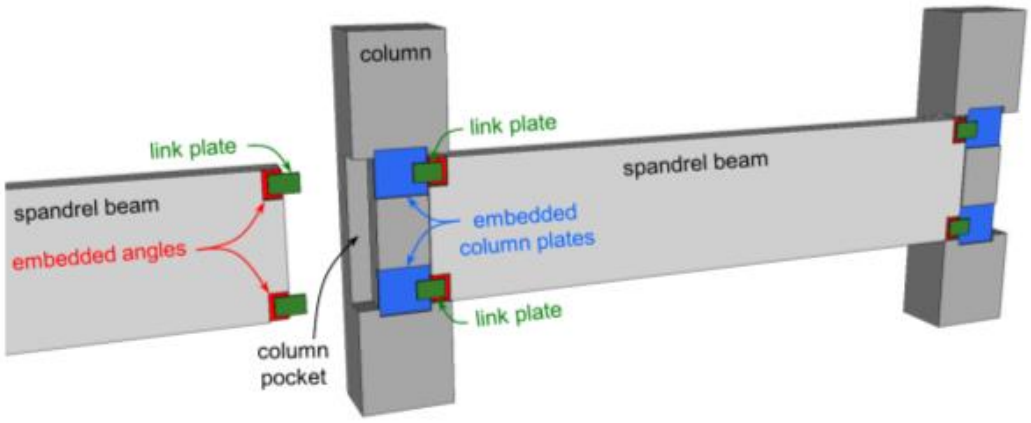

Figure 2.2 Illustration of perimeter moment frame showing link-plate connections and placement of spandrel beams within pockets in the columns (Main et al., 2015)

2.3 Design and dimensions of the OMRF test specimen

The full-scale model represents the exterior moment frame in the north-south direction at the third-story level, as indicated in Figure 2.1 (Main et al., 2015). The OMRF test specimen member sizes and reinforcement details are shown in Figure 2.3.

The cross section of each precast structural element in the test specimen is a direct representation of the full-scale prototype design; however, in order to fit within the testing facility located at ERDC, Vicksburg, MS, the span length of the test specimens was reduced from the prototype design of 30 ft (9.1 m) to 25 ft (7.6 m). For discussion herein, the front of each specimen denotes the surface on which the link plates were welded when making the moment connections, and the designations “left beam” and “right beam” correspond to the orientation of the beams when viewing the front of the specimen. As indicated in Figure 2.3, the left beam (Beam-L) was on the east side of the testing facility, and the right beam (Beam-R) was on the west side.

The reinforcement selected in the design of the precast elements was ASTM A706 Grade 60 bars. A variety of A706 size designations were used to reinforce the precast structural members, ranging from #4 (#13) to #10 (#32) bars. The inserted plates and angles were made of ASTM A36 (2009) steel with a yield strength, (f_y, equal to 36 ksi (250 MPa).

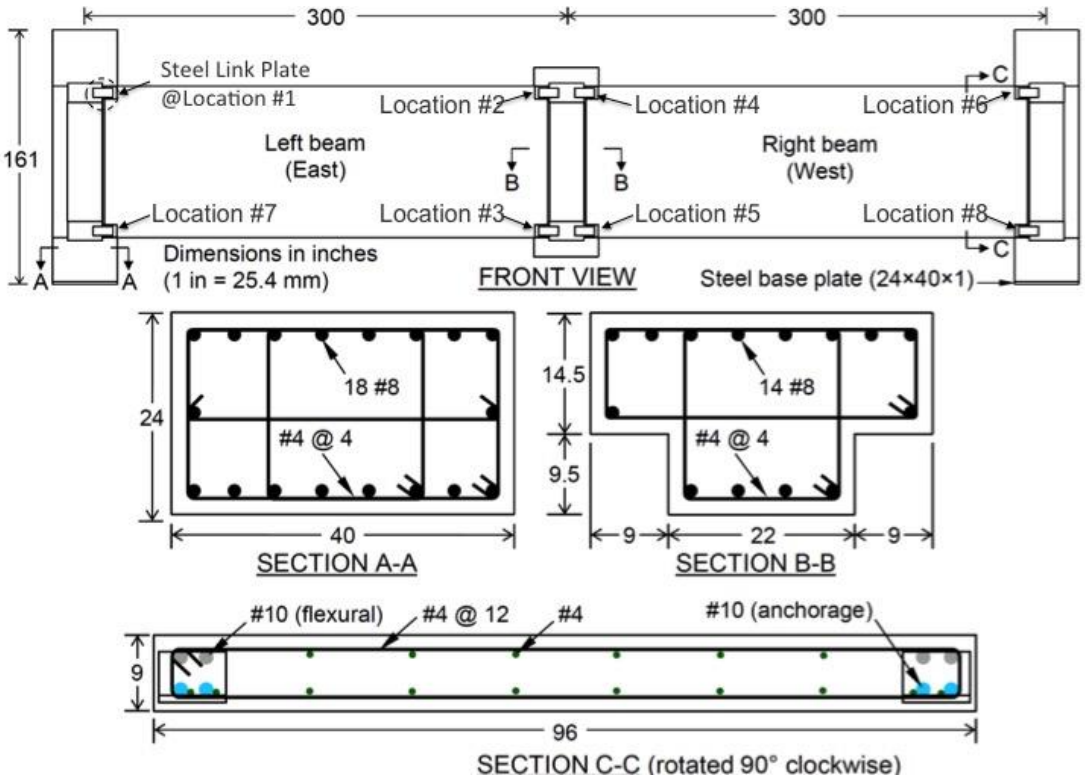

Figure 2.3 OMRF test specimen design details (Main et al., 2015)

2.3.1 Design of spandrel beams

The spandrel beams (Figure 2.4) were designed using reinforced precast concrete with a maximum compressive strength of 6,000 psi (41.4 MPa) and the following dimensions: 277-in. (7035.8-mm) long by 9-in. (228.6-mm) thick by 96-in. (2438.4-mm) deep as shown in Figure 2.4. The reinforcement detail for each spandrel beam consisted of multiple A706 #4 (#13) Grade 60 steel bars, four A706 #10 (#32) Grade 60 steel longitudinal bars, four A36 steel angles, and a pair of A706 #10 (#32) Grade 60 anchor bars welded to each angle. A cross-section of the spandrel beam detailing the reinforcement is shown in Figure 2.3 (Section C-C).

The #4 (#13) Grade 60 steel bars were designed to form a double mat, spaced at 12 in. (304.8 mm) in both directions. The four #10 (#32) Grade 60 longitudinal bars (flexural) designed to be placed behind the anchor bars near the back surface of the spandrel beams are shown in Figure 2.3 (Section C-C). In addition, four A36 steel angles with the following dimensions: 8 in. (203.2 mm) by 6 in. (152.4 mm) by 1 in. (25.4 mm) by 8 in. long (203.2 mm) were designed to be embedded at each corner as illustrated in Figure 2.4. In an effort to facilitate the discussion, the embedded angles at the top corners were denoted as M6, and the bottom pair were denoted as M7 in each beam, as shown in Figure 2.4. The welding detail of the A706 #10 (#32) Grade 60 anchor bars to the corner embedded angles is shown in Figure 2.5. Two A706 #10 (#32) Grade 60 anchor bars, 72-in. (1828.8-mm) long, were designed to be welded with flare-bevel-groove welds to the bottom embedded angles M7 of each beam. In addition, two 92-in.- (2336.8-mm-) long A706 #10 (#32) Grade 60 anchor bars were also welded to the top corners of the embedded angles M6.

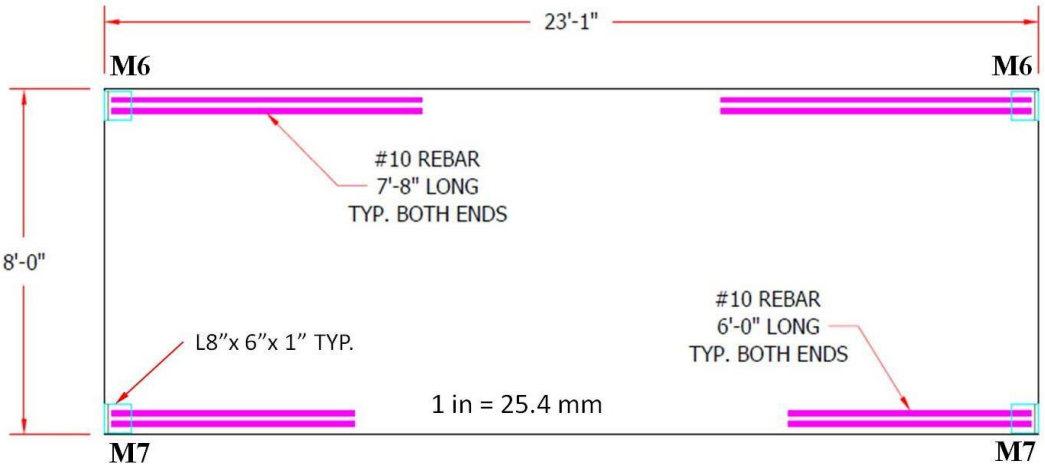

Figure 2.4 OMRF typical layout of the spandrel beams

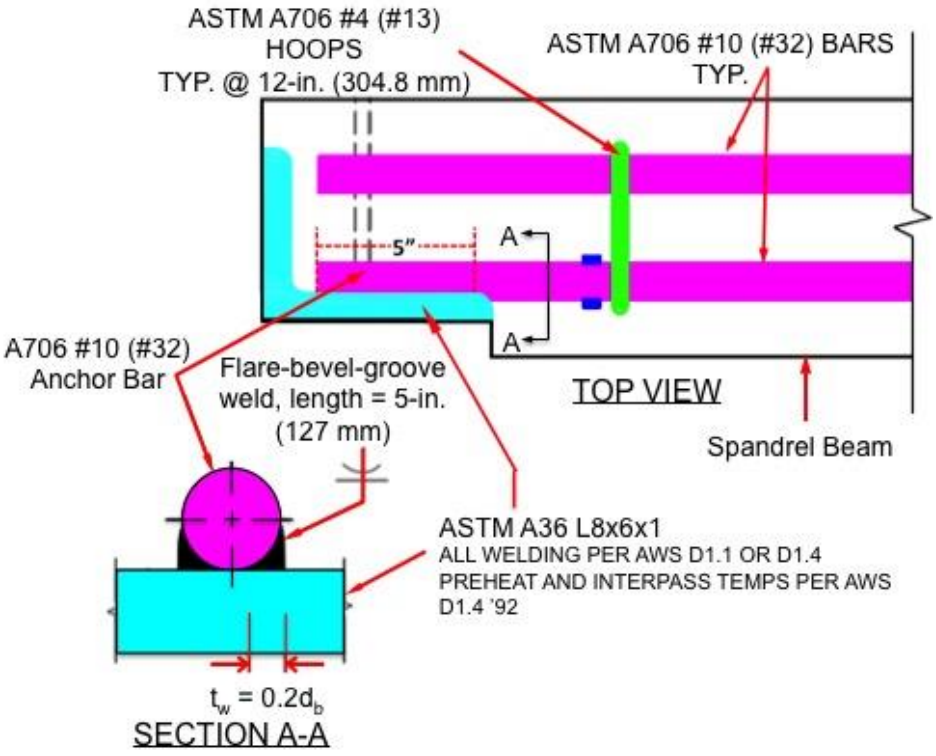

Figure 2.5 Welding details on M6 and M7 beam embedded angles

2.3.2 Design of columns

The columns cross-sections are shown in Figure 2.3 (Section A-A), which was reduced to a T-shape in the connection regions to form pockets for the spandrel beams as illustrated in Figure 2.3 (Section B-B). Details of the end-columns and center column/stud are shown in Figure 2.6 and Figure 2.7, respectively.

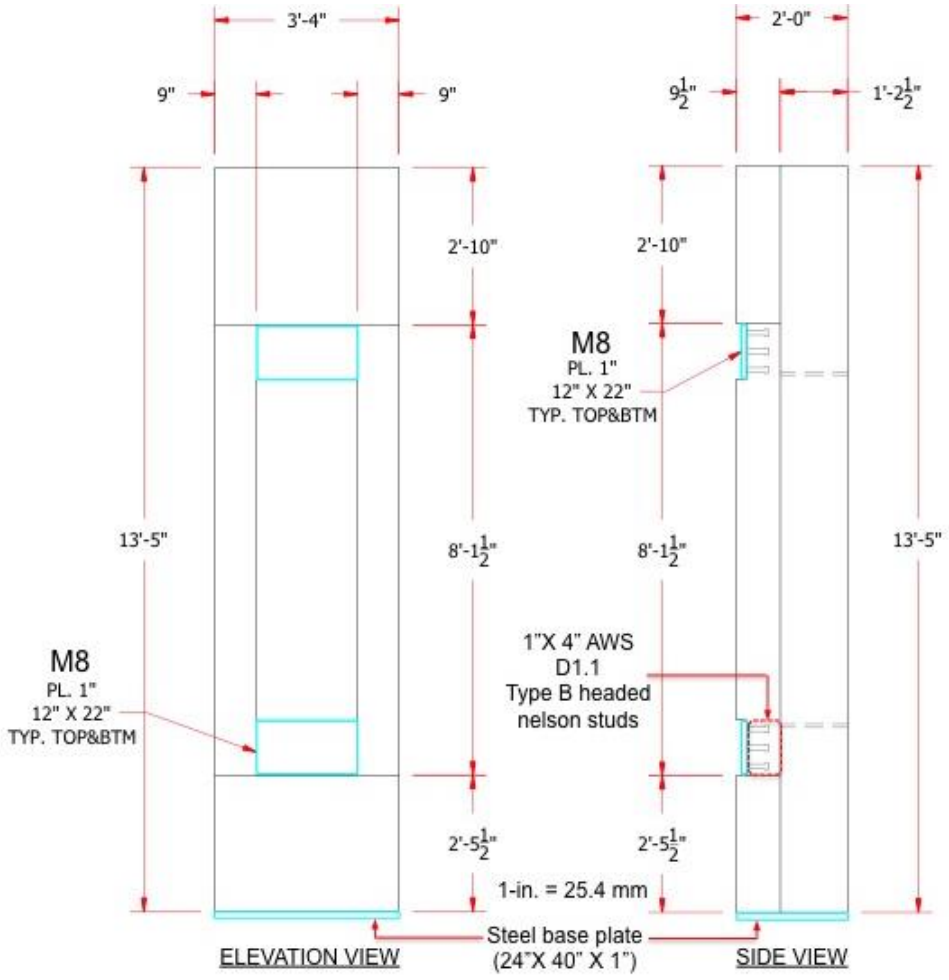

Figure 2.6 Test specimen design of end-columns

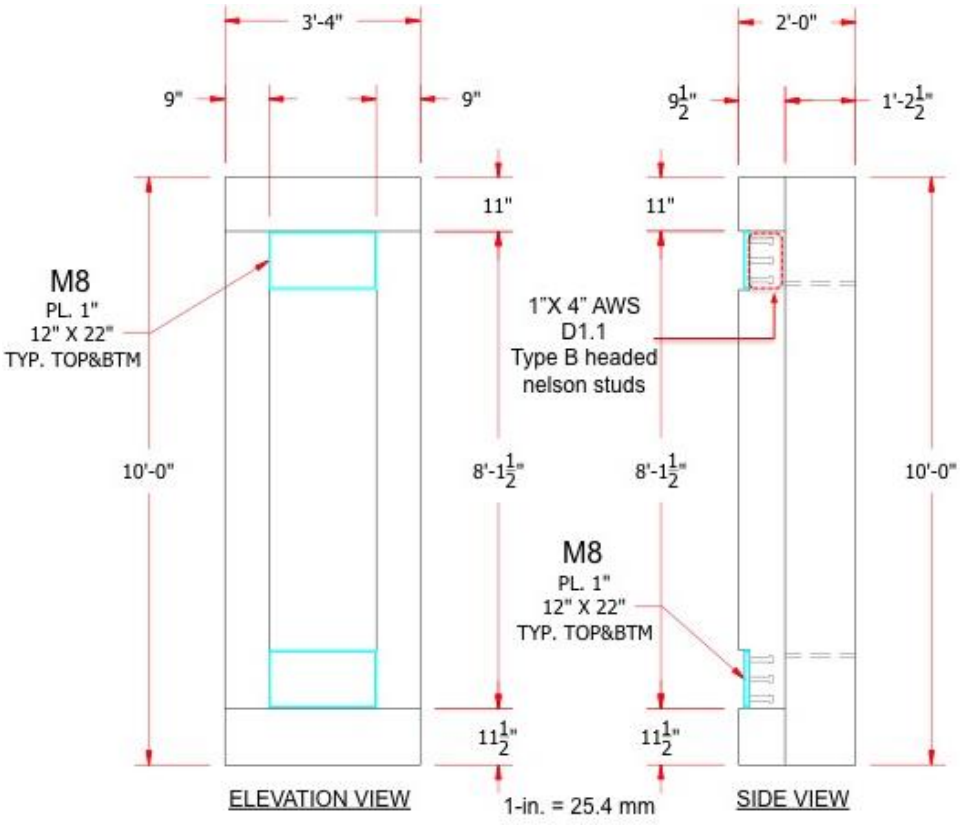

Figure 2.7 Test specimen design of center column/stud

Column reinforcement consisted of multiple A706 #4 (#13) Grade 60 steel hoops, spaced vertically at every 4 in. (101.6 mm), as well as 22 - A706 #8 (#25) Grade 60 steel bars positioned parallel to the vertical edge, spaced at every 5 in. (127 mm) around the column perimeter. In addition, three A36 steel plates were embedded in the concrete, two 22-in. (558.8-mm) by 12-in. (304.8-mm) by 1-in. (25.4-mm) steel plates at the front face of the columns, and one 24-in. (609.6-mm) by 40-in. (1016-mm) by 1-in. (25.4-mm) steel plate at the base. Each of the steel plates was embedded to the column using nine 1-in. (25.4-mm) by 4-in. AWS D1.1 Type B headed nelson studs (AWS, 2010). In effort to facilitate the discussion, the embedded steel plates at the front face of the columns were

denoted as M8. Additionally, the column vertical reinforcing bars were welded to the A36 steel base plates.

2.3.3 Design of beam-to-column moment connection

The PCI-developed prototype alternative beam-to-column connection ductile design was implemented in the test specimen. The moment resistant connection detail consisted of A36 steel link plates welded to the embedded M6 and M7 A36 steel angles at each corner of the spandrel beams, as well to the embedded M8 A36 steel plates in the columns. Figure 2.8 (Section B-B) presents the connection details. A total of eight 12-in.- (304.8-mm) long by 5.5-in.- (139.7-mm-) high by 1-in.- (25.4-mm-) A36 steel link plates were welded to the beam and column plates using fillet welds, as specified in Figure 2.8 (Section B-B). In addition, eight ASTM A193 Grade B7 steel rods were incorporated into the design of the prototype moment resistant frame in an effort to provide torsional resistant. These rods were designed to be installed through the spandrel beams and columns are shown in Figure 2.5 (top view).

This connection design was intended to enhance the rotational capacity of the moment frame by providing additional ductility at the connections. This enhancement in rotational capacity could represent an advancement of the state of the art, in particular in the design of precast concrete multi-story buildings, since it could minimize the potential of precast concrete structures to undergo progressive collapse behavior after a local failure of an exterior critical element, i.e., column.

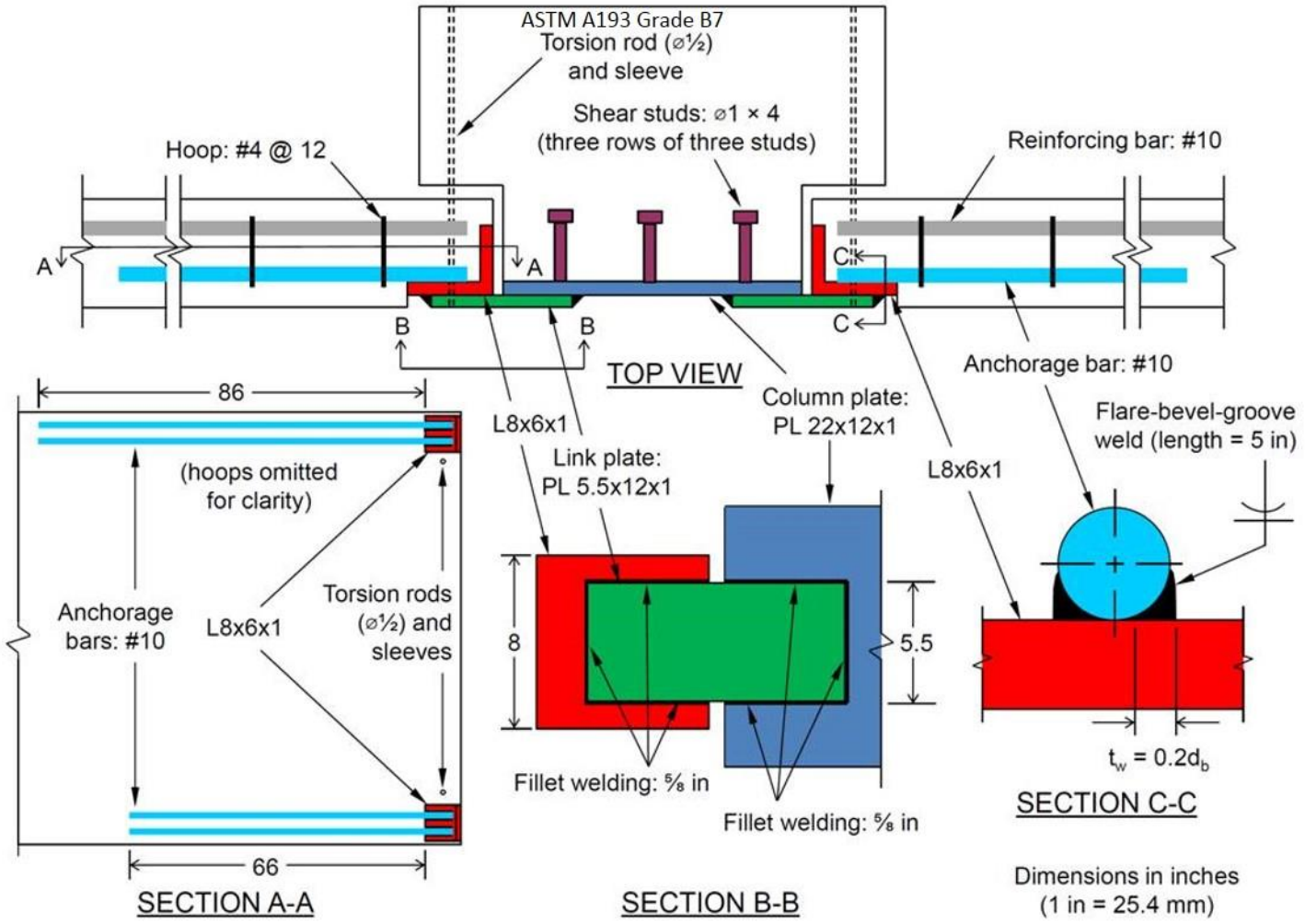

Figure 2.8 Test specimen connection details (Main et al., 2015)

CHAPTER III

EXPERIMENTAL PROCEDURES

This chapter discusses the materials used and the fabrication of the test specimen. The instrumentation plan and the test procedure are also described.

3.1 Materials

3.1.1 Concrete

All precast structural members were cast using concrete with a specified compressive strength of 6,000 psi (41.4 MPa). Type III cement was used with natural sand. The maximum coarse aggregate size used was 1 in. (24.5 mm), with a nominal maximum size of 0.75 in. (19 mm). The water-cement ratio by weight was 0.37. The average air content percentage (%) was 4.5%. The mix was designed to give a concrete slump of 4 in. (101.6 mm).

3.1.2 Steel reinforcement and steel components

The type reinforcement used in the fabrication of the test specimen was ASTM A706 Grade 60. The A706 bars are deformed and plain low-alloy weldable steel bars for concrete reinforcement applications. The A706 bars have specified minimum yield and tensile strengths of 60 ksi (413.7 MPa) and 80 ksi (551.58 MPa), respectively, with a nominal yield and ultimate strains of 0.0021 in./in. and 0.120 in /in., respectively. The

reinforcement detail of the OMRF contains a variety of A706 bar size designations, ranging from #4 (#13) to #10 (#32).

In addition, a number of ASTM A36 steel plates were embedded in the precast concrete elements. These A36 steel plates had a yield strength of 36 ksi (250 MPa). Moreover, four ASTM A193 Grade B7 bolts were installed through sleeves in the beams and columns on each beam to provide torsion restraint for the spandrel beams (Figure 3.1). Each rod had a yield strength of 125 ksi (862 MPa).

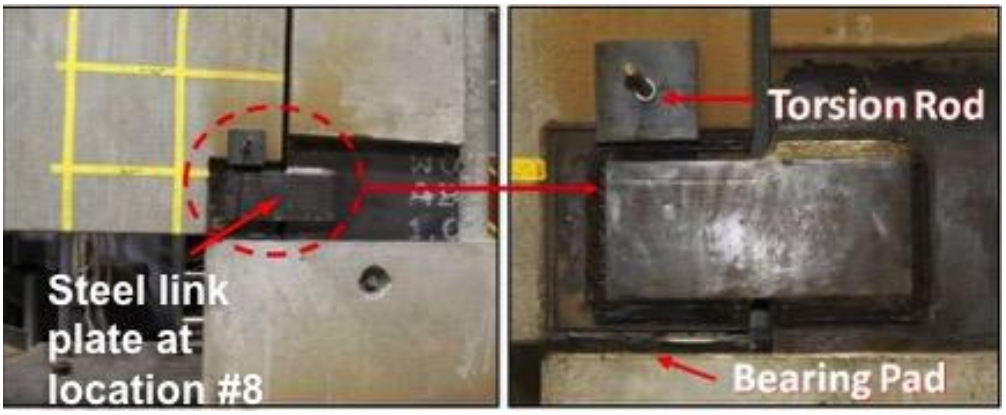

Figure 3.1 Torsion rods across beam and column, and bearing pad at location #8

3.1.3 Material tests

3.1.3.1 Concrete mechanical properties

Twenty-four standard 6-in. (152.4-mm) by 12-in. (304.8-mm) concrete control cylinders were cast during the fabrication of the OMRF precast elements. Twelve control cylinders were used to examine the precast concrete mix compressive strength and the other twelve to examine its tensile capacity by conducting splitting tensile tests.

Both material testing procedures were conducted at 28 days of concrete curing time. Results of these concrete control cylinder tests are presented in Appendix B. Table B.1 shows the compressive strength data of the tested cylinders, and Table B.2 shows the tensile strength data. The average measured 28-day compressive strength of concrete was 5653 psi (38.9 MPa), and the average 28-day splitting tensile strength of concrete was 457 psi (3.1 MPa).

3.1.3.2 Steel reinforcement mechanical properties

A designated number of A706 steel bars were sent to Bodycote for tensile testing. Bodycote then tasked Exova Inc. to conduct all the experiments following the ASTM E8 procedure. Table 3.1 shows the ultimate strain recorded from the tensile tests. Figure B.1 through Figure B.6 show the strain response of the tested A706 samples. The average yield (*fy*) and ultimate strength (*fu*) were 71.84 ksi (495.32 MPa) and 105.69 ksi (728.71 MPa), respectively. These values were 20% higher than the nominal yield strength and 32% higher than the minimum tensile strength.

The A706 stress-strain curves shown in Figure B.1 through Figure B.6 displayed a sharp yield point followed by a gradual second-degree curve that extended to a strain of 0.180 in./in., 50% higher than the nominal tensile strength value. The average elongation at rupture over a 2-in. (50.8-mm) gauge length was 24% and was 26% over the 1-in. (25.4-mm) gauge length.

Table 3.1 Tensile strength values of reinforcement bars in test specimen – ASTM E8

Bar Size	Yield Strength, *fy* ksi (MPa)	Tensile Strength, *fu* ksi (MPa)	Fracture Strain, %EL
#10 (#32)	69.6 (479.9)	105.2 (725.3)	24% [1]
#10 (#32)	69.0 (475.7)	101.4 (699.1)	24% [1]
#8 (#25)	73.0 (503.3)	107.7 (742.6)	24% [1]
#8 (#25)	73.9 (509.5)	107.5 (741.2)	24% [1]
#4 (#13)	72.7 (501.2)	106.4 (733.6)	26% [2]
#4 (#13)	75.6 (521.2)	106.4 (733.6)	27% [2]

[1]Gauge length: 2 in. (51 mm)
[2]Gauge length: 1 in. (25 mm)

3.2 Fabrication of test specimen

The beams and columns were prefabricated and cured off-site from ERDC's testing facility. After the 28 days of curing time, five of the structural members were transported to Vicksburg, MS, for assembling and testing. Metromont Inc. was also responsible for the forming, casting, and curing of the OMRF test specimen.

3.2.1 Forming of precast structural elements

The first step in the fabrication of the test specimen was to construct five plywood formworks. The first two formworks were built for the spandrel beams with the dimensions of 277-in. (7035.8-mm) long by 96-in. (2438.4 mm) high by 9-in. (228.6-mm) deep. The beam formworks were built flat along the 96-in. (2438.4-mm) width over a special vibrating table. Then, the three columns formworks were built flat along their back over a similar vibrating table.

All the formworks were fabricated of 0.75-in.- (19.05-mm-) thick plywood panels and multiple 2-in.- (50.8-mm-) by 4-in.- (101.6-mm-) wooded studs. The formworks were designed to be a very rigid structure that would withstand the process of placing the reinforcement, the concreting, and vibrating of the structure without undergoing detectable deflection. After the formworks were completed, the reinforcement was placed and tied as specified in the design drawings (Appendix C).

3.2.2 Fabricating and placing the reinforcement and steel components

3.2.2.1 Placing of spandrel beam reinforcement and steel components

The first reinforcement placed on the formwork was that for the two spandrel beams. The assembled spandrel beam reinforcement consisted of multiple #4 (#13) Grade 60 longitudinal bars and hoops, 16 #10 (#32) Grade 60 bars cut at different lengths, and four embedded A36 L8x6x1 steel angles as shown in Figure 2.5 and Figure 3.2.

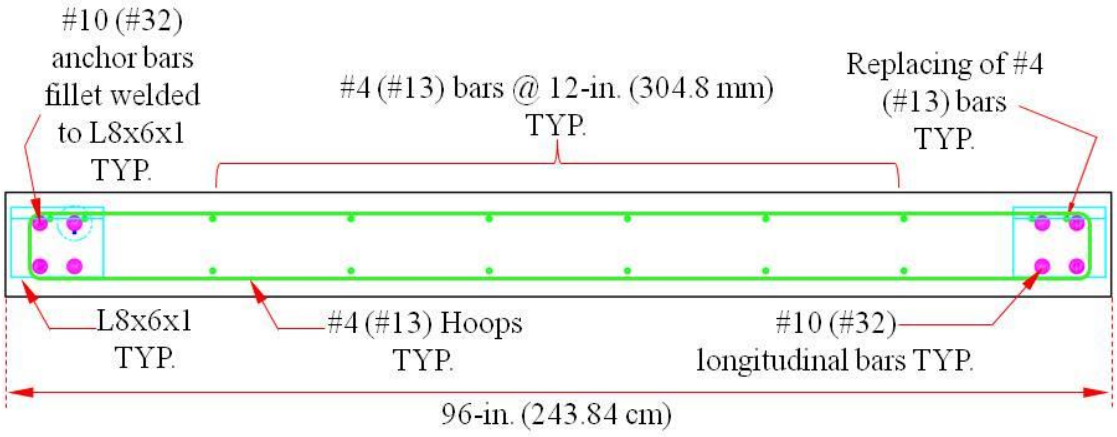

Figure 3.2 Spandrel beams reinforcement details

First, multiple #4 (#13) Grade 60 bars were cut and bent in accordance with the specification drawings to form hoops. These #4 (#13) hoops were then placed on the formworks at 12 in. (304.8 mm) apart, parallel to the 96-in. (2438.4-mm) dimension.

Second, 40 #4 (#13) Grade 60 bars were cut to length. Twenty of these lengths were then placed, spaced, and tied securely at about 12 in. (304.8 mm) apart over multiple plastic 2-in.- (50.8-mm-) high reinforcement chairs spread across the formworks to form the bottom bar mat.

Third, 8 #10 (#32) Grade 60 longitudinal bars were cut to length, and all the strain gauges were properly installed as specified in the instrumentation plan presented in Section 3.4. Four of these #10 (#32) bars were then placed, spaced, and tied securely on the formworks following the design specifications to complete the bottom mats.

Fourth, the top #4 (#13) Grade 60 longitudinal bars shown in Figure 3.2 were placed in a similar fashion over multiple plastic 5-in.- (127-mm-) high plastic reinforcement chairs across the formwork.

And fifth, 16 A706 #10 (#32) Grade 60 bars were selected; eight were cut to a length of 66 in. (1676.4 mm) and the other eight to 92 in. (2336.8 mm). These bars were welded using fillet welds in equal pairs to A36 L8x6x1 steel angles as shown in Figure 2.8 (Section A-A). Before placing the angles, all the strain gauges were properly attached to the anchor bars following the instrumentation plan. Then, these M6 and M7 steel angles were positioned at the top corners of the spandrel beams and tied to the formwork. Once the anchor bars and angles were positioned, the remaining #4 (#13) Grade 60 hoops were placed, spaced, and tied on top to complete the reinforcement.

In an effort to facilitate the transportation of the beams to the testing facility as well as their assembling into the frame, a number of lifting components were tied to the reinforcement prior to concrete placement. Four MB Dogbone 4T anchors, 5.5-in. (139.7-mm) long, were installed across the front face of the beams to lift them in a horizontal position. In addition, two BS Italia 6T TS Safelift were positioned over the top of the beam and anchored to the formwork to enable the vertical lifting of the beams during the assembling process.

All the instrumentation cables were securely placed along the bars and then through the bottom of the formwork. Each cable was labeled to ensure proper identification in the instrumentation and testing phases. This completed the placing of the spandrel beams' reinforcement and steel components.

3.2.2.2 Column reinforcement and steel components

Once the placement of the reinforcement in both spandrel beams was completed, the fabrication and placement of the columns' reinforcement began. Contrary to the spandrel beams, the reinforcement of the columns was assembled outside the formwork and then placed in as a whole. The assembled column reinforcement consisting of multiple #4 (#13) Grade 60 hoops spaced at every 4 in. (101.6 mm) along the columns height, and 22 #8 (#25) Grade 60 vertical bars cut at lengths are shown in Figure 2.3. In addition to the reinforcement, two A36 steel plates were positioned and tied over the reinforcement prior to concrete placement.

First, multiple #4 (#13) Grade 60 bars were cut and bent in accordance with the specification drawings to form hoops. These #4 (#13) Grade 60 hoops were then placed on the formworks spaced at 4 in. (101.6 mm) along the height.

Second, 66 #8 (#25) Grade 60 vertical bars were cut to length, then placed, spaced, and tied to the hoops, at 22 #8 (#32) Grade 60 vertical bars per column. Once the rebar cage was completed, the reinforcement was placed inside the column's formworks over multiple 2-in. (101.6-mm) plastic reinforcement chairs.

And third, after securing the cage inside the formwork, the nelson studs were welded to the A36 steel plates. These M8 steel plates (two plates per column) were then positioned and tied over the reinforcement on the formwork.

To facilitate the transportation of the columns to the testing facility as well as their assembling into the frame, a number of lifting components were tied to the reinforcement prior concreting. Two MB Dogbone 4T anchors, 5.5-in. (139.7-mm) long, were installed across the front face of the columns to lift them in a horizontal position. In addition, a triple strand loop with a diameter of 0.5 in. (12.7 mm) was positioned and tied to the reinforcement at the top of the precast elements to enable the vertical lifting of the columns during the assembling process. This completed the placing of the columns' reinforcement and steel components.

3.2.3 Concrete placement in structural elements

The concrete for the beams and columns was then placed on May 29, 2009 in one continuous operation, taking about 4 hours total. The concrete was mixed in concrete trucks with a capacity of 8 cyd (6.12 m^3) per truck. Four truck batches of 8 cyd (6.12 m^3) were used to cast the structural elements. The proportions of the mix used are given in Section 3.1. Six control cylinders were cast from each concrete truck batch following the procedure specified in the ASTM C39 (2009).

The concrete was placed first in the spandrel beam and then in the columns. Figure 3.3 shows a frame taken from the first spandrel beam during the placement process. Figure 3.4 shows the center column right before was cast. The concrete was adequately compacted using an external vibrator, better known as a vibrating table in the precast industry. Vibration tables are rigid decks mounted on flexible supports that operate at 3,000 to 6,000 vibrations per minute (vpm).

As previously mentioned, the formworks were built on top of these vibrating tables. These external vibrators were operating continuously throughout concrete placement. During the initial stages of the concrete placement, the vibrating tables were set to operate at a rate of 3,000 vpm but then were gradually increased to 4,500 vpm. The procedure allowed adequate consolidation of the concrete between and around the reinforcement.

After the concrete was placed and vibrated, the top surfaces were finish hours later as specified in the design drawings. The tops of the spandrel beams were finished using a light broom, and the tops of the columns with a sack rub finish. The formworks were removed within 72 hours, and the elements were then placed inside an oven for special curing for an additional 25 to 26 days. Following the curing time, all five of the structural members were transported to Vicksburg, MS for assembling and testing.

Figure 3.3 Concrete placement in OMRF's spandrel beam

Figure 3.4 Concrete placement in OMRF's center column/stud

3.2.4 Assembly of the OMRF test specimen

The first steps for assembling the OMRF test specimen were to erect, align, and weld both end-columns to the reaction structure's footing as shown in Figure 3.5. The bottom 24-in. (609.6-mm) by 40-in. (1016-mm) by 1-in. (25.4-mm) A36 steel base plates embedded in the end-columns were welded using fillet welds around the base plates' perimeters to the reaction structure's footings. Then, the center column/stud was securely suspended in place over the two, 2-ton (1.81-tonne) hydraulic jacks that were anchored to a steel table, as shown in Figure 3.6. After successfully positioning the center column/stud, four bearing pads with a thickness of 0.5 in. (12.25 mm) each were then placed over the columns notches to serve as energy absorbers at the interface of the spandrel beams and columns.

Once the bearing pads were placed, the spandrel beams were assembled. The spandrel beams were carefully inserted in the column notches over the bearing pads using a 30-ton (27.22-tonne) crane as shown in Figure 3.7. A clearance of 1 in. (25.4 mm) was allowed between the columns and the spandrel beams. Then, the beam-to-column connections (steel links plates) were welded in place.

The steel link plates at location #7 and #8 (see Figure 2.3) were the first two connection plates welded between the M6 steel angles and the M8 steel plates. Next, the steel link plates at locations #1 and #5 were welded into place, followed by the steel link plates at locations #2, #3, #4, and #5. Each steel link plate was positioned over the embedded steel components to ensure an equal welding length, as illustrated in Figure 2.8 (Section B-B). All steel link plate joints were welded using fillet welds with a thickness of 0.625 in. (15.9 mm).

Figure 3.5 Welding of end-columns to reaction structure's footing

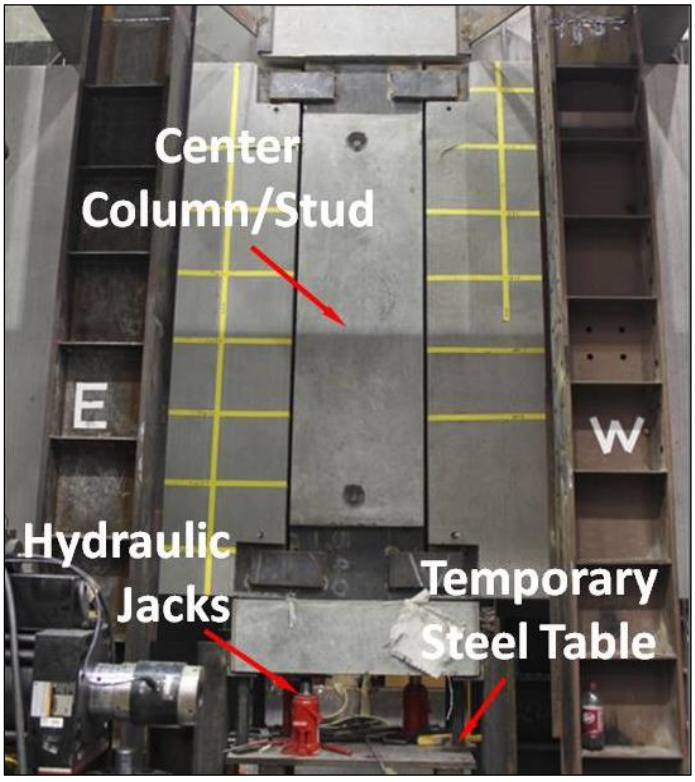

Figure 3.6 Assembly of unsupported center column

After successfully welding the steel link plates, the ASTM A193 Grade B7 torsion rods were inserted through the torsion sleeves and securely tightened with nuts on both sides. These torsion rods were inserted through a prefabricated sleeve to provide torsional resistance in the assembly as shown Figure 3.1.

Figure 3.7 Assembly of spandrel beams into the moment frame

3.3 Testing procedure

3.3.1 Reaction structure and loading device

A schematic view of the test setup is shown in Figure 3.8. A MTS hydraulic actuator (ram), shown in Figure 3.9, with a capacity of 600 kips (2669 kN) and a 20-in. (508-mm) stroke was chosen as the loading device to apply the slowly-increasing static load over the unsupported center column/stud. The load was applied under a vertical displacement-control scenario at an initial rate of 0.02 in./min.

In Figure 3.8 and Figure 3.10, it is observed that the horizontal movements of the ram's steel plate was restrained by four steel columns positioned at each corner of the plate. A roller-bearing support arrangement at the four corners of the ram's steel plate allowed free vertical displacement of the member along the four steel columns (see Figure 3.11). The ram's steel plate also contributed to restraining the horizontal movement of the center column, thereby keeping the applied load in the vertical direction and limiting eccentricity of the load.

A pair of steel plates was positioned at the lower end of the center column/stud, against both sides, to restrain out-of-plane motion. These steel plates were anchored to the rail steel columns by steel angles welded to both the steel plate restraints and the steel rail columns. This setup is shown in Figure 3.12(a) and (b). Two 600-in.-long (15240 mm) W16x67 steel beams shown in green in Figure 3.8, were connected by four short steel beams, shown in blue, to form a steel framework. Figure 3.13 shows the location of the short beams.

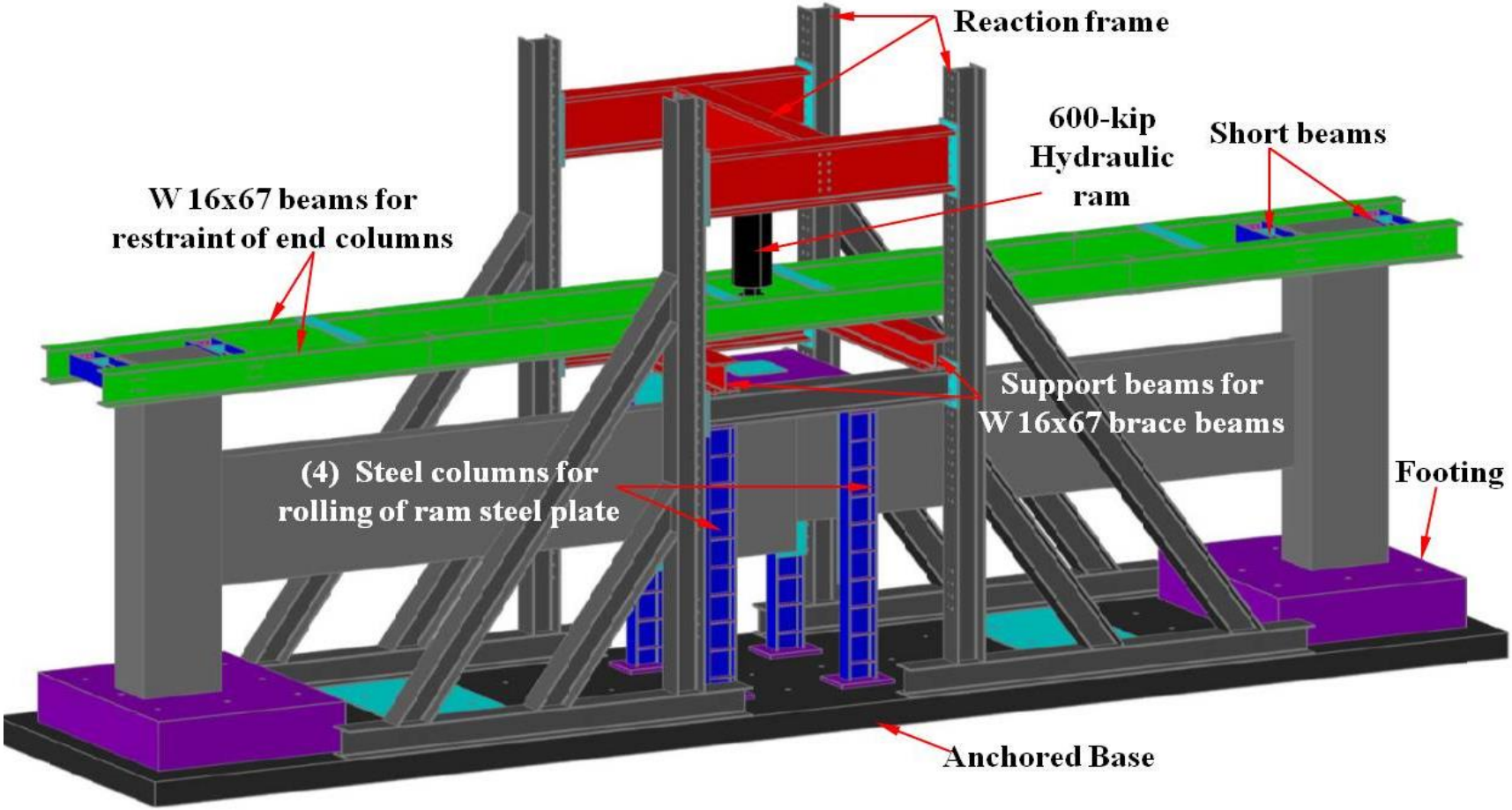

Figure 3.8 OMRF's setup in ERDC reaction structure

This steel framework was then positioned along the top of the test specimen with a clearance of 1 in. (25.4 mm) between the surface of the end-columns and the short beams. The purpose of this upper steel framework was to restrain the end-columns from buckling or moving horizontally. Schematic views of the OMRF test specimen depicting the idealized boundary conditions are shown in Figure 3.14(a) and (b).

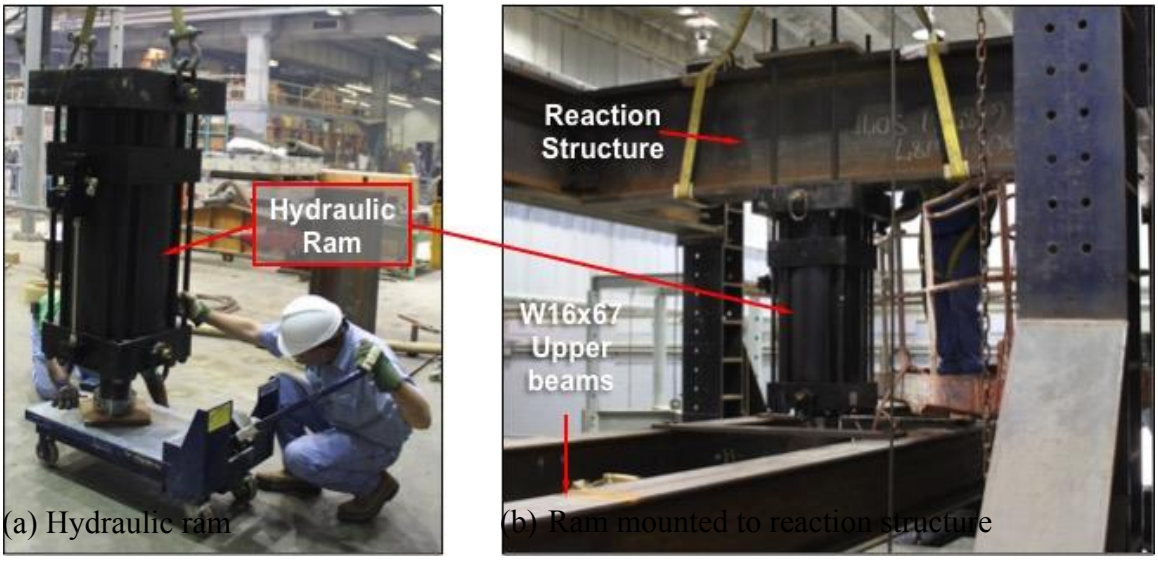

Figure 3.9 ERDC's 600-kip (267-kN) hydraulic ram

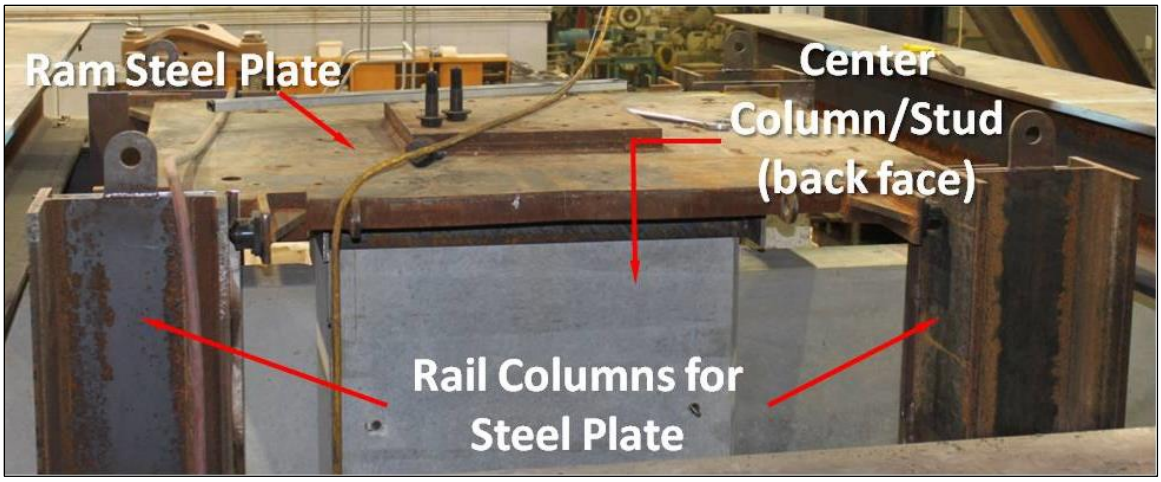

Figure 3.10 Ram steel plate and rail columns of reaction structure

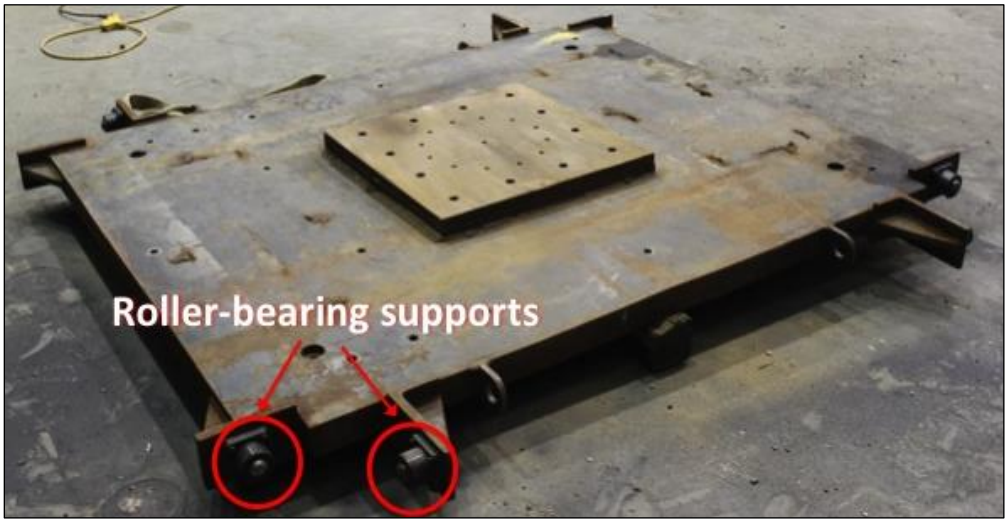

Figure 3.11 Roller-bearing supports in ram steel plate

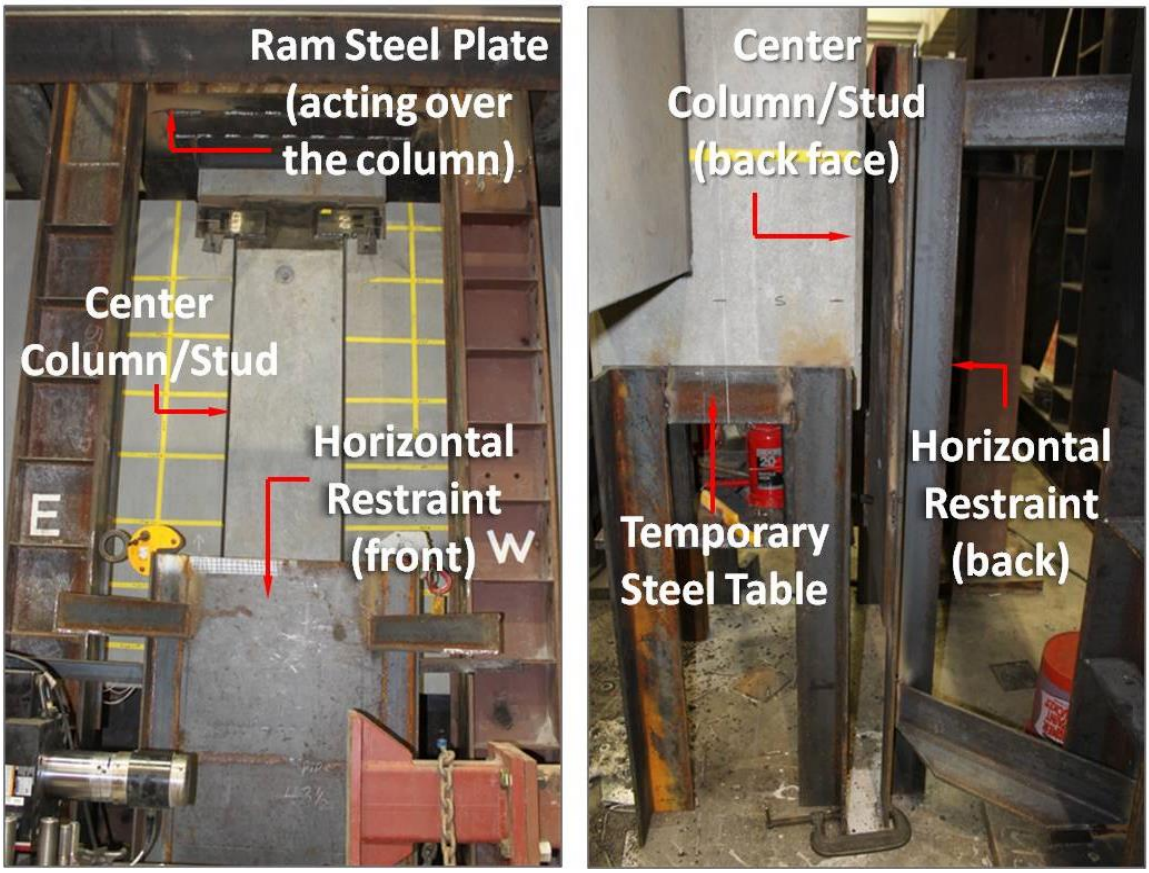

(a) Horizontal restraint at the front face of center column

(b) Horizontal restraint at the back face of center column

Figure 3.12 Reaction structure horizontal restraints at center column/stud: (a) front face, (b) back face

Figure 3.13 Reaction structure restraint short beams

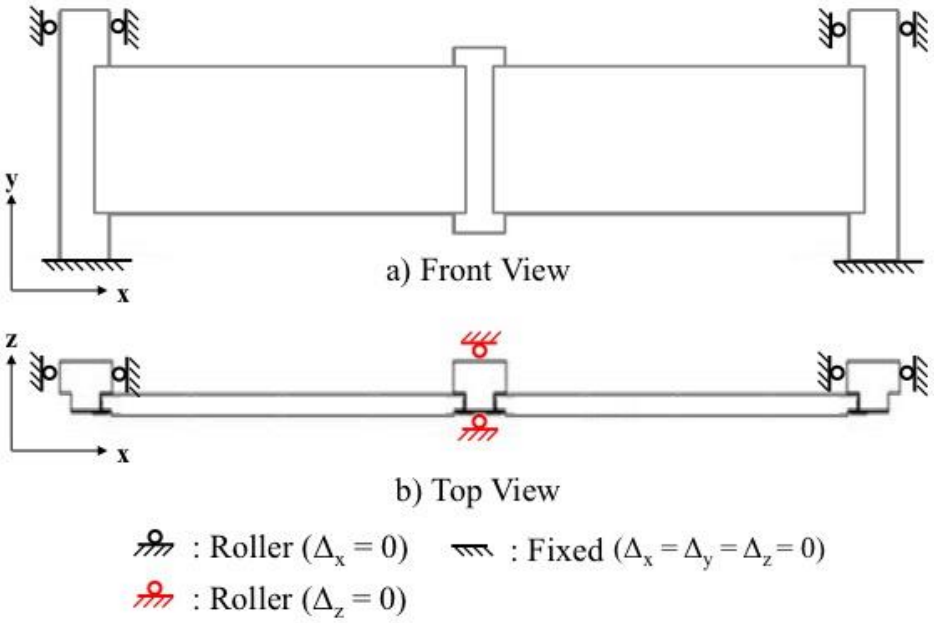

Figure 3.14 OMRF's idealized boundary conditions: (a) front view, (b) top view

3.4 Test measurements and instrumentation

After successfully completing the fabrication and assembling of the OMRF test specimen in the reaction structure, the instrumentation phase was initiated. Seventy-one recording channels were used in the execution of the experiment. Fifty-seven of these channels were recorded at a sample rate of 40 samples per second (Hz), eight at a high-speed sample rate of 2 MHz, and six on both sample rates. Table 3.2 describes the type of measurement, channel labeling, and number of channels for each of the instrumentation components, as well as Table A.1 and Table A.2 in Appendix A.

Table 3.2 Instrumentation plan matrix

Type of Gauge	Measurement Number	Number of Channels
Load Cell	L-95A	1
Differential Pressure Gauge	L-95B	1
"String Potentiometer" Gauges	D-83, 85, 86, 88	4
Linear Variable Differential Transformer (LVDT)	LVDT-81, 90	2
Inclinometers	R-91, 92, 93, 94	4
Internal Strain Gauges	εH-41 - 127	16
Rosette External Strain Gauges		24
Single External Strain Gauges		9
Load Cells for Torsion Bar Tensile Loads	T1, T2	2
Acoustic Emission Sensors	AE1, AE2	2
Accelerometers	L1, L2	6
Total:		**71**

The data included information on the applied load, column/beam displacements, joint rotations, strains on reinforcement bars and the exterior steel connections plates, tension in the torsion bars connecting the beams to the columns, and acoustic emissions near the center column-beam connections.

The term “pseudo-static response” was used to reference the data recorded at a sample rate of 40 Hz. The term “high-frequency response” was used to reference the data recorded at 2 MHz.

3.4.1 Pseudo-static response channels

Sixty-one channels were recorded at a frequency rate of 40 Hz. These channels were designated to record the applied loads, vertical and horizontal displacemenst, rotations, strain measurements, and torsion forces in the test specimen through the execution of the test.

3.4.1.1 Load cell and differential pressure gauge measurements

As the MTS hydraulic ram was used to apply a vertical downward quasi-static displacement to the unsupported center column/stud, the load was been recorded using two different instruments. One of those instruments was an external 400-kip (1779-kN) load cell installed at the end of the ram (Figure 3.15), and the other was a differential pressure sensor with a capacity of 3,000 psi (34.5 MPa) inside the servo-hydraulic actuator (ram). The differential pressure sensor recorded the hydraulic pressure exerted on the piston rod.

After successfully installing the load cell at the end of the ram’s stroke, the system was positioned over the center column/stud and securely fastened to the reaction structure. Figure 3.9(b) shows the ram anchored in the reaction structure.

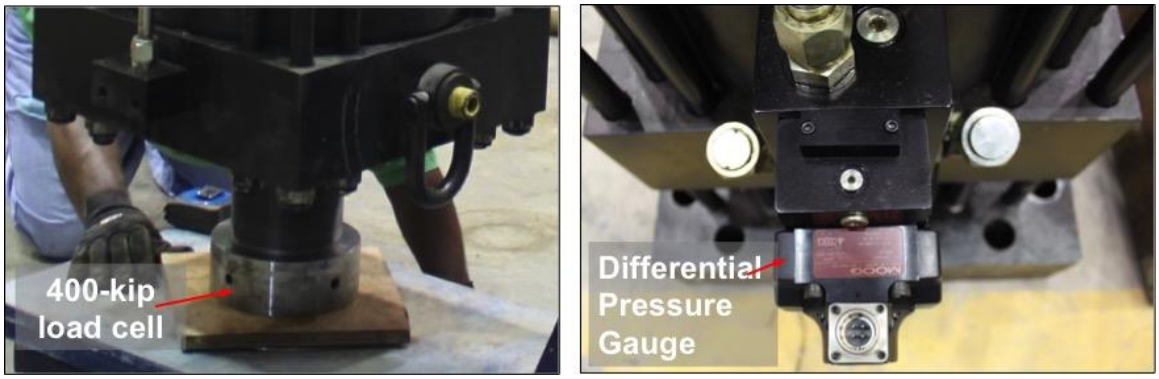

(a) Load Cell (b) Differential Pressure Gauge

Figure 3.15 Load Cell (400-kip) (1779-kN) and differential pressure sensor

3.4.1.2 Displacement and deflection measurements

Deflections were measured at six locations along the OMRF test specimen, two vertical measurements from the bottom of the spandrel beams, at mid-span, and four measurements at the columns, i.e., two vertical measurements from below the center column/stud, and two horizontal measurements at the end-columns at mid-elevation. The locations and labeling of these displacement gauges is shown in Figure 3.16.

The vertical displacement measurements were obtained by four string potentiometers with a 72-in. (1.8-m) range with an accuracy of 0.001 in. (0.025 mm). The horizontal measurements were made by two linear variable differential transformers (LVDTs) with a range of 6 in. (152 mm) and an accuracy of 0.005 in. (0.127 mm) as depicted in Figure 3.16.

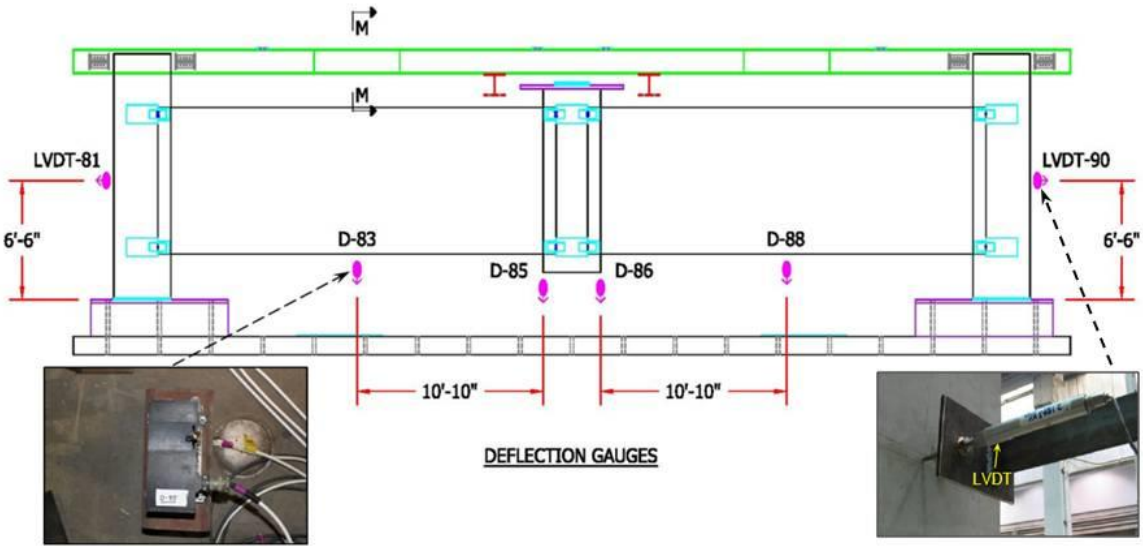

Figure 3.16 Location of displacement gauges in the test specimen

3.4.1.3 Inclinometers

Rotational measurements were made with four digital inclinometers installed on top of the spandrel beams. The locations and labeling of these instruments is shown in Figure 3.17. The inclinometers were installed at 18 in. (45 cm) offsets from the columns on top of the concrete beams on each corner for two rotational gauges on each beam. These instruments were meant to measure the rotation at the supports as the displacements of the OMRF test specimen increased.

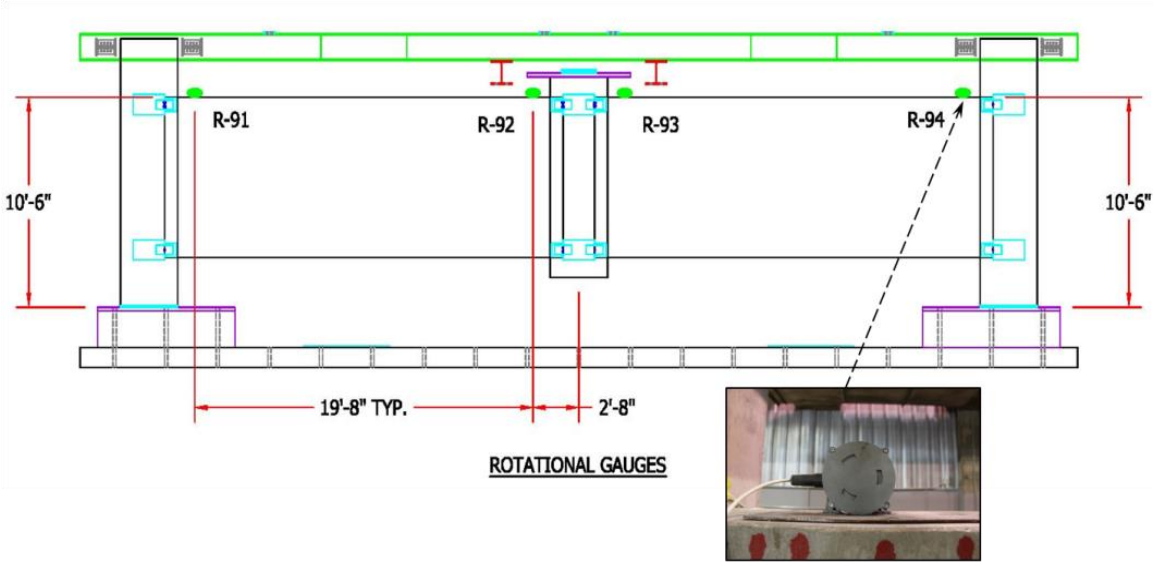

Figure 3.17 Location of inclinometers gauges in the test specimen

3.4.1.4 Strain measurements

The locations of the strain gauges placed on the #10 (#32) Grade 60 reinforcement bars and the steel link plates are shown in Figure 3.18 through Figure 3.22. To facilitate the discussion, the strain gauges attached to the reinforcement were denoted as internal strain gauges, and the ones on the steel link plates as external strain gauges.

3.4.1.4.1 Internal strain gauges

Each beam contained eight internal strain gauges placed on steel reinforcing bars. Figure 3.18 through Figure 3.21 depict the locations of the internal strain gauges attached to the reinforcement bars in the spandrel beams.

The reinforcement strains were measured using Micro-Measurements/ Vishay Inc. EA-06-250BF-350. These gauges had a nominal grid size of 0.25-in. (6.35-mm) length by 0.125-in. (3.18-mm) width and a resistance of 350 ± 0.3% ohms. The bars to be

gauged in the spandrel beams were prepared for gauging by cleaning and lightly sanding with emery cloth at the gauge locations. The gauges were then bonded to the bars with a heat-curing epoxy. After the installed strain gauges were inspected, the locations were waterproofed using several layers of a synthetic compound.

Beam-L contained two internal strain gauges at the right bottom corner of the beam attached to the #10 (#32) Grade 60 top anchor bar of the M7 A36 steel angle, two at the left top corner attached to the #10 (#32) Grade 60 top anchor bar of the M6 A36 steel angle, and four at mid-span on the outer most #10 (#32) Grade 60 longitudinal (flexural) reinforcing bars (two gauges on top and two on bottom) as shown in Figure 3.18 and Figure 3.19.

Beam-R contained two internal strain gauges at the left bottom corner of the beam attached to the #10 (#32) Grade 60 top anchor bar of the M7 angle (Figure 3.20), two at the right top corner attached to the #10 (#32) Grade 60 top anchor bar of the M6 angle (Figure 3.20), and four at mid-span on the outer most #10 (#32) Grade 60 longitudinal (flexural) reinforcement bars, (two on the top and two on the bottom) (Figure 3.21). All of the internal strain gauges were installed in pairs at three and nine o'clock on the rebar cross-sectional area. Figure 3.20 and Figure 3.21 show the location and labeling of the #10 (#32) Grade 60 anchor bars' strain gauges.

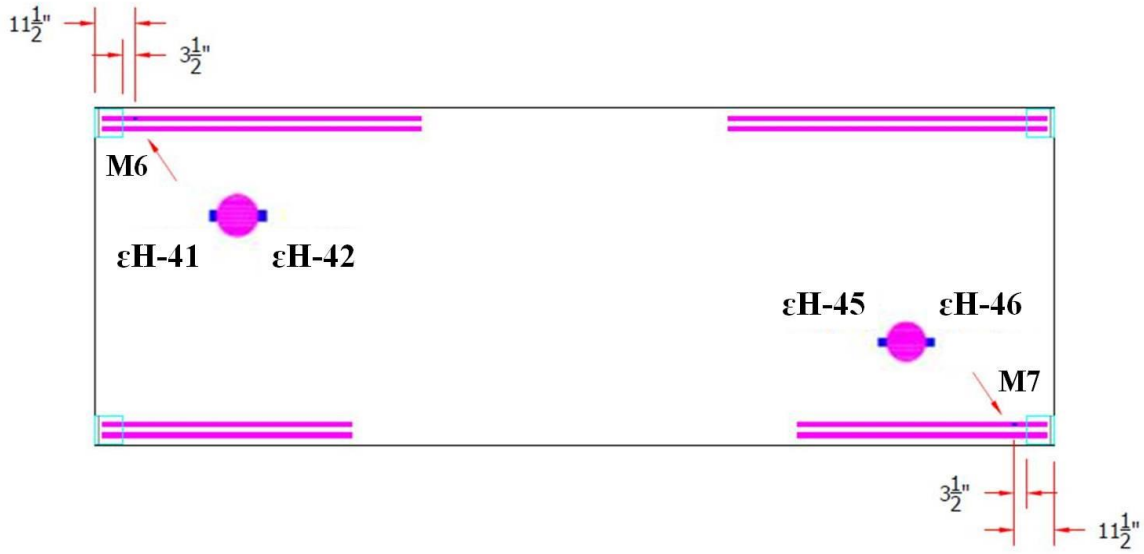

Figure 3.18 Beam-L – Internal strain gauges on steel anchor bars at M6 and M7 plates

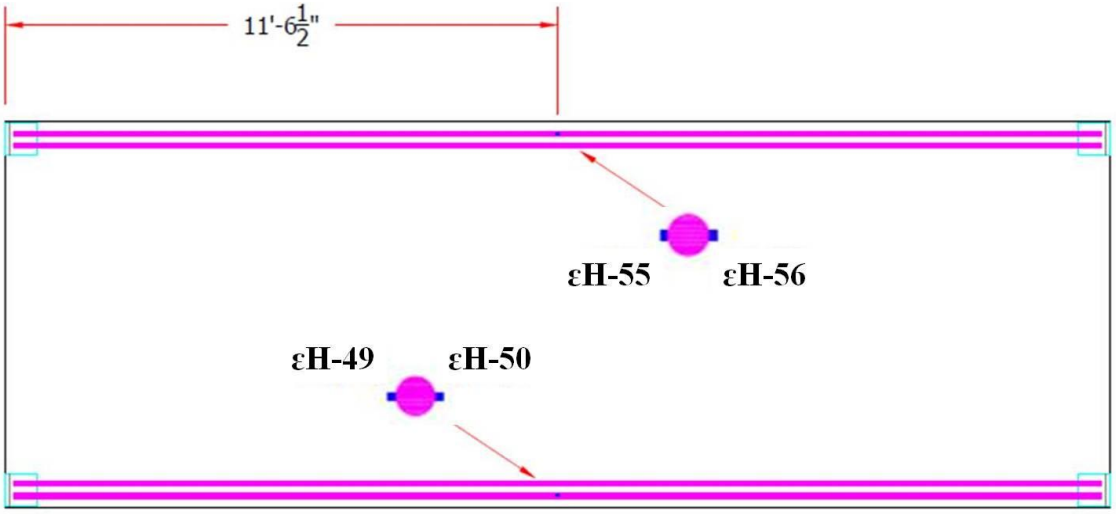

Figure 3.19 Beam-L – Internal strain gauges at mid span of long anchor bars

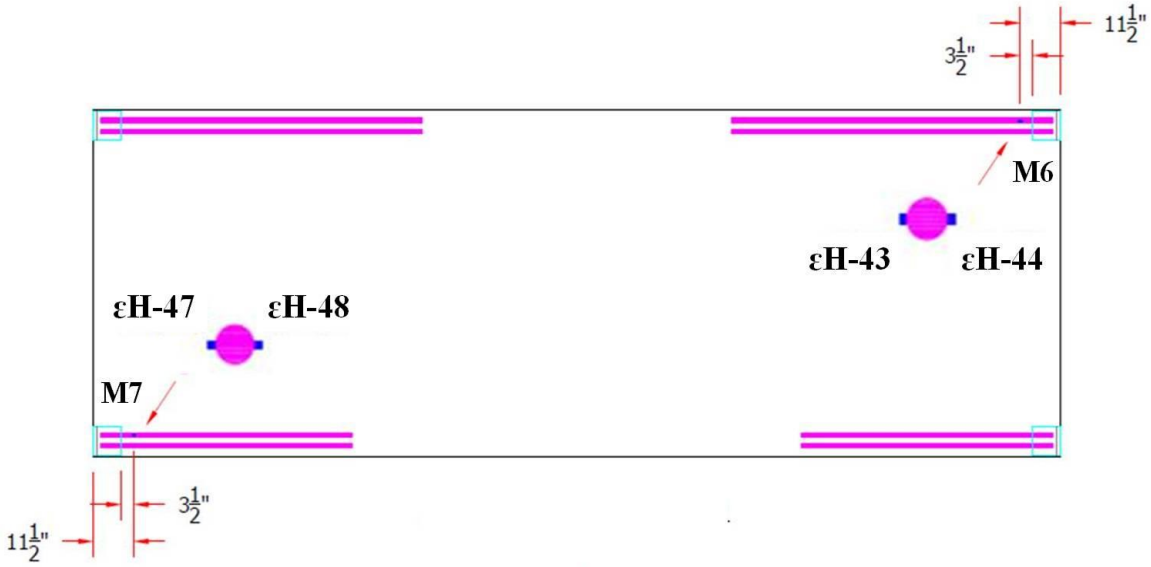

Figure 3.20 Beam-R – strain gauges on steel anchor bars at M6 and M7 plates

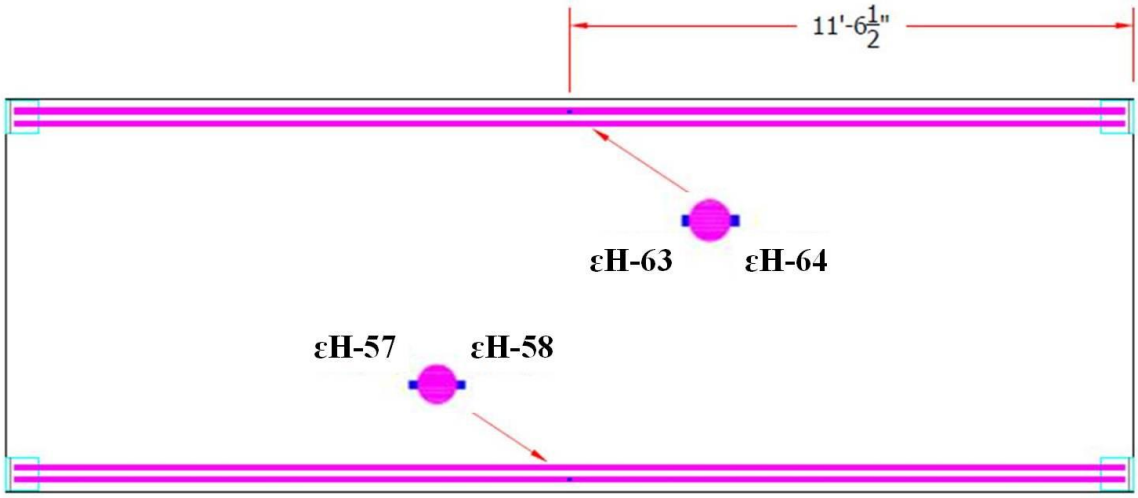

Figure 3.21 Beam-R –strain gauges at mid span of #10 (#32) flexural bars

3.4.1.4.2 External strain gauges

Thirty-three external strain gauges were employed in the execution of the experiment. Thirty of them were on the front face of the steel link plates and the other three on the upper W16x67 steel beam, at mid-span.

Two different types of strain gauges were placed on the steel link plates. On some of these plates, Micro-Measurements/Vishay Inc. CEA-06-250UR Strain Rosettes (consisting of three strain gauges at 45°) were used. Micro-Measurements/Vishay Inc. CEA-06-375UW single strain gauges were also used. The CEA-06-250UR strain gauge had a nominal grid size of 0.25 in. (6.35 mm) length by 0.120 in. (3.05 mm) width and a resistance of 350 ± 0.3%. The CEA-06-375UW single strain gauge had a nominal grid size of 0.375-in. (9.53-mm) length by 0.180-in. (4.57-mm) width and a similar resistance of 350 ± 0.3%. The installation procedure followed in the placement of the external gauges was very similar to the one followed for the reinforcement strain gauges.

Figure 3.22 shows an overview layout of each location where the strain gauges were positioned in the steel link plates, as well as the strain gauge configurations used at each location.

In addition, three additional CEA-06-375UW single strain gauges were installed at mid-span on one of the upper W16x67 steel beams that braced the end-columns. These gauges measured the axial strain in this beam. The strain recorded in this bracing beam is due to forces caused by deformation of the end columns toward each other in the near vertical plane of the beam deformation. Figure 3.22, (Section BM), shows the location of each of the single strain gauges installed on the upper brace steel beam.

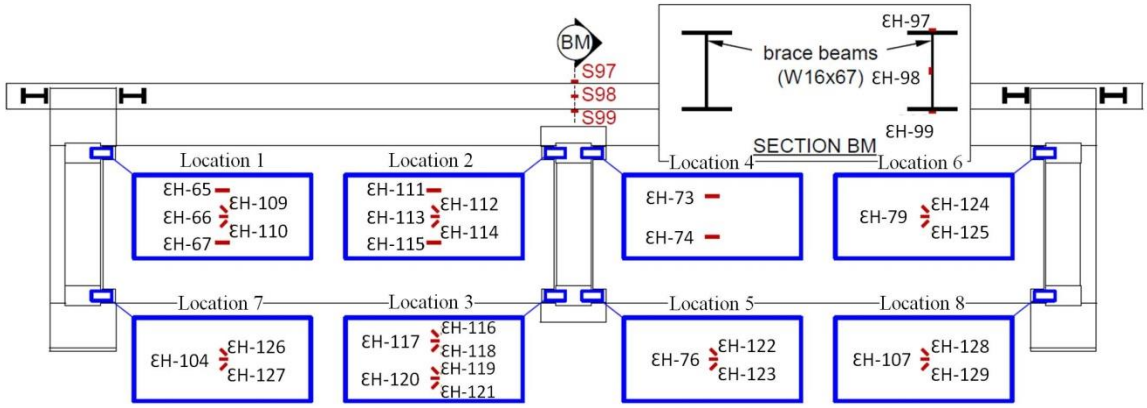

Figure 3.22 Location of strain gauges on link steel plates and upper brace steel beam

3.4.1.5 Tension in torsion bars

In an effort to measure the tension forces associated with the rotation of the OMRF test specimen over its x-axis (as defined in Figure 3.14), two "doughnut" load cells were installed on the bottom center torsion rods as shown in Figure 3.23. This tension forces were measured using SENSOTEC/ Model No. 1706 load cells. These units have a capacity of 40 kips (178 kN), with an output excitation voltage of 10 V.

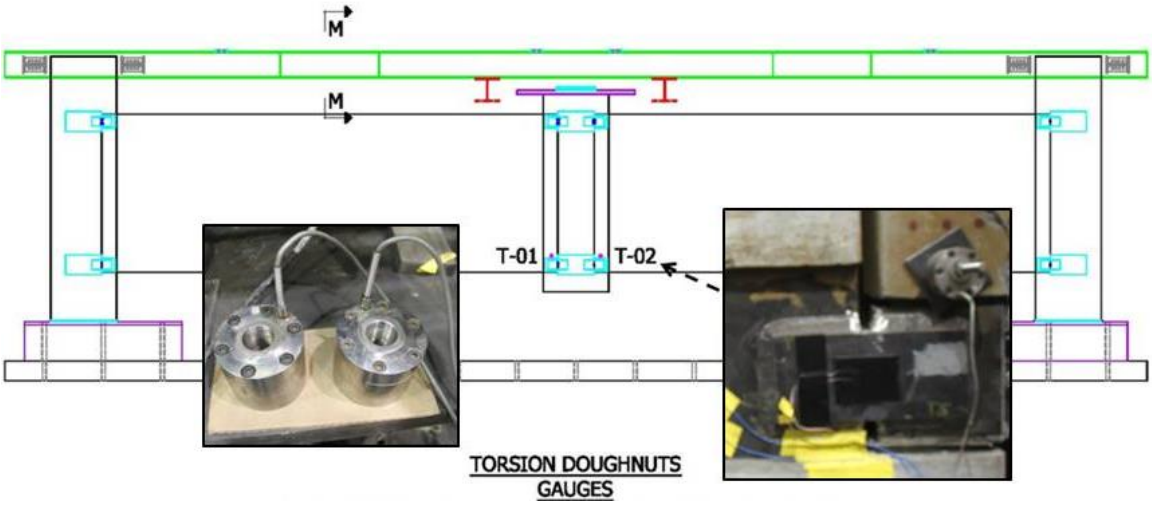

Figure 3.23 Location of the torsion doughnuts load cells

3.4.2 High-frequency response channels

High-frequency response instruments were installed on the test specimen in an effort to provide critical data to successfully assess the performance of the steel link plates as well as monitor the propagation of concrete yield lines. Fourteen sensors were recorded at the highest available sampling rate of 2 MHz. The sensors included two acoustic emission sensors, six accelerometers, one load cell, and five strain gauges. Channels L-95A, εH-45, εH-47, εH-116, εH-117, and εH-118 were dual recorded at the lower sample rate 40 Hz and at 2 MHz. Table 3.3 shows the list of channels recorded at 2 MHz and the sensor types.

Table 3.3 High-speed (2 MHz) channel matrix

Channel No.	Channel Name	Sensor Type
1	L1A	Accelerometer
2	L1B	Accelerometer
3	L1C	Accelerometer
4	L2A	Accelerometer
5	L2B	Accelerometer
6	L2C	Accelerometer
7	AE1	Acoustic Emission
8	AE2	Acoustic Emission
9	L-95A	Load Cell
10	M7-45 (εH-45)	Strain
11	M7-47 (εH-47)	Strain
12	T3-S1 (εH-116)	Strain
13	T3-S2 (εH-117)	Strain
14	T3-S3 (εH-118)	Strain

3.4.2.1 Acoustic emission sensors

Two acoustic emission (AE) sensors were monitored during the experiment's execution. The AE sensors behaved like high-frequency accelerometers that responded to stress waves originating from stimuli in the test beam (theoretically resulting from internal damage such as cracking) reaching the surface or boundaries where the AE sensors were located. These sensors contain a crystal that responds to energy in a non-linear fashion, with bandwidths from 60 to 1000 KHz as shown in Figure 3.24. Figure 3.25 shows one of the AE sensors. These AE sensors (Model SE900-MWB) were manufactured by Dunegan, and both were powered by a Model 500J 15-volt supply. Both

AE sensors were installed on the bottom M8 plate in the center column/stub as shown in Figure 3.26.

The purpose of the AE sensors was an attempt to record information on the pattern and growth of acoustic emissions that occurred during test execution to potentially allow correlation of the results with the observed and measured damage states inferred from analyses or other recorded data to better understand the nonlinearity of the system. These data were to be used to help understand the progressive collapse behavior or damage propagation due to a brittle failure in the connections of a precast concrete building. Figure 3.26 shows the locations of the AE sensors on the test specimen.

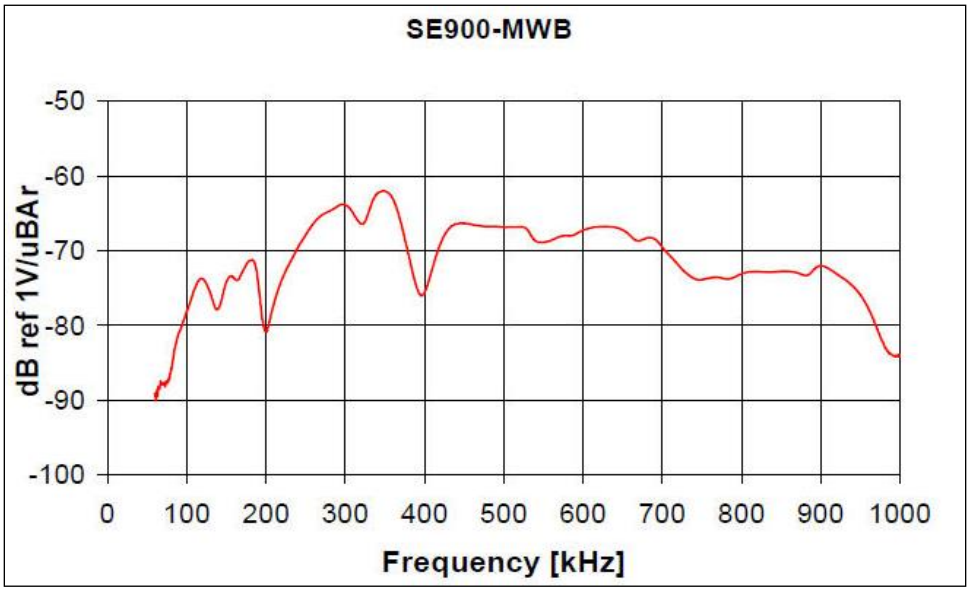

Figure 3.24 Score Dunegan SE900-MWB calibration curve (Score Atlanta Inc., 2012)

Figure 3.25 Acoustic emission sensor (Score Atlanta Inc., 2012)

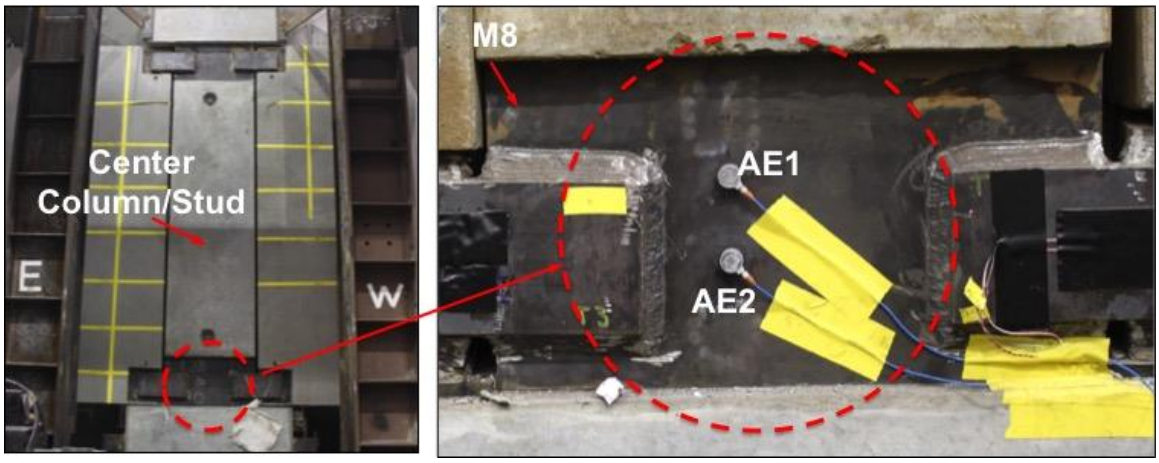

Figure 3.26 Location of acoustic emission sensors at bottom M8 plate in center column

3.4.2.2 Accelerometers

As part of the investigation, a total of six 7270 Endevco/Model No.7270A series of piezoresistive accelerometers were installed on the test specimen. They were strategically installed along the bottom centerline of the spandrel beams, as shown in Figure 3.27. The purpose of the accelerometers was to assess whether global instability could be determined, e.g., gross changes in the dynamic properties, linear or nonlinear, during the execution of the test, and as possibly indicate damage growth.

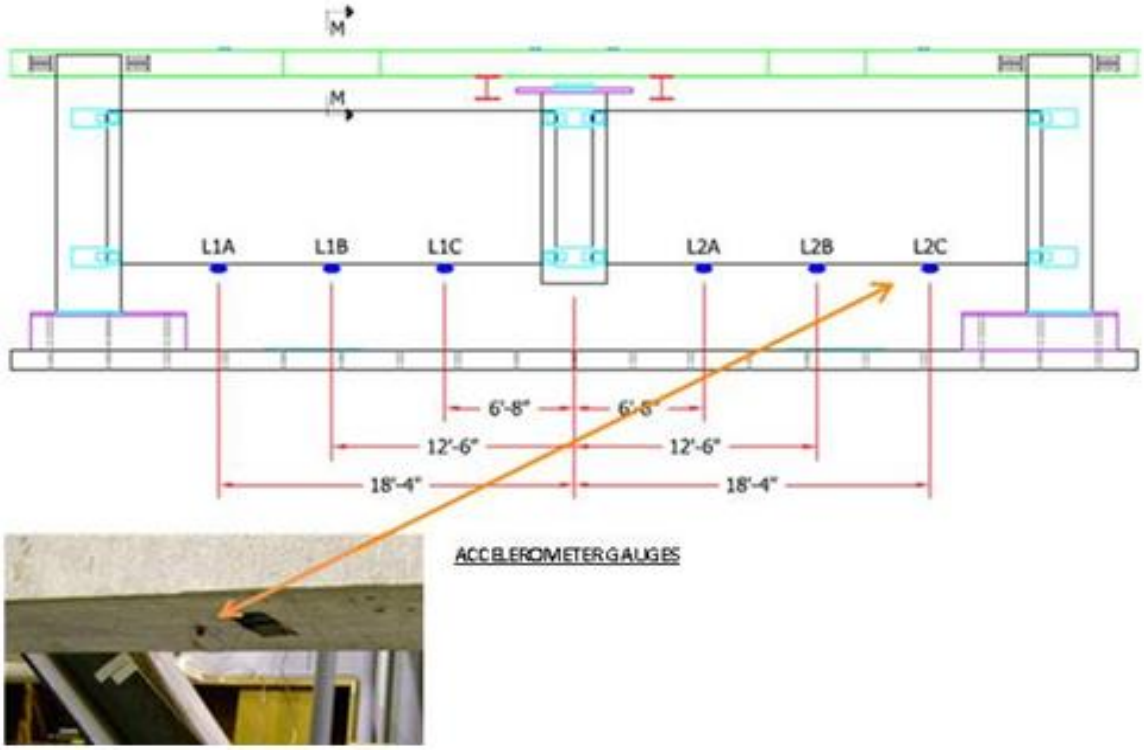

Figure 3.27 Location of accelerometers at bottom centerline of spandrel beam

3.4.3 Photography

The experiment was recorded using three standard video cameras positioned on the front of each column. These high-definition cameras were set to record at a default speed of 60 frames per second (fps). Quality videos were recorded in all three of the cameras. These data played a key role in the posttest forensic examination procedure.

3.5 Experiment loading procedure

The quasi-static test was conducted by inducing a downward displacement of the unsupported center column/stud. This displacement was controlled at an initial rate of 0.02 in./min (0.51 mm/min). However, as the displacement increased, the rate was adjusted throughout the experiment at sponsor's discretion.

The stroking of the actuator was manually controlled from the instrumentation room. An external 400-kip (1779-kN) load cell was installed at the end of the ram's stroke to record the applied load over the center column/stud at each displacement increment. This applied load was later validated when compared to the recorded data by the internal differential pressure gauge in the hydraulic ram.

Minutes before the experiment began, the hydraulic jacks were lowered and the temporary steel table was removed from the bottom of the center column/stud. This action induced a column removal scenario in the OMRF test specimen, forcing the steel link plates to uphold the bending moments at the joints associated with the dead load. At this time, the remaining instrumentation was installed. The string potentiometers were hooked along the bottom of the spandrel beams, and the LVDTs were set. After successfully resetting the potentiometers and the LVDTs, the data acquisition systems were activated, and the recording of data was initiated.

The column was preloaded with an approximated initial ram hydraulic pressure of 10 psi (0.0689 MPa) in order to ensure a uniform contact over the top of the center column/stud. At this point, the cameras were set to record. This initial pressure was maintained for 10 minutes, then the ram began to be stroke downward against the ram steel plate; consequently, the center column/stud began to vertically displace. The pressure generated because of the ram acting over the center column and the resistance of the test specimen to deflect was measured by the load cell and the internal differential pressure gauge. The ram's stroke was kept in contact with the center column throughout the experiment.

In an effort to examine the adequacy of the steel link plates to redistribute load along the assembly after a local failure, or the propagation of concrete yield cracks, the stroking was paused in multiple occasions throughout the experiment. The pauses were taken at every three to five minutes depending on the observed failure modes and lasted up to 15 minutes in some cases. These pauses facilitated the investigators to examine the performance of the steel link plates, as well as monitor the propagation of concrete cracks along the OMRF test specimen throughout the experiment.

After 296 minutes of testing time, the experiment was stopped. A peak maximum load of 168.2 kips (748 kN) at 216.15 minutes and a final center vertical displacement of 17.8 in. (452 mm) were recorded. A posttest forensic examination was conducted immediately after to document the damage associated with the loading.

CHAPTER IV

EXPERIMENTAL RESULTS

A summary of the experimental results are presented in this chapter. All of the data records are presented in Appendix A. An overview (Section 4.1), a general description of the performance of the structure (Section 4.2), a description of the posttest damage observations (Section 4.3), and the characteristics of the loads placed on the test specimen, as well as the performance of the instrumentation system and data produced (Section 4.4), are presented herein. Further discussion and analyses of the results are presented in Chapter V.

4.1 Overview

The experiment was conducted on October 5, 2011. An existing reaction structure described in Chapter III was used to test the OMRF specimen under a quasi-static load, force displacement-controlled. The experiment was stopped after 296 minutes of testing. A peak maximum load of 168.2 kips (748 kN) at 216.1 minutes and a final center vertical displacement of 17.8 in. (452 mm) were recorded. As previously discussed in Chapter III, the data collected in this experiment were recorded using two separate data acquisition systems recording at different sample rates. The pseudo-static response was recorded on a Synergy data acquisition system at a frequency of 40 Hz with a minute-based (min) time scale. The high-frequency response was recorded using a similar data acquisition system but at a sample rate of 2 MHz with a millisecond (msec) time scale.

4.2 OMRF overall structural performance

A plot of the applied load versus center vertical displacement is shown in Figure 4.1. The load on the structure was increased following an initial displacement-controlled rate of 0.02 in./min (0.51 mm/min); however, this rate was modified as the Center Vertical Displacement (Δ) increased throughout the test. The vertical displacement of the center column, denoted by Δ, was obtained as an average of the displacements measured from the bottom corners of the center column/stud (D-85 and D-86).

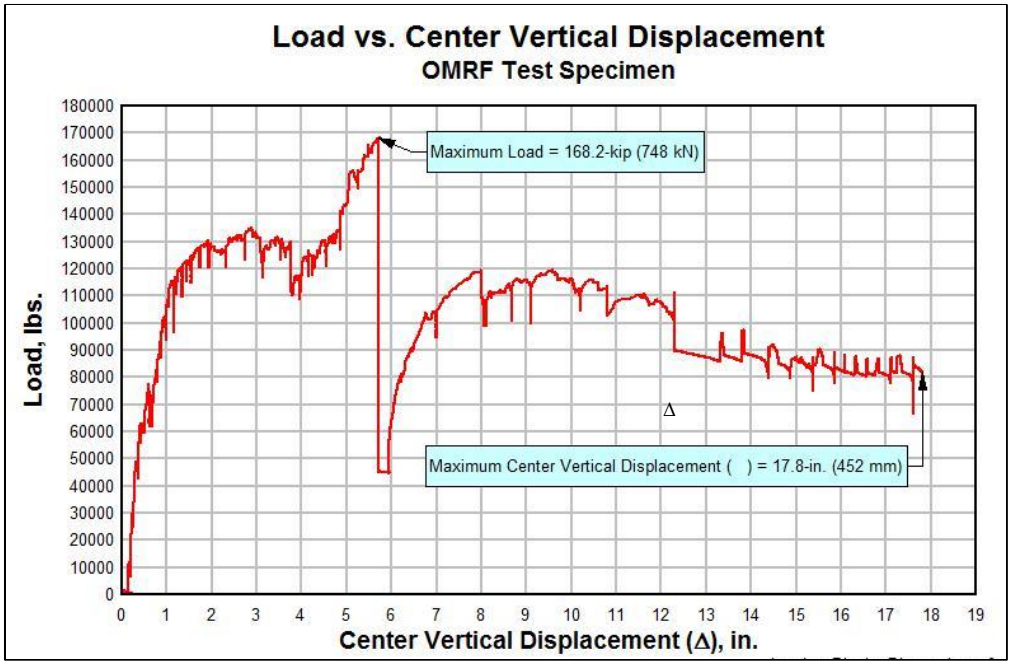

Figure 4.1 Applied load vs. vertical center displacement of OMRF

When subjected to the monotonically increasing vertical displacement of the unsupported center column/stud, the specimen exhibited an initial elastic response dominated by flexure. However, as the steel link plates at locations #2 and #4 (denoted in

Figure 2.3) yielded, concrete cracks developed in the beams near these steel link plates as shown in Figure 4.2. Figure A.9 and Figure A.11 show load-strain plots for steel link plates #2 and #4, respectively. These concrete cracks in the beams were first observed when the specimen reached an approximate Δ of 0.38 in. (9.6 mm) at 42.92 minutes of testing. After a ten-minute pause, the load continued to be increased over the center column. The OMRF specimen showed resistance to flexure; however, as the load increased, both end-columns began to show well-defined diagonal cracks at the bottom corner as shown in Figure 4.3. These concrete cracks in the end-columns were first observed when the OMRF reached an approximate Δ of 1.8 in. (45.7 mm) at 120 minutes of testing. Then after a brief pause, the displacement in the ram continued to be increased. The first crack in the unsupported center column or stud was then observed as shown in Figure 4.4.

Figure 4.2 Elevation view, development of the first observed cracks in the beams near the top of the center column/stud, at Δ of 0.38 in. (9.6 mm)

Following the development of these concrete cracks in all of the structural elements, the OMRF specimen continued to deflect as the applied load was increased. Considerable scabbing of concrete cover, some of fairly large size, was visible, especially in the vicinity of the left (east) end-column. At this point, significant deformation was observed in the steel link plates. By the time the OMRF reached an approximate Δ of 3.79 in. (96.4 mm), it became evident that the 1-in. (25.4-mm) gaps between the beams and the columns were now closed, allowing the bearing of the beams against the columns. At this time, major concrete cracks began to develop surrounding the top M8 plate in the left (east) end-column, and a considerable amount of debris of scabbed concrete fell from behind the plate, resulting in the complete detachment of the M8 embedded plate from the end-column.

The detachment of the M8 plate of the left (east) end-column aggravated the out-of-plane behavior of the OMRF as it deflected downward. This failure also contributed to the already beam-to-column bearing action. The load continued to increase over the center column, and at the time the OMRF specimen reached an approximate Δ of 5.69 in. (144.5 mm), the bottom #10 (#32) Grade 60 anchor bar welded to the right (M7) embedded angle in Beam-L failed, and the upper anchor bar failed immediately after. After a ten-minute pause, the experiment was resumed. When the Δ of 14.40-in. (366.0-mm) mark was reached, a considerable amount of debris of scabbed concrete began to fall from behind the M8 plate embedded on the right end-column, resulting in its complete detachment. All eight torsion bars fractured. The experiment was continued until a maximum Δ of approximately 17.8 in. (452 mm) was reached.

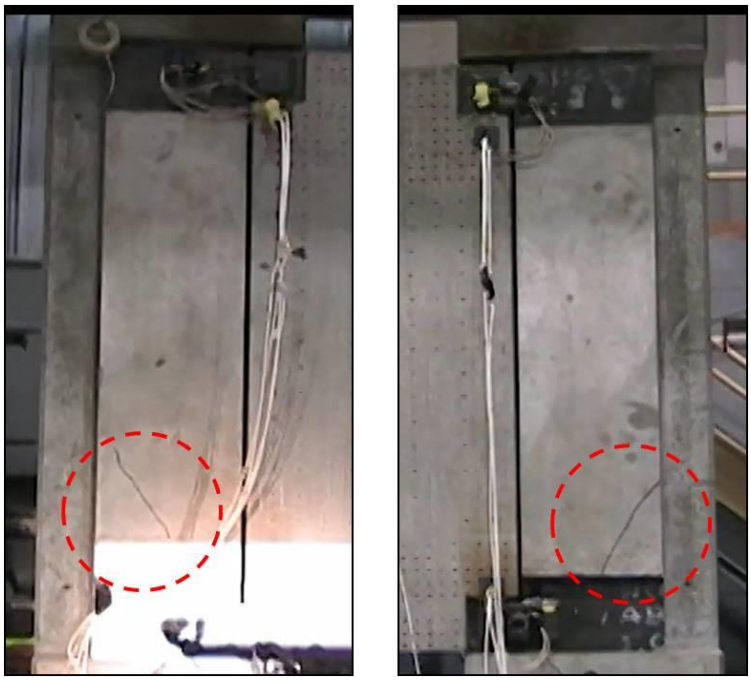

a) Left (east) end-column b) Right (west) end-column

Figure 4.3 Elevation views, development of the first observed cracks in the end-columns at Δ of 1.8 in. (45.7 mm)

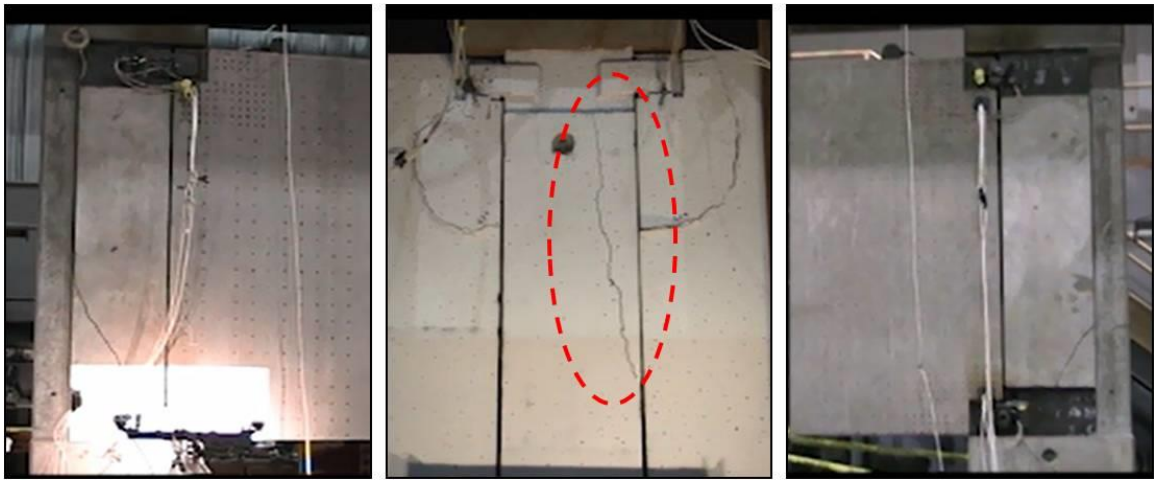

(a) Left (east) end-column (b) Center column/stud (c) Right (west) end-column

Figure 4.4 Elevation views, development of the first observed crack in center column at Δ of 2.1 in. (52.7 mm)

Figure 4.5 shows pretest and posttest views, respectively, of the experimental specimen.

(a) Pretest elevation view of OMRF specimen

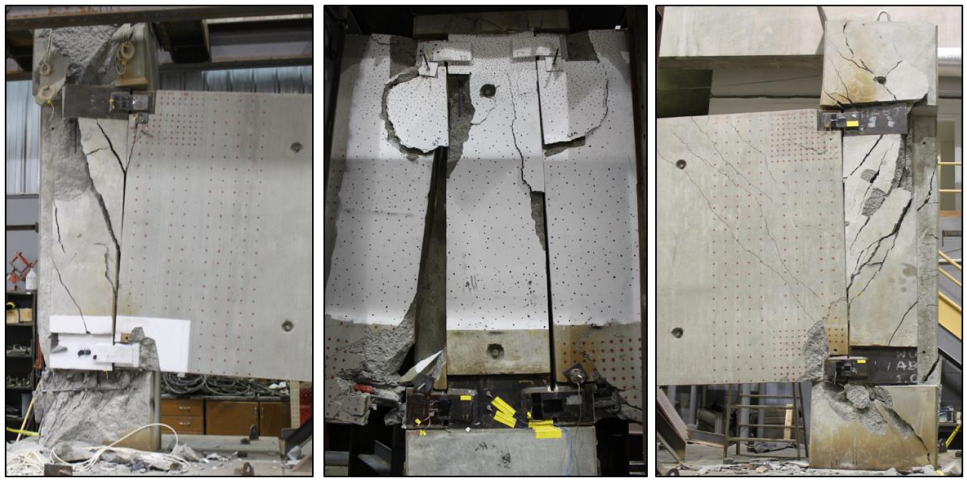

(b) Posttest elevation view of OMRF specimen

Figure 4.5 Pretest vs. posttest views of the OMRF test specimen

4.3 Posttest structural damage observations

Figure 4.5(b) shows the posttest structural damage of the OMRF test specimen. All structural members suffered major damage. Damage was particularly heavy at the

end-columns. A considerable amount of debris, some fairly large in size up to approximately 20 in. (508 mm) by 12 in. (305 mm), had fallen from the OMRF test specimen. Major concrete cracks developed along the assembly due to the high-magnitude bending moments at the supports.

4.3.1 Posttest damage of columns

4.3.1.1 Left (east) end-column posttest damage

Figure 4.6 shows the posttest condition of the left (east) end-column. Major flexural concrete cracks were observed in the structural element. Some of these cracks were over 2-in. (50.8 mm) wide and 48-in. (1219 mm) long. The observed crack pattern gave an indication of the high-magnitude bending moment to which the column was subjected. The end-columns reacted to the lateral-torsional response of the beams and were bending out of the plane of the beam-column setup. These cracks were first observed when the system exceeded the 1.8-in. (45.7-mm) Δ mark. This caused the system to exhibit plastic behavior, resulting in permanent deformation and concrete cracks.

Much distress and scabbing of the concrete at the bottom of the column was observed. A closer view of the bottom area of the column is shown in Figure 4.7. Much of the concrete had completely fallen away, and much reinforcement was exposed. A similar behavior was observed around the top M8 embedded plate (see Figure 4.8). As cracks began to become more defined around the steel plate, concrete began to fall, exposing the reinforcement at the top of the column as well as contributing to the partial detachment of the M8 plate from the column.

(a) Front view (b) Back view

Figure 4.6 Elevation views, posttest damage of left (east) end-column

Figure 4.7 Elevation view, posttest damage of bottom of left (east) end-column

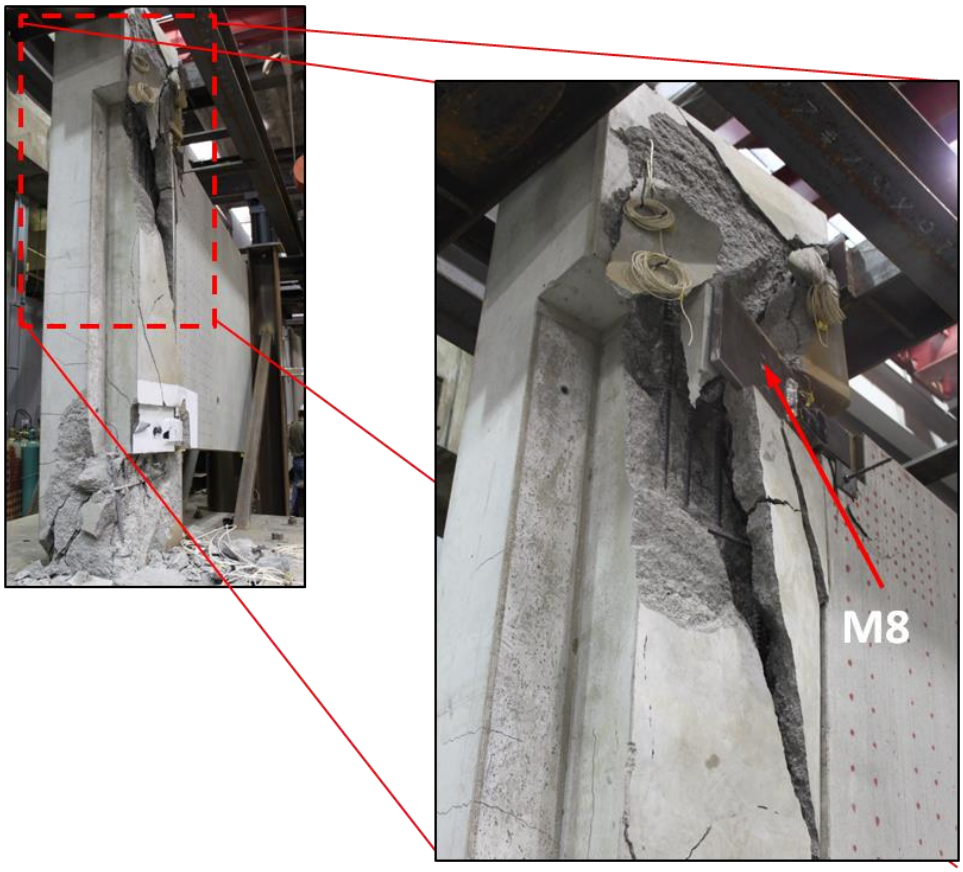

Figure 4.8 Elevation views, detachment of the upper M8 plate in the left (east) end-column

4.3.1.2 Unsupported center column/stud posttest damage

Figure 4.9 shows the posttest structural damage of the top front face of the center column/stub. The center column suffered much less damage than both end-columns. However, evidence of crushed concrete can be observed along both inner edges. Also, cracks were over 0.5-in. (12.7-mm) wide in places. The first crack in the center column was observed when the OMRF specimen reached a vertical displacement of 2.1 in. (53.3 mm), at which time Beam-R began to push against the top of the center column. The second dominate crack developed later in the test and was a consequence of the

bearing action between Beam-L and the center column. A slight counterclockwise rotation of the center column/stub toward the left (east) end-column occurred.

Figure 4.9 Elevation view, posttest condition of the center column/stud

4.3.1.3 Right (west) end-column posttest damage

Figure 4.10 shows the posttest condition of the right (west) end-column. A considerable volume of dislodged concrete is evident, especially in the vicinity of the top M8 steel plate. The crack pattern observed in this column is similar to the one observed in the left (east) end-column but in the opposite direction. Some of these cracks were over 2-in. (50.8-mm) wide and 45-in. (1143-mm) long. However, when the posttest condition

of the right (west) end-column was examined and compared to the posttest condition observed in the opposite end-column, it was obvious that the damage in the right column was not as severe as in the left.

A closer view of the cracks developed in the bottom portion of the right (west) end-column is shown in Figure 4.11. The concrete had partially fallen away near the steel link plate location #8, but the reinforcement was not exposed. This concrete scabbing indicates a high concentration of stress occurred at the supports. A similar behavior was observed around the top M8 embedded plate but at a greater magnitude. Extensive fracture of the concrete was observed around the top M8 plate (Figure 4.12). Reinforcement near the top of the column was exposed, and the M8 plate was partially detached from the top of the right (west) end-column.

Although the data collected from the LVDTs at the end-columns indicated a predominant outward movement during the latter minutes of testing time, the direction of the cracks exhibited at the front faces of both end-columns indicated an opposite (inward) movement toward the center stub. The incongruity in behavior could be a result of the development of two separate forces acting at opposite directions along the same axis at the end-columns due to the eccentricity between the centerlines of the spandrel beams and the end-columns. The outer-edges of the T-shape end-columns were rotating outward, but the inner-edges inward towards the center column. Since both LVDTs were installed against the outer edge of the end-columns, both data records evidenced outward movement (see Figure 4.12).

(a) Front view (b) Back view

Figure 4.10 Elevation views, posttest damage of right (west) end-column

Figure 4.11 Elevation view, posttest damage of bottom of the right (west) end-column

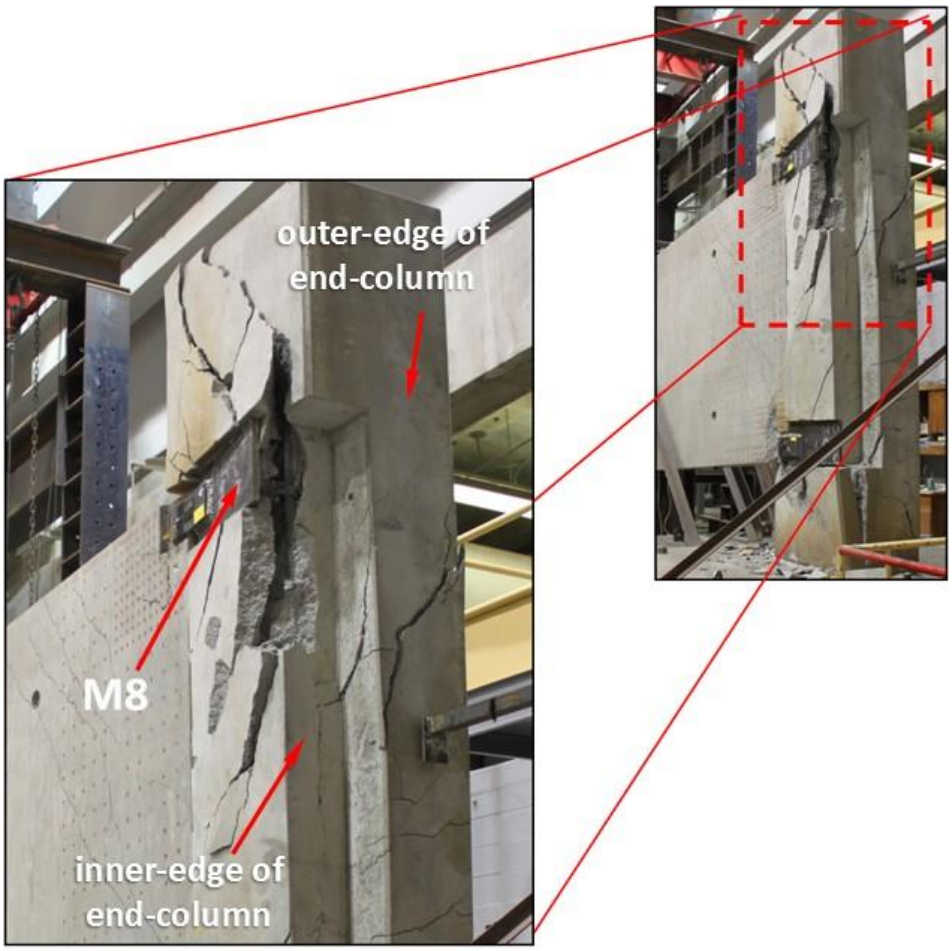

Figure 4.12 Elevation views, detachment of the upper M8 plate in the right (west) end-column

4.3.2 Spandrel beams posttest damage

The spandrel beams suffered significant damage. Major cracks developed in both beams, indicating the formation of shear cracks in the concrete due to bearing, particularly near the steel link plate locations #2 and #4, as shown in Figure 4.13. In addition, large concrete chunks fell from the beams throughout the experiment, mainly from the bottom edges near the center column as shown in Figure 4.14. Concrete also fell

from the bottom corners near the steel link plate locations #7 and #8 as shown in Figure 4.15.

All eight torsion rods installed at corners of the beams failed, with the exception of the two bottom center rods located where the load cells were installed. Failure of the torsion rods indicated some out-of-plane behavior of the end column-beam connection region.

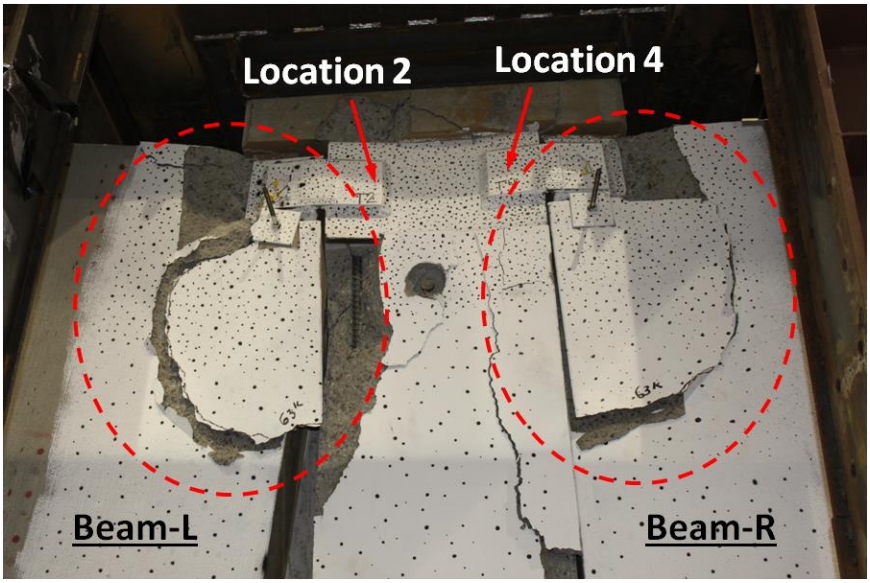

Figure 4.13 Elevation view, posttest damage of the spandrel beams near the top of the center column/stud

(a) Bottom/left side view of center column and beam

(b) Bottom/right side view of center column and beam

Figure 4.14 Side view, posttest damage of the bottoms of the spandrel beams near the center column/stud

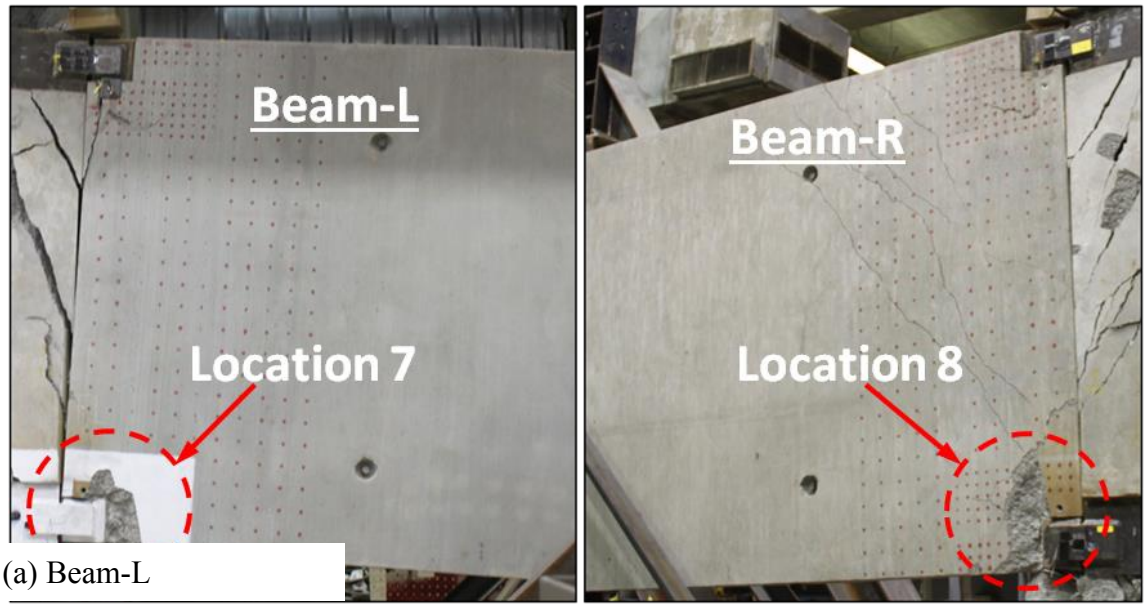

(a) Beam-L

(b) Beam-R

Figure 4.15 Elevation views, posttest damage of spandrel beams near the end-columns

The combination of out-of-plane flexural behavior carried by the assembly evidenced in Figure 4.16 and the extensive crushing of concrete observed at the beam's bottom edges near the center column (Figure 4.14) exposed the reinforcement detail near the steel plate at location #3. This consequently induced the bars to a combination of tension load and bending moment that resulted in the failure of both of the anchor bars welded to the M7 steel angle in Beam-L, as shown in Figure 4.17. The bottom anchor bar fractured at an approximate Δ of 5.69 in. (144.5 mm), which consequently overloaded the upper anchor bar causing it to fail immediately after. Following the failure of the bottom anchor bars, the spandrel beams began to bear against the columns, inducing the beams to compressive forces at opposite directions. The bottom-left corner of Beam-L pushed against the bottom of the left (east) end-column, and the top-right corner pushed against the top of the center column. For Beam-R, the top-left corner pushed against the center column, and the bottom-right corner pushed against the right (west) end-column. This behavior corresponded to the development of additional concrete cracks along the beams. At the time that the second (upper) anchor bar of the M7 angle fractured, the beam was no longer attached to the steel link plate at location #3, contributing to the already out-of-plane behavior and the bearing of the beams against the columns.

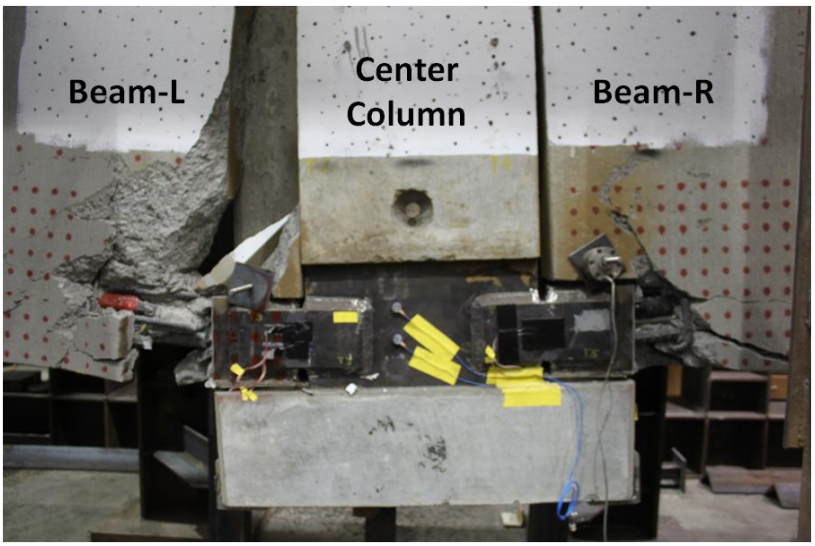

Figure 4.16 Elevation view, posttest damage of the spandrel beam at the bottom connections to the center column

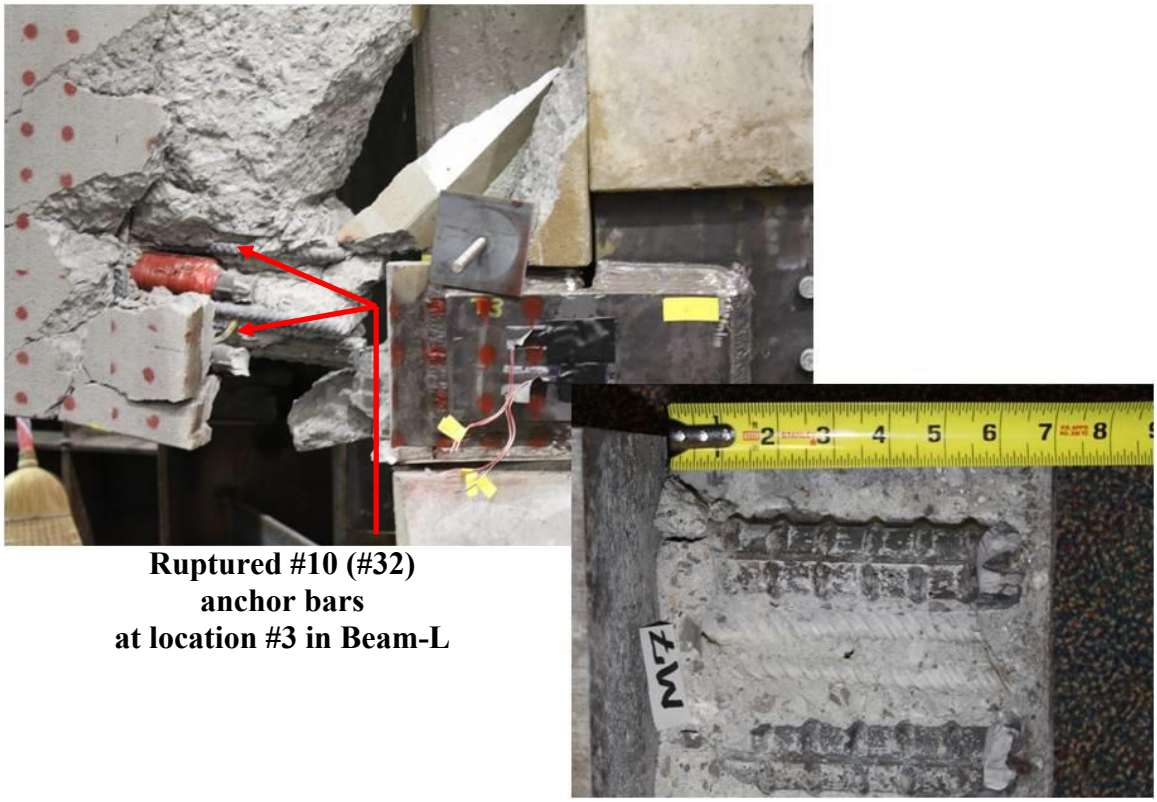

Figure 4.17 Fractured anchor bars of M7 angle plate in Beam-L (elevation view)

4.3.3 Steel link plates posttest damage

All steel link plates exhibited significant permanent deformation; however, none of them fractured. The shape at which the steel link plates deformed was evidence of torsional behavior along the assembly. At the end of the experiment, only five of the eight steel link plates remained attached to the assembly. Steel link plates at locations #1, #3, and #6 were detached from the assembly due to multiple structural failures.

4.4 Loading characteristics and measurements

The 17.8 in. (452.1 mm) of maximum vertical displacement at the center of the assembly was induced by a hydraulic ram stroking downward over the top of the unsupported center column/stud. The ram was stroked following a displacement-controlled scenario. The center column/stud was loaded at an initial displacement rate of 0.02 in./min. (0.51 mm/min); however, this rate was varied throughout the experiment. The actual displacement increment followed throughout the experiment is described in Table 4.1. In an effort to evaluate the assembly's condition, multiple pauses were taken throughout the experiment.

Table 4.1 Description of the experiment displacement-controlled loading scenario

Start Time (hr)	Center Ram Displacement (in.)	Load (kips)	Time Finished (hr)	Pause (min.)
1053	0.10	8	1055	-
1057	0.20	25	1059	02:00
1102	0.30	43	1105	03:00
1108	0.40	61	1112	03:00
115	0.50	60	1118	03:00
1119	0.70	76	1121	01:00
1131	0.80	86	1137	10:00
1140	0.90	96	1142	03:00
1146	1.00	106	1150	04:00
1152	1.20	101	1156	02:00
1158	1.40	124	1203	02:00
1213	1.60	127	1221	10:00
1222	1.80	131	1231	01:00
1233	2.00	121	1239	02:00
1249	2.40	128	1300	10:00
1302	2.80	123	1309	02:00
1312	3.20	127	1318	03:00
1320	3.60	129	1323	02:00
1325	4.00	117	1330	02:00
1340	5.00	127	1352	10:00
1354	5.84	47	1359	02:00
1407	7.00	100	1415	08:00
1422	8.00	100	1431	07:00
1432	9.00	105	1446	01:00
1448	10.00	112	1454	02:00
1456	12.00	106	1503	02:00
1504	15.00	71	1508	01:00
1509	17.8	53	1513	01:00

4.4.1 Experiment data records

The pseudo-static response data and the high-frequency response data are summarized in Section 4.4.1.1 and Section 4.4.1.2, respectively .The recorded data are presented in Appendix A. The pseudo-static records are shown in Figure A.1 through Figure A.31, and the high-frequency records are in Figure A.32 through Figure A.37.

4.4.1.1 Pseudo-static measurements

4.4.1.1.1 Load measurements

The displacement of the ram was increased incrementally, reaching a maximum applied load of 168.2 kips at 216 minutes of testing time. Two different sensors were used to measure the vertical load applied to the specimen, an external load cell with a capacity of 400 kips (1779 kN) connected to the end of the ram's stroke, and an internal differential pressure gauge in the MTS ram with a capacity of 600 kips (2668 kN). Figure 4.18 shows a comparison of the values obtained by the two gauges. The coefficient of correlation (r) between the recorded data of the two sensors is 0.997, indicating minor differences between the two measurements. Therefore, either of the two load measurements can be used to discuss the performance of the specimen. In this report, L-95A was used to plot the data records presented in Appendix A.

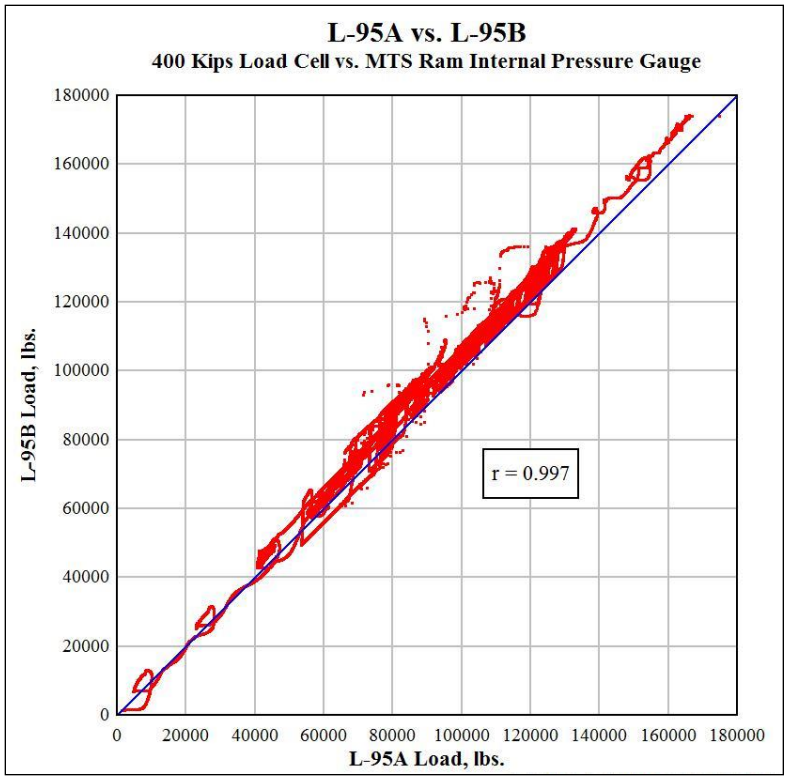

Figure 4.18 Load cell vs. MTS ram internal differential pressure sensor correlation

4.4.1.1.2 Displacement measurements

The displacement records are presented in Appendix A. Figure A.1 shows all of the vertical displacements recorded versus the applied concentric load throughout the execution of the experiment. The maximum vertical displacements at each gauge were 8.9 in. (226.1 mm) (D-83), 18.5 in. (469.9 mm) (D-85), 17.0 in. (431.8 mm) (D-86), and 8.3 in. (210.82 mm) (D-88), resulting in a center column average vertical displacement of 17.8 in. (452.1 mm).

Figure A.2 shows the horizontal displacements of the end columns measured at mid-height of the beams. Positives values in the plot indicate an inward displacement towards the center column. During the initial stages of the experiment, both end-columns

exhibited inward rotation towards the center column. However, as the displacement increased, both supports began to rotate outward. The end-columns' reverse in rotational direction happened at different times in the experiment.

During the posttest forensic exam, it was observed that the LVDTs shifted approximately 0.5 in. (12.7 mm) from their original position. This variable could have potentially affected the reading of the horizontal measurements, especially during the final stages of the test.

4.4.1.1.3 Inclinometers measurements

The inclinometer records are presented in Figure A.3. During the experiment, inclinometers R-91 and R-92 malfunctioned due to a cutoff in the instrumentation line by a scabbed concrete fragment from the test specimen. Figure A.3 shows the angles of rotation in degrees at the columns versus the applied load. The rotations that the system reached at the end of the test were 1.4º (0.02443 rad) (R-93) and 1.0º (0.01745 rad) (R-94). The maximum rotational values were 3.76º (0.06981 rad) (R-93) and 4.06º (0.08726 rad) (R- 94).

4.4.1.1.4 Strain measurements

The strain records are presented in Figure A.4, which shows the recorded strains at the anchor bars located at the upper end corners of the beams (M6) versus the applied load. Each of the curves in the graph exhibit a positive behavior, implying that these #10 anchor bars were mostly in tension throughout the entire execution of the test.

The strains in the top anchor bars located at the bottom center corners of the beams (M7) are shown in Figure A.5. These bottom #10 anchor bars were also in tension

throughout the test. Both fractured anchor bars welded to the M7 angle in the left (east) beam failed due to the high deformation caused by high tensile stress levels.

Figure A.6 and Figure A.7 show the internal strain of the outer-most bars of the beams. All strain measurements in the outer-most bars were significantly less than the nominal yield strain of A706 (0.2% or 0.002 in./in.), indicating that at mid-span, the beams remained in the elastic range throughout the test.

A total of thirty-three external strain gauges were placed at selected locations among the eight steel connecting plates in the OMRF. Figure A.8 through Figure A.15 show the recorded strains in each of the ductile connection plates versus the applied load. A total of eight rosettes were mounted on seven different ductile connection plates. The following arrangement was utilized in this report: Gauge A (ε_a) at (-45°), Gauge B (ε_b) at (0°), and Gauge C (ε_c) at (+45°). Strain transformations were applied to the rosette data to obtain vertical and shear strains in addition to axial strains. However, these transformations are applicable only for elastic behavior, and yielding of the link plates occurred very early in the response at Δ of approximately 0.38 in. (9.6 mm) or earlier. The shear and vertical strain values in this early stage of the response were not found to provide significant insights into the behavior of the assembly, so only axial strain values are presented in this report.

4.4.1.1.5 Torsion load cells

The torsion records are presented in Appendix A. Figure A.17 shows the recorded tension loads on the torsion rods located at the bottom center beam-column connection. The red load curve shows the change in tension force on the bottom-left torsion rod (T1), and the blue curve shows the change in tension force on the bottom-right torsion rod

(T2). The maximum tension forces measured by the load cells on the torsion bars were 7.3 kips (32.5 kNs) (T1) and 53.5 kips (238 kNs) (T2). The difference between these measurements can be explained by two major factors. Although the two loads tracked qualitatively well during the initial response phase, any misalignment between the beam-to-column connections would have generated tension forces on the torsion bars during the end of the first-quarter of the testing time. Also, the failure of both M7 anchor bars in Beam-L induced torsional loading.

4.4.1.2 High-frequency measurements

As previously discussed in Chapter III, the high frequency data were recorded as a set of discrete time events. The offset in minutes from the zero trigger point in the pseudo-static data is noted in the title of each transient data plot. Over seventy transient events were captured by the acoustic emission sensors during the experiment. The majority of the AE events captured in the test showed data trends of dynamic activity that could possibly be correlated to damage growth or even some of the failure modes or incidents discussed herein. However, in the absence of a high-fidelity numerical model capable of simulating the non-linear behavior, it becomes very challenging to correlate these high-frequency readings to damage growth along the assembly. Therefore, only the three most evident and significant events will be summarized herein and related to specific incidents. Table 4.2 details the number of transient events with the most significant acoustic emission responses. All three of these events (185, 194, and 195) correlate to evident physical damage observed along the assembly.

The high-frequency response data recorded during each of the most significant transient events are presented in Appendix A. The data recorded corresponding to

transient events (185), (194), and (195) are presented in Figure A.32 through Figure A.37.

Table 4.2 Seven most significant acoustic emission response transient events

Transient Event	Time (min)	Signal Amplitude (V)	Accelerometer Activity	Strain Activity	Load Activity
185	213.20	0.4	x		
194	216.15	14	x	x	x
195	276.53	14	x	x	x

CHAPTER V

DISCUSSION AND EVALUATION OF RESULTS

This chapter presents the discussion and evaluation of the experimental results for the OMRF test specimen that tested under a column removal scenario as described in Chapter III. The structural performance, observed failure modes in the specimen, and measurements recorded during the experiments are discussed herein. Both the observed behavior and the recorded data provide insights into the performance of the specimens under the column removal scenario. Section 5.1 provides an evaluation of the structural performance and observed failure modes throughout the different stages of the experiment. Section 5.2 presents engineering analyses regarding the performance of the beam-to-column connection detail. Section 5.3 discusses the development of arching action in the assembly, and Section 5.4 provides a summary of the observed failures that played a significant role in the overall performance of the OMRF test specimen.

5.1 Structural responses and observed failure modes

This section presents the observations and analyses of results from the execution of the OMRF experiment. The observed behavior and failure modes are discussed. The results of interest are data from the displacement transducers, inclinometers, strain gauges, acoustic emission sensors, accelerometers, and load cells.

The applied load and center vertical displacement curves recorded from the OMRF experiment are shown in Figure 5.1. The vertical displacements vs. time plotted in

Figure 5.1 correspond to the measurements obtained by D-85 and D-86 at the center unsupported column. In order to facilitate the evaluation, the forensic examination was divided into five response zones (I, II, III, IV, V). These zones are depicted in Figure 5.1. The incidents denoted in Figure 5.1 are related to either failure of structural elements, arching action behavior, concrete crack growth and scabbing, or any other failure mode observed in the test specimen throughout the different response zones of the experiment as depicted in Figure 5.2. Table 5.1 presents the applied load and the average center-column deflection values (D-85 and D-86) at the time each incident occurred.

As previously discussed in Chapter III, a number of channels were recorded at a higher frequency rate (2 MHz), as a set of discrete time events. The transient events captured by the AE sensors are also marked in Figure 5.1 along the time axis. The time of the three most significant events are noted also in Figure 5.1. The offset in minutes from the zero trigger point in the pseudo-static data is noted in the title of each transient data plots. Table 5.2 details the three most significant transient events' acoustic emission responses and denotes the related incident. The rest of AE events captured in the test will not be discussed in this chapter because of the absence of a high-fidelity numerical model capable of simulating the non-linear behavior critical to successfully correlate the high-frequency readings to any damage growth along the assembly during the first three response zones.

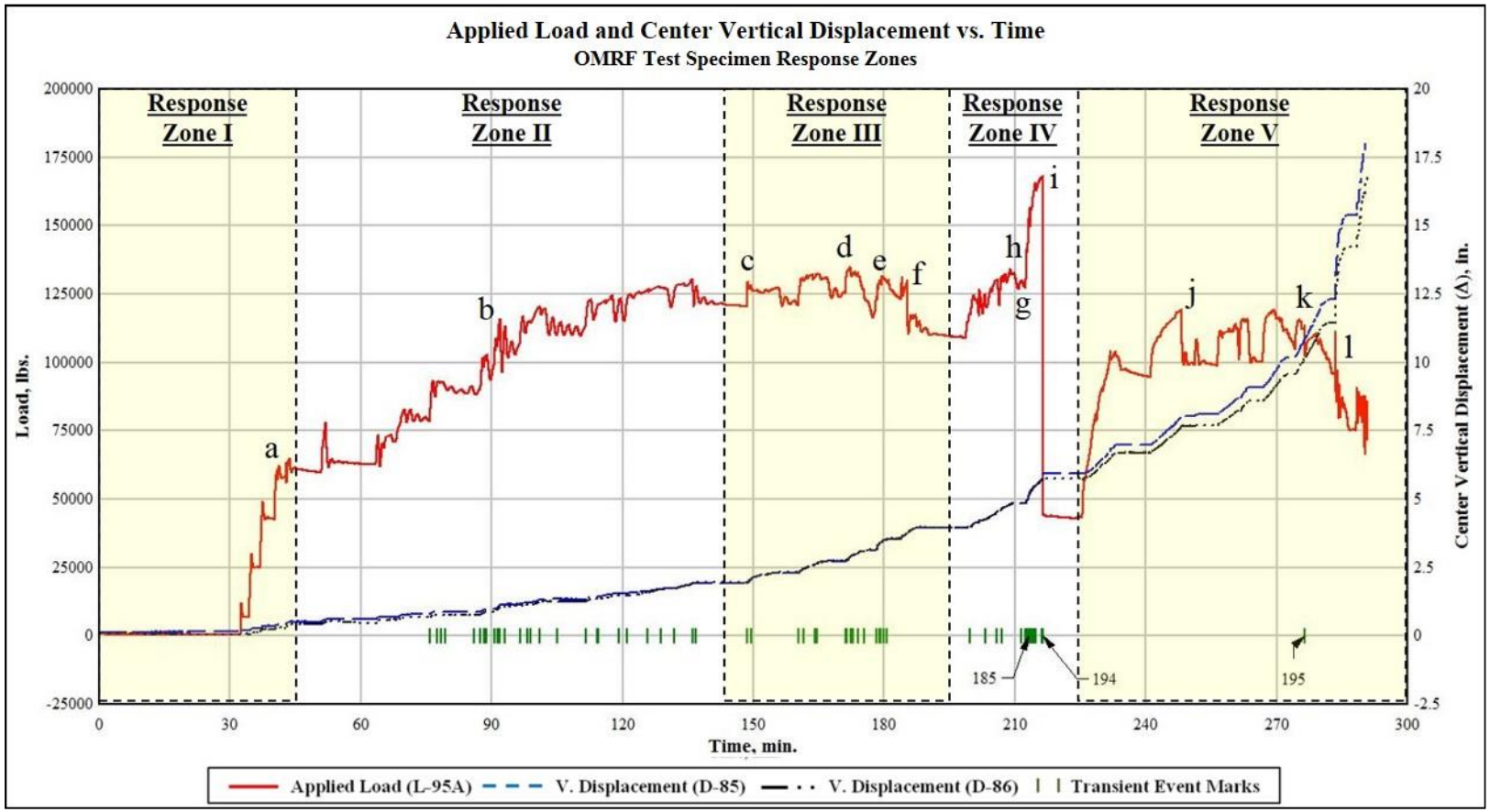

Figure 5.1 Applied load and center vertical displacement vs. time with AE event marks

Table 5.1 Incidents linked to structural responses observed throughout the experiment

Incident	Time (min.)	Applied Load (L-95A)		Δ		Response Zone
		(kip)	(kN)	(in.)	(mm)	
a	42.92	63.2	281	0.38	9.6	I
b	91.90	115.8	515	1.10	27.9	II
c	149.50	127.8	569	2.08	52.7	III
d	172.20	135.0	600	2.91	73.9	
e	184.60	131.4	584	3.63	92.1	
f	185.40	129.2	531	3.79	96.4	
g	212.50	129.7	577	4.85	123.3	IV
h	214.66	165.7	737	5.50	139.8	
i	216.15	168.2	748	5.69	144.5	
j	248.17	119.2	530	7.86	200.0	V
k	276.53	113.4	504	10.60	269.0	
l	284.50	83.0	369	14.40	366.0	

Table 5.2 Three most significant acoustic emission response transient events and the related incident

Transient Event	Time (min)	Signal Amplitude (V)	Related to Incident
185	213.20	0.4	g
194	216.15	14	i
195	276.53	14	k

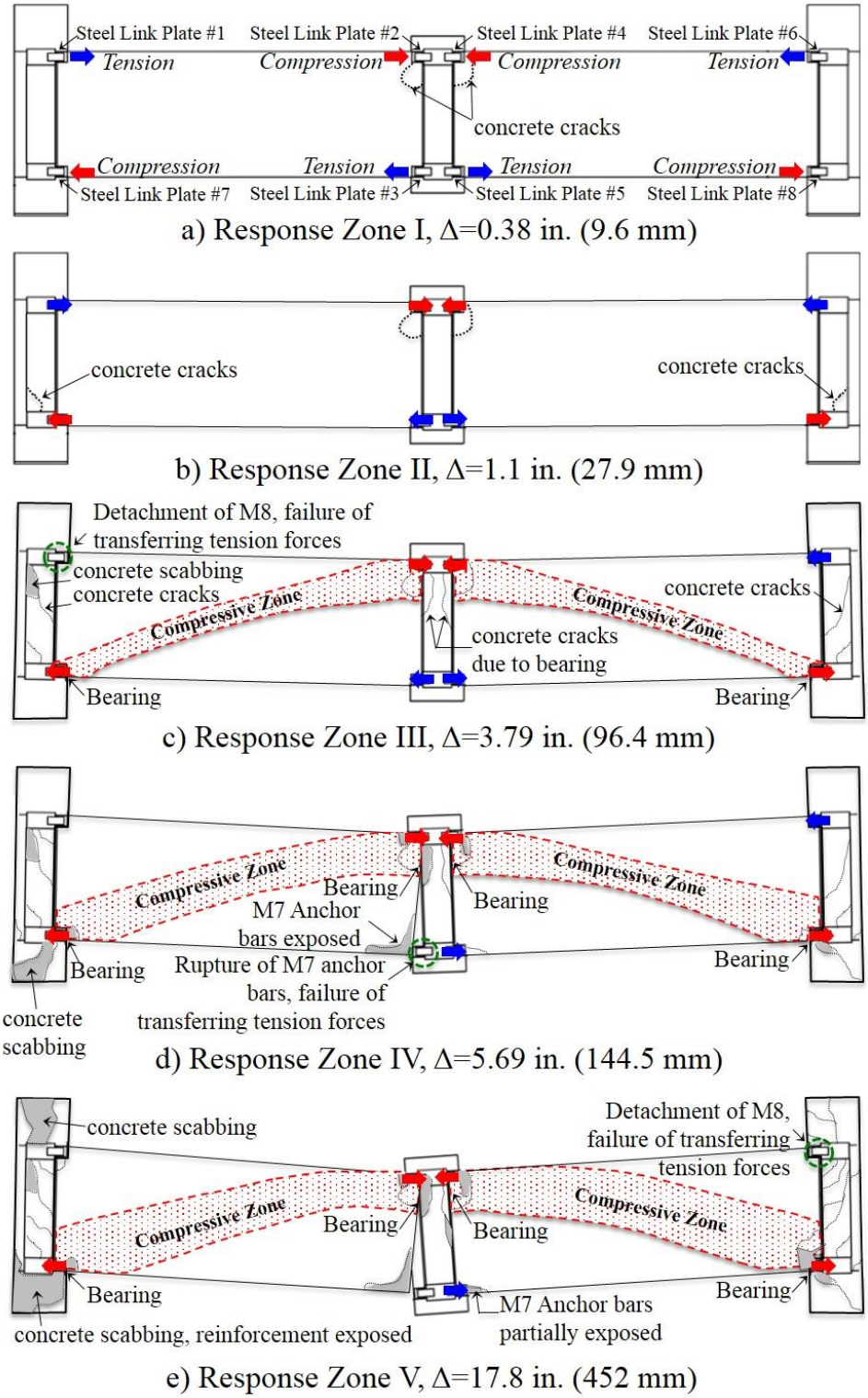

Figure 5.2 Elevation view of OMRF test specimen, damage per response zones

5.1.1 Forensic examination of response zone I

Response zone I is dominated by the observation of the first concrete cracks in the OMRF specimen, benchmarking the end of the system's elastic region and the beginning of plastic behavior. The applied load and vertical displacement response of the specimen was essentially linear up to incident (a) in Figure A.18. At the point when the applied load reached 63.2 kips (281 kN), with a Δ of approximately 0.38 in. (9.6 mm) at 42.92 minutes of test time, the first cracks were observed at the top-center of the OMRF. Figure 5.3 illustrates the location of the crack pattern. As illustrated in Figure 5.2(a), tensile forces in the bottom link plates at the center column were balanced by compressive forces in the top link plates. At the time the steel link plates reached yield point, they began to bend in a plastic fashion. The eccentricities in the transfer of forces, as illustrated in Figure 5.4(a), resulted in out-of-plane bending of the steel link plates and anchor bars, as illustrated in Figure 5.4(b). Thus, the system exceeded its elastic capacity and exhibited plastic behavior, resulting in permanent deformation. This incident corresponds to the abrupt change in displacement observed in Figure A.18, at 42.92 minutes of test time.

Incident (a) can also be evaluated by the data recorded in the external strain gauges located in the steel link plates #2 and #4. Figure A.19 depicts the abrupt drop in load at the time the system reached the 63.2-kip (281-kN) mark, as well as the subsequently abrupt increase in strain in the steel link plate #2(a) and in the steel link plate #4(b). These records are representative of a drastic reduction in stiffness due to concrete cracks. The steel link plates were now carrying the flexural load with plastic behavior.

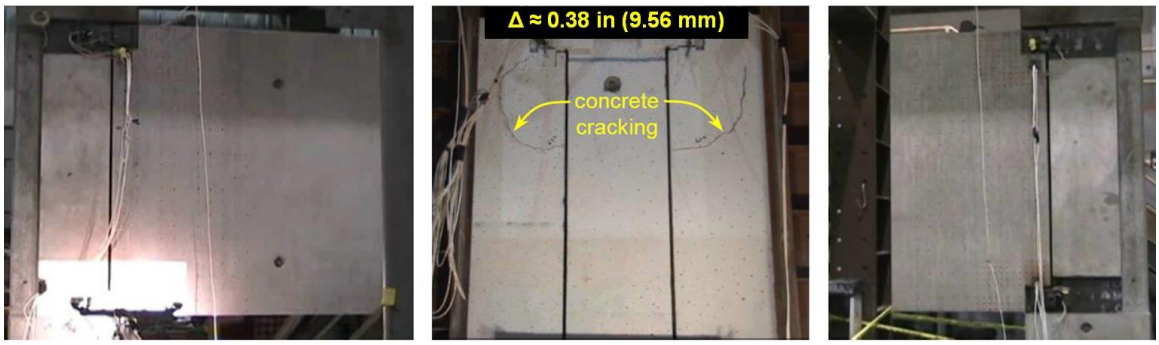

(a) Left (east) end-column (b) Center column/stud (c) Right (west) end-column

Figure 5.3 Elevation view, response zone I – incident (a): first observed concrete cracks on the test specimen at the center, 63 kips (280 kN)

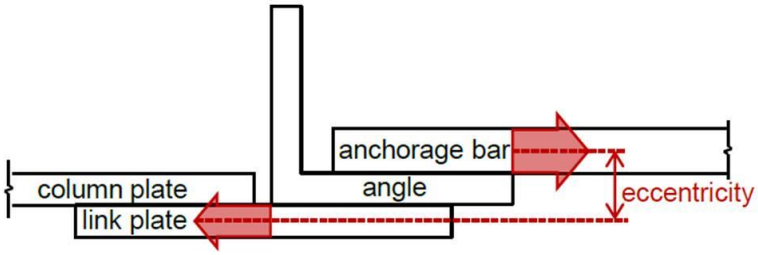

a) Eccentricity in forces

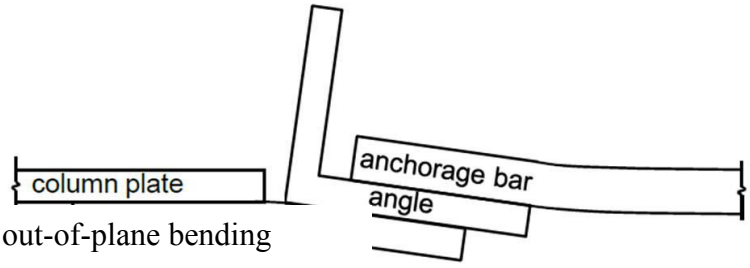

b) Resulting out-of-plane bending

Figure 5.4 Top view of link plate connection showing (Main et al., 2015).

Unfortunately, none of the AE sensors captured this incident. It is very probable that the stress waves that propagated from the structural cracks observed at incident (a) did not exceed the sensor's amplitude arbitrary set level for detection of surface waves by the AE sensors at the bottom of the center column.

5.1.2 Forensic examination of response zone II

Response zone II is characterized by the development of the first concrete cracks at the end-columns as shown in Figure 5.2(b). The vertical load and displacement curves shown in Figure A.20 indicates a typical plastic response, i.e., minimum increments in load correspond to large vertical displacements, until a sudden drop in load was observed at 91.9 minutes of test time, benchmarking incident (b). The load continued to be carried by flexural action along the assembly. However, further reduction in resistance occurred at incident (b) when the system reached a vertical load of 115.8 kips (515 kN), with a Δ of approximately 1.10 in. (27.9 mm). The reduction in resistance was triggered by the high magnitude bending moments that began to create well-defined diagonal concrete cracks at the support. This localized structural response is marked and labeled in Figure A.21 as incident (b). Figure 5.5 provides an image illustrating the cracks at the end-columns.

The direction of the cracks observed at the supports in Figure 5.5 could be interpreted as being due to rotational displacement of the end-columns toward the center. Moreover, the development of the concrete cracks could also be associated with torsional loading across the y-axis due to the eccentricity of centerlines between the end-columns and the spandrel beams.

Figure A.21(a) shows a sudden increment in horizontal inward movement at the support at incident (b). This change in slope is associated with the reduction in resistance due to the concrete cracks, consequently rotating the whole system towards the center. Subsequently, the end-columns reacted to the lateral-torsional response forcing them to bend out-of-plane. Incident (b) was also evident in the external strain gauges located in the steel link plates #7 and #8. Figure A.21(b) shows the abrupt drop in load at the time the system reached the 115.8-kip (515-kN) mark, and a subsequent abrupt increase in strain in the steel link plates #7 and #8 was observed, indicative of a significant reduction in resistance due to the concrete cracks. The steel link plates were then carrying additional flexural loads.

At the time the concrete cracks developed in the column, the OMRF specimen was forced to redistribute load in order to preserve structural stability. This action consequently increased the deformation in the top M7 anchor bars at the center, as well as in all steel link plates of the OMRF specimen, since these elements were now carrying the flexural loads.

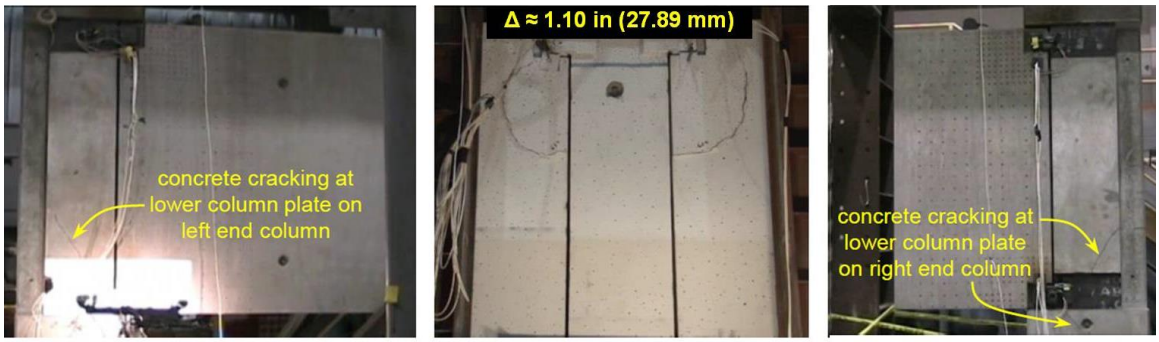

(a) Left (east) end-column (b) Center column/stud (c) Right (west) end-column

Figure 5.5 Elevation view, response zone II – incident (b): end-columns first concrete cracks at 114 kips (507 kN)

5.1.3 Forensic examination of response zone III

In the response zone III, loads were resisted through a combination of flexural action and the development of arching action. Four incidents, (c, d, e and f), were observed within this response zone. Figure A.22 benchmarks each of these incidents at its respective time of occurrence. After a 10-minute pause in loading between response zones II and III, an abrupt increment in vertical center displacement occurred. At the time the OMRF specimen reached the 127.8-kip (569-kN) load mark with a Δ of approximately 2.08 in. (52.7 mm) at 149.5 minutes of testing time, the #10 (#32) Grade 60 anchor bars welded to the left (M7) embedded angle in Beam-R reached yielding and began to exhibit a significant increase in plastic strain. This is benchmark incident (c) in Figure A.22. Figure 5.6 shows the location of the M7 anchor bars in the OMRF test specimen. The high magnitude tension forces acting at the bottom-center induced the M7 anchor bars in Beam-R to yield. Approximately ten minutes later, the opposite set of M7 anchor bars in Beam-L reached yielding. Both responses are depicted in Figure A.23.

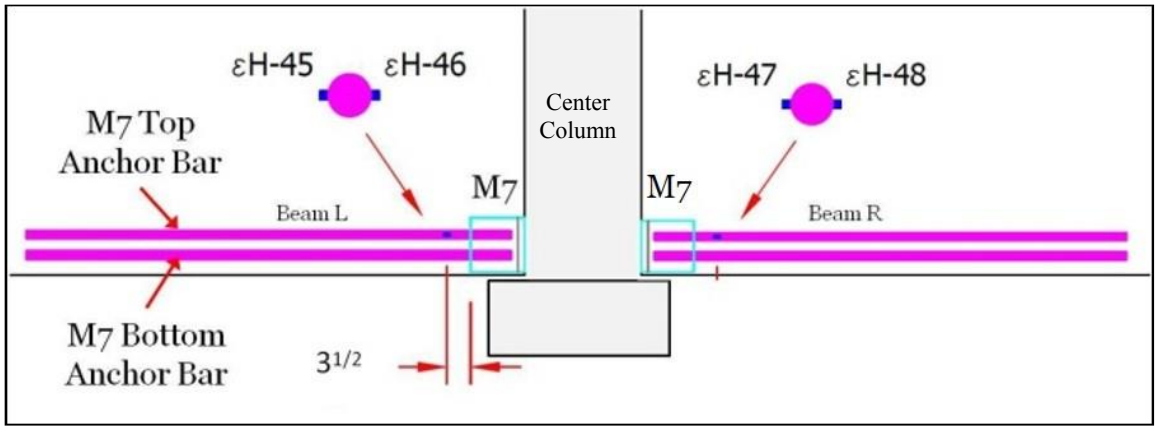

Figure 5.6 Location of M7 anchor bars

During the initial stages of the experiment, both end-columns showed an inward rotation towards the center column as depicted in Figure A.23. However, at the time the incident (c) occurred, a reverse in rotational direction was observed in the left (east) end-column from inward to outward, as well as a sudden inward rotation in the opposite end-column towards the center column (Figure A.24).

Following incident (c), an increase in resistance was observed in the OMRF specimen until the initial peak load was reached. At the time the center column reached a Δ of approximately 2.91 in. (73.9 mm) at 172.2 minutes of testing time, the load reached an initial peak load of 135 kips (600.51 kN), and then began to decrease. This initial peak load is benchmarked in Figure A.22 as incident (d). The reduction in applied load after incident (d) corresponds to the reverse in rotational direction of the end-columns as depict in Figure A.23.

The structural response observed beyond incident (d) reflected the significance of the discussed incidents (b) and (c) in the overall structural performance of the OMRF. The concrete crack growth at the supports and out-of-plane flexural behavior were some

of the major factors that contributed to the failure modes observed at incident (e). At the time the OMRF specimen reached a Δ of approximately 3.63 in. (92 mm) at the 184.6-minutes mark, a drop in load benchmarked incident (e) in (Figure A.22). This incident was associated with the observation of well-defined concrete cracks around the perimeter of the upper M8 embedded plate in the left (east) end-column. In addition to an increase of concrete cracks at the end-columns due to the concentration of stresses induced by high-magnitude bending moments at the support, an increment in torsional load resulted from the out-of-plane flexural behavior. Ultimately, the concrete cracked in the end-columns, consequently reducing the bond between the nelson studs welded to the plate (see Section 3.2.2.2) and the concrete, and initiating the detachment of the M8 plate from the left (east) end-column (Figure 5.7)

The initiation of detachment of the M8 plate corresponds to the drop in load observed in the torsional doughnut load cell (T2). Figure A.25 shows a sudden drop in load at 184.6 minutes of test time. This behavior is interpreted as a reduction in torsional load due to the partial detachment of the upper M8 plate in the left (east) end-column. Incident (e) is also evidenced by the sudden increment in strain captured in the pseudo-static response data recorded by the strain gauges located in steel link plate #1. Figure A.26 shows an abrupt drop in load associated with an abrupt change in strain measurements in the steel link plate #1 at incident (e). The concrete crack growth resulted in the detachment of the M8 plate, reducing the flexural resistance capacity of the system. Consequently, the beams began to bear against the columns due to the closing of the gap between them as it deflected, leading to an arching action (Figure 5.7). Soon after the initial cracks were observed around the M8 plate, the system began to show well-defined

cracks at the bottom of the end columns and at the top of the center column/stud, as shown in Figure 5.7. These cracks were formed by the concentration of stresses due to the bearing of the spandrel beams against the center column.

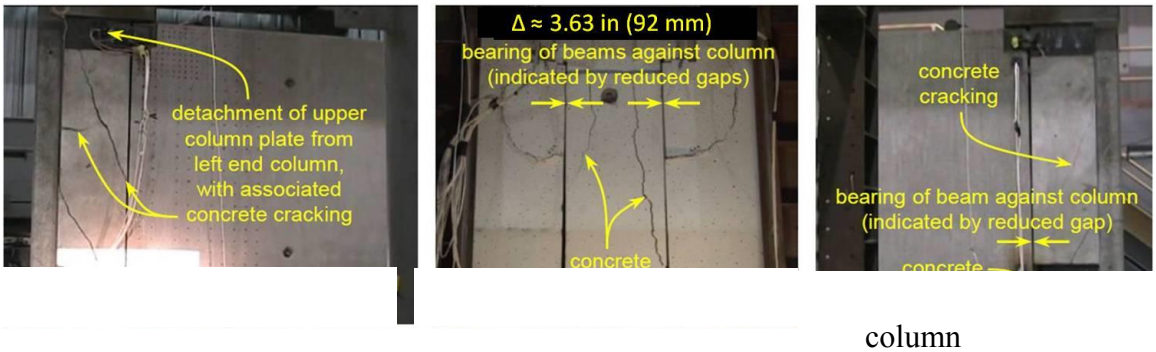

Figure 5.7 Elevation view, response zone III – incident (e): concrete crack growth around top M8 plate at left (east) end-column, initiation of bearing of beams to columns

The concrete cracks around the M8 plate continued to grow beyond the time of the incident (e) benchmark. At the time the center-deflection reached an approximately 3.79 in. (96.4 mm), a chunk of scabbed concrete fell from behind the top M8 plate in the left (east) end-column (Figure 5.8). This failure corresponded to the complete detachment of the M8 embedded plate from the end-column. The detachment of the M8 plate is benchmarked as incident (f) in Figure A.22. A drop in load at the 185.38-minute mark of test time, as shown in Figure A.26, along with a drastic increase in strain exhibited at steel link plate #1 may represent an episode of redistribution of load by the system to the undamaged structural elements after the detachment of the M8 plate. Figure A.25 also shows a drop in torsional load associated with incident (f) due to the detachment of the

M8 plate. Figure 5.9 illustrates the crack growth around the vicinity of the top M8 embedded plate in the left (east) end-column.

Figure A.24 evidenced a reverse in rotational direction of the end-columns following incident (f). At the time the top M8 plate in the left (east) end-column detached, the tension forces that were initially pushing the left (east) end-column inward towards the center column were released. This action allowed the left (east) end-column to rotate outward and the spandrel Beam-L to rotate towards the center column. As a result, the initial 1-in. (25.4-mm) gap between the beams and columns closed, as illustrated in Figure 5.2(c). The top ends of each beam began to bear against the center column, while the bottom ends of each beam began to bear against the end columns, enabling the development of arching action. Arching action became evident at a center column displacement of about 3.79 in. (96.4 mm) after incident (f). Increased vertical loads were developed in this stage, along with increased compressive forces in the beams, as the beams began to push the end-columns outward. This behavior was evidence in the data recorded by the LVDTs, located at the mid-span of the end-columns (see Figure A.2). These data depicts a significant increase in horizontal displacement after the 129-kip (531-kN) load mark, strengthening the belief that the end-columns began to rotate toward the center column after incident (f) due to the development of the arching action in the assembly. A schematic view of the OMRF specimen describing the damage stage at the end of response zone III is shown in Figure 5.2(c).

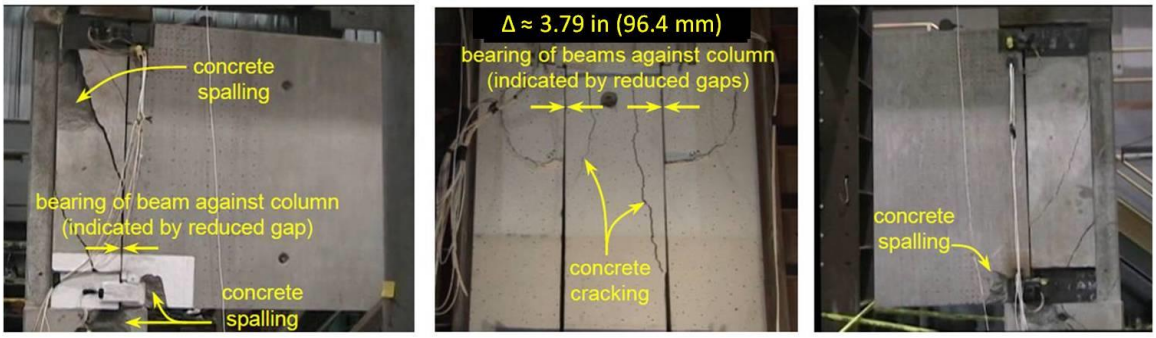

a) Left (east) end-column b) Center column/stud c) Right (west) end-column

Figure 5.8 Elevation view, response zone III – incident (f): initial bearing of beams against columns.

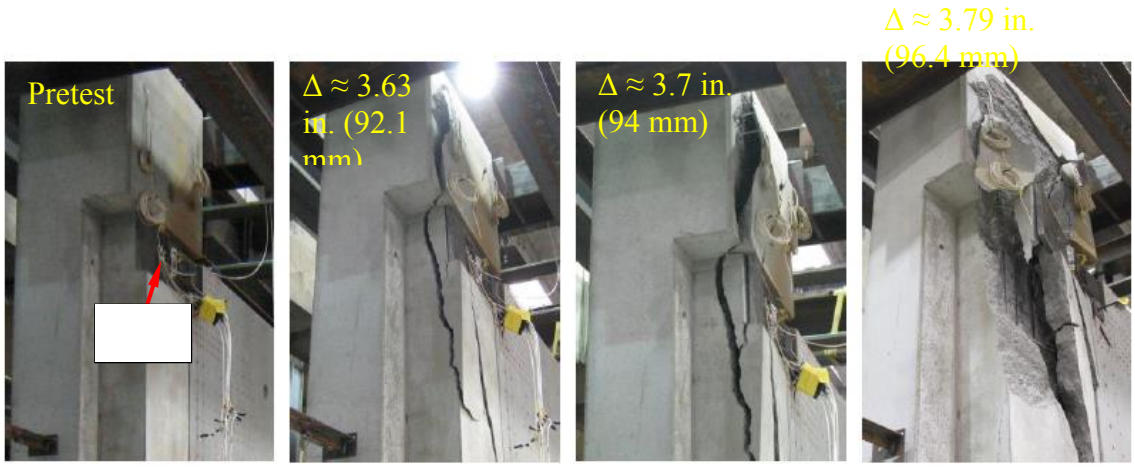

Figure 5.9 Development of concrete cracks around the upper M8 plate in left (east) end-column; detachment of M8

5.1.4 Forensic examination of response zone IV

The response zone IV is characterized by the development of arching action due to bearing of the beams against the columns. Figure A.27 shows the load and displacement vs. time data recorded within response zone IV, as well as the incidents observed within. The specimens continued to carry loads primarily through arching

action but at a reduced capacity because of multiple failures that reduced the resistance of the beam-to-column connections. Specifically, these failures degraded the capacity for transfer of tensile forces through the steel link plate connections at the upper steel link plate #1 on the left (east) end-column and at the lower steel link plate #3 on the center column/stud, as illustrated in Figure 5.2(d). These major incidents are marked as (g, h, and i) within the response zone in Figure A.27, and each incident is linked to a specific structural response.

After an 8-minute pause, following incident (f), the test was resumed. Succeeding the detachment of the M8 plate as discussed in Section 5.1.3, the OMRF specimen began to show additional signs of resistance reduction. However, at the time the OMRF specimen reached a Δ of approximately 4.85 in. (123.3 mm) at 212.5 minutes of test time, the load resistance ramped up again due to the system's ability to develop additional capacity through arching action. The top corner of each beam beared against the center column, and the bottom corner of each beam beared against the end-columns. Such bearing was evidenced by closing the gaps between the beams and columns. Figure 5.10 shows associated cracking and scabbing of concrete in regions where bearing forces were developed. This increase in stiffness due to arching action is benchmarked as incident (g) in Figure A.27 and Figure A.28. The structural behavior exhibited by the OMRF specimen after incident (g) is illustrated by Figure A.28. The abrupt increment in load carried by the system, with a minimum increment in vertical displacement depicted in Figure A.28, is characteristic of arching action developing along the moment frame.

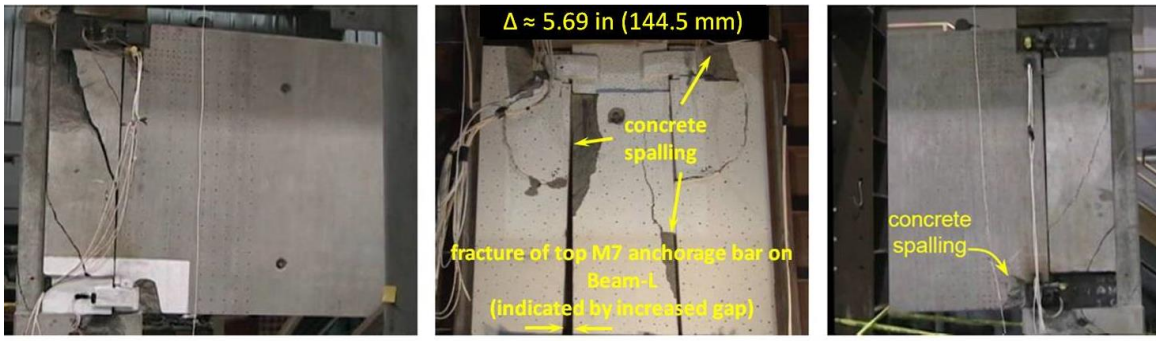

(a) Left (east) end-column (b) Center column/stud

Figure 5.10 Elevation view, response zone IV – incidents (g), (h) and (i): concrete spalling due to arching and rupture of the upper M7 anchorage bar

Incident (g) generated stress waves that were captured by the AE as surface waves. Figure A.32(a) shows the low-level acoustic emission response, transient event (185) associated with incident (g), and the high-frequency acceleration measurements captured by the accelerometer gauges associated with transient event (185). Figure A.32(b) shows an acceleration peak-to-peak signal of 1 g in L1A, and of 2.1 g's in L1C; (see Figure 3.27 for the locations of the gauges). This dynamic acceleration was associated with concrete crack growth in the bottom corner of Beam-L due to the concentration of stresses induced by the development of the arching action at the base of Beam-L at the left (east) end-column next to steel link plate #7.

Although the increment in vertical displacement was minimal compared to the observed increase in load during the development of the arching action, additional concentration of stresses resulting from the minimal change in displacement caused the cracked concrete to fall from the bottom connections at the base of the center column /stud (Figure 4.14). This tension failure observed in the concrete is benchmarked as incident (h) in Figure A.29. At the point the OMRF specimen reached a Δ of

approximately 5.5 in. (140 mm) at 214.66 minutes of test time, massive chunks of scabbing concrete began to fall from underneath the beams at the base of the center column.

In spite of the reduction in resistance experienced in incident (h), the load continued to increase steeply due to the arching action until it reached an ultimate peak of 168.2 kips (748 kN) with a Δ of approximately 5.69 in. (144.5 mm). At this point the load dropped sharply to only 25% of its peak value at 216.15 minutes of testing. This event is benchmarked in Figure A.27 as incident (i).

The drastic structural response observed in incident (i) was observed immediately after the fracture of the #10 (#32) Grade 60 anchor bars welded to the bottom connecting M7 angle on the left side of the center column/stud (see Figure 5.6 for location details). The lower M7 anchor bar failed first, consequently overloading the upper anchor bar causing it to fail immediately after benchmarking incident (i). Unfortunately, no strain gauge was attached to the lower M7 anchor bar. However, since the failure of the top bar occurred immediately after the failure of the bottom bar, the strain readings in the internal strain gauges (εH–45 and -46) located on the top M7 anchor bar provided information to determine an approximated fracture strain (ε_f), at which the both bars failed.

Figure A.5 and Figure A.30 shows the strain measurements in the top M7 anchor bar under discussion. The strain vs. time curves shown in Figure A.30 depict a significant difference between (εH–45 and -46) strain measurements. After analyzing the posttest deformation observed in the M7 anchor bars and identifying the location of the gauges, it was determined that the combination of loading conditions to which the bars were subjected corresponded to the recorded strain measurements. Records from both strain

gauges (εH–45 and -46, located at nine o'clock and three o'clock, respectively) (see Figure 3.18), depict an initial tensile deformation. However, as the displacement increased, the center column began to displace horizontally, inducing out-of-plane bending at the M7 anchor bars. This out-of-plane behavior became evident in the strain records of εH–45 (see Figure A.30) with a reduction in the strain readings due to compression deformation resulting from the out-of-plane bending. Since the strain record of εH–46 showed tensile behavior, it was chosen to obtain an approximate fracture engineering tensile strain for the M7 anchor bars.

Hence, based on the εH–46 data, both anchor bars ruptured at an approximate fracture engineering strain (ε_f) of 0.029 in./in. at 216.15 minutes of test time (see Figure A.30). The strain value of 0.029 in./in. is almost seven times lower than the average fracture engineering tensile strain (ε_{tf}) of the #10 (#32) Grade 60 bars determined in the material property study to be 0.18 in./in. documented in Appendix B. This decrease in strain readings corresponds to an apparent reduction in deformation capacity of 84%, when (ε_f) and (ε_{tf}) are compared.

During the posttest forensic examination it was found that the location and characteristics exhibited in both M7 anchor bar planes of failure were almost identical. Both fractured at the end of the flare-bevel-groove weld on the connecting angle, as is evident in Figure 5.11, which shows the connecting angle and welded anchor bars recovered from the specimen after the test. Figure 4.17 shows the posttest damage stage of the steel link plate #3 and anchor bars connection detail.

The structural deformation resulting from the failure of the anchor bar welded to the M7 angle was large enough to be evident in the data recorded at the high sample rate,

2 MHz, and at the low rate, 40 Hz, since the energy was high enough to cause considerable deformation within a short duration of 50 msec. Figure A.33 shows the acoustic emission response at transient event 194 associated with incident (i) and the dynamic drop in load of 25% of peak load in less than 35 msec. Figure A.34 shows the high-frequency acceleration measurements captured by the accelerometer gauges in transient event 194. Figure A.34(b) shows an acceleration peak-to-peak signal of 1000 g's in L1C at transient event 194. Figure A.35(a) shows a significant variation in strain in all gauges associated with the connection detail of steel link plate #3. Specifically, Figure A.35(b) shows that εH–45 captured a transient strain variation of approximately 0.0155 in./in. at the moment that the anchor bar fractured. The fracture of the anchor bars also resulted in the detachment of steel link plate #3 from the center column. This event is evidenced by the pseudo-static data collected in the strain rosettes gauges on the steel link plate #3 (Figure A.10); all strain gauges were clipped soon after the failure of the anchor bar. An increase in counter-clock rotation of the center column/stud toward the left (east) end-column was also observed soon after the M7 anchor bars failed.

Perhaps the connection design between the anchor bars and the embedded angles (M6 and M7) explains the reason why these bars failed before reaching the documented (ε_{tf}) in the material property study. All of the anchor bars in the specimen were welded to the embedded angles (M6 and M7) on each corner of the beams. This welding process could have developed a "heat-affected zone" in the bars that changed its mechanical properties causing both to behave as a brittle material when subjected to high magnitude tensile/bending loads, (to be discussed in Section 5.2.1).

The test was executed under a displacement-controlled scenario. At the time the top M7 anchor bar ruptured, the specimen suffered a dynamic displacement of 0.3 in. (7.6 mm) in less than 35 msec (see Figure A.33), and the ram could not keep up with the dynamic response, resulting in a misread in the load cell (L-95A) and the differential pressure gauge (L-95B). Figure 4.17 illustrates the posttest structural damage to the M7 angle connected to steel link plate #3. A schematic view of the damage and failure modes observed within response zone IV is shown in Figure 5.2(d). Also, the right (west) end-column began to exhibit outward rotation following incident (i) as depict in Figure A.24.

Figure 5.11 Different angles showing the location of fracture of the M7 anchor bars embedded in Beam-L near the center column

5.1.5 Forensic examination of response zone V

Response zone V is characterized by the continued development of arching action, the fracture of the torsion bars, and the detachment of the top M8 plate at the right (west) end-column. Figure A.31 shows the load and displacement vs. time data recorded within response zone V, and the incidents observed within. A total of four major incidents, (j, k, and l), were observed within this response zone. Each incident is linked to

a specific event that resulted in the reduction of structural stability and, consequently, permanent deformation. A schematic view of the posttest damage observed at the end of the response zone V is shown in Figure 5.2(e).

After the fracture of the anchor bars discussed in response zone IV, the load increased steeply as the specimen developed additional resistance through arching action, reaching 70% of the peak load until incident (j) occurred. At the time the OMRF specimen reached a Δ of approximately 7.86 in. (200 mm), at 248.17 min, a sudden drop in load was observed. This abrupt change in load is benchmarked in Figure A.31 as incident (j). Incident (j) is associated with two simultaneous localized failures observed in the OMRF specimen: (1) the fracture of the lower torsion bar at the right (west) end-column, and (2) diagonal cracking and shear deformation of the right end-column below beam level. Figure 5.12(c) shows the structural damage observed because of incident (j).

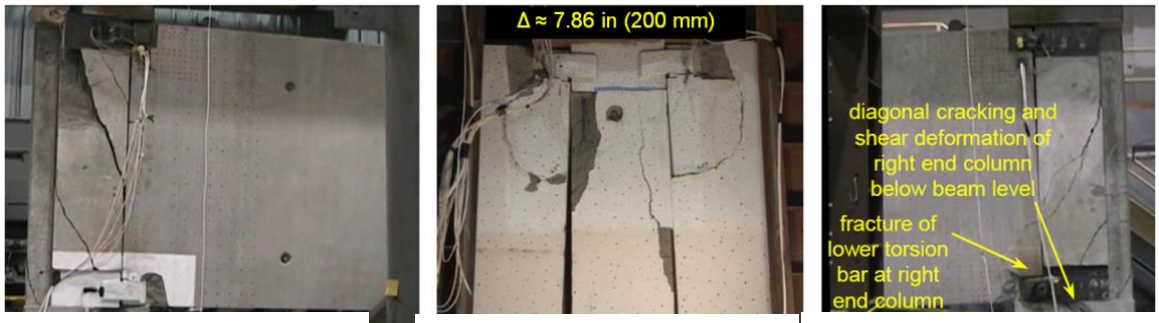

(a) Left (east) end-column (b) Center column/stud (c) Right (west) end-column

Figure 5.12 Elevation view, response zone V – incident (j): fracture of lower torsion bar in right end-column

The large vertical displacement observed in the system following incident (e), and later intensified after incident (i), induced torsional loads along the system forcing it to bend and rotate counter-clock toward the left (east) end-column. These torsional loads may have intensified after incident (i), causing the bar to suffer a tensile failure. Unfortunately, none of the data sets captured incident (j), since the torsion load cells (T1 and T2) were clipped during incident (i), and the fracture did not cause significant dynamic deformation to trigger the AE sensors. Shear deformation of the right end-column continued throughout the remainder of the test.

Another drop in load was observed at the time the OMRF specimen reached a Δ of approximately 10.6 in. (269 mm), at 276.53 minutes of testing. This abrupt change in load is benchmarked as incident (k) in Figure A.31. Incident (k) is also associated with three simultaneous structural failures: (1) the fracture of the lower torsion bar at the left (east) end-column due to torsional loads, (2) the shear deformation of the left (east) end-column below beam level, (which continued throughout the remainder of the test), and (3) the development of well-defined cracks around the perimeter of the top M8 plate embedded in the right (west) end-column. Figure 5.13 shows the structural damage observed because of incident (k). Shear deformation of the left (east) end-column occurred with extensive concrete scabbing. Figure 5.14 shows the final stage viewed from several angles.

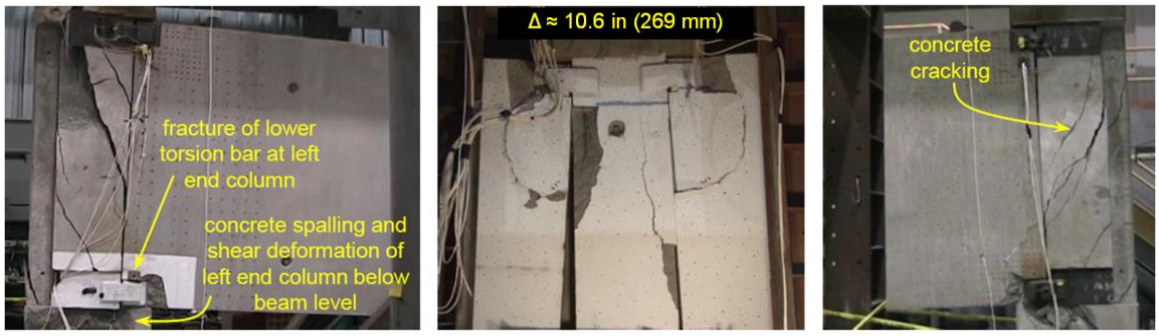

(a) Left (east) end-column (b) Center column/stud (c) Right (west) end-column

Figure 5.4(k): View, response zone V – incident (k): bar in left end-column, and cracking around top M8 plate in right (west) end-column

After closely examining the posttest damage to the end columns, it was observed that both columns suffered torsional rotation about the vertical y-axis. This rotation is attributed to the out-of-plane behavior generated by the eccentricity of forces at the connection (see Figure 5.4(b)), in addition to the axial moment generated by the eccentricity between the columns and the spandrel beam centerlines, especially during the development of the arching action.

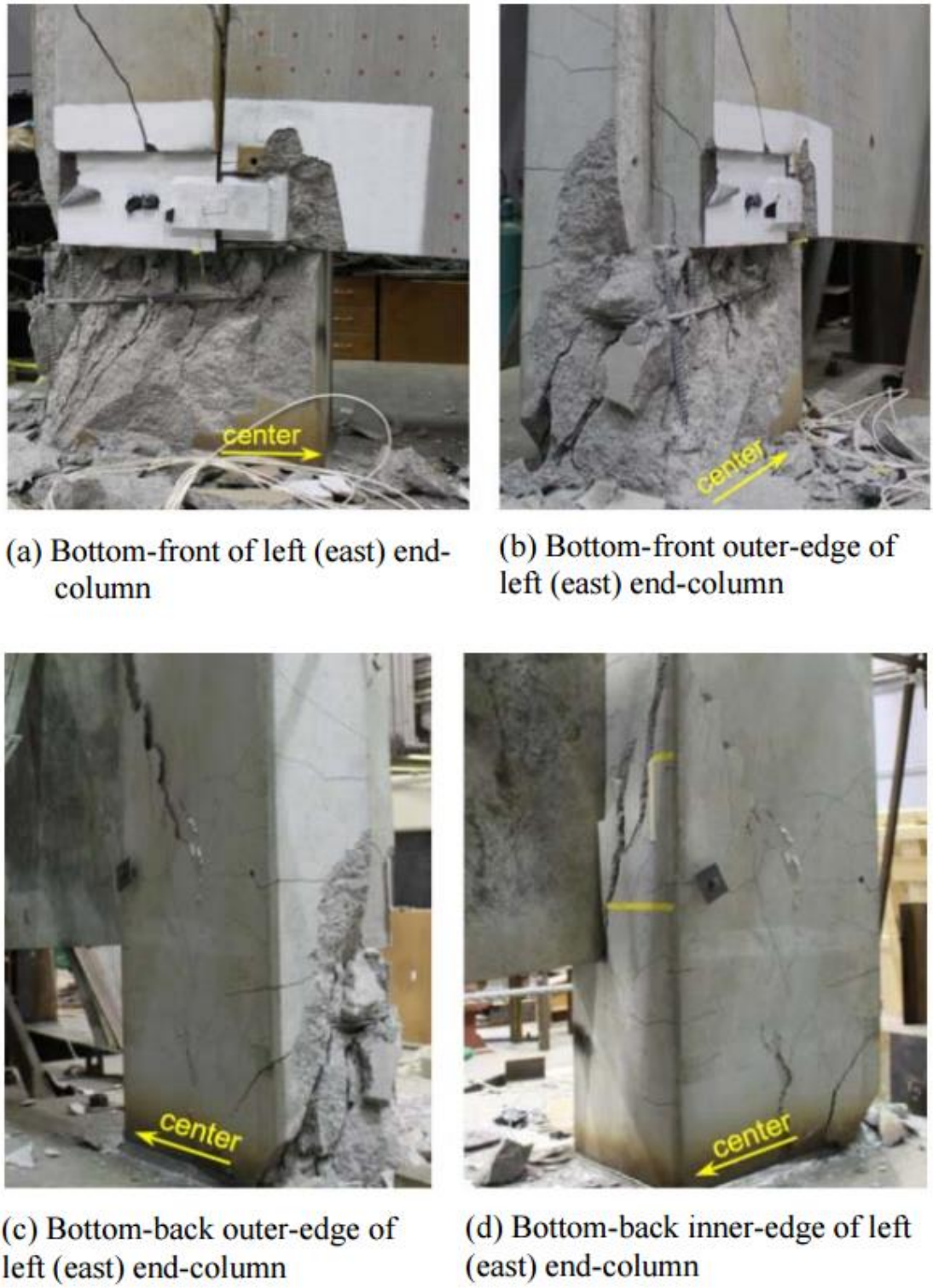

(a) Bottom-front of left (east) end-column

(b) Bottom-front outer-edge of left (east) end-column

(c) Bottom-back outer-edge of left (east) end-column

(d) Bottom-back inner-edge of left (east) end-column

Figure 5.14 Elevation view, posttest damage to the left (east) end-column

The structural deformation resulting from the failures within incident (k) was high enough to generate stress waves that were detected by the high-frequency data AE sensors. Figure A.36 shows the acoustic emission response at 276.53 minutes of test time (transient event 195), with an abrupt drop in load of 10 kips (44.5 kN) within a short time of 25 msec (see Figure A.36(b)). Figure A.37 shows the high-frequency acceleration measurements captured by the accelerometer gauges in transient event 195. Figure A.37(b) shows an acceleration peak-to-peak signal of 160 g's in L1A at transient event 195. The acceleration is associated with the shear deformation of the left (east) end-column below beam level and resulted in a significant reduction in load due to the displacement-controlled force scenario followed in the experiment.

The OMRF specimen continued deflecting beyond incident (k); however, the propagation of cracks along the system, in addition to the system's out-of-plane deflecting behavior, began to diminish the ability to maintain arching action. The top torsion bar through the right (west) end-column was ejected, and concrete began to fall from the perimeter of the top M8 plate in the same column. By the time the OMRF specimen reached a Δ of approximately 14.4 in. (366 mm), the upper M8 plate was detached from the right end-column, benchmarking incident (l). The structural damage observed at incident (l) is shown in Figure 5.15. The failure observed in incident (l) was similar to the failure observed previously on the left (east) end-column in incident (f). Figure 5.16 shows the detachment of the upper M8 plate in the right (west) end-column. This failure was accompanied by cracking and scabbing of concrete on the right (west) end column. Shear deformation of the right (east) end-column occurred with extensive concrete scabbing, Figure 5.17 shows the final stage viewed from several angles. Finally,

as the load continued to decrease, large chunks of scabbing concrete began to fall from the specimen. The test was terminated at a Δ of approximately 17.8 in. (452.12 mm).

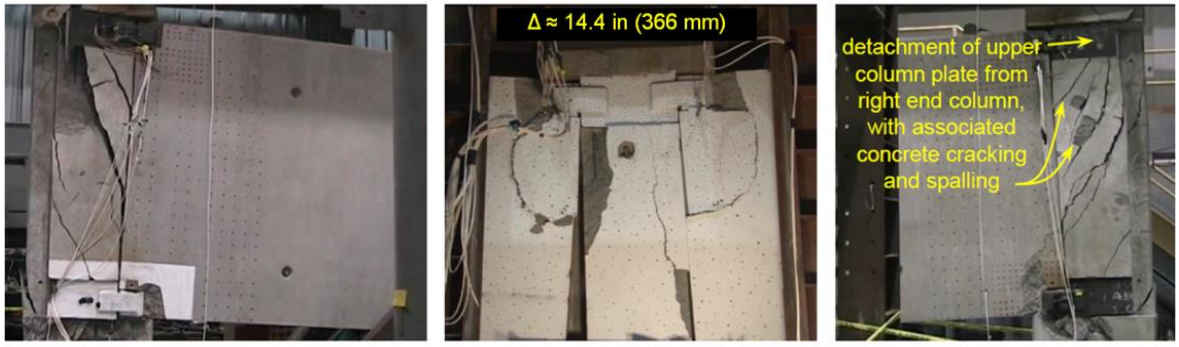

(a) Left (east) end-column (b) Center column/stud (c) Right (west) end-colum

Figure 5.15 Elevation view, response zone V – incident (l): detachment of the upper M8 plate embedded in the right (west) end-column

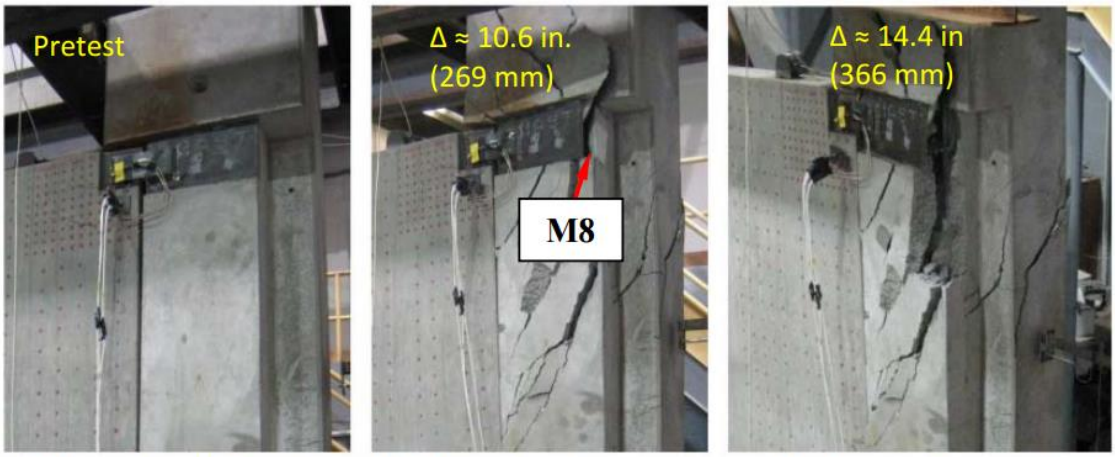

(a) Pretest right (west) end-column, elevation view (b) Posttest right (west) end-column, elevation view (c) Posttest right (west) end-column, outer-edge view

Figure 5.16 Response zone V – incident (l): detachment of the upper M8 in the right (west) end-column

(a) Bottom-front of right (west) end-column

(b) Bottom-front outer-edge of right (west) end-column

(c) Bottom-back outer-edge right (west)

(d) Bottom-back inner-edge of right (west) end-column

end colum

Figure 5.17 Elevation view, posttest damage to the right (west) end-column

5.2 Performance of beam-to-column connection prototype design

Although none of the steel link plates ruptured, two M7 anchor bars failed as discussed in incident (i). The failure of the bars could have potentially reduced the flexural capacity of the assembly. Yet, an empirical approach should be developed to determine if in fact the failure of the anchor bars reduced the overall flexural capacity of the assembly, as well as to determine if the failure occurred prematurely. Nonetheless, as the displacement increased, the steel link plates began to also exhibit an out-of-plane behavior that could have also adversely affected the overall performance of the OMRF test specimen.

Furthermore, each of the T-shape exterior columns were designed to withstand a combined service load of approximately 81.1 kips (360.8 kN). The intended purpose of the beam-to-column prototype design under investigation was to enable the assembly to withstand the column's service load after the removal of an exterior column. The steel link plates were designed to transfer the load bridging to the undamaged columns by coupling forces to maintain stability.

The test peak load was 168.2 kips (748 kN) (just before the M7 anchor bars fractured). Therefore, if the prototype beam-to-column design is only considered for the fourth floor, the prototype will not be able to withstand the removal of an exterior column from the same floor because it only reached 32% of the total combined service load from the above floors (533.3 kips (2372 kN)) required to prevent collapse.

However, if the beam-to-column prototype design is incorporated in all of the perimeter OMRFs joints of the precast structure, there is a potential for the system to withstand the removal of the exterior column from the fourth floor. Nonetheless, multiple

unknowns such as the interaction of the surrounding frames in the distribution of loads after the failure will also need to be considered in the overall performance of the prototype connection design.

Section 5.2.1 describes the empirical evaluation used to determine if the failure of the M7 anchor bars occurred prematurely. Section 5.2.2 provides a detail description about the performance of steel link plates coupling.

5.2.1 Bottom-center anchor bars

Figure 5.18(a) shows a schematic view of the OMRF test specimen. In the absence of a high-fidelity numerical model capable of simulating the non-linear behavior exhibited by the OMRF test specimen, the performance of the beam-to-column connection prototype design was examined as a simplified frame using reinforced concrete structures design standards (ACI 318-08) along with the experimental data. In light of the fact that none of the steel link plates failed or ruptured but that the anchor or the embedment details did fail, a simplified full-scale model was considered for representation of the OMRF test specimen as shown in Figure 5.18(b).

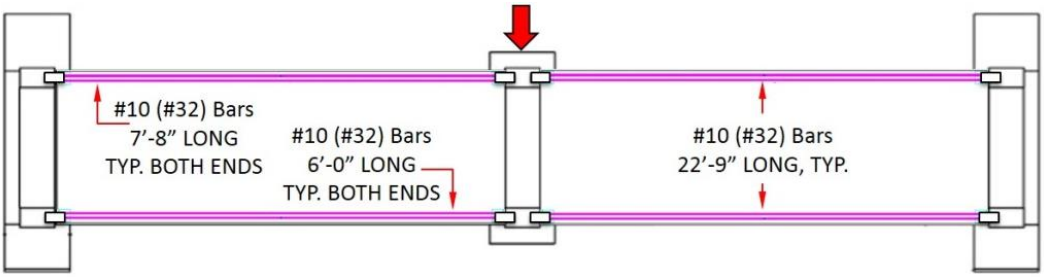

a) OMRF reinforcement detail.

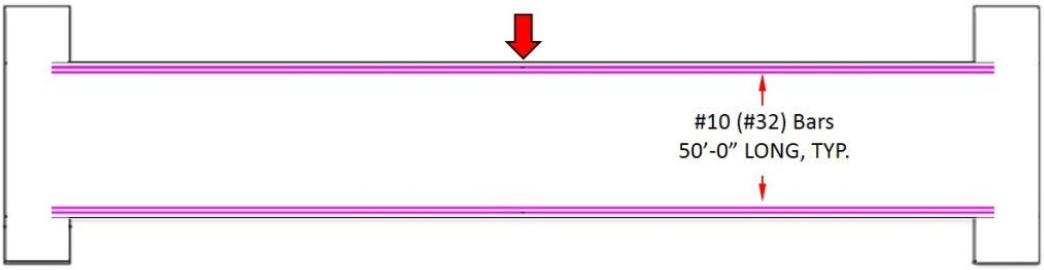

b) Simplified OMRF reinforcement detail.

Figure 5.18 Elevation view of simplified-frame of the OMRF test specimen

This simplified OMRF model consisted of a continuous doubly-reinforced, monolithic concrete deep beam with end-columns. Reinforcement was four continuous A706 #10 (#32) Grade 60 bars in the top and bottom of the beam. Each of the bars was spaced at 3.75-in. (95-mm) center-to-center with a 2-in. (50.8-mm) cover all around. The area of steel was equal to 5.08 in.^{2} (6.45 cm^2) in each area of reinforcement, the compression zones, as well as in the tension zones.

The approach considered the following tasks:

1. determination of the cross-section's nominal flexural strength (Mn) of the simplified OMRF frame,
2. determination of the experimental strain readings at each incident from the M7 anchor bars from channels εH-46 and -48,

3. determination of the stress associated with the experimental strain reading using the data from the material property study on the A706 Grade 60 bars,

4. calculation of the associated sectional moment (Ma) per incident, and

5. establishment of a relationship between the calculated cross-sectional flexural nominal strength and the calculated associated sectional moment to examine the performance of anchor bars in the tension zone.

The objective of this empirical approach was to determine an approximate applied moment at which the anchor bars failed, as well as to determine whether the 84% reduction in strain capacity observed in the M7 anchor bars, (discussed in Section 5.1.4), could be translated into a premature failure of the anchor bars.

PTC Mathcad Prime® 3.1 (Mathcad, 2015), an engineering calculation software, was used to calculate the simplified frame's cross-sectional flexural nominal strength. The stress block used in the determination of the nominal strength is shown in Figure 5.19. The terms in Figure 5.19 are as defined later for equations 5.1 through 5.6. All of the parameters and material mechanical properties in the simplified frame were duplicated from the actual OMRF test specimen, including the concrete strength, as well as the grade, size, and location of the reinforcement bars. However, the length of the anchor bars in the simplified-frame were extended along the full beams.

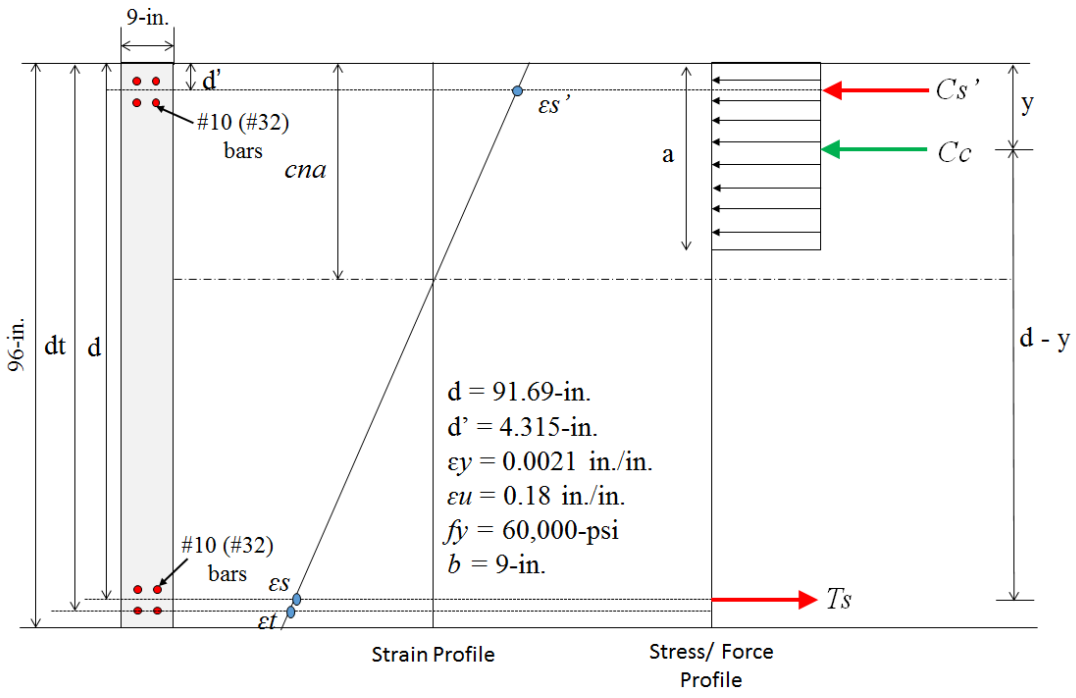

Figure 5.19 Stress block of simplified OMRF test specimen

Before successfully determining the cross-section flexural nominal capacity, the depth of the concrete neutral axis (*cna*), the tension zone force (*Ts*), concrete compression zone force (*Cc*), and the steel compression zone force (*Cs'*) were required to be calculated. However, since a doubly reinforced "deep" beam was under study, a number of assumptions were taken into consideration before calculating any additional design parameters. These assumptions were:

1. perfect bond between the steel reinforcement and the concrete,
2. pure axial loading conditions, no out-of-plane behavior or torsion,
3. compression zone steel does not yield. The strain in the compression reinforcement (εs') never exceeded yielding, meaning that the deformation in the upper reinforcement detail remained in the elastic region. Therefore, the stress in the compression reinforcement, denoted as (fs'), was equal to fs' = Es* εs', where Es is the modulus of elasticity of the reinforcement steel,

4. tension zone steel does yield. The strain in the tension reinforcement (εs) did exceed yielding, which means that the bars were deforming in a plastic manner. Therefore, the yield strain (εy) was εy < εs; however, the ultimate strain (εu) was εu < εs, consequently fy < fs < fu, where the steel yield stress is denoted as (fy), the stress in the tension steel as (fs), and the steel ultimate stress as (fu).

In practice, an elastic perfectly-plastic model is often used to define $fs = fy$ in the tension zone. However, due to the natural non-linear behavior of the A706 reinforcement within its plastic region (Figure 5.20(a)), a fourth-order polynomial curve fit was plotted over the plastic region in the stress vs. strain curve obtained from the material property study documented in Appendix B, as shown in Figure 5.20(b).

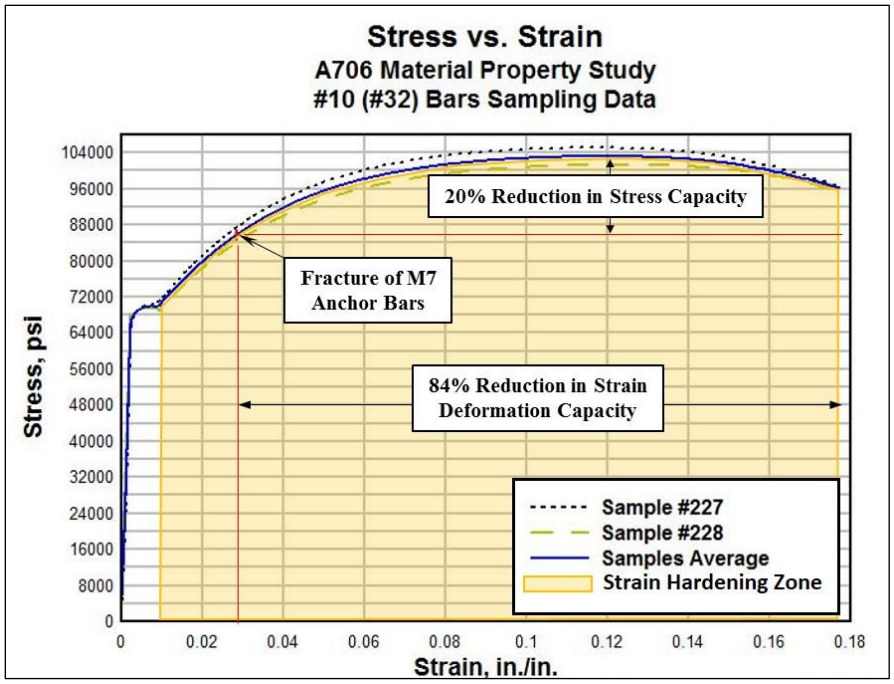

(a) A706 Sampling Data

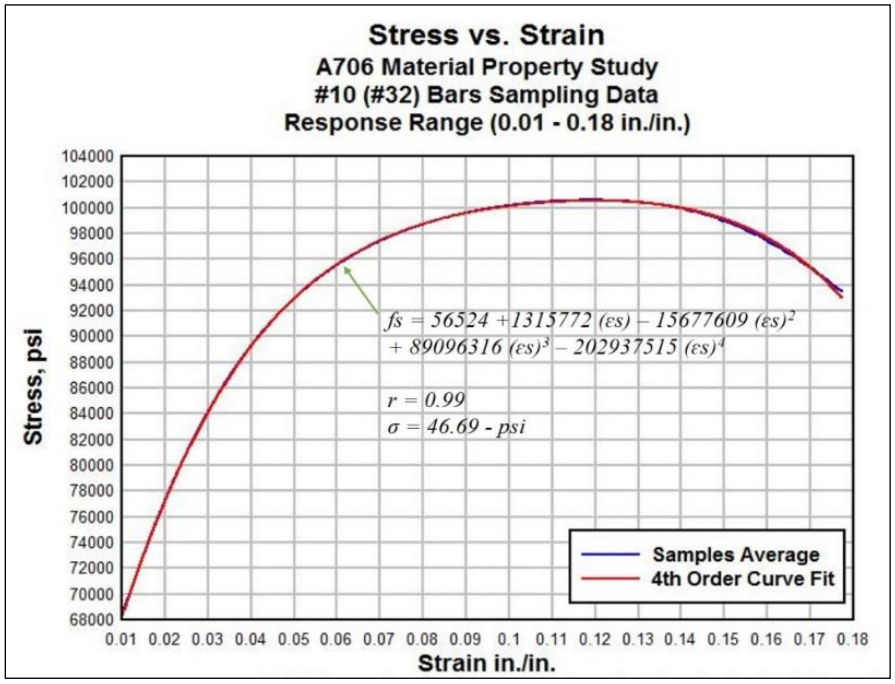

(b) Curve fit to A706 sampling data

Figure 5.20 A706 material sample data and curve fit to determine *fs*

The fourth-order curve equation shown in Figure 5.20(b) was obtained using DPlot (Dplot, 2015), a graphing software designed to let scientist and engineers plot, manipulate, and analyze high-frequency data.

After establishing force equilibrium in the cross-section shown in Figure 5.19 as described in equation 5.1, the statistical equation was then used to substitute *fs* in equation 5.2 below to determine the concrete neutral axis location, as follows.

$$Ts - Cs' - Cc = 0 \tag{5.1}$$

$$Ts = As\,(fs) \tag{5.2}$$

$$Cs' = As'\,(fs') = As'\,(Es)(\boldsymbol{\varepsilon} s') \tag{5.3}$$

$$Cc = 0.85\,(fc')\,(b)\,(0.75)\,(cna) \tag{5.4}$$

The strains $\boldsymbol{\varepsilon}s'$ and $\boldsymbol{\varepsilon}s$ were determined using similar triangles in the strain profile shown in Figure 5.19 as follows.

$$\boldsymbol{\varepsilon}s' = \left(\frac{cna - \mathrm{d}'}{cna}\right) * 0.003 \tag{5.5}$$

and

$$\boldsymbol{\varepsilon}s = \left[\left(\frac{\mathrm{d}-\mathrm{d}'}{cna-\mathrm{d}'}\right) * \boldsymbol{\varepsilon}s'\right] - \boldsymbol{\varepsilon}s' \tag{5.6}$$

where,

Ts = Tension zone force

Cs' = Steel compression zone force

Cc = Concrete compression zone force

As = Area of steel in the tension zone

fs = Stress in tension steel

As’ = Area of steel in the compression zone

Es = Modulus of Elasticity

εs’ = Strain in the compression steel

fc’ = Concrete compressive strength

b = Beam cross-section width

cna = depth to neutral axis

d’ = Depth from the top of the beam to the center of mass of the steel detail in the compression zone

d = Depth from the top of the beam to the center of mass of the steel detail in the tension zone

εs = Strain in the tension zone

The equations were then inserted into Mathcad to solve for the depth of the concrete neutral axis, which was equal to 7.5 in. (190.5 mm). Having this parameter calculated, the assumptions regarding the tension and compression zones were then verified, (εs’ < εy) and (εy < εs). Once verified, the cross-section’s flexural nominal strength was calculated using moment equilibrium in the cross-section shown in Figure 5.19 as follows.

$$Mn = Cs' (d - d') + Cc (d - y) \quad (5.7)$$

where,

Mn = Flexural nominal strength

Cs’ = Steel compression zone force

d’ = Depth from the top of the beam to the center of mass of the steel detail in the compression zone

d = Depth from the top of the beam to the center of mass of the steel detail in the tension zone

Cc = Concrete compression zone force

y = a/2; a = height of stress block as defined by ACI 318-08

The resulting flexural nominal strength was equal to 3,284.17 kip-ft (4,452.73 kN-m). Then, the strain readings from the upper M7 anchor bars from both beams were determined for incidents (a) through (i). The strain readings are tabulated in Table 5.3.

Departing from the assumption that the anchor bars were only deforming due to axial loading, the strain readings were used to determine the associated stress (*fsa*) from the stress vs. strain curves obtained in the material property study depicted in Figure 5.20(a). The associated stresses are also tabulated in Table 5.3. Based on the experimental observation discussed in Section 5.1, the M7 anchor bars in Beam-R yielded at incident (c). The data shown in Table 5.3 also indicate that the M7 anchor bars yielded at incident (c). The associated stress in the top M7 anchor bar in Beam-R resulted in 63,815-psi (439.9 MPa) as shown in Table 5.3. This value matched the A706 typical minimum yielding stress, supporting the empirical procedure as a practical approach to analyze the experimental results.

After calculating the associated stresses in relation to the experimental strain readings per incident, the associated sectional moment (Ma) was calculated using moment equilibrium in the cross-section (Figure 5.19). These moments represent an empirical approximation of the forces acting on the cross-section throughout the experiment. The associated sectional moments, tabulated in Table 5.4, were also

calculated using Mathcad (Mathcad, 2015) for incidents (a) through (i), using the following equation.

$$Ma = Cs'(y - d') + Ts\ (d - y) \tag{5.8}$$

where,

Ma = Associated sectional moment

Cs' = Steel compression zone force

y = a/2; a = height of stress block

d' = Depth from the top of the beam to the center of mass of the steel detail in the compression zone

d = Depth from the top of the beam to the center of mass of the steel detail in the tension zone

This experimental data facilitated the development of a simplified mathematical approach to examine the performance of the anchor bars, but most importantly provided the data to determine if the ruptured bars failed prematurely, possibly indicating poorly-designed spandrel beams.

Once the associated sectional moments (Ma) were calculated, they were compared to the previously calculated simplified-frame cross-sectional nominal flexural strength values. A simple mathematical approach was used to establish a relationship between them. The associated sectional moment (Ma) value was divided by the simplified-frame nominal flexural strength (Mn) value at each incident. These values were then multiplied by 100, resulting in a percentage intended to describe the level of performance at which the anchor bars were acting at each incident in terms of the

simplified cross-sectional flexural nominal capacity. These percentages are tabulated in Table 5.4.

Table 5.3 Associated stress to experimental strain readings per incidents

Incident	Δ		M7 Steel Angles' Anchor Bars					
	(in.)	(mm)	Strain Beam-L (εH-46)	Associated Stress (*fsa*)		Strain Beam-R (εH-48)	Associated Stress (*fsa*)	
				(psi)	MPa		(psi)	MPa
a	0.38	9.6	0.001421	36,130	249.1	0.001647	43,356	298.9
b	1.1	27.9	0.001699	45,127	311.1	0.00191	51,979	358.4
c	2.08	52.7	0.002055	56,721	391.1	0.002395	63,815	439.9
d	2.91	73.9	0.023619	79,964	551.1	0.022809	79,448	547.8
e	3.63	92.1	0.02726	82,462	568.6	0.023144	79,653	549.2
f	3.79	96.4	0.027321	82,497	568.8	0.023192	79,664	549.3
g	4.85	123.3	0.027951	82,898	571.6	0.023197	79,678	549.4
h	5.5	139.8	0.028117	82,998	572.3	0.023373	79,780	550.1
i	5.69	144.5	0.029006	83,095	572.9	0.023623	80,009	551.6

Table 5.4 Associated sectional moment obtained using experimental strain readings per incidents

	Beam-L			Beam-R		
	Ma		Performance (Ma)/(Mn)*100	Ma		Performance
Incident	kip-ft	kN-m		kip-ft	kN-m	(Ma)/(Mn)*100
a	1335.83	1.81	41%	1607.50	2.18	49%
b	1674.17	2.27	51%	1932.50	2.62	59%
c	2110.83	2.86	64%	2377.50	3.22	72%
d	2985.00	4.05	91%	2965.83	4.02	90%
e	3079.17	4.17	94%	2973.33	4.03	91%
f	3080.00	4.18	94%	2973.33	4.03	91%
g	3095.00	4.20	94%	2974.17	4.03	91%
h	3099.17	4.20	94%	2978.33	4.04	91%
i	3102.50	4.21	94%	2986.67	4.05	91%

According to the experimental observations, both anchor bars failed within Response Zone IV. First, the bottom anchor bar and then immediately the top at incident (i). From the empirical approach, it is determined that the bars apparently failed when

they reached 94% of the simplified cross-section's nominal flexural strength, suffering a reduction of 6% of the expected design performance.

Based on this empirical procedure, none of the M7 anchor bars suffered a premature brittle failure. In fact, both of the ruptured anchor bars in Beam-L failed beyond yielding, suffering permanent deformation until ruptured. However, judging by the severe deformation and damage observed during the posttest forensic examination of the OMRF test specimen, it is easy to conclude that all of the bottom anchor bars were subjected to a combination of severe loading conditions. This reasoning may explain the failure of the M7 anchor bars at 94% of design performance. However, when the observed failure strain is compared to the one obtained in the material property study documented in Appendix B, it's still uncertain as to why the bars failed so promptly within the plastic region before reaching the expected failure engineering strain. Figure 5.20(a) shows a graphic representation of the stress vs. strain relationship of the A706 #10 (#32) Grade 60 bars tested as part of the material property study. The M7 anchor bars observed failure strain of 0.029 in./in. is marked in Figure 5.20(a). When the observed failure strain is compared to the material sample data, an 84% reduction in deformation capacity and a 20% reduction in ultimate stress are observed.

Hence, after successfully completing the experiment, both ruptured anchor bars were removed from the OMRF test specimen, and the bars' failure profiles were closely examined. During the examination, it was determined that even though the anchor bars fractured at different times, the location and the characteristics exhibited in both planes of failure were almost identical. Both fractured at the end of the flare-bevel-groove weld on the connecting M7 angle (see Figure 2.5). Figure 5.21 shows a close-up view of the

fractured surface of both M7 anchor bars. Flat surface, very little necking, chevron marks, and crystallization are some of the characteristics found on the fracture surface of the bars. These characteristics are typically representative of a material failure affected by "heat-affected zones." These facts consequently strengthen the belief that the anchor bars were affected by a "heat-affected zone", especially the ruptured M7's bottom anchor.

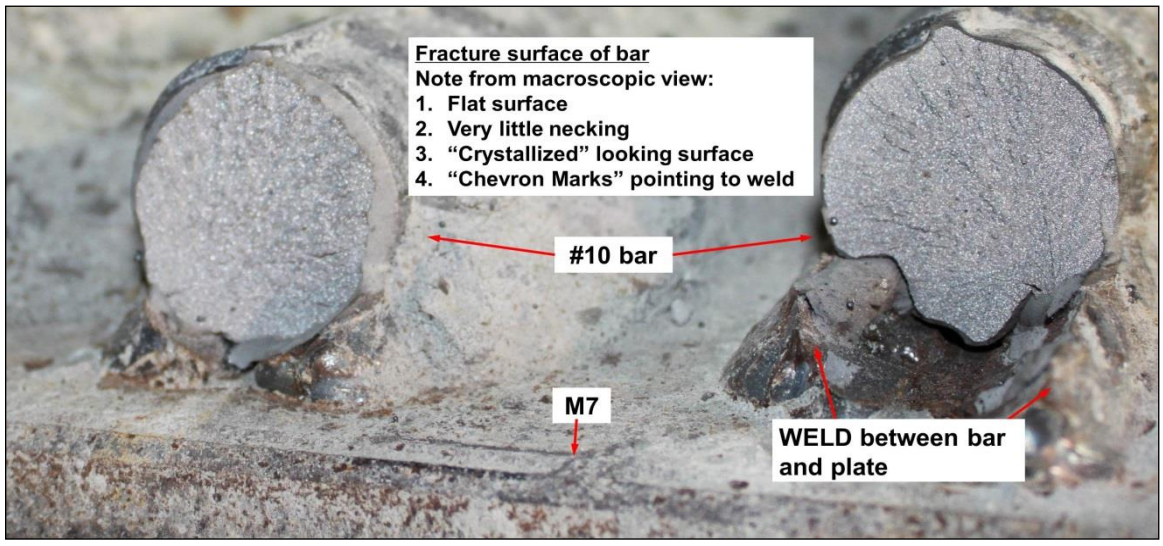

Figure 5.21 Close-up view of the fractured profile of both failed M7 anchor bars

The term "heat-affected zone" is used to describe a portion of the base metal that was not melted during brazing and cutting/welding/cooling, but whose microstructure and mechanical properties were altered by the heat transmitted by a near weld (Gunaraj and Murugan, 2002). Studies by Gunaraj and Murugan demonstrated that this alteration can be detrimental, causing stresses that reduce the strength of the base material, leading to brittle failures of critical structural elements. A "heat-affected zone" usually occurs

inside the metal and cannot be seen. ASTM A706 Grade 60 bars are considered weldable; nevertheless, subjecting any steel bars to high temperatures can potentially alter the bars' mechanical properties.

This theory that the bars were affected by the welding and cooling process was also considered by NIST to investigate the brittle failure of a similar M7 detail connection used in the design of a SFRM. NIST conducted a tensile strength test following ASTM E8 (2015) of an A706 (2015) #11 (#35) Grade 60 welded anchor bar connection recovered from a SFRM specimen previously tested by ERDC, in which a similar bar failure profile was observed.

The component used in the NIST test setup was retrieved from a location in the previously tested SFRM specimen that was subjected to predominantly compressive loads. The connection design for the SFRM was very similar to the OMRF, with only two main differences, i.e., (1) bar size, and (2) the quantity of bars per steel angle plate. The SFRM had three bars connected to the embedded angle plate in each corner of the spandrel beams. The recovered three-bar connection detail was sawed through the angle and link plate to isolate a single anchorage bar for testing along with a strip of angle having a width of 4.5 in. (114 mm) welded to the #11 (#35) bar. The experimental setup is illustrated in Figure 5.22. A complete design of experiment and the experimental procedures followed in the execution of the component bar test are documented in Main et al. (2015).

The results of the welded bar component test are shown in Figure 5.23. Figure 5.23(a) shows the stress-strain curve obtained from the welded bar component test along with that obtained from tensile testing of a #11 (#35) bar for comparison. The yield stress

is almost equivalent in both cases, and the welded bar showed only slightly lower stress in the post-yield work-hardening phase. However, the welded bar had significantly reduced ductility with the ultimate stress being reached at an engineering strain of 0.092 in./in. and fracture occurring immediately thereafter without appreciable necking. In contrast, the ultimate stress was reached at an engineering strain of 0.111 in./in. in the bar tensile test and was followed by significant necking and softening prior to fracture.

The weld in the bar had also significantly reduced its deformation capacity, with a fracture stress reached at an engineering strain of 0.092 in./in., compared to the tensile test bar that reached a fracture stress at an engineering strain of 0.15 in./in., which resulted in a large reduction of 38% in deformation capacity when the welded bar data are compared to the tensile test data.

Figure 5.23(b) shows the fractured anchor bar after the component test. It is evident that the fracture occurred at the end of the weld, very similar to the plane of failure observed in OMRF M7 anchor bars (see Figure 5.11). NIST reported that the reduced ductility of the welded anchor bar is believed to have been caused by changes in material properties in the "heat-affected zone" near the weld in the SFRM specimen, e.g., microstructural changes such as the formation of brittle martensite, adversely affecting the overall structural performance of the SFRM prototype model.

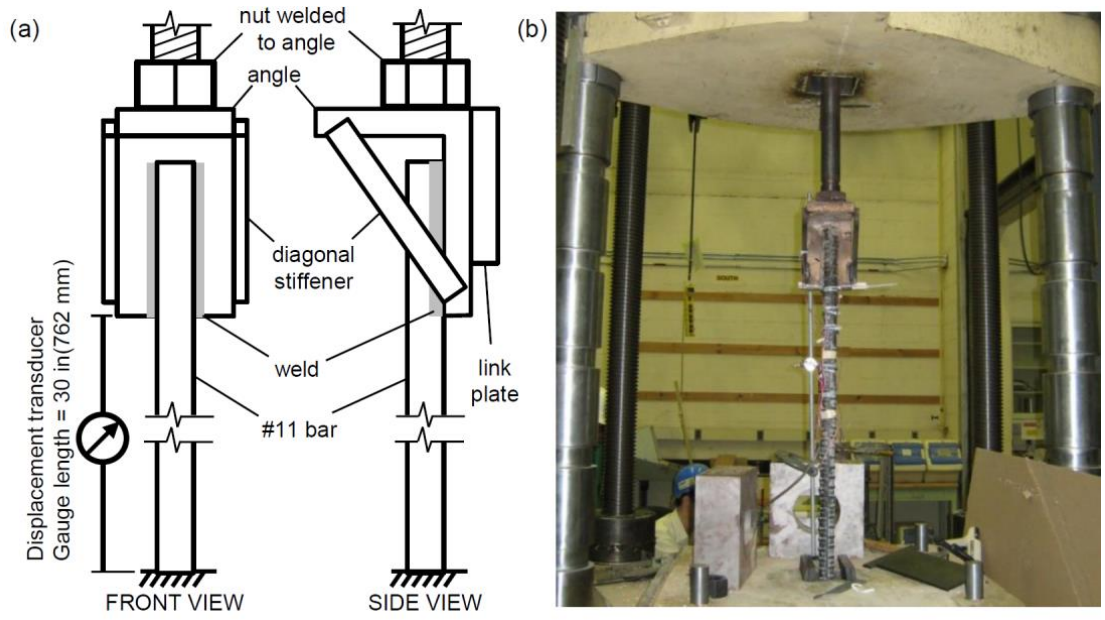

(a) Schematic view. (b) Elevation view of test setup.

Figure 5.22 Component test setup for welded anchor bar (Main et al., 2015)

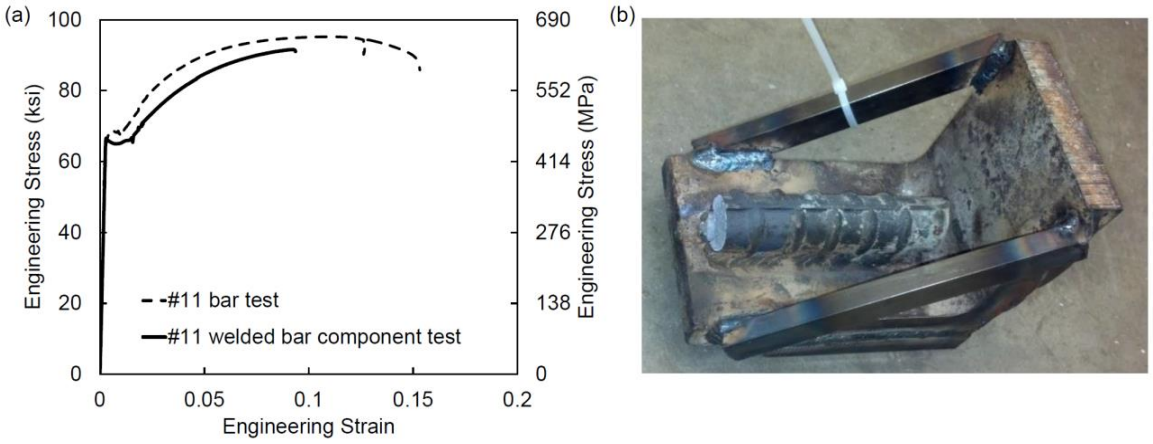

(a) Stress-strain curve. (b) Fractured anchor bar.

Figure 5.23 Results of welded anchor bar component test (Main et al., 2015)

Therefore, the data collected from the component test of the SMRF, #11 (#35) welded bar, is indicative of a possible development of a similar phenomenon in the #10 (#35) M7 anchor bars in the OMRF specimen. This phenomenon could have also adversely reduced the ductility and the deformation capacity of the bottom M7 anchor bars, preventing the bars from undergoing a strain hardening behavior that may have enhanced the levels of plastic deformation typical in A706 reinforcement bars as depict in Figure 5.20(a). Nonetheless, multiple unknown factors could have also contributed to the observed 84% reduction in deformation capacity of the A706 M7 anchor bars.

5.2.2 Steel link plates

As previously discussed, although all of the steel link plates exhibited high deformation, none of them ruptured. Nonetheless, as the displacement increased, the plates began to exhibit an out-of-plane behavior that adversely affected the overall performance of the OMRF test specimen. Once the steel link plates yielded and the displacement continued to increase, an eccentricity in the transfer of forces between the anchor bars and the steel link plates (as shown in Figure 5.4) resulted in an out-of-plane bending behavior that directly affected the overall performance. Such eccentricity was evident in all of the steel link plates.

The vertical displacement recorded in all four “string potentiometer” gauges at each incident is illustrated in Figure 5.24. This graphical representation of the OMRF vertical displacement progression throughout the experiment is evidence of the lack of symmetry in the assembly. Certainly, the failure of the second (top) M7 anchor bar at incident (i) had the most significant impact into the out-of-plane behavior. The eccentricity of forces caused by the offset of the steel link plates to the anchor bars could

have also played a role in the premature failure of the M7 anchor bars, as well as the detachment of the top M8 embedded plates at the end-columns. These two principal failures had a direct impact on the overall performance of the OMRF test specimen.

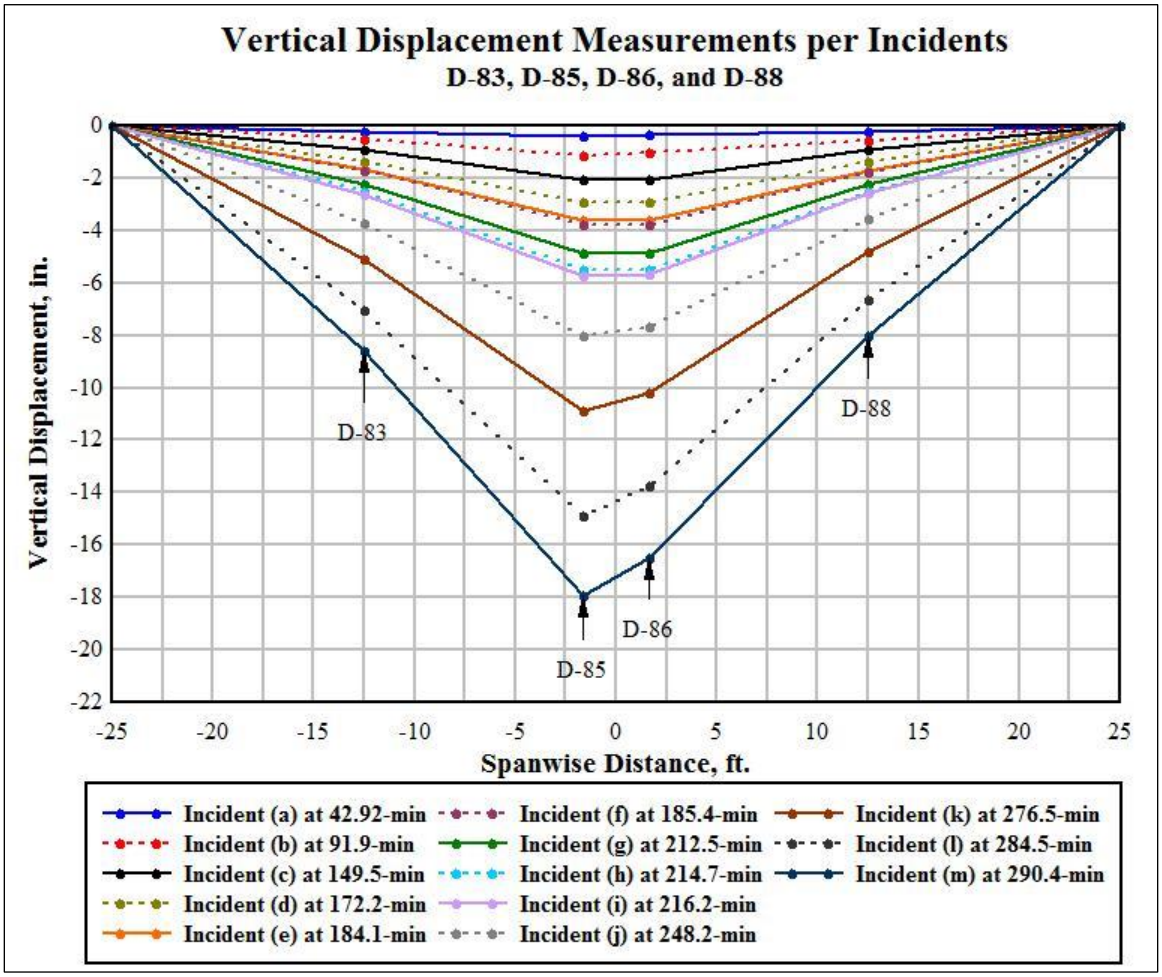

Figure 5.24 Vertical displacement measurements by incidents

Strain rosettes were located at a number of locations on the link plates, and stress transformations were applied to the rosette data to obtain normal and shear stresses. However, these transformations are applicable only for elastic behavior, and yielding of

the link plates occurred very early in the response at Δ of approximately 0.38 in. (9.6 mm) or earlier. The maximum shear and normal stress values in this early stage of the response were not found to provide significant insights into the behavior of the assembly, so only axial strain values were used for discussion in this report.

5.2.2.1 Steel link plate at location 1

The steel link plate at location #1 exhibited severe deformation due to the high magnitude bending moments acting at the end-columns. A posttest well-defined clockwise rotation towards the center column/stud was observed in this link plate as shown in Figure 5.25. In addition, considerable out-of-plane permanent deformation along the z-axis and towards the back of the OMRF test specimen was observed. This out-of-plane motion was attributed to the eccentricity of forces at the connection.

The strain data collected in all gauges attached to the front face depicted high levels of tension strain readings (Figure A.8), implying that, during the initial response zones, the link plate #1 was acting in tension to provide equilibrium in the assembly. However, at the time the M8 embedded plate in the left (east) end-column detached, the strain data in link plate #1 flattened, forcing the assembly to redistribute load to the undamaged steel link plates to preserve structural stability.

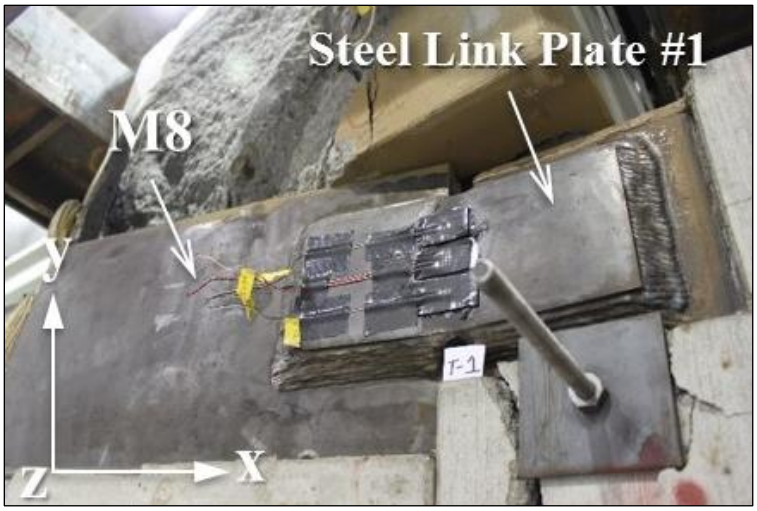

Figure 5.25 Close up view to posttest damage steel link plate #1

5.2.2.2 Steel link plate at location 2

The steel link plate at location #2 exhibited mainly out-of-plane deformation due to the eccentricity forces between the anchor bars and the steel plate, as well as due to the development of arching action in the system (see Figure 5.2). A posttest well-defined out-of-plane bending deformation along the z-axis towards the front of the specimen was observed in this link plate as shown in Figure 5.26.

The strain data that was collected in all gauges attached to the front face depicted high levels of compression strain readings (Figure A.9), which implies that the steel link plate #2 was acting in compression to provide equilibrium in the assembly.

As the center column displacement increased, the steel link plate #2 was forced to bend out-of-plane towards the front of the test specimen.

Figure 5.26 Close up view to posttest damage steel link plate #2

This out-of-plane behavior was also aggravated by the development of the arching action along in the assembly. Once the spandrel beams began to bear against the top of the center column/stud and to the bottom of the end-columns, the test specimen began to gain resistance to deflection because of the development of a compression zone (Figure 5.2(c)). This phenomenon forced the steel link plate #2 to continue acting in compression to preserve equilibrium in the assembly. However, it also forced the connecting plate to provide resistance to the out-of-plane behavior induced by the eccentricity of forces at the connection, as well as the eccentricity of forces between the assembly's centroid and the deflection axis or beam's centerline.

5.2.2.3 Steel link plate at location 3

The steel link plate at location #3 exhibited tensile behavior throughout the experiment. Considerable out-of-plane permanent deformation along the z-axis and

towards the back of the OMRF test specimen was observed as shown in Figure 5.27. This out-of-plane motion was also attributed to the eccentricity of forces at the connection.

The strain data collected in all gauges attached to the front face of the steel link plate depicted high levels of tension strain readings (Figure A.10), which implies that, during the initial response zones, the link plate #3 was acting in tension to provide equilibrium in the assembly. The out-of-plane motion, in addition to the possible development of a "heat-affected zone" in the anchor bars, could have played an important role in the failure of both bars, as discussed in Section 5.2.1. The failure of the second (top) M7 anchor bar consequently caused the detachment of the steel link plate #3 from the assembly, forcing the undamaged steel link plates to carry additional load. The failure also contributed significantly to the shifting of the specimen towards the right (west) end-column as shown in Figure 5.2(d) and Figure 5.24, incident (i).

Figure 5.27 Close up view to posttest damage steel link plate #3

5.2.2.4 Steel link plate at location 4

The steel link plate #4 exhibited a similar behavior to that exhibited by the steel link plate #2. Considerable out-of-plane deformation due to the eccentricity forces between the anchor bars and the steel plate, as well as due to the development of arching action in the system (Figure 5.2(c)) was observed. Posttest out-of-plane bending deformation along the z-axis towards the front of the specimen was observed in this link plate as shown in Figure 5.28.

The strain data collected in both gauges that was attached to the front face of the steel link plate #4 depicted high levels of compression strain readings Figure A.11), which implies that, during the initial response zones, this link plate was acting in compression to provide equilibrium in the assembly. Unfortunately, only two single strain gauges were attached to the front face of the connecting plate; therefore, the state of plane stress could not be calculated for any point in the steel link plate.

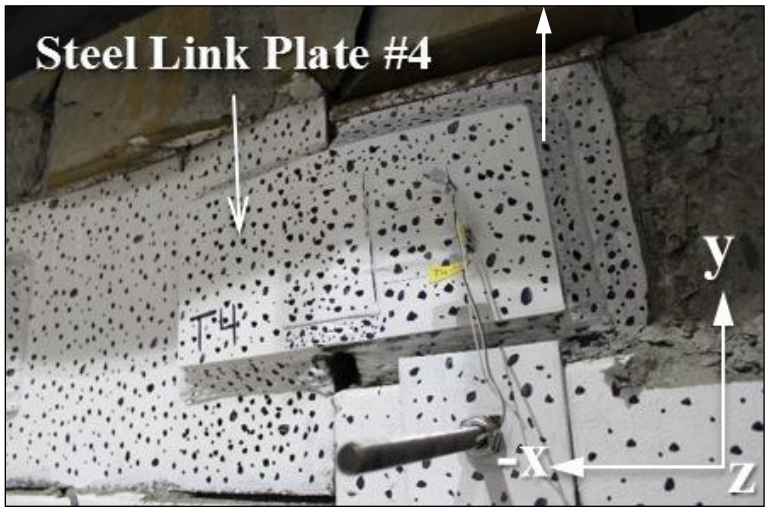

Figure 5.28 Close up view to posttest damage of steel link plate #4

5.2.2.5 Steel link plate at location 5

The steel link plate #5 exhibited a similar behavior to that of steel link plate #3. Tensile behavior was observed throughout the experiment. Considerable out-of-plane permanent deformation along the z-axis and towards the back of the OMRF test specimen was observed. Figure 5.29 shows the posttest damage of steel link plate #5.

The strain data collected in all gauges that was attached to the front face of the steel link plate depicted high levels of tension strain readings (Figure A.12), which implies that, during the initial response zones, link plate #5 was acting in tension to provide equilibrium in the assembly. In contrast to steel link plate #3, none of the anchor bars welded to steel link plate #5 ruptured. The shifting of the specimen towards the right (west) end-column resulted from the failure of the anchor bars at incidents (i), and may have relieved some of the tension forces acting along steel link plate #5 and the attached anchor bars, which prevented the anchor bars from failing.

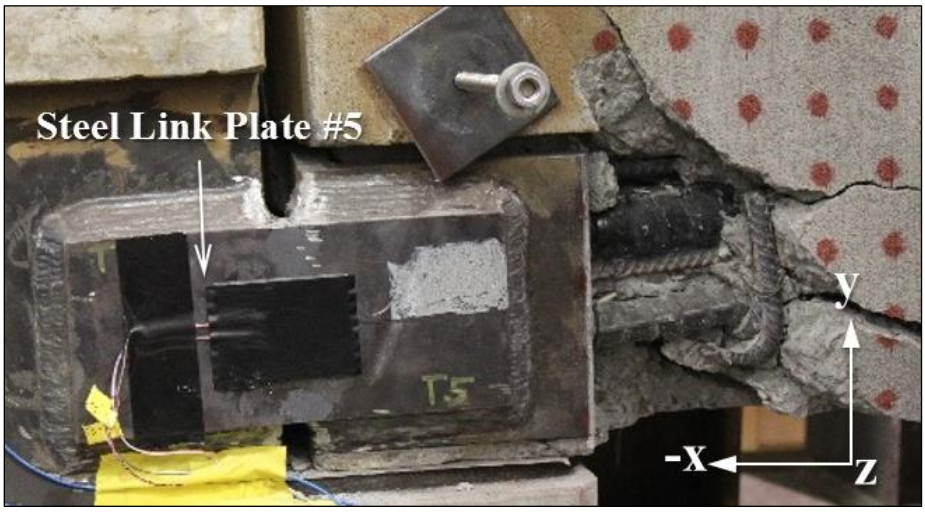

Figure 5.29 Close-up view to posttest damage steel link plate #5

5.2.2.6 Steel link plate at location 6

The steel link plate at location #6 exhibited severe deformation due to the high magnitude bending moments acting at the end-columns. A posttest well-defined counter clockwise rotation towards the center column/stud was observed in this link plate as shown in Figure 5.30. In addition, considerable out-of-plane permanent deformation along the z-axis and towards the back of the OMRF test specimen was observed.

The strain data collected in all gauges attached to the front face depicted high levels of tension strain readings (Figure A.13), which implies that, during the initial response zones, the link plate #6 was acting in tension to provide equilibrium in the assembly. However, at the time the M8 embedded plate in right (west) end-column detached within response zone V, the strain data for link plate #6 flattened.

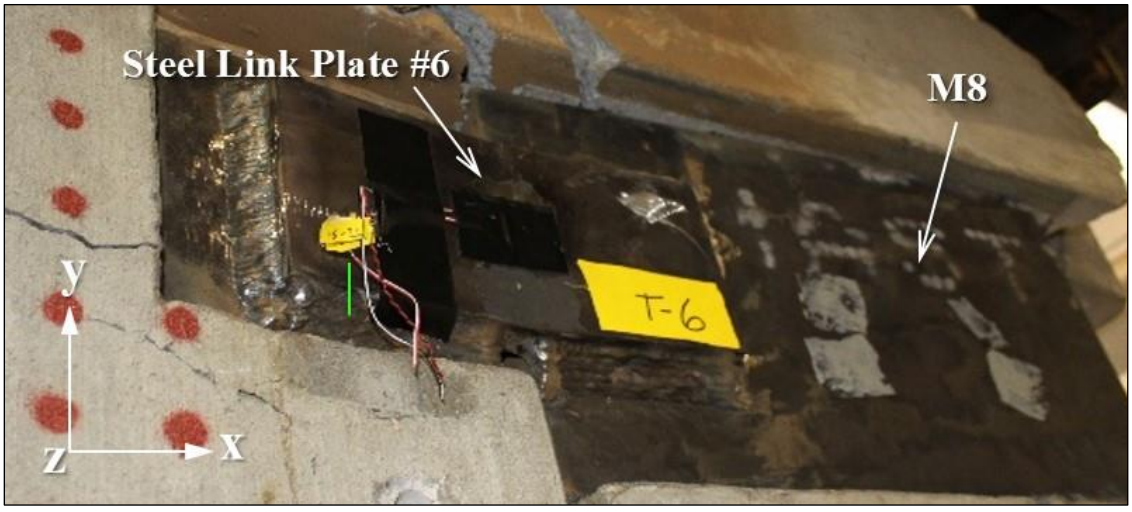

Figure 5.30 Close-up view to posttest damage steel link plate #6.

5.2.2.7 Steel link plates at location 7 and 8

The steel link plates at locations #7 and #8 exhibited very similar behaviors. Both link plates were severely deformed from a combination of bending, shearing, and out-of-plane loading conditions, in addition to the compressive forces transferred to the plates from the development of arching action in the system (Figure 5.2(e)). Figure 5.31 and Figure 5.32 show the posttest damage on steel link plates #7 and #8, respectively.

As the arching action developed in the assembly, the spandrel beams began to bear against the end-columns causing high concentrations of stresses around the vicinity of steel link plates #7 and #8. The steel link plates at the bottom ends provided much of the resistance to the applied forces of the arching action due to cracking and scabbing of the surrounding concrete.

The strain data collected in all gauges attached to the front faces of both plates depicted high levels of compression strain readings (Figure A.14 and Figure A.15), which implies that steel link plates #7 and #8 were acting in compression to provide equilibrium in the assembly.

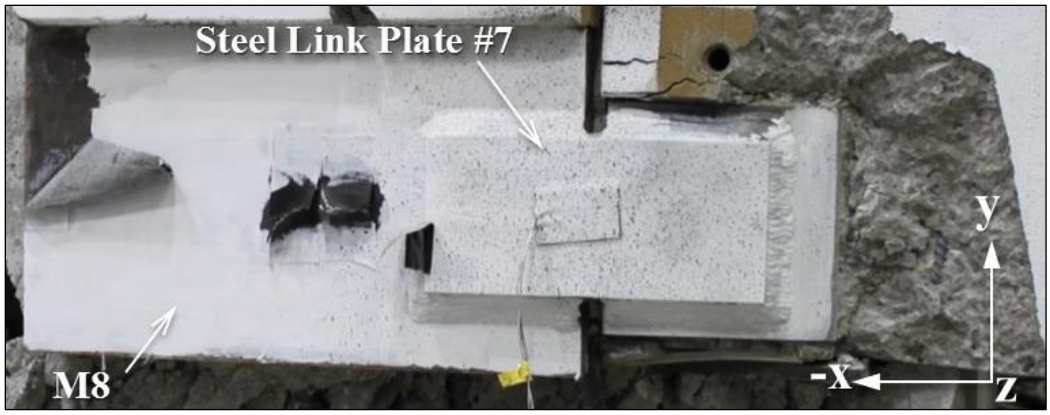

Figure 5.31 Close up view to posttest damage steel link plate #7

Figure 5.32 Close up view to posttest damage steel link plate #8

5.3 Development of arching action

Arching action or compression membrane action is a term normally used to describe a typical phenomenon in reinforced concrete slabs or deep beams, particularly due to restraint at the supports. When the natural tendency to expand under loading is restrained at the ends, the development of arching action enhances the strength of the structural component.

A very similar phenomenon was observed in the OMRF test specimen. For this purpose, the term "arching action" is used herein to describe the enhancement in capacity observed in the system prior to the failure of the M7 anchor bars, and even for a short period afterward. Once the steel link plates yielded, the clearance between the spandrel beams and the columns was reduced, subsequently enabling the bearing of the spandrel beams to bear against the top of the center column/stud and against the bottom of the end-columns, forming a compressive zone along the assembly in an arch shape as shown in Figure 5.2(e).

In full-scale testing and computational modeling of reinforced concrete moment frames under a column removal scenario, Lew et al., 2011 observed that an arching action stage was followed by a catenary action stage in which tensile forces developed in the beams provided additional load-carrying capacity. For the Lew et al. study, tensile forces developed in the beams when the deflection of the center column was approximately equal to the depth of the beams. However, the precast concrete spandrel beams considered in this study were much deeper than the reinforced concrete beams considered by Lew et al., and failures of the precast concrete specimen occurred when the deflections of the center column remained less than three-quarter of the beam depth. Catenary action did not develop for the precast concrete specimens considered in this study.

The diagonal cracking, scabbing, and shear deformation of the end-columns observed in these tests (see Figure 5.14 and Figure 5.17) indicate that lateral forces due to beam arching action could potentially result in shear failure of columns, particularly considering the eccentricity between the centerline of the columns and the spandrel

beams. These lateral forces exceeded the capacity of the torsion rods (see Figure 3.1) enabling each end-column to torque around its own vertical axis. The failure of these torsion rods resulted in the observed severe deformation at the supports. If arching action is to be exploited in resisting vertical loads under column removal scenarios, care must be taken to ensure that the columns adjacent to the missing column can resist the lateral loads induced by arching action.

In evaluating the potential for column shear failure, gravity loads from the upper stories should be considered in combination with shear forces due to arching action. The potential for shear failure is of particular concern for columns that have spandrel beams framing into the connections from only one side, like the end-columns considered in these tests. For an intermediate column in a moment frame, the spandrel beam framing into the connection from the adjacent bay would provide some resistance to rotation and horizontal displacement of the column, thus reducing the flexural and shear demands on the column (Main et al., 2015). Corner columns, therefore, need particular attention in evaluating the potential for shear failure due to arching action. Hence, innovative design techniques should be developed to minimize the eccentricity between the centerlines of the structural components on external multi-story building frames, and to ensure that the columns adjacent to the missing column can resist the lateral loads induced by arching action.

5.4 Summary of observations

In an effort to summarize the observed structural response and overall performance of the OMRF test specimen, the following list of major factors was developed.

1. An average maximum center vertical deflection of 17.8 in. (452.12 mm) was measured at the end of the experiment.

2. An average maximum beam-to-column joint rotation of 3.92° (0.06842 rad) was measured at the end of the experiment.

3. The eccentricity in the transfer of horizontal forces between the steel anchor bars and the steel link plates that induced out-of-plane loads and deformation to both steel components (Figure 5.4) significantly affected the performance of the connection detail, degrading the capacity of the connection to transfer load to the supports.

4. The development of an arching action was observed in the system. As discussed in Section 5.3, the development of arching action in the system could potentially enhance the capacity, especially during the late stages of deflection. However, if the design does not provide the necessary resistance to the lateral forces induced by such arching action, these lateral forces could result in a shear failure of the supports. The arching action in the OMRF system induced severe deformation in the end-columns, and the torsion rods failed to overcome these lateral forces, enabling the end-columns to torque. This behavior contributed to the detachment of two M8 steel plates, degrading the capacity of the system to carry load.

5. M7 anchor bars in Beam-L location #3 (Figure 4.17) ruptured. At the time the center column/stud reached a vertical displacement of 5.69 in. (144.5 mm), both M7 anchor bars ruptured. Although it was determined through the empirical procedure that none of the bars failed prematurely, it is evidenced that they both fractured promptly within the plastic region before reaching strain hardening. A combination between the out-of-plane behavior in the transfer of horizontal forces in the connection detail (Figure 5.4), in addition to the heat-affected-zone in the anchor bars induced during the welding and cooling process of the bars, may explain the reduction in deformation and strength capacity. The rupture of the anchor bars aggravated the already existing out-of-plane behavior along the system, forcing the assembly to shift to the right (west) column.

6. A peak load of 168.2 kips (748 kN) was carried by the assembly. The peak load was only 32% of the 533.3 kips (2372 kN) total combined service load that would be required to withstand to prevent collapse as a result of the additional loading from the above floors after the removal of the exterior T-shape column in the fourth floor. The beam-to-column prototype steel-coupling-connection design cannot withstand the removal of a column from the fourth floor. Such residual capacity indicates that the beam/column assembly would only prevent collapse if located at the ninth story of the building, and the column removal occurred at that level. The approximate combined service load at the ninth story column is 128 kips (570 kN). However, there is a potential for the system to withstand the service load if the prototype is incorporated in all joints in the perimeter OMRFs of the precast structure.

CHAPTER VI

SUMMARY, CONCLUSIONS, AND RECOMMENDATIONS

6.1 Summary

An experimental evaluation of a precast concrete beam-column connection system consisting of three columns and two deep spandrel beams was presented. The beam-column system represents a portion of the structural system of a ten-story precast concrete-frame building designed for office occupancy and seismic zone SDC-B. The specimen was subjected to monotonically increasing vertical displacement of the unsupported center column/stud to observe overall and localized behavior, including the performance of the beam-to-column prototype connection design and the development of arching action under a simulated column removal scenario. The vertical displacement of the center column/stud was increased until the specimen's load-carrying capacity was considered inadequate. Experimental data were successfully collected at two different frequencies. These unique data were critical to the physical examination of the performance of the OMRF prototype design.

In the earliest stages of the experiment, the behavior of the OMRF specimen was dominated by flexure. With increased vertical displacement of the unsupported center column, the frame began to show well-defined cracks within the system reducing its capacity and forcing the steel link plates to resist the bending moments and maintain structural stability. The experimental evaluation also revealed the development of out-of-

plane bending moments along the system, possibly resulting from the eccentricities of forces transferred through the beam-to-column connections, in addition to the eccentricity between the columns' and beams' centerlines. The introduction of these out-of-plane bending forces into the system, in addition to the likely development of a "heat-affected zone" in the anchor bar near the weld, contributed to the fracture of the bottom #10 (#32) Grade 60 steel reinforcing anchor bars welded to the M7 angle at the bottom-center in Beam-L. In fact, both M7 anchor bars fractured at a relatively small beam joint rotation (Θ_u) value of 1.09° (0.01896 rad). Both bar fractures exhibited very similar failure planes, distinctive of a possible "heat-affected zone."

The out-of-plane bending moments also contributed to the bond failure that led to the detachment of the upper (M8) embedded plates in the end-columns, initially in the left (east) column and later in the right. The result was the complete detachment of the steel link plate #1 and later of the steel link plate #6 from the assembly. As the vertical displacement increased, the gap or space between the beam and column gradually closed, and the beams began to bear against the columns. As a result, additional resistance occurred through the development of significant compressive forces associated with arching action. However, at the time the load reached a maximum value of 168.2-kip (748-kN), the upper anchor failed. The failure of the upper #10 (#32) Grade 60 anchor bar welded to the M7 embedded plate resulted in the complete detachment of the steel link plate #3 from the assembly, consequently imposing additional out-of-plane bending forces to the remaining steel link plates connected to the assembly. The system continued to carry load without collapsing, but heavily relied on the additional resistance provided by the post-ultimate compressive forces developed through the arching action.

During the post-ultimate stages of the experiment, a significant increase was observed in crack propagation at the end-columns due to lateral forces imposed by the arching action and the ongoing out-of-plane behavior. The diagonal cracking, concrete scabbing, and shear deformation observed in the end-columns due to these forces may indicate a shear failure of the end-columns resulting in a potential for a major catastrophe. The propagation of cracks also led to the detachment of the upper M8 plate in the right (west) column.

6.2 Conclusions

Based on the study reported herein, the conclusions are as follow.

1. The prototype OMRF specimen beam-to-column connection design is not adequate to withstand load under a column removal scenario from the fourth floor. However, if the prototype connection is incorporated in all joints in the perimeter OMRFs of the precast structure, there is a potential to withstand because of the distribution of loads.

2. The OMRF moment-frame withstood an average maximum center vertical displacement of 17.8 in. (452 mm) and an average maximum beam-to-column joint rotation of 3.92° (0.06842 rad).

3. Multiple failure modes occurred throughout the experiment. The three major failures identified were the following.

4. The M7 anchor bars located at the bottom-right of BEAM-L failed due to the out-of-plane bending behavior caused by the eccentricity of forces, as well as the development of a "heat-affected-zone" from the welding process of the bars to the steel angle. Therefore, the eccentricity in the transfer of forces through the beam-to-column steel link plate connection detail should be either eliminated or mitigated. Also, the connection design of the anchor bars to the M6 and M7 angles should be substituted with a mechanical connection.

5. The torsion rods ruptured, allowing the moment-frame to rotate and bend out of plane. Therefore, the capacity of the torsion rods must be improved.

6. Detachment of the top M8 embedded plates from the end-columns, due to the torsional moment developed at the supports, resulted from the out-of-plane behavior. Therefore, the eccentricity between the columns' and the spandrel beams' centerlines must be reduced to minimize torsional moment at the supports.

7. Although none of the steel link plates fractured, and the empirical approach suggests a minor reduction of 6% in flexural capacity even after the failure of the bottom M7 anchor bars and the detachment of the M8 plates from the end-columns, it was evident that such failure modes negatively influenced the long-term structural performance of the OMRF prototype design.

8. After carefully examining the posttest damage of the structural elements, it was evident that the end-columns suffered severe damage due to the combination of out-of-plane loads. The severity of the damage suggested a possible catastrophic shear failure at the end-columns if the experiment would have continued.

9. The data from the acoustic emission sensors were recorded at 2 MHz and showed trends useful for future development of a prediction methodology to identify imminent progressive or disproportionate collapse in precast concrete structures.

Unfortunately, there are no available experimental data of a SDC-B cast-in-place concrete moment frame specimen for comparing the potential benefits of using this precast OMRF prototype design over a cast-in-place design. However, NIST has conducted much research through the development of high-fidelity computational models capable of simulating, to a certain degree, the structural behavior of multiple precast assemblies and investigating the nonlinear behavior.

6.3 Recommendations

Based on the study reported herein, the following actions are recommended for future testing, analytical research, and design modification.

1. A new three-dimensional design should replace the current design to avoid or minimize the consequences of inducing the out-of-plane bending moments into the assembly.

2. An increase in column dimensions will allow a reduction of the eccentricity between the centerlines of the columns and spandrel beams.

3. To avoid the development of a "heat-affected zone" during the welding/cooling process of the bars to the angles that may jeopardize the structural integrity of the bar, a mechanical connection should be considered in lieu of the weld. This change could significantly enhance the OMRF's large-deflection structural performance.

4. The development of a computational model is recommended to investigate the potential structural benefits of redesigning the connection details.

5. An investigation of the potential benefits of using Ultra-High-Performance-Concrete (UHPC) in the prototype design is recommended. A high-strength concrete may minimize the crack propagation at the end-columns due to the bending, torsional, and lateral forces. UHPC may also provide additional bond strength to the M8 plate connecting plates at the columns and reduce the concrete scabbing at the bottom of the supports that results from the compressive forces associated with the arching action.

6. It is also recommended to investigate the influence of the surrounding structural systems, such as adjacent moment frames connected to each other by the prototype design, on the response of the precast concrete OMRF specimen.

7. To prevent shear failure, the end-column's reinforcement detail must be reviewed to ensure adequate steel in regard to sustaining the inward motion towards the failed center column.

8. For future experiments, it is recommended to record all sensors at a sampling rate of no less than 1 kHz. The additional data points could provide crucial insight for explanation of the structural responses captured by the AE sensors. Additionally, the number of AE sensors on the end-columns should be increased.

9. A series of quarter-scale test specimens with a statistical approach of experimental design could be useful in identifying and evaluating factors leading to imminent collapse. The smaller and repeatable experiments could be conducted to focus on specific behavior and failure modes as well as for examining techniques for monitoring structural health over time.

10. It is recommended that further analysis of the rate of observed acoustic emission events prior to and after the failure of the second M7 bar and the M8 embedded plate be conducted. This research could provide critical insight to diagnose or identify internal failure modes that could lead to progressive collapse.

REFERENCES

ACI - 318. "Building Code Requirements for Structural Concrete and Commentary." ACI 318-05 and 318R-08, American Concrete Institute, 2008.

American Welding Society (AWS). "Structural welding code – steel." AWS D1.1/ D1.1M:2010, Miami, FL, 2010.

ASCE 7-05. "Minimum Design Loads for Buildings and Other Structures." Standard ASCE/SEI 7-05, American Society of Civil Engineers, Reston, Virginia, 2005.

ASCE 7-10. "Minimum Design Loads for Buildings and Other Structures." Standard ASCE/SEI 7-10, American Society of Civil Engineers, Reston, Virginia, 2010.

ASTM A36. (n.d.). "Standard Specification for Carbon Structural Steel." Retrieved on July 8, 2009, from http://www.astm.org/Standards/A36.htm.

ASTM C39. (n.d.). "Standard Test Method for Compressive Strength of Cylindrical Concrete Specimens" Retrieved on July 8, 2009, from https://www.astm.org/Standards/C39.htm.

ASTM A706/A706M-15. "Standard Specification for Deformed and Plain Low-Alloy Steel Bars for Concrete Reinforcement." Retrieved on December 17, 2015, from http://www.astm.org/Standards/A706.htm.

ASTM E8 – ASTM E8/E8-15a. "Standard Test Methods for Tension Testing of Metallic Materials." Retrieved on December 17, 2015, from http://www.astm.org/ Standards/E8.htm.

Burnett, E.F.P. "Abnormal Loading and Building Safety." SP-48, American Concrete Institute, Farmington Hills, Michigan, 1975.

Chahal, S. "The Phenomenon of Prefabrication: Pre-casting in Contemporary Construction", Retrieved November 11, 2016, from http://sumitchahal.blogspot.com/2014/12/the-phenomenon-of-prefabrication.html.

CP 110. "Code of Practice for Structural use of Concrete, British Standards Institution, London, 1976.

Department of Defense, (DOD). "Design of Buildings to Resist Progressive Collapse." Unified Facilities Criteria, (UFC 4-023-03), 25 January 2005.

Dplot. Graph computer software for scientist and engineers, Version 2.3.5.3, HydeSoft Computing, LLC ©, May 2015.

Ellingwood, B., R. Smilowitz, D. Dusenberry, D. Duthinh and H. S. Lew. "Best Practices for Reducing the Potential for Progressive Collapse in Buildings." NISTIR 7396, National Institute of Standards and Technology, Gaithersburg, Maryland, February 2007.

Elliott, K. S. and C. K. Jolly. "Multi-Story Precast Concrete Framed Structures." Blackwell, West Sussex, United Kingdom, 2013, chapter 9.

Engström, B. "Connections between precast components." Nordisk Betong, Journal of the Nordic Concrete Federation, 2(3), 1990, pp. 53-56.

Figueroa, J. "Learning from Building Failures1968 Ronan Point Tower", University of Texas – Architectural Engineering program Retrieved July 30, 2014, from <https://buildingfailures.wordpress.com/author/jfigueroa2014/.

GSA 2013. "Progressive Collapse Analysis and Design for New Federal Buildings and Major Modernization Projects." GSA 2013, General Services Administration, October 24, 2013.

Gunaraj V. and N. Murugan. "Prediction of Heat-Affected Zone Characteristics in Submerged Arc Welding of Structural Steel Pipes." Journal Article in the Welding Journal, Welding Research, January 2002.

Highrise Fire Fighting CONSTRUCTION MATERIALS, "Materials found in the construction of High-rise buildings" Retrieved July 30, 2016. <http://www.highrisefirefighting.co.uk/material.html>.

Kang, S.B., and K. H. Tan. "Behavior of precast concrete beam–column sub-assemblages subject to column removal." Engineering Structures, 93, 2015, pp. 85-96.

KTBD. Khobar Towers bombing in Dhahran, Saudi Arabia on 25 June 1996. This image is a work of a U.S. military or Department of Defense employee. As a work of the U.S. federal government, the image is in the public domain. Source: Retrieve on November 20, 2015, from http://en.wikipedia.org/wiki/Khobar_Towers_bombing.

Kim, J., Dasgupta, P., and Ghosh, S.K. "Assessment of the ability of seismic structural systems to withstand progressive collapse: design of precast concrete frame building (seismic design category B)." Report submitted to the National Institute of Standards and Technology, Gaithersburg, Maryland, 2009.

Lew, H.S., Y. Bao, F. Sadek, J. A. Main., S. Pujol, and M.A Sozen. "An experimental and computational study of reinforced concrete assemblies under a column removal scenario." NIST Technical Note 1720, National Institute of Standards and Technology, Gaithersburg, Maryland, October 2011.

MacLeod, I. “Moder Structural Analysis: Modeling Process and Guidance”, Thomas Telford Ltd., November 2005. Retrieved February 3, 2017 from <http://www.imacleod.com/msa/images/image002.jpg>.

Main, J. A., Y. Bao, H.S. Lew, F. Sadek, V. P. Chiarito, S. D. Robert, and J. O. Torres-Alamo. “An Experimental and Computational Study of Precast Concrete Moment Frames under a Column Removal Scenario.” NIST Technical Note 1886, National Institute of Standards and Technology, Gaithersburg, Maryland, September 2015.

Mathcad, PTC Mathcad Prime 3.1, PTC ©, acceded in September 2015.

Nimse, R.B., D.D. Joshi, and P. V. Patel. “Behavior of wet precast beam column connections under progressive collapse scenario: an experimental study.” Int. J. Adv. Struct. Eng., 6, 2014, pp. 149-159.

Nimse, R.B., D.D. Joshi, and P. V. Patel. “Experimental study on precast beam column connections constructed using RC corbel and steel billet under progressive collapse scenario.” Proc., 2015 Structures Congress, ASCE, Reston, VA, 2015.

PCI. Precast/Prestressed Concrete Institute (PCI). “PCI Design Handbook.” 7th Edition, Chicago, IL, 2010.

Pearson, C. and Delatte, N. "Ronan Point Apartment Tower Collapse and its Effect on Building Codes." J. Perform. Constr. Facil., 10.1061/ (ASCE) 0887-3828(2005)19:2(172), 172-177, 2015.

Regan, P.E. “Catenary tests on composite precast–in situ concrete composite floors.” Report to the Department of Environment, The Polytechnic of London, 1974.

Sadek, F., J. A. Main, H. S. Lew, S. D. Robert, V. P. Chiarito, S. El-Tawil. “An Experimental and Computational Study of Steel Moment Connections under a Column Removal Scenario.” NIST Technical Note 1669, National Institute of Standards and Technology. Gaithersburg, Maryland, September 2010.

Schultz, D., E. Burnett, and M. Fintel. “A Design Approach to General Structural Integrity – Design and Construction of Large Panel Concrete Structures, Supplemental Report A, 1978.

Score Atlanta Inc. Score Dunegan SE 900-MWB Datasheet. Retrieved August 7, 2012, from <https://score-atlanta.com/products/pdf/SE900-MWB%20Datasheet.pdf>.

Somes, N. F. “Abnormal Loading on Buildings and Progressive Collapse, in Building Practices for Disaster Mitigation (Wright, Kramer and Culver, eds.).” Building Science Series No. 46, National Bureau of Standards, Washington, DC, 1973.

Tohidi, M., J. Yang and C. Baniotopoulos. “An Improved Tie Force Method for Progressive Collapse Resistance of Precast Concrete Cross Wall Structures.” World Academy of Science, Engineering and Technology, International Journal of Civil, Environmental, Structural, Construction and Architectural Engineering, Vol: 8, No: 1, 2014.

APPENDIX A

DATA RECORDS

A.1 Instrumentation matrixes

Table A.1 Pseudo-static response instrumentation legend

Measurement No.	Measurement Type	Measurement Location
L-95A	Applied Load	400 K Load cell/MTS ram positioned at the center of the center column
L-95B	Pressure	MTS Ram Internal Pressure Gauge
D-83	Displacement	Beam-L, At mid span measured from bottom face/center line of beam-column connection
D-85	Displacement	Center column, Left measured from bottom face/center line of beam-column connection
D-86	Displacement	Center column, Right measured from bottom face/center line of beam-column connection
D-88	Displacement	Beam-R, At mid span measured from bottom face/center line of beam-column connection
LVDT-81	Displacement	East end column, At mid-point of column
LVDT-90	Displacement	West end column, At mid-point of column
R-91	Rotation	Beam-L, East end-column
R-92	Rotation	Beam-L, Center column
R-93	Rotation	Beam-R, Center column
R-94	Rotation	Beam-R, West end-column
εh-41	Strain	Beam-L, Top anchor bar at top left M6 embedded angle
εH-42	Strain	Beam-L, Top anchor bar at top left M6 embedded angle
εH -43	Strain	Beam-R, Top anchor bar at top right M6 embedded angle
εH -44	Strain	Beam-R, Top anchor bar at top right M6 embedded angle
εH -45	Strain	Beam-L, Top anchor bar at bottom right M7 embedded angle
εH -46	Strain	Beam-L, Top anchor bar at bottom right M7 embedded angle
εH -47	Strain	Beam-R, Top anchor bar at bottom left M7 embedded angle
εH -48	Strain	Beam-R, Top anchor bar at bottom left M7 embedded angle
εH -49	Strain	Beam-L, Outermost bottom bar at mid-span
εH -50	Strain	Beam-L, Outermost bottom bar at mid-span

Table A.1 (Continued)

Measurement No.	Measurement Type	Measurement Location
εH -57	Strain	Beam-R, Outermost bottom bar at mid-span
εH -58	Strain	Beam-R, Outermost bottom bar at mid-span
εH -55	Strain	Beam-L, Outermost top bar at mid-span
εH -56	Strain	Beam-L. Outermost top bar at mid-span
εH -63	Strain	Beam-R, Outermost top bar at mid-span
εH -64	Strain	Beam-R, Outermost top bar at mid-span
εH -65	Strain	East end column - Beam-L, Shear tab #1, Top single
εH -66	Strain	East end column - Beam-L, Ductile Plate #1, Rosette (0°)
εH -67	Strain	East end column - Beam-L, Ductile Plate #1, Bottom single
εH -109	Strain	East end column - Beam-L, Ductile Plate #1, Rosette (+45°)
εH -110	Strain	East end column - Beam-L, Ductile Plate #1, Rosette (-45°)
εH -111	Strain	Center column - Beam-L, Ductile Plate #2, Top single
εH -112	Strain	Center column - Beam-L, Ductile Plate #2, Rosette (+45°)
εH -113	Strain	Center column - Beam-L, Ductile Plate #2, Rosette (0°)
εH -114	Strain	Center column - Beam-L, Ductile Plate #2, Rosette (-45°)
εH -115	Strain	Center column - Beam-L, Ductile Plate #2, Bottom single
εH -116	Strain	Center column - Beam-L, Ductile Plate #3, Top Rosette (+45°)
εH -117	Strain	Center column - Beam-L, Ductile Plate #3, Top Rosette (0°)
εH -118	Strain	Center column - Beam-L, Ductile Plate #3, Top Rosette (-45°)
εH -119	Strain	Center column - Beam-L, Ductile Plate #3, Bottom Rosette (+45°)
εH -120	Strain	Center column - Beam-L, Ductile Plate #3, Bottom Rosette (0°)
εH -121	Strain	Center column - Beam-L, Ductile Plate #3, Bottom Rosette (-45°)

Table A.1 (Continued)

Measurement No.	Measurement Type	Measurement Location
εH -73	Strain	Center column - Beam-R, Ductile Plate #4, Top single
εH-74	Strain	Center column - Beam-R Ductile Plate #4, Bottom single
εH -76	Strain	Center column - Beam-R, Ductile Plate #5, Rosette (0°)
εH -79	Strain	West end column - Beam-R Ductile Plate #6, Rosette (0°)
εH -104	Strain	East end column - Beam-L, Ductile Plate #7, Rosette (0°)
εH -107	Strain	West end column - Beam-R Ductile Plate #8, Rosette (0°)
εH -122	Strain	Center column - Beam-R Ductile Plate #5, Rosette (+45°)
εH -123	Strain	Center column - Beam-R, Ductile Plate #5, Rosette (-45°)
εH -124	Strain	West end column - Beam-R, Ductile Plate #6, Rosette (+45°)
εH -125	Strain	West end column - Beam-R, Ductile Plate #6, Rosette (-45°)
εH -126	Strain	East end column - Beam-L, Ductile Plate #7, Rosette (+45°)
εH -127	Strain	East end column - Beam-L. Ductile Plate #7, Rosette (-45°)
εH -128	Strain	West end column - Beam-R, Ductile Plate #8, Rosette (+45°)
εH -129	Strain	West end column - Beam-R, Ductile Plate #8, Rosette (-45°)
εH -97	Strain	Top lateral steel brace beam for columns, Center of top flange
εH -98	Strain	Top lateral steel brace beam for columns, Mid-height of interior web
εH -99	Strain	Top lateral steel brace beam for columns, Center of bottom flange
T1	Torsion Load Cell	Center column-Beam-L, Bottom Torsion load cell
T2	Torsion Load Cell	Center column-Beam-R, Bottom Torsion load cell

Table A.2 High-frequency response instrumentation legend

Channel Name	**Sensor Type**
L1A	Accelerometer
L1B	Accelerometer
L1C	Accelerometer
L2A	Accelerometer
L2B	Accelerometer
L2C	Accelerometer
AE1	Acoustic Emission
AE2	Acoustic Emission
L-95A	Load Cell
M7-45 (εH -45)	Strain
M7-47 (εH -47)	Strain
T3-S1 (εH -116)	Strain
T3-S2 (εH -117)	Strain
T3-S3 (εH -118)	Strain

A.2 Experiment pseudo-static response data records (40 Hz)

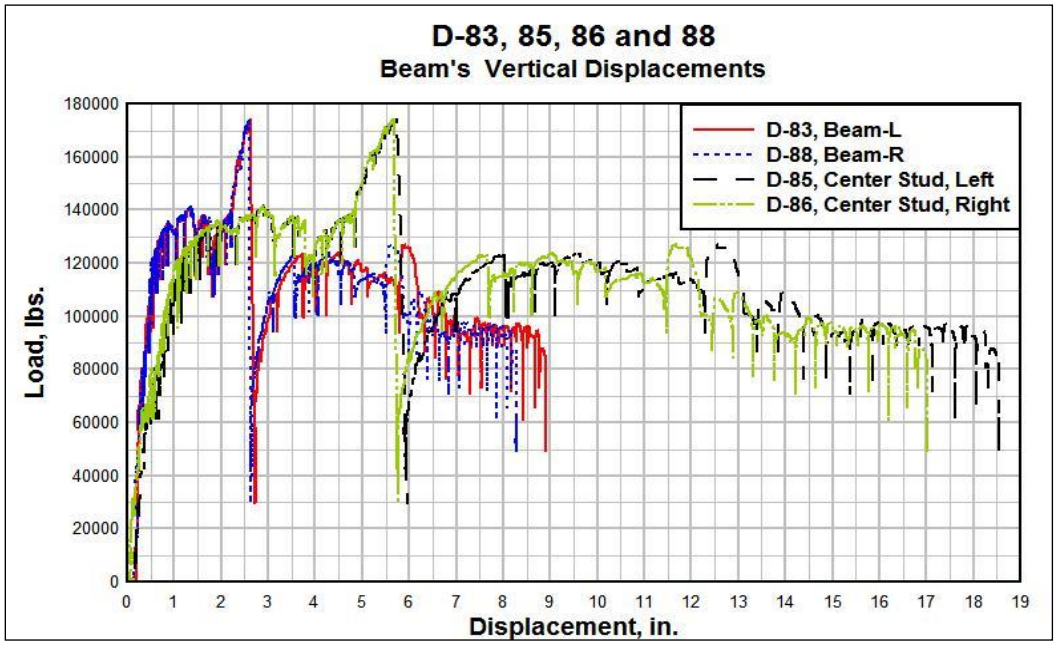

Figure A.1 Beam vertical displacements from gauges D–83, D-85, D-86, and D-88

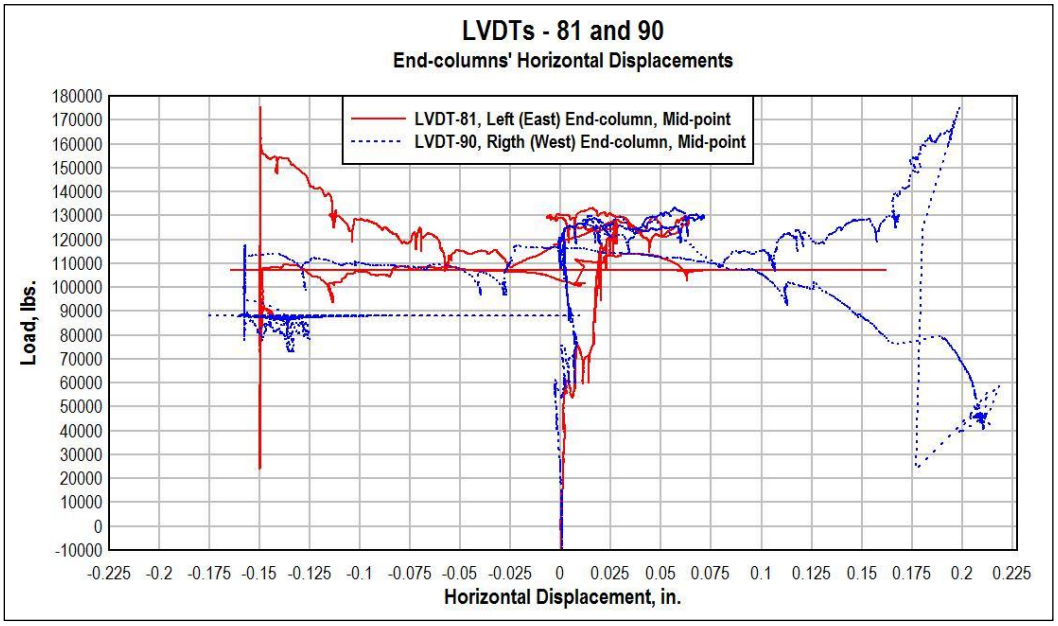

Figure A.2 Horizontal displacement of end-columns (LVDTs 81 and 90)

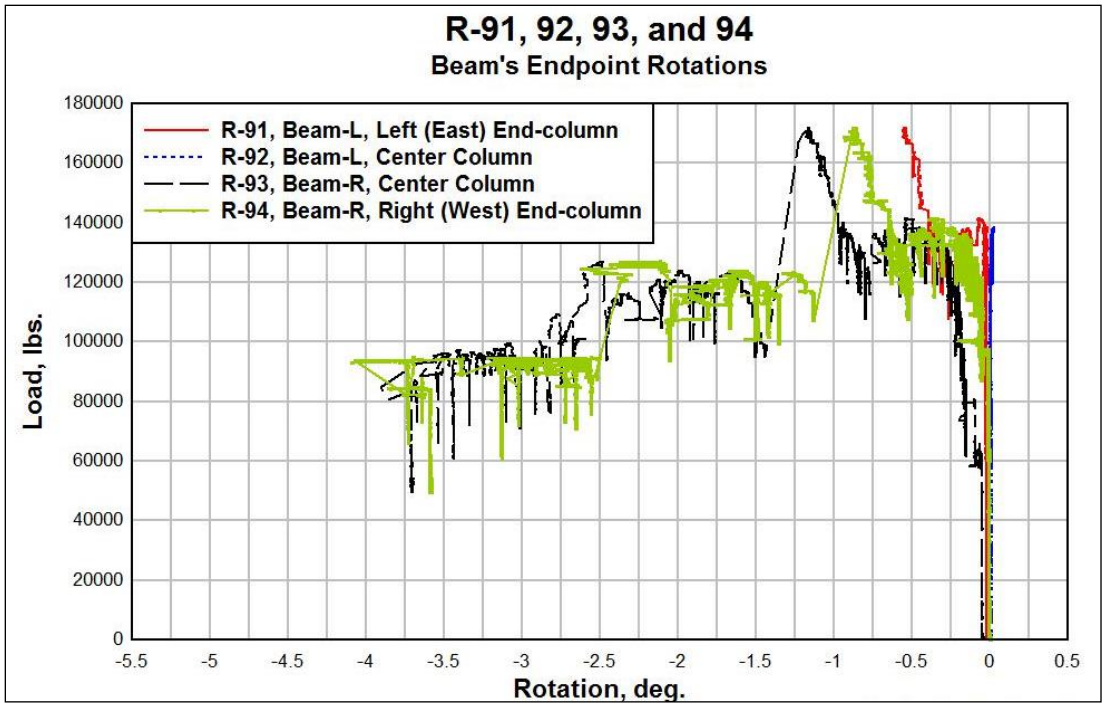

Figure A.3 Beam endpoint rotations

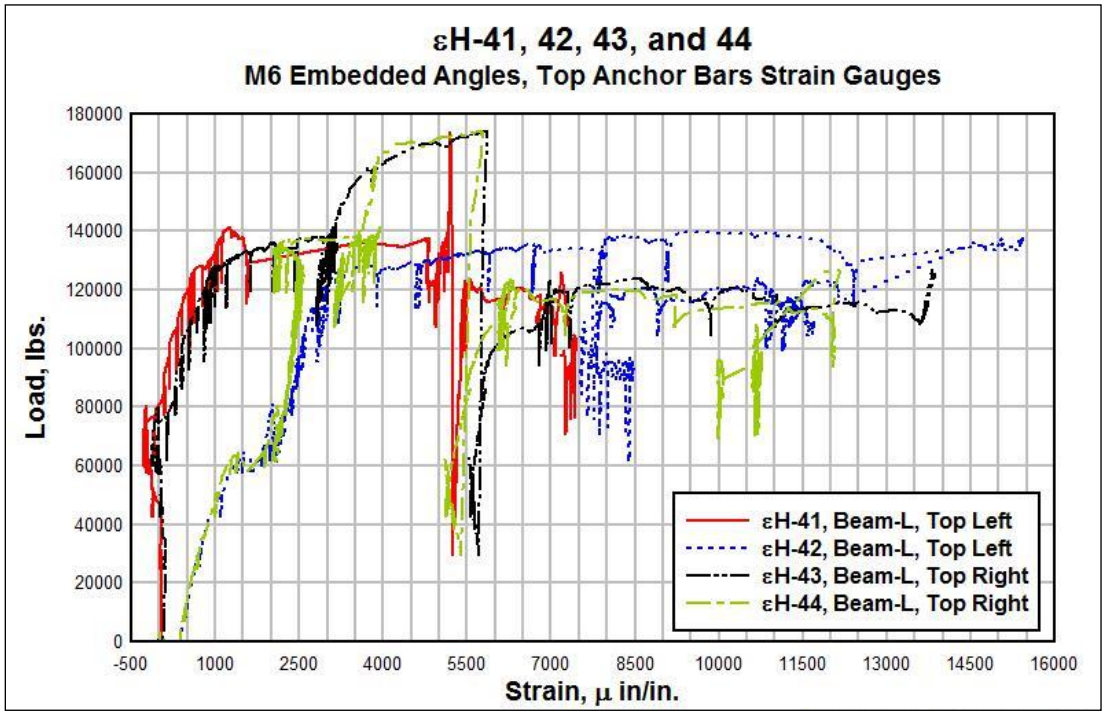

Figure A.4 Strains in top anchor bars in M6 embedded angle

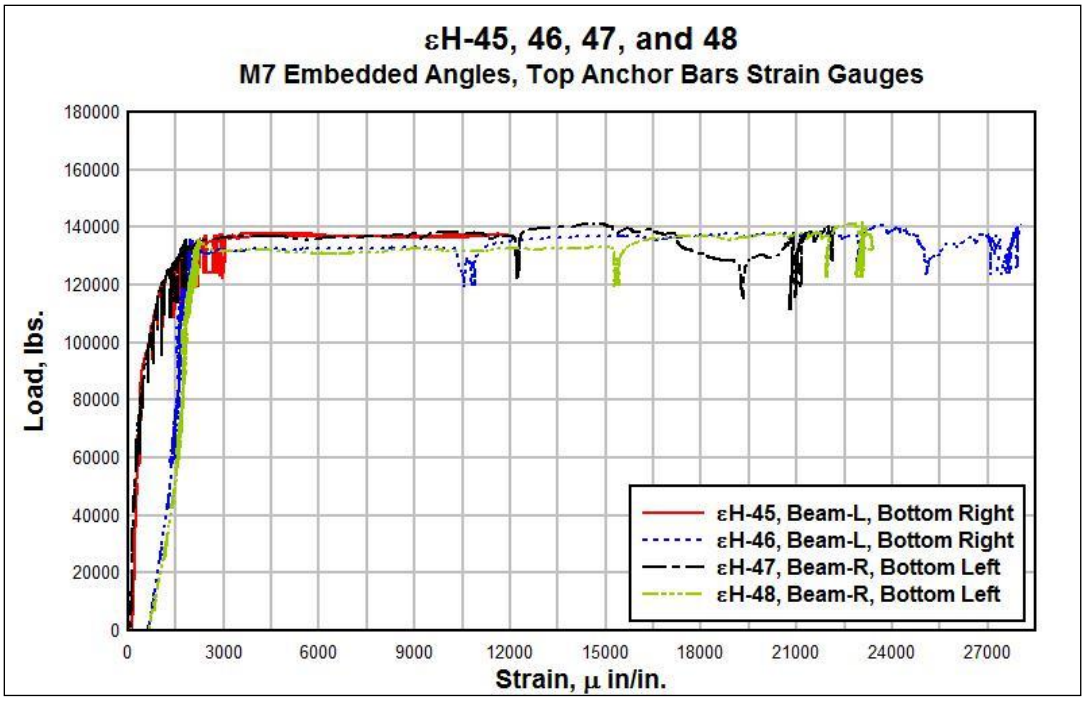

Figure A.5 Strains in top anchor bars in M7 embedded angle

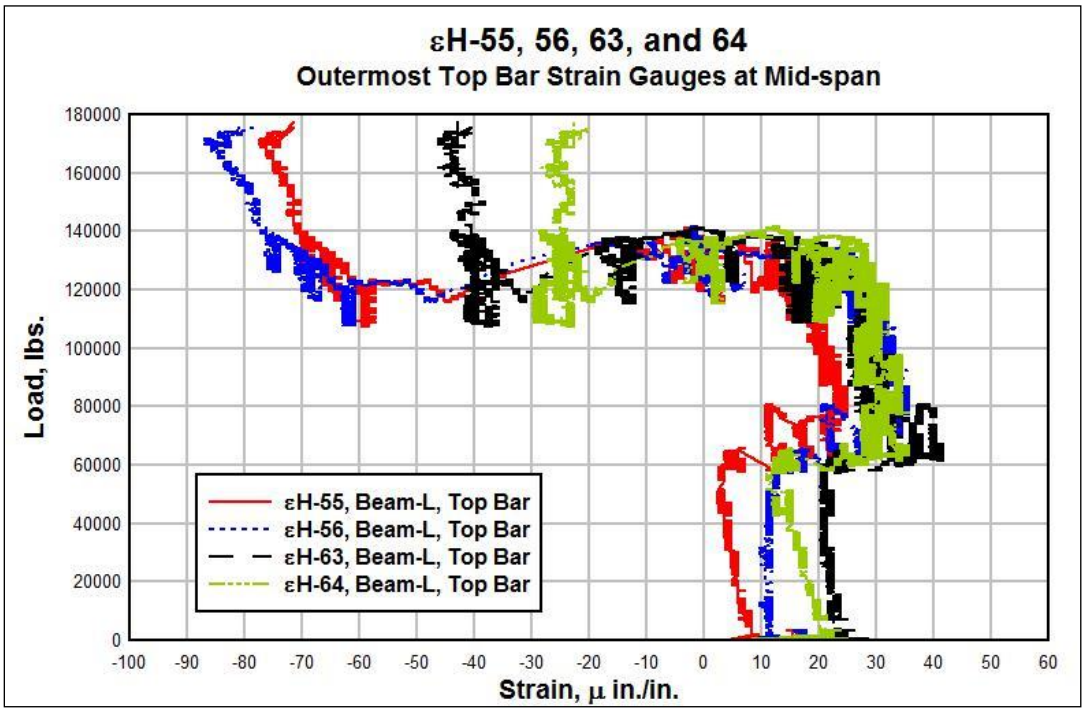

Figure A.6 trains in outer-most top bars at mid-span

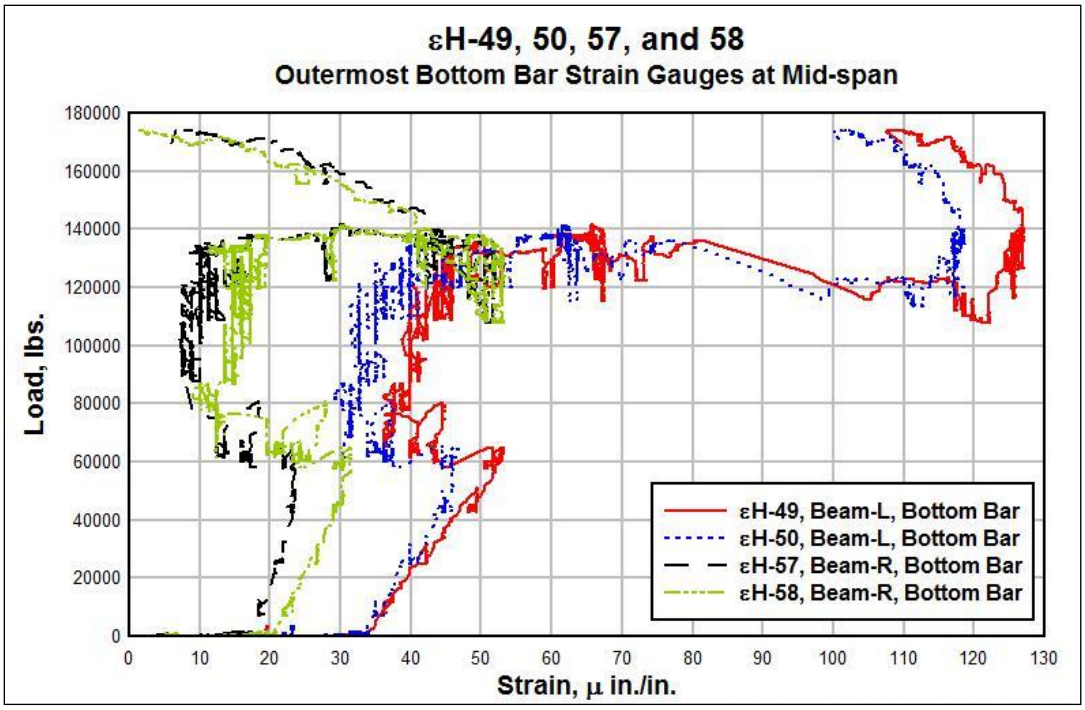

Figure A.7 Strains in outer-most bottom bars at mid-span

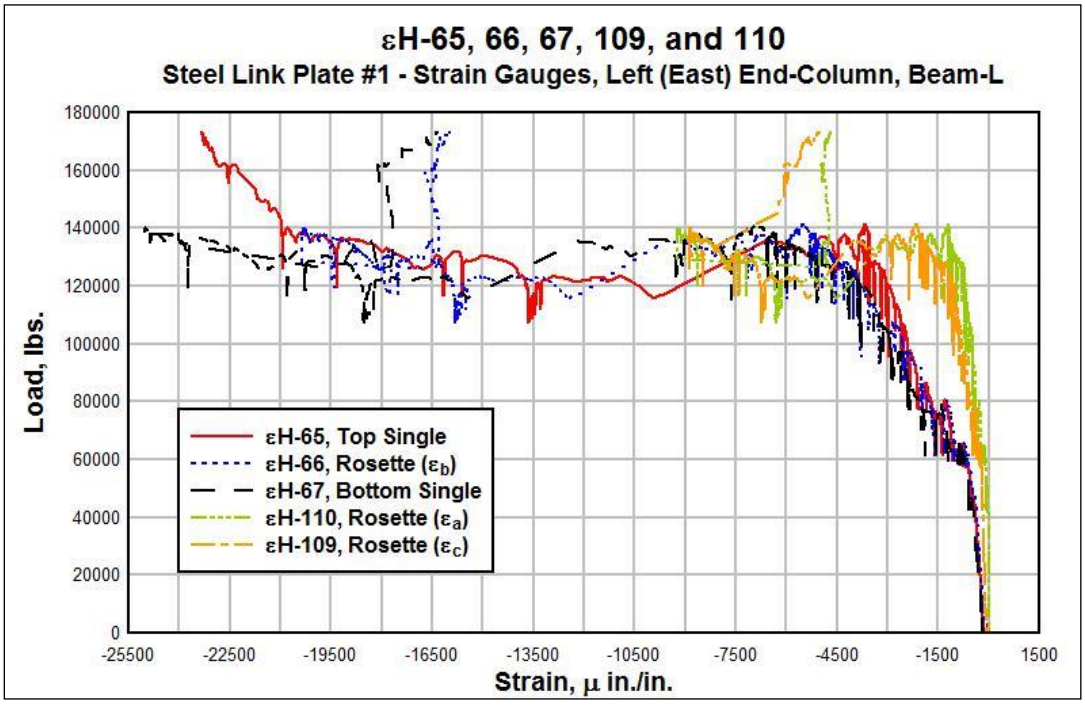

Figure A.8 Strains in steel link plate #1, left (east) end-column, Beam-L

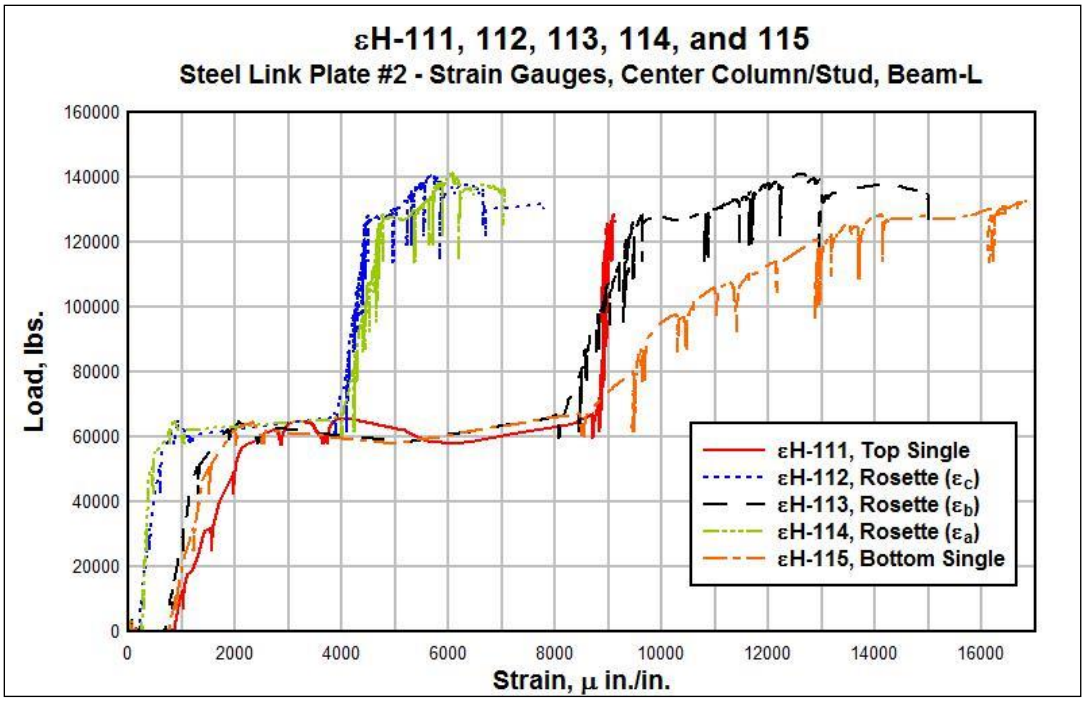

Figure A.9 Strains in steel link plate #2, center column, Beam-L

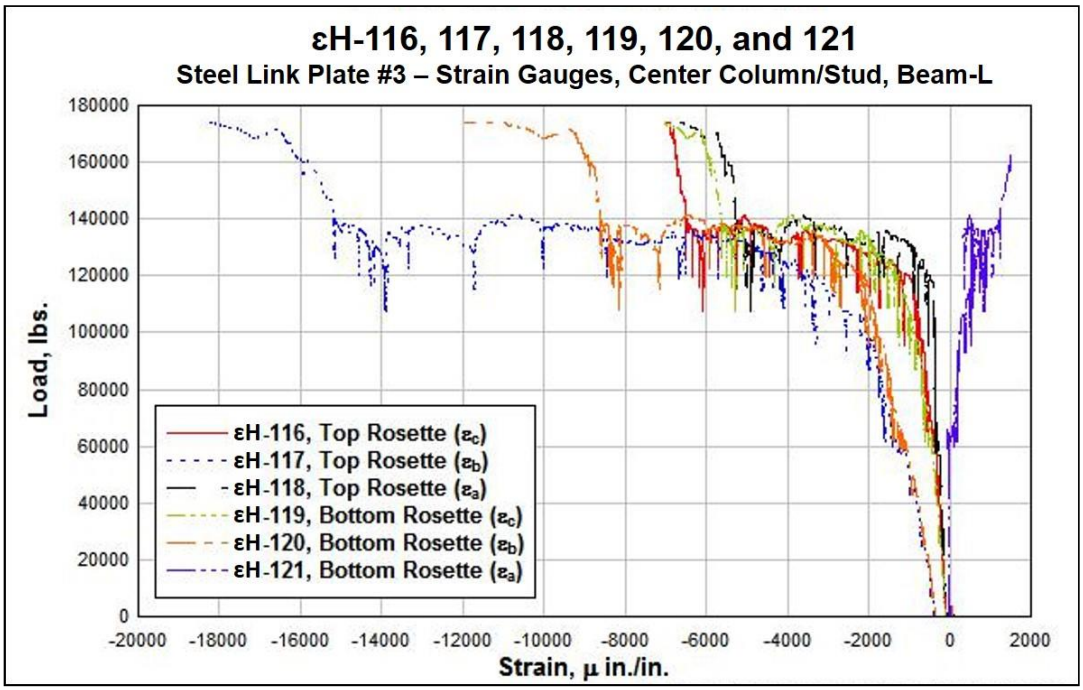

Figure A.10 Strains in steel link plate #3, center column, Beam-L

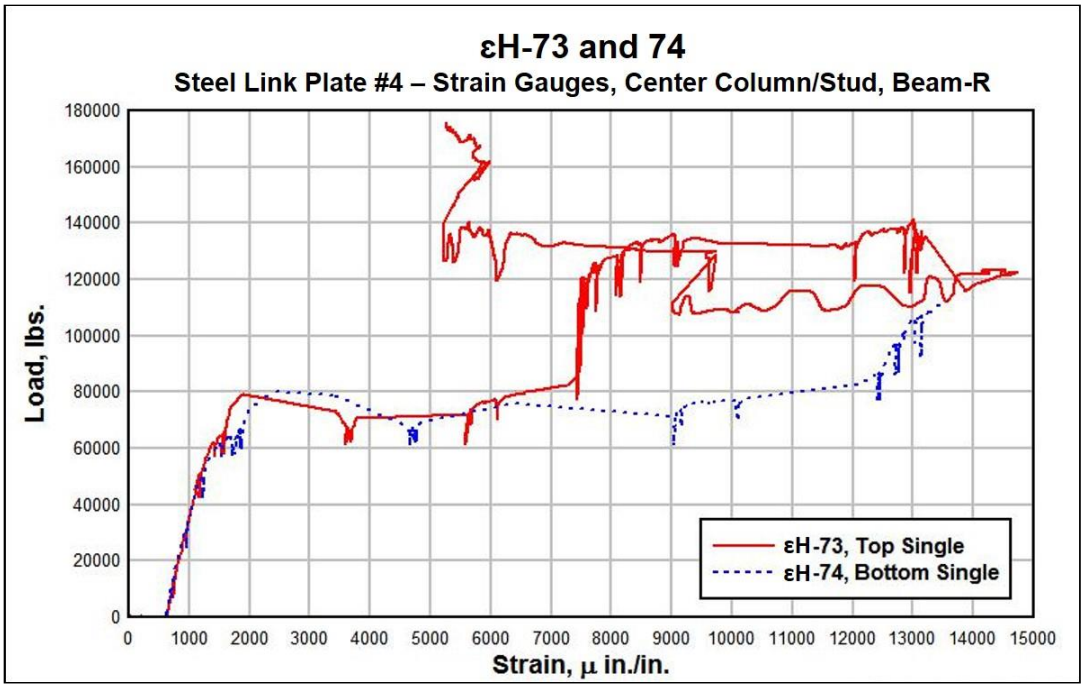

Figure A.11 Strains in steel link plate #4, center column, Beam-R

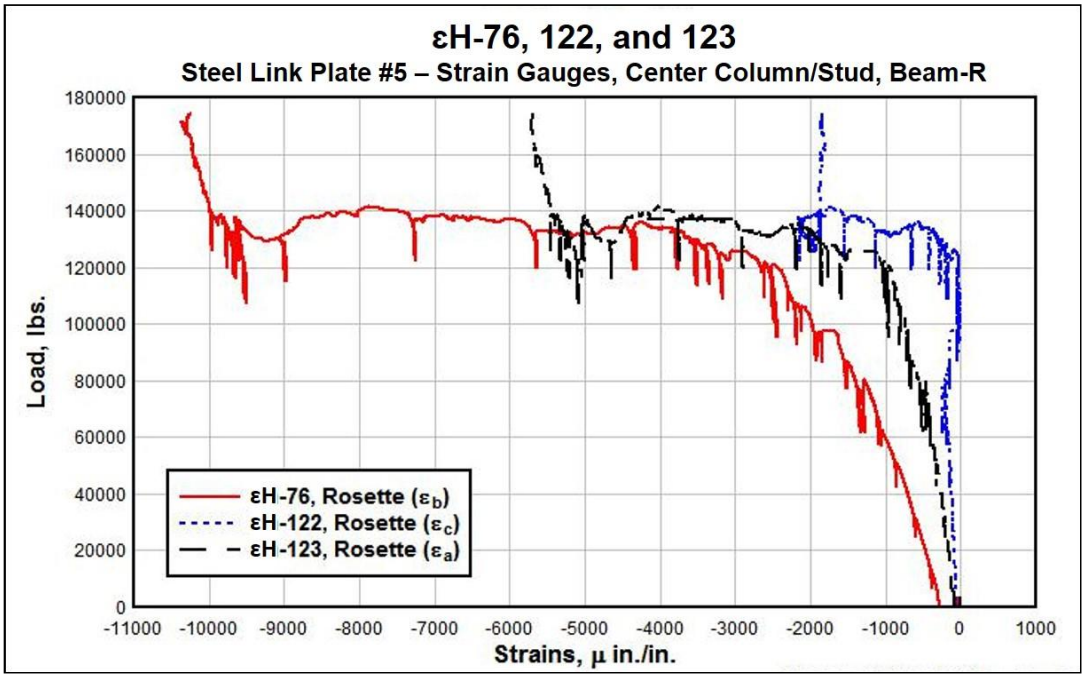

Figure A.12 Strains in steel link #5, right (west) end-column, Beam-R

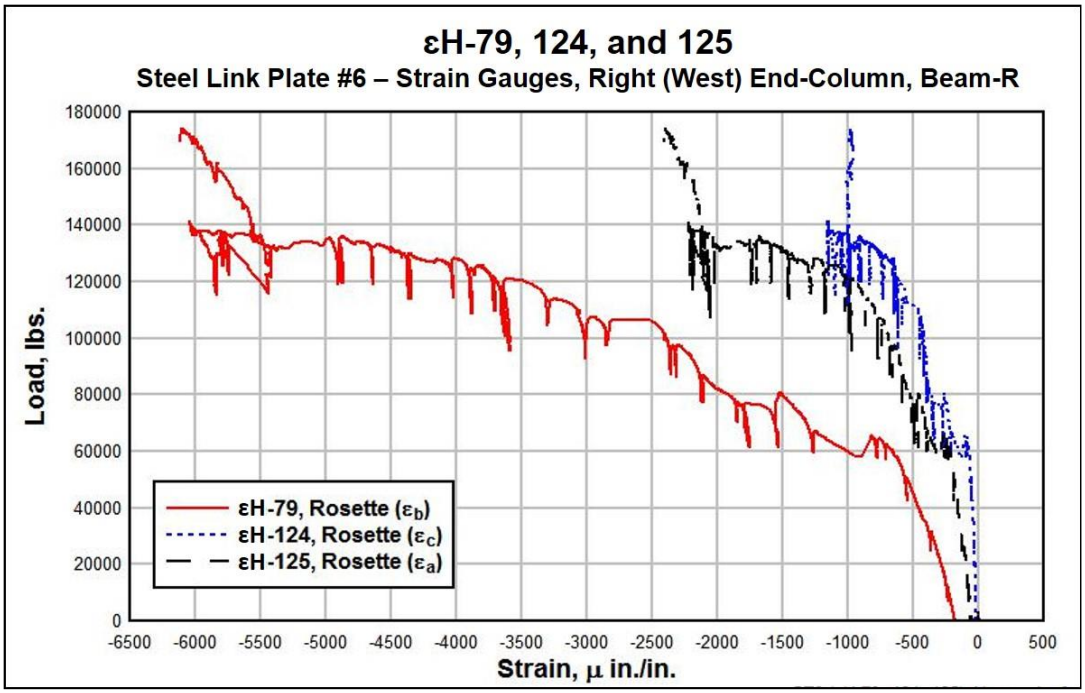

Figure A.13 Strains in steel link plate #6, center column, Beam-R

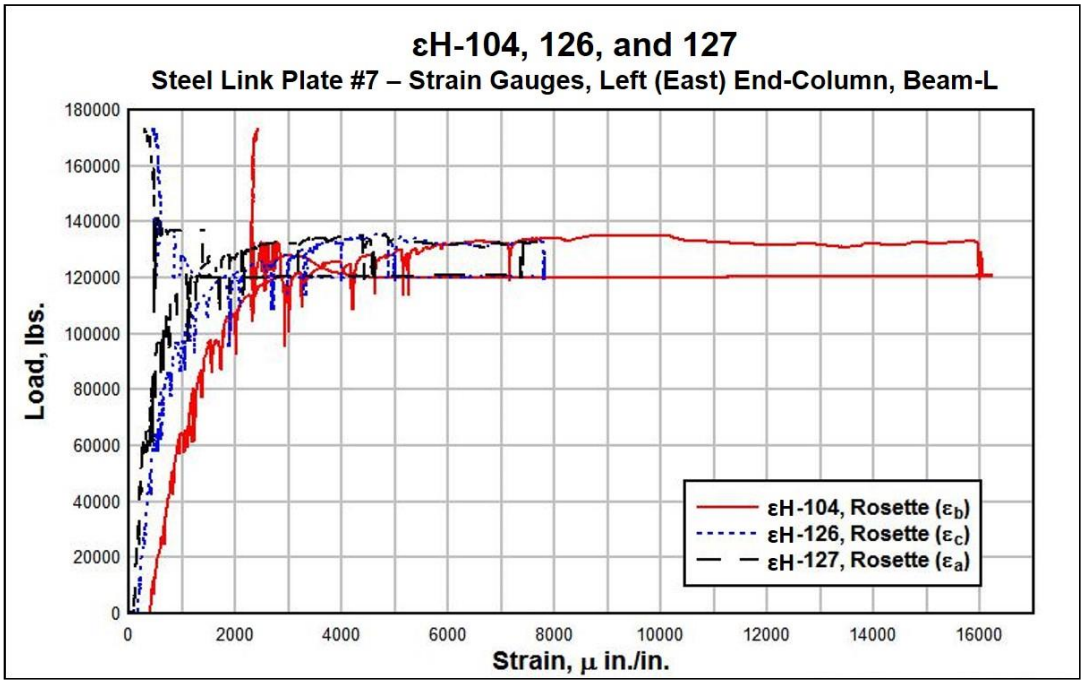

Figure A.14 Strains in steel link #7, left (east) end-column, Beam-L

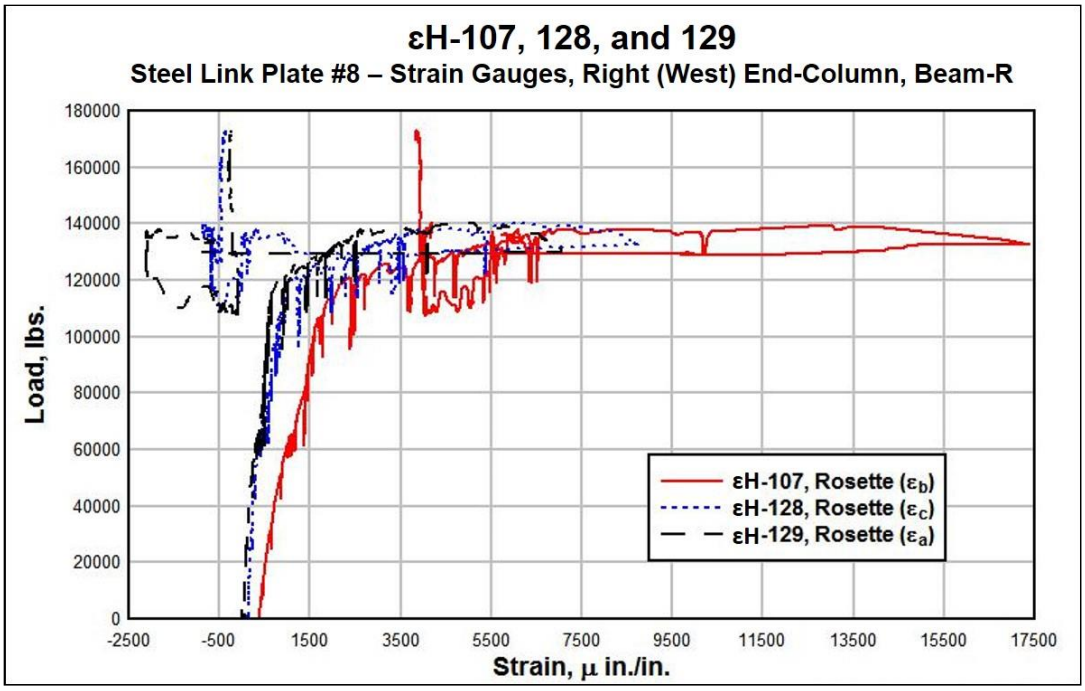

Figure A.15 Strains in steel link #8, right (west) end-column, Beam-R

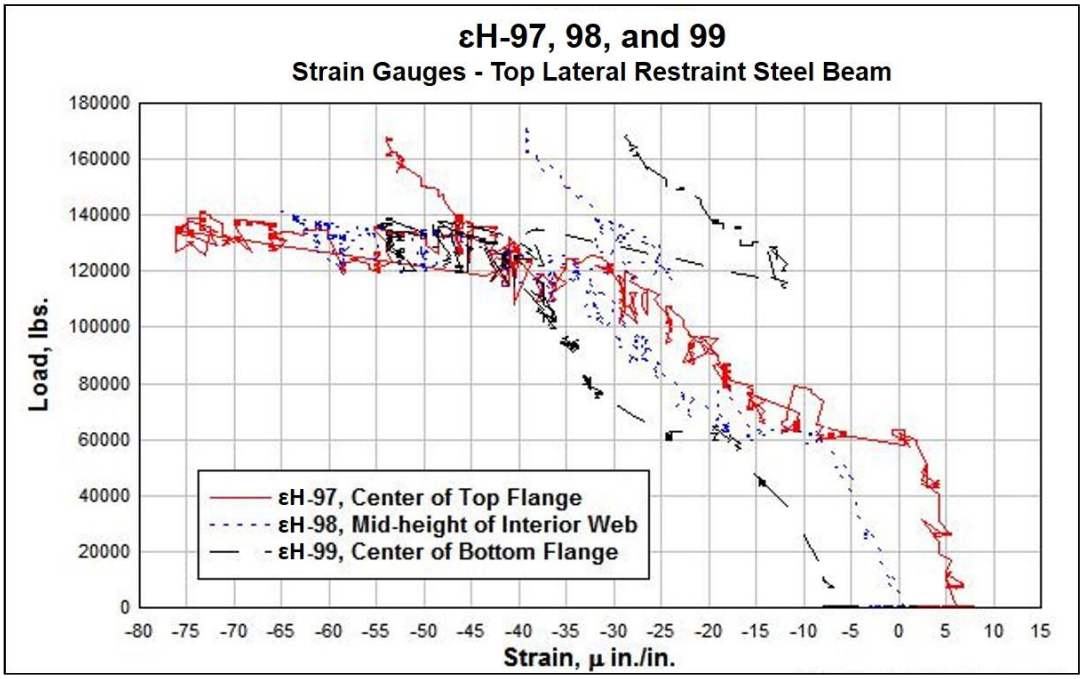

Figure A.16 Strains in top lateral restraint steel beam

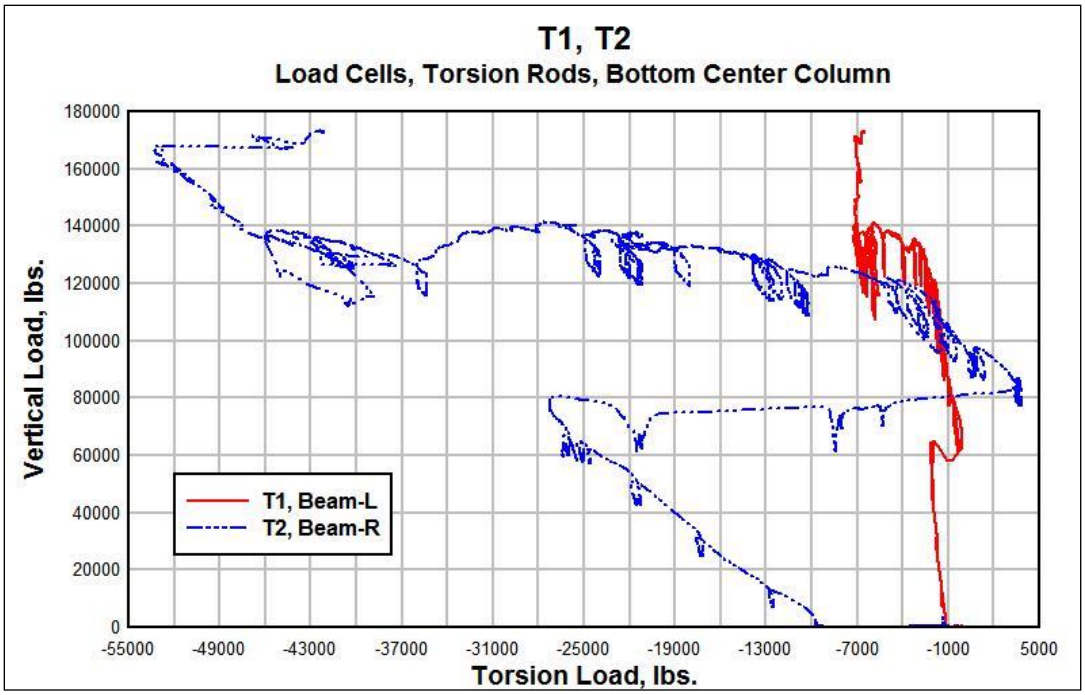

Figure A.17 Load cells on torsion rods bottom center column

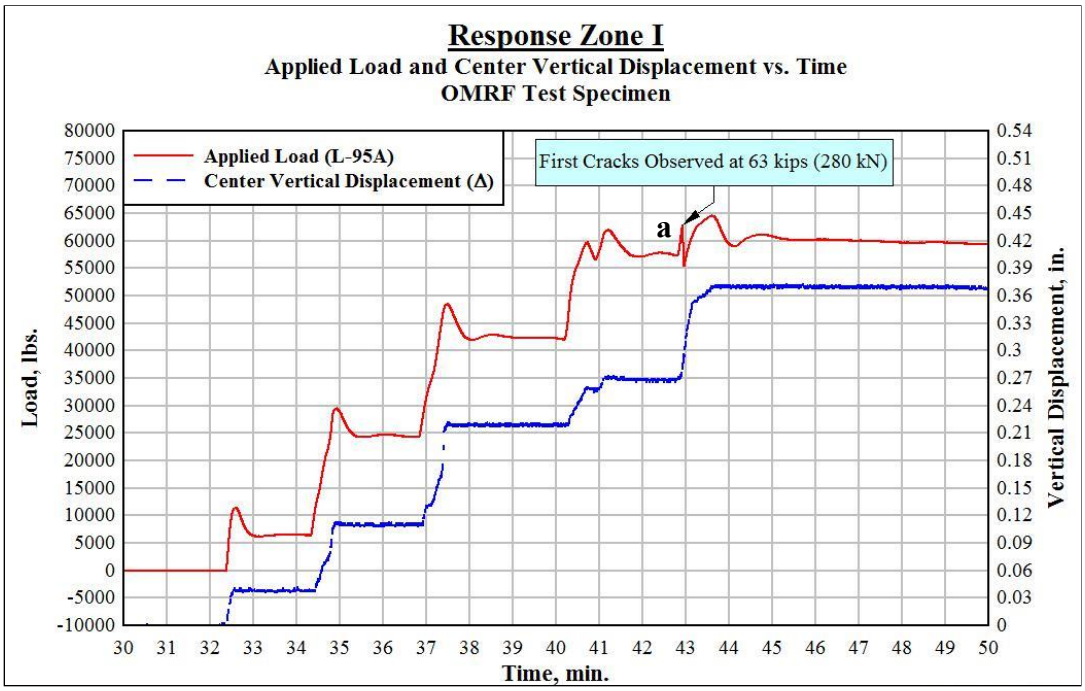

Figure A.18 Response zone I – load and displacement vs. time, incident (a): load vs. displacement, first cracks observed at 63.2 kips (281 kN)

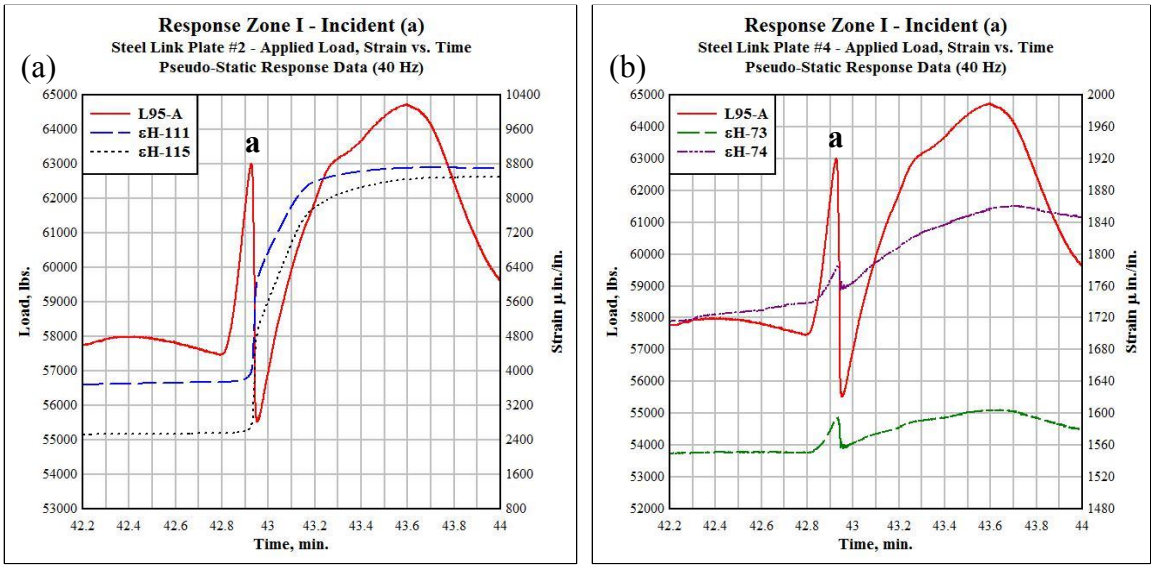

Figure A.19 Response zone I - incident (a): drop in load, increment in strain in steel link plates #2-(a), and #4-(b)

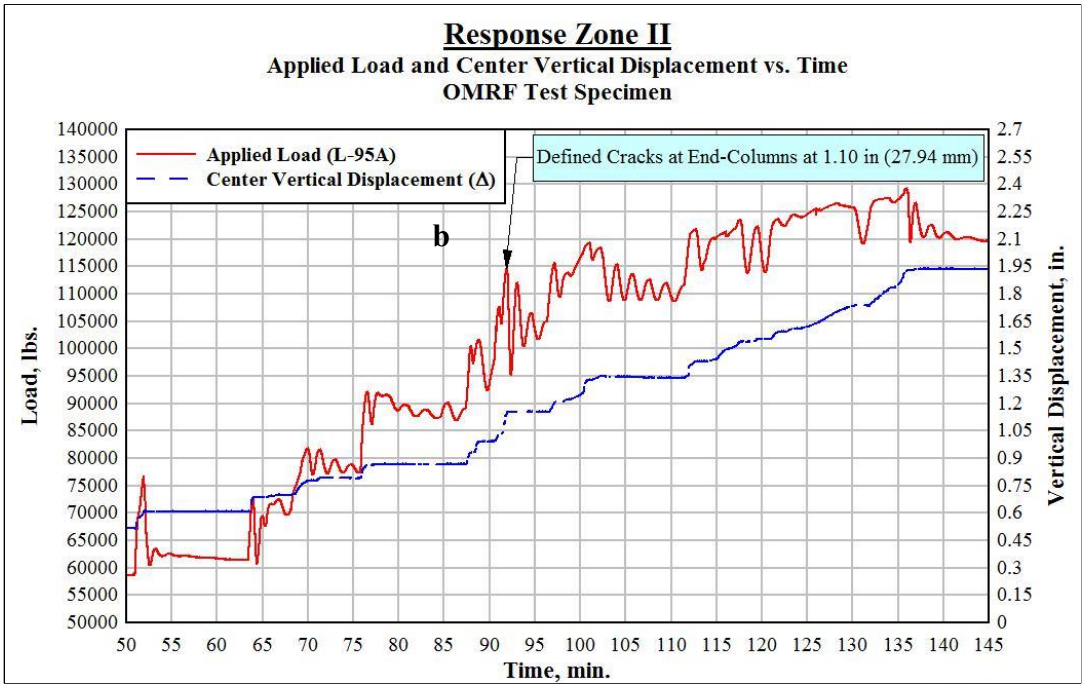

Figure A.20 Response zone II – load and displacement vs. time, incident (b): first cracks observed in end-columns

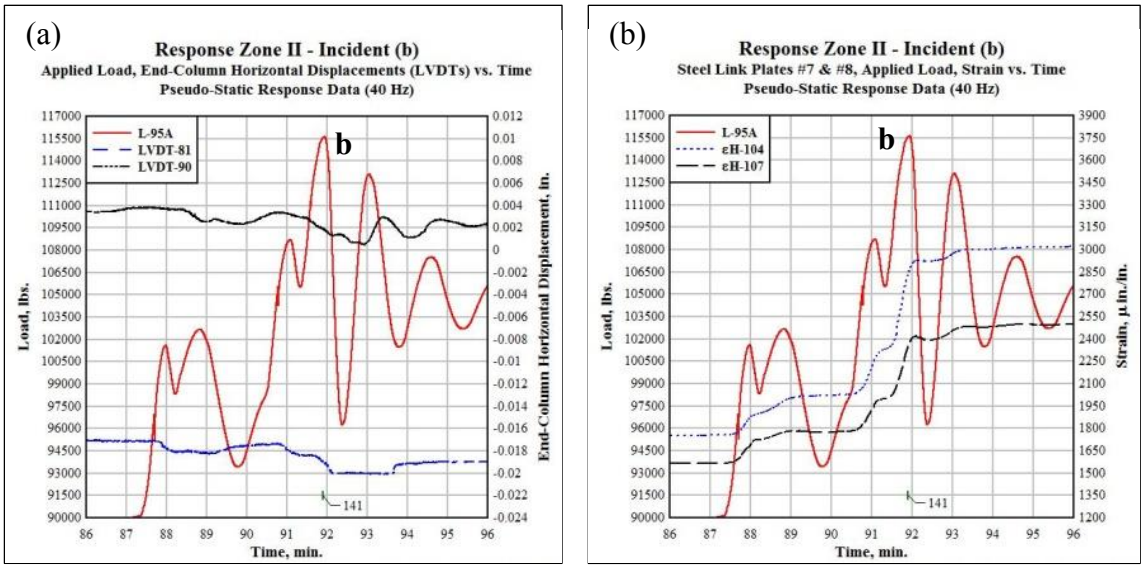

Figure A.21 Response zone II – Incident (b): (a) drop in load, increment in end-column horizontal displacement; (b) drop in load, increment in strain in steel link Plates #7 and #8

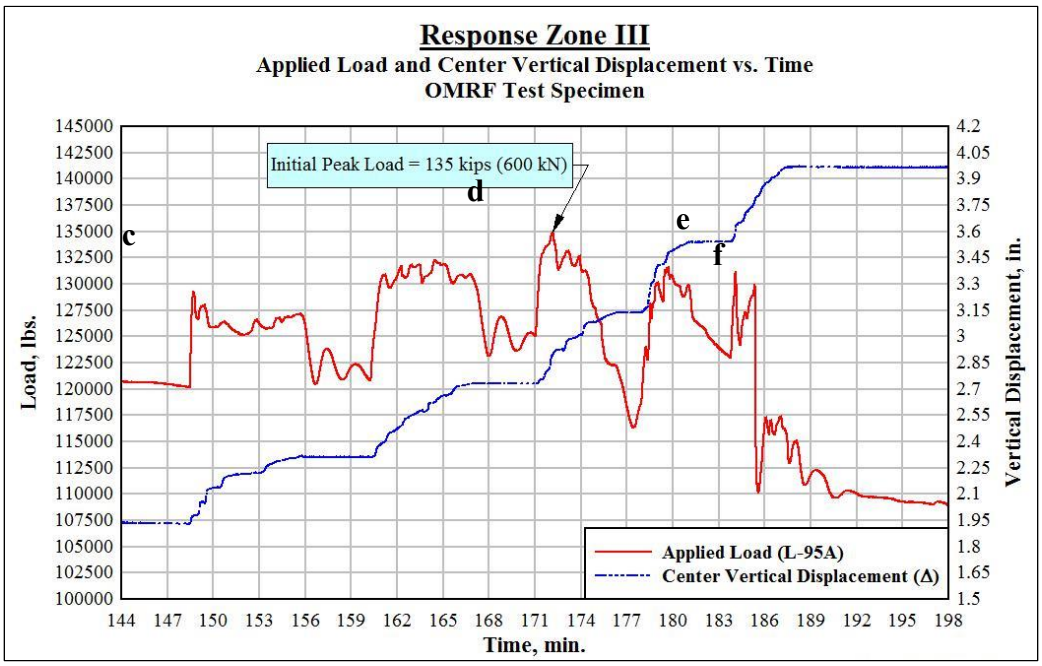

Figure A.22 Response zone III: load and displacement vs. time, yielding of M7 bottom bar at incident (c), initial peak load at incident (d), cracking around left-top M8 plate at incident (e), and detachment of M8 plate at incident (f)

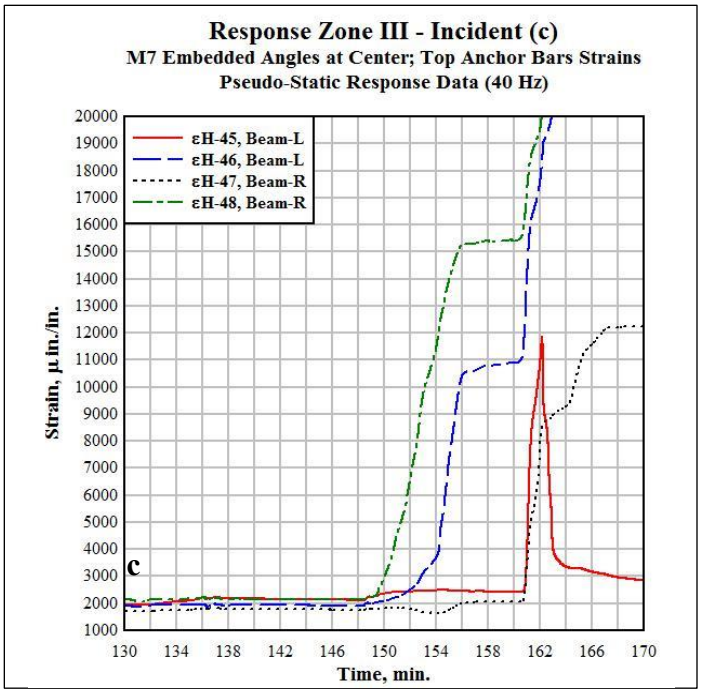

Figure A.23 Response zone (III) – incident (c): strain in center-top M7 anchor bars

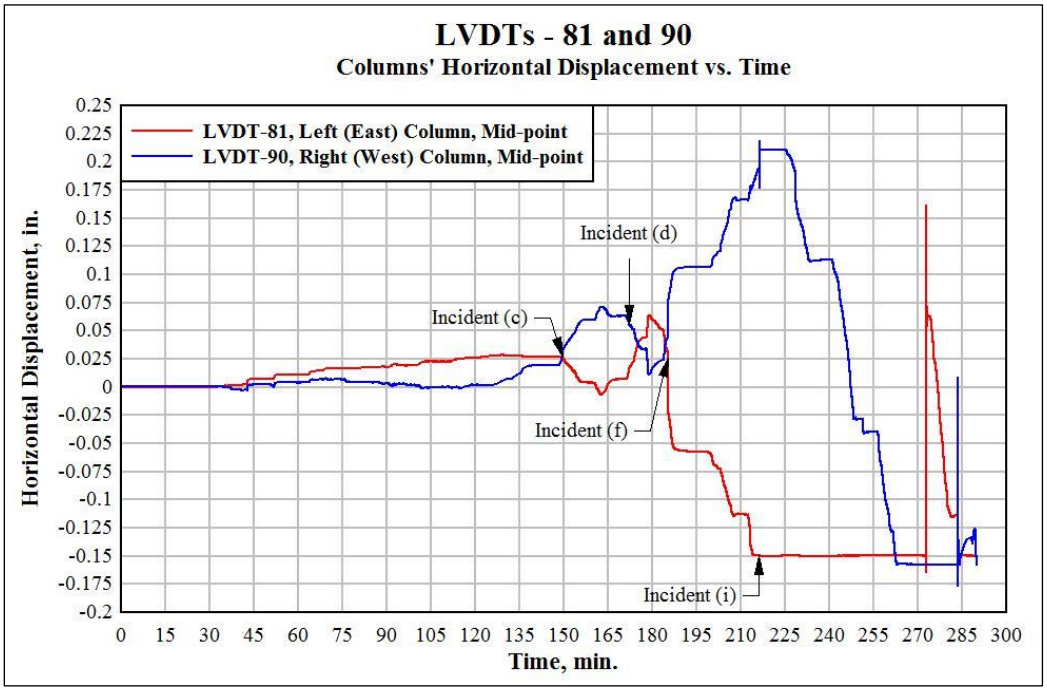

Figure A.24 LVDTs horizontal displacement measurements vs. time

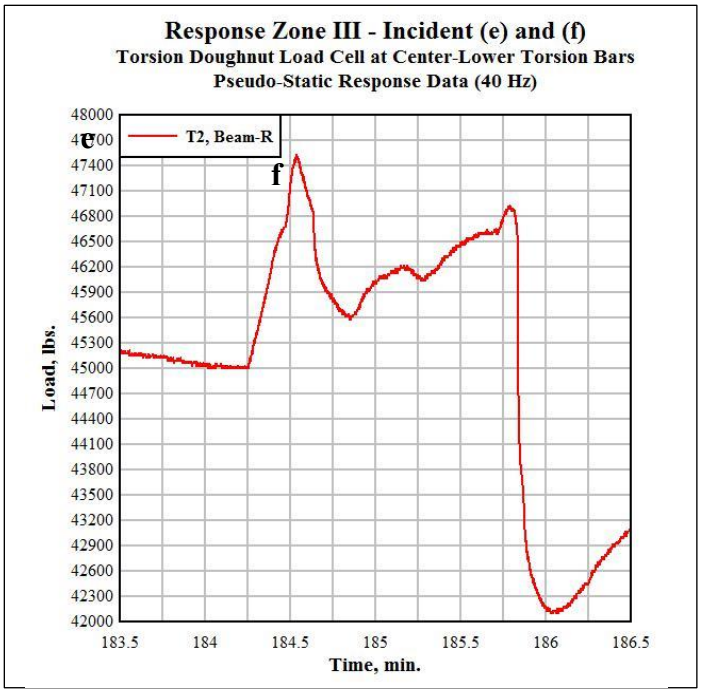

Figure A.25 Response zone III – incidents (e) and (f): drop in torsion load at (T2)

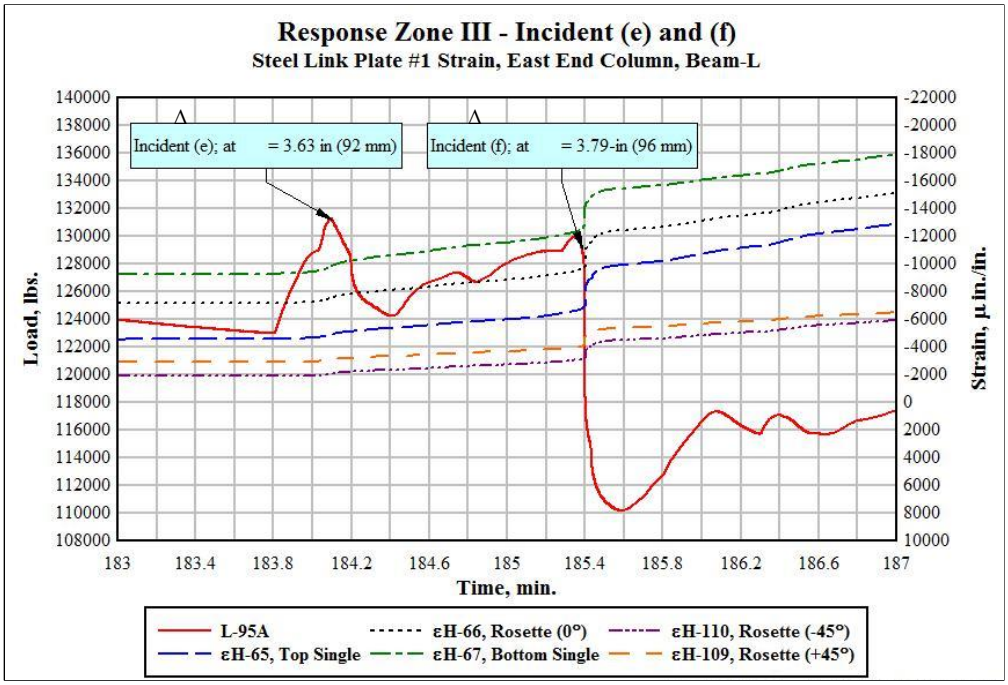

Figure A.26 Response zone III – incidents (e) and (f): steel link plate #1

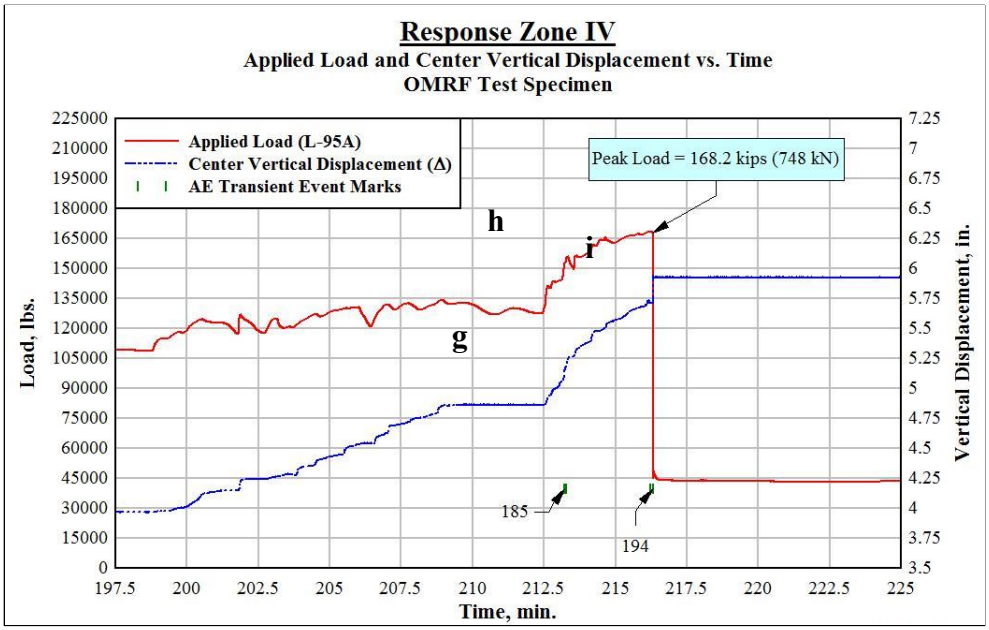

Figure A.27 Response zone IV: load and displacement vs. time, development of arching action at incident (g), concrete scabbing at the bottom corners of beams towards the center at incident (h), and brittle failure of top M7 anchor bar at incident (i)

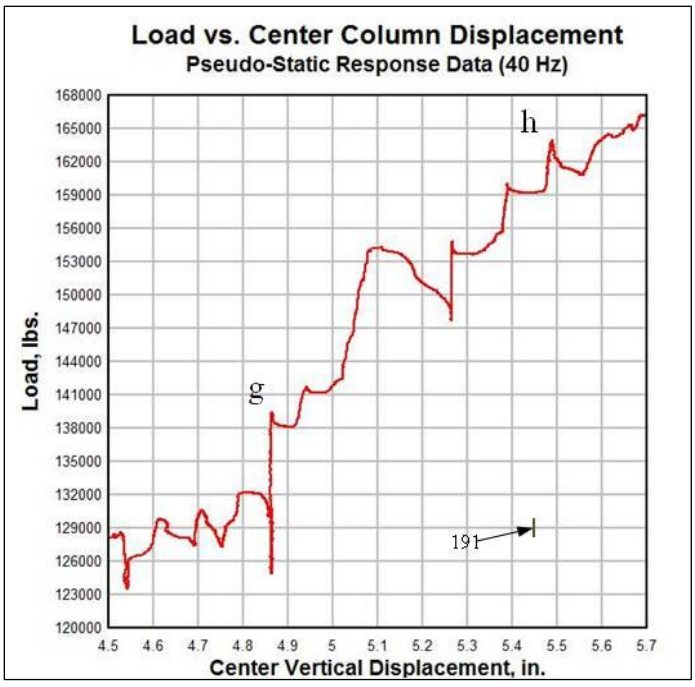

Figure A.28 Response zone IV – incidents (g) and (h)

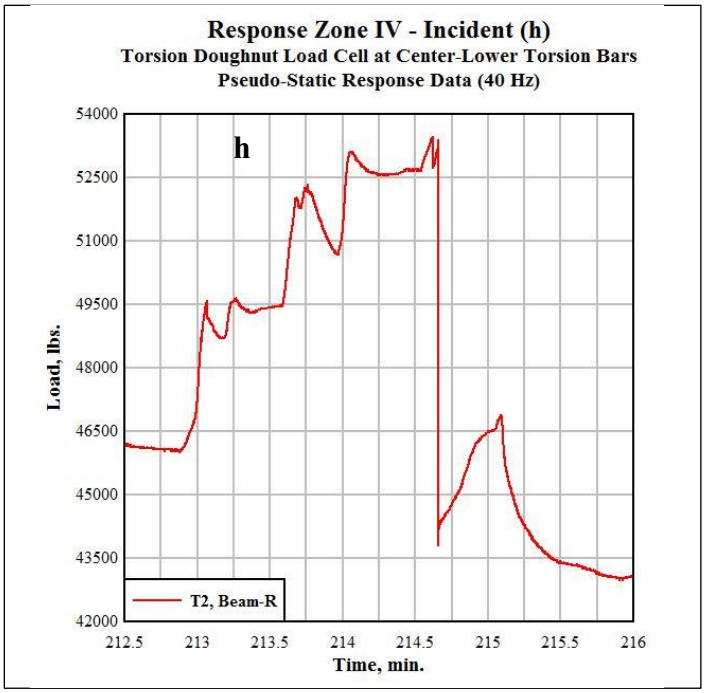

Figure A.29 Response zone IV – incident (h): drop in torsion load at (T2)

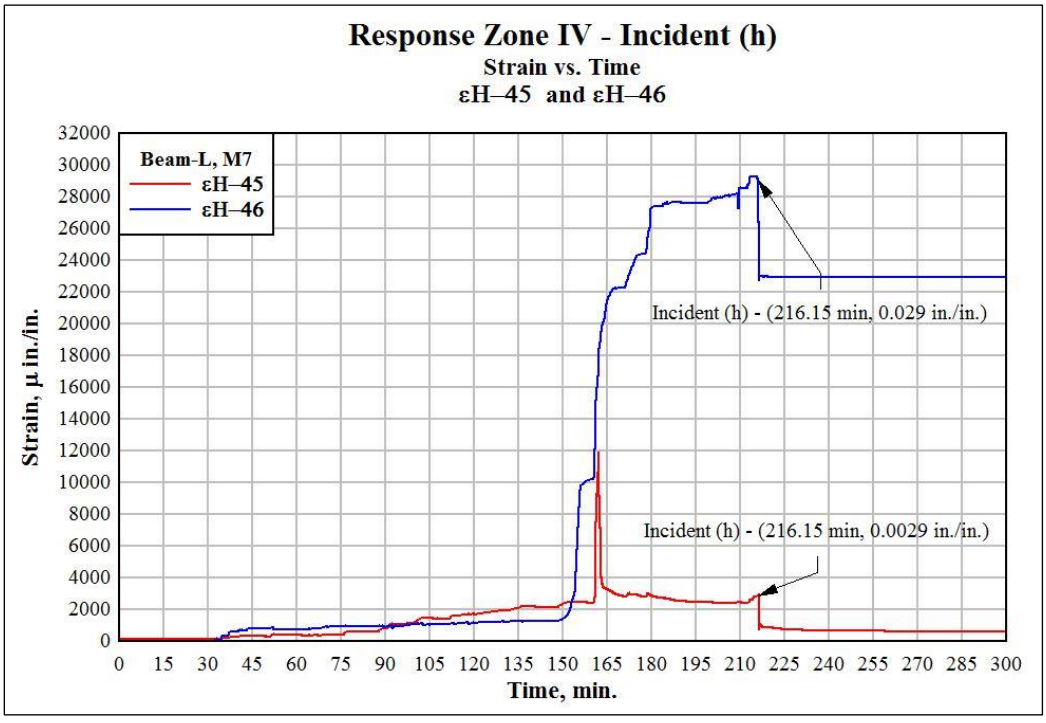

Figure A.30 Response Zone IV – incident (h): Beam-L M7, strain vs. time

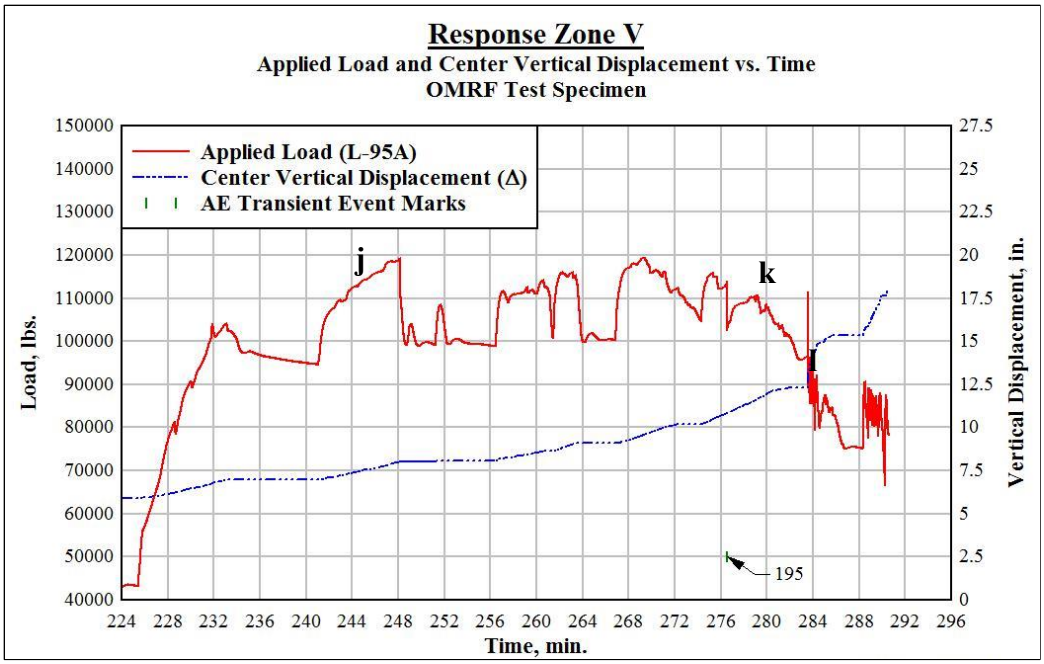

Figure A.31 Response zone V: load and displacement vs. time, torsion bars ejected at incidents (j) and (k), detachment of top M8 plate on right (west) end-column at incident (l)

A.3 Experiment high-frequency response data records (2 MHz)

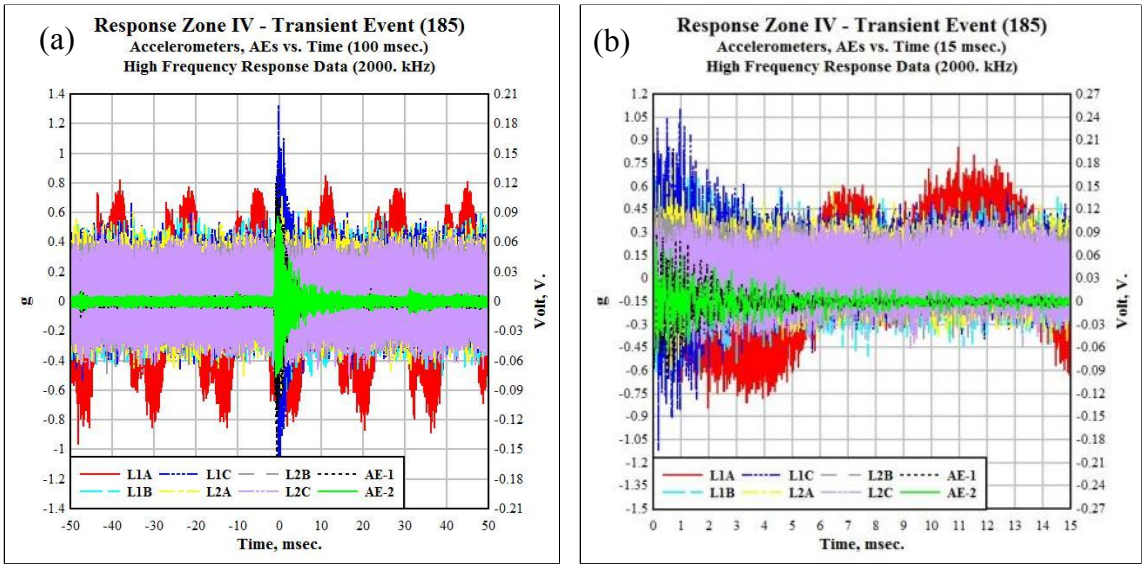

Figure A.32 Transient event (185): (a) acceleration, AE vs. time (100 msec.); (b) acceleration (Beam-L), AE vs. time (15 msec)

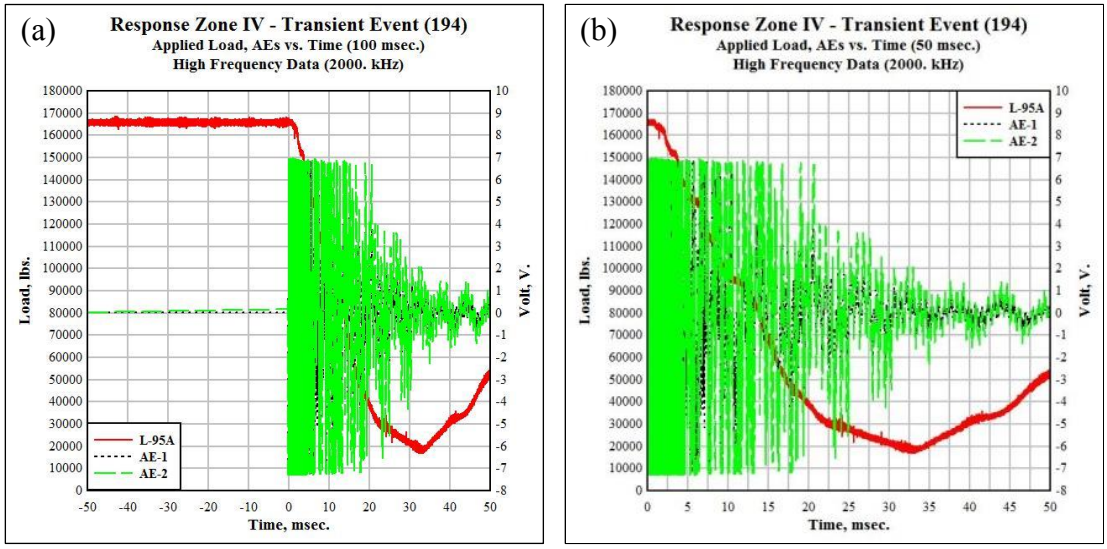

Figure A.33 Transient event (194): acoustic emission activity at 216.15 min. of testing, (a) 100 msec, (b) 50 msec

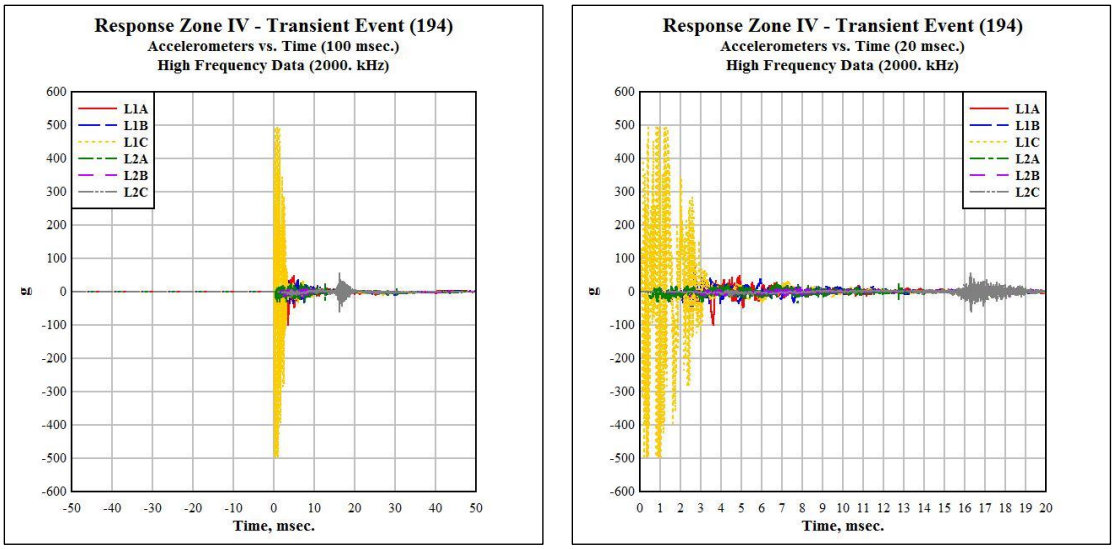

Figure A.34 Transient event (194): acceleration activity at 216.15 min. of testing, (a) 100 msec, (b) 20 msec

(b)

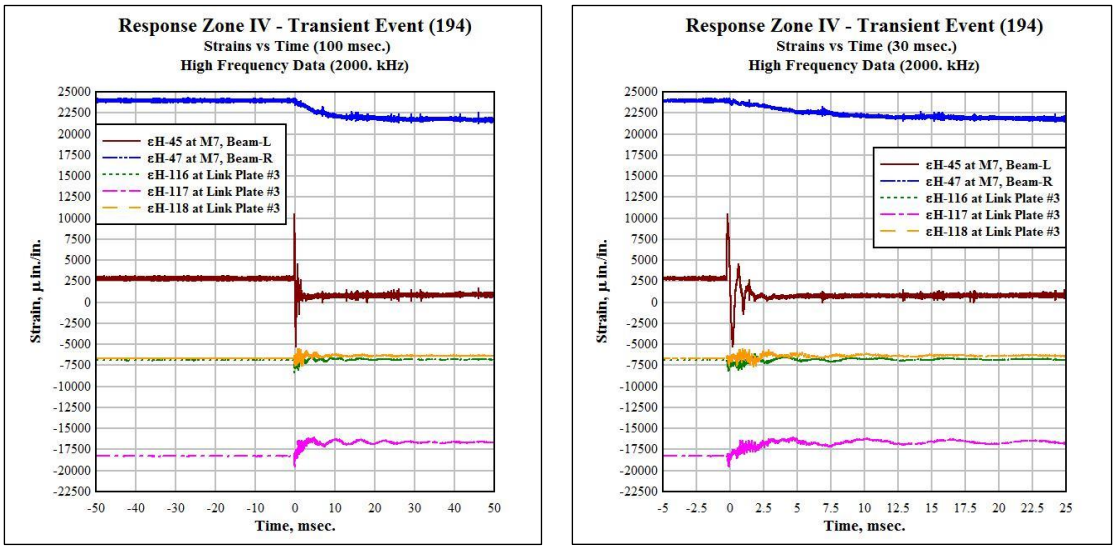

Figure A.35 Transient event (194): strain activity at 216.15 min. of testing, (a) 100 msec, (b) 30 msec

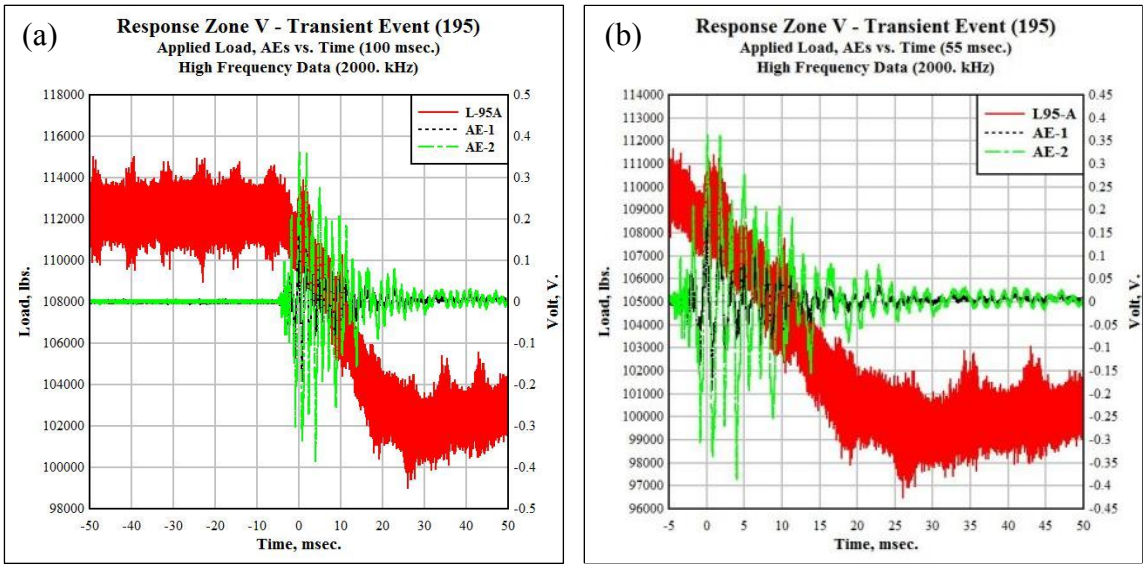

Figure A.36 Transient event (195): acoustic emission activity at 276.53 min. of testing, (a) 100 msec, (b) 55 msec

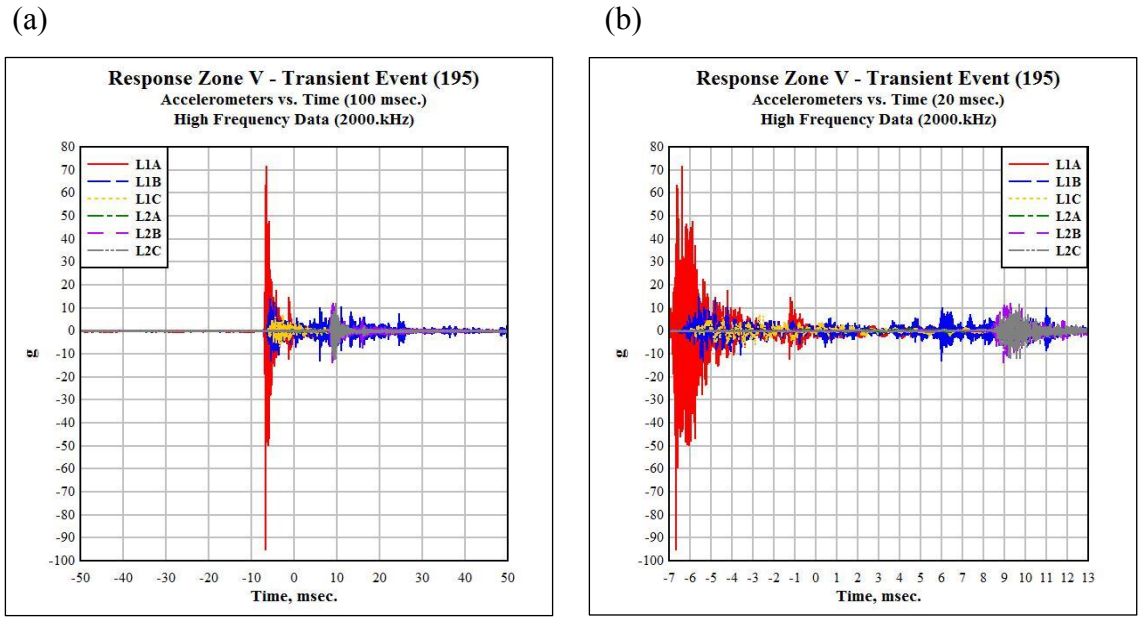

Figure A.37 Transient event (195): accelerometer, activity at 276.53 min. of testing, (a) 100 msec, (b) 20 msec

APPENDIX B

MATERIAL PROPERTY STUDY

B.1 Concrete material property study

The average measured 28-day compressive strength of concrete was 5653-psi (38.9-MPa) and the average 28-day splitting tensile strength of concrete was 457- psi (3.1-MPa). Table B.1 and Table B.2 show average values of the measured mechanical properties of the reinforcing bars used to fabricate the specimens.

Table B.1 28-Day compressive strength sampling test result

28-Day Sampling Testing		
Sampler I.D.	**Compressive Strength (psi)**	**Peak Load (lbf)**
SR 1-1	5366	67428
SR 1-2	5694	71555
SR 1-3	5551	69758
SR 2-1	5765	72448
SR 2-2	5862	73665
SR 2-3	6085	76470
SR 3-1	5746	72202
SR 3-2	5630	70752
SR 3-3	5710	71758
SR 4-1	5458	68588
SR 4-2	5413	68022
SR 4-3	5558	69843
Average:	**5653.17**	**71040.75**

Table B.2 28-Day splitting tensile strength sampling test result

Specimen Identification	Splitting Tensile Strength (psi)	Peak Load (lbf)
SR 1-1	355	18159
SR 1-2	400	20306
SR 1-3	361	18344
SR 2-1	608	30689
SR 2-2	511	25776
SR 2-3	431	21730
SR 3-1	476	24035
SR 3-2	492	24837
SR 3-3	489	24789
SR 4-1	470	23701
SR 4-2	442	22113
SR 4-3	445	22402
Average	**456.67**	**23073.417**

B.2 Reinforcement A706 Samples Tensile Test Data

A total of twenty-two bars were sent to Bodycote for Tensile Test – ASTM E8. Table B.3 shows the ultimate strain recorded from the tensile test of 8 rebar samples. The OMF SDC-B was designed using the following bar sizes, with the exception of the #11 rebar, which was part of the SMF prototype design. Figure B.1 to Figure B.6 show the strain response of the tested A706 samples.

Table B.3 Rebar samples sent to Boycote for tensile test – ASTM E8

Sample #	Bar Size	Symbol	Diameter	Label	Yield Strength, *fy* ksi (MPa)	Tensile Strength, *fu* ksi (MPa)	Fracture Strain, %EL
225	#11	V-36W4	1-3/8”	#A	70.4 (485.4)	105.4 (726.7)	22%[1]
226	#11	V-36W4	1-3/8”	#A	70.5 (485.4)	105.5 (727.4)	23%[1]
227	#10	V-32W4	1-1/4”	#B	69.6 (479.9)	105.2 (725.3)	24%[1]
228	#10	V-32W4	1-1/4”	#B	69.0 (475.7)	101.4 (699.1)	24%[1]
231	#8	∞C25W4	15/16”	#D	73.0 (503.3)	107.7 (742.6)	24%[1]
232	#8	∞C25W4	15/16”	#D	73.9 (509.5)	107.5 (741.2)	24%[1]
222	#4	∞C13W4	1/2”	#H	72.7 (501.2)	106.4 (733.6)	26%[2]
223	#4	∞C13W4	1/2”	#H	75.6 (521.2)	106.4 (733.6)	27%[2]

[1]Gauge length: 2 in. (51 mm)
[2]Gauge length: 1 in. (25 mm)

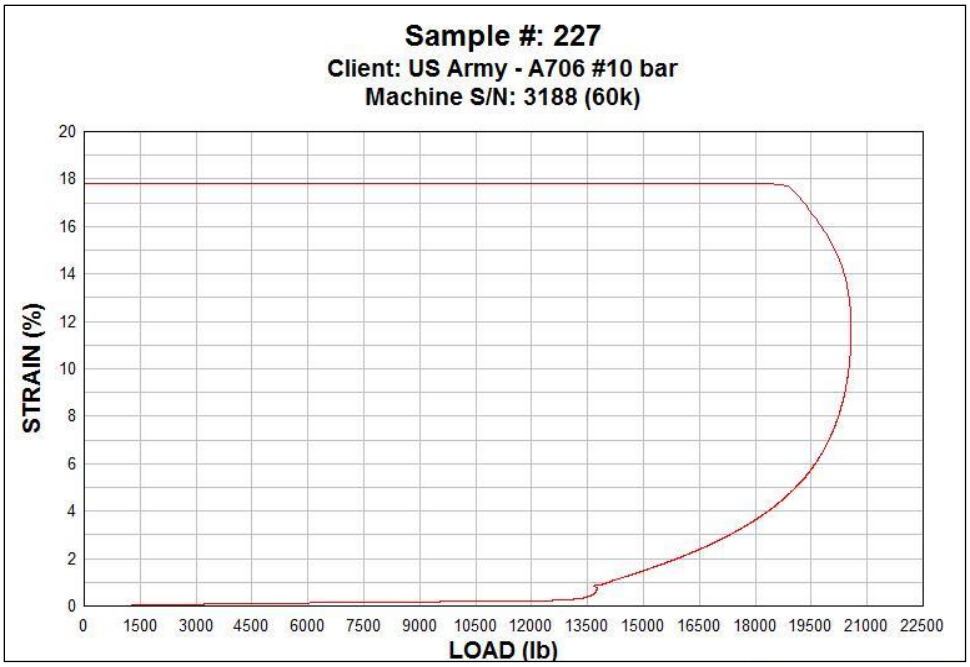

Figure B.1 Tensile test A706 - #10 bar, sample #227, strain vs. load graph

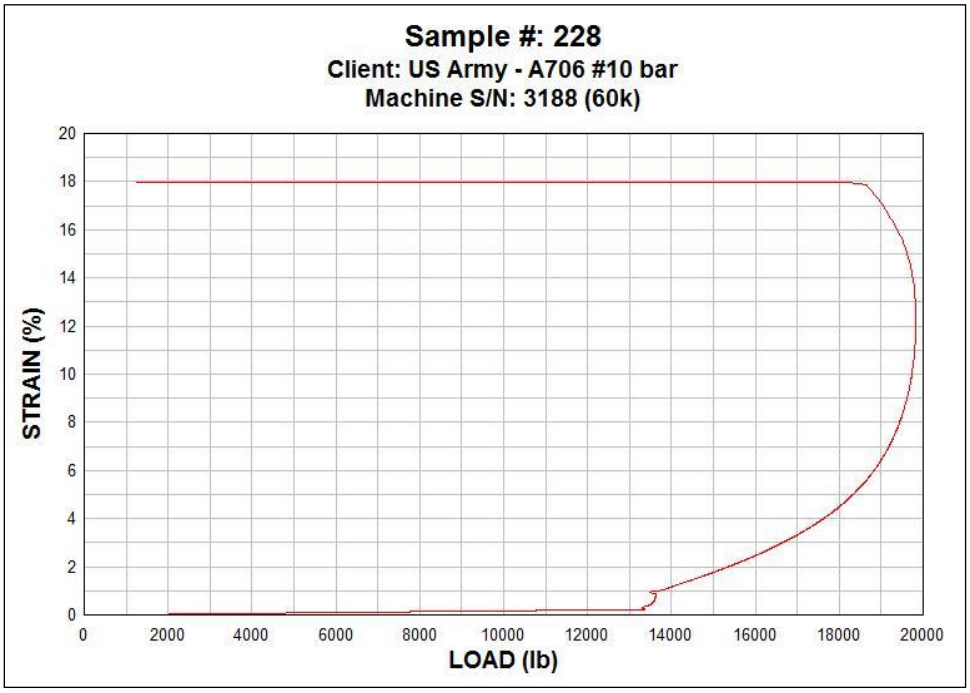

Figure B.2 Tensile test A706 - #10 bar, sample #228, strain vs. load graph

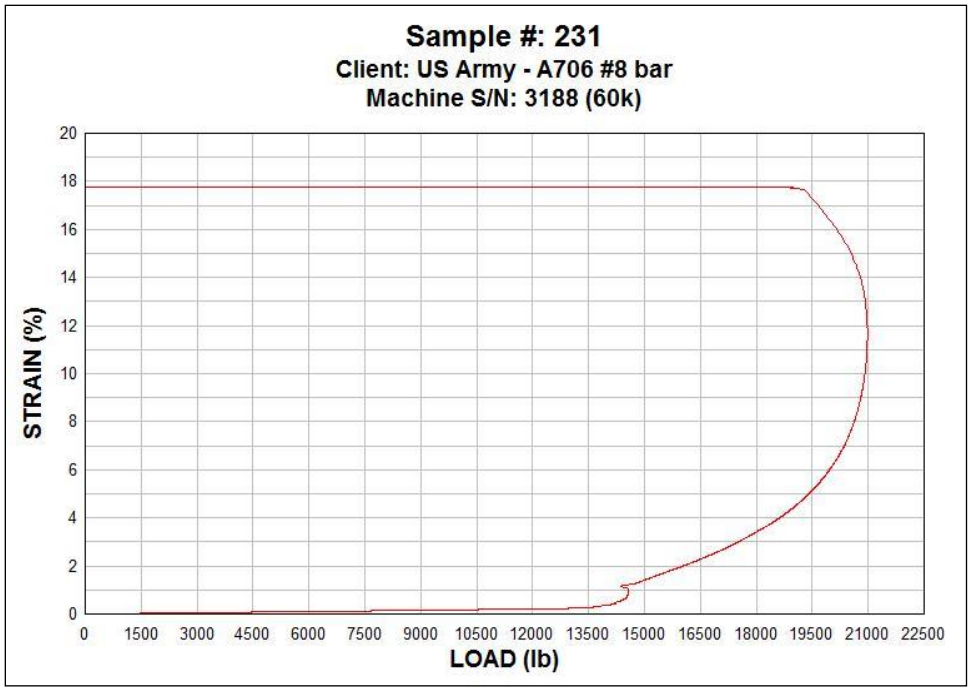

Figure B.3 Tensile test A706 - #8 bar, sample #231, strain vs. load graph

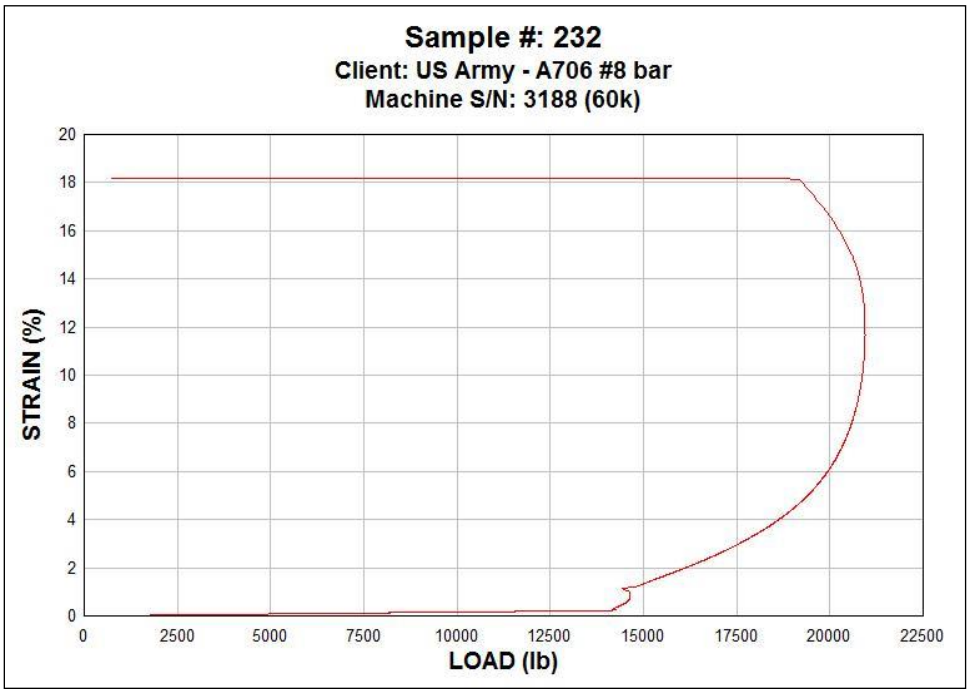

Figure B.4 Tensile test A706 - #8 bar, sample #232, strain vs. load graph

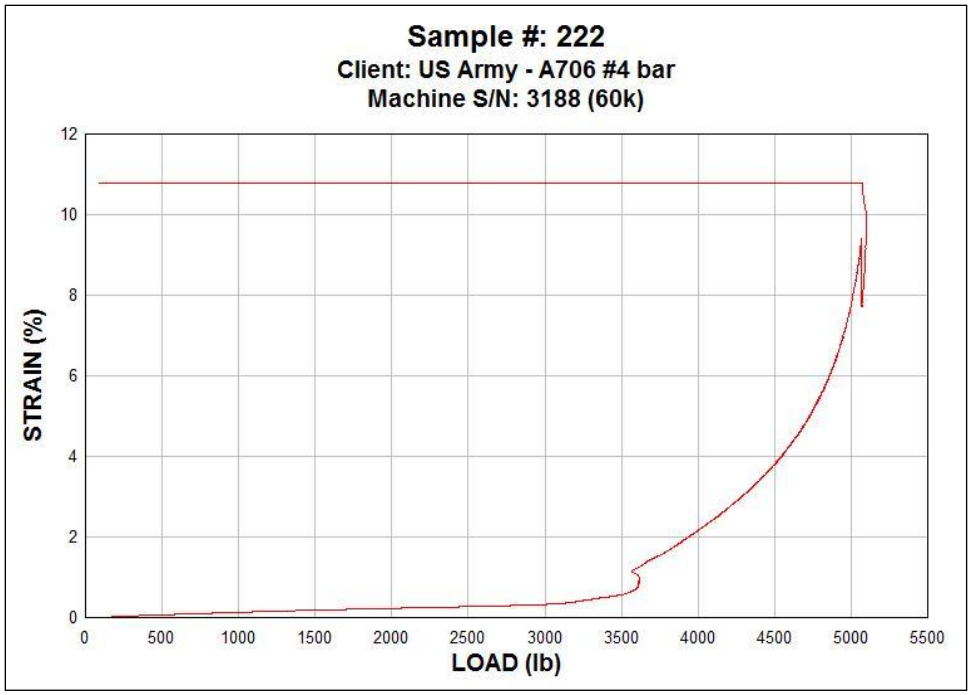

Figure B.5 Tensile test A706 - #4 bar, sample #222, strain vs. load graph

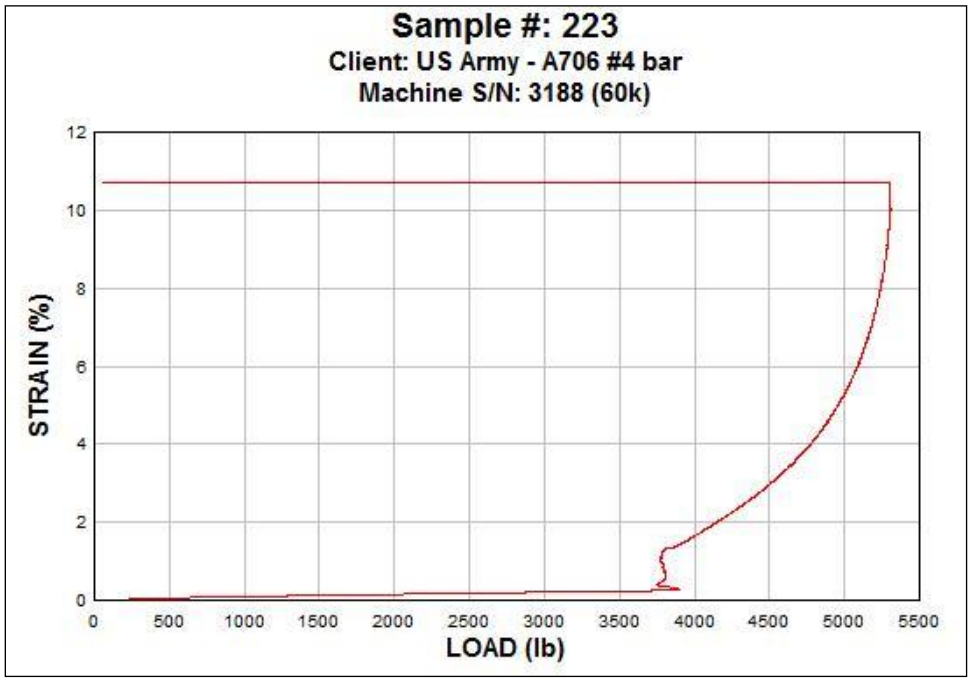

Figure B.6 Tensile test A706 - #4 bar, sample #223, strain vs. load graph

APPENDIX C

OMRF TEST SPECIMEN: FABRICATION DRAWINGS

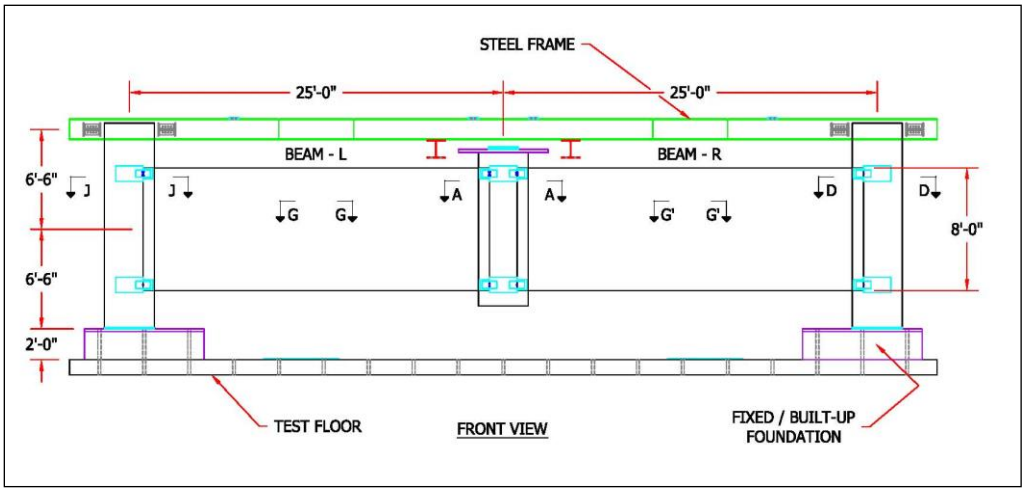

Figure C.1 Overview of instrumentation layout of SDC-B

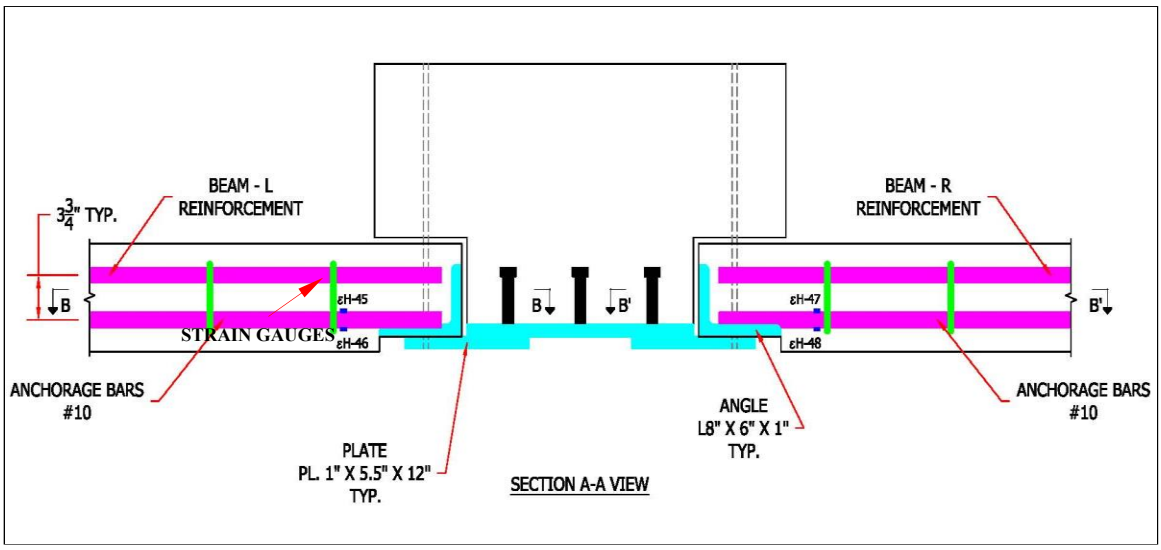

Figure C.2 Section A-A of SDC-B overview layout

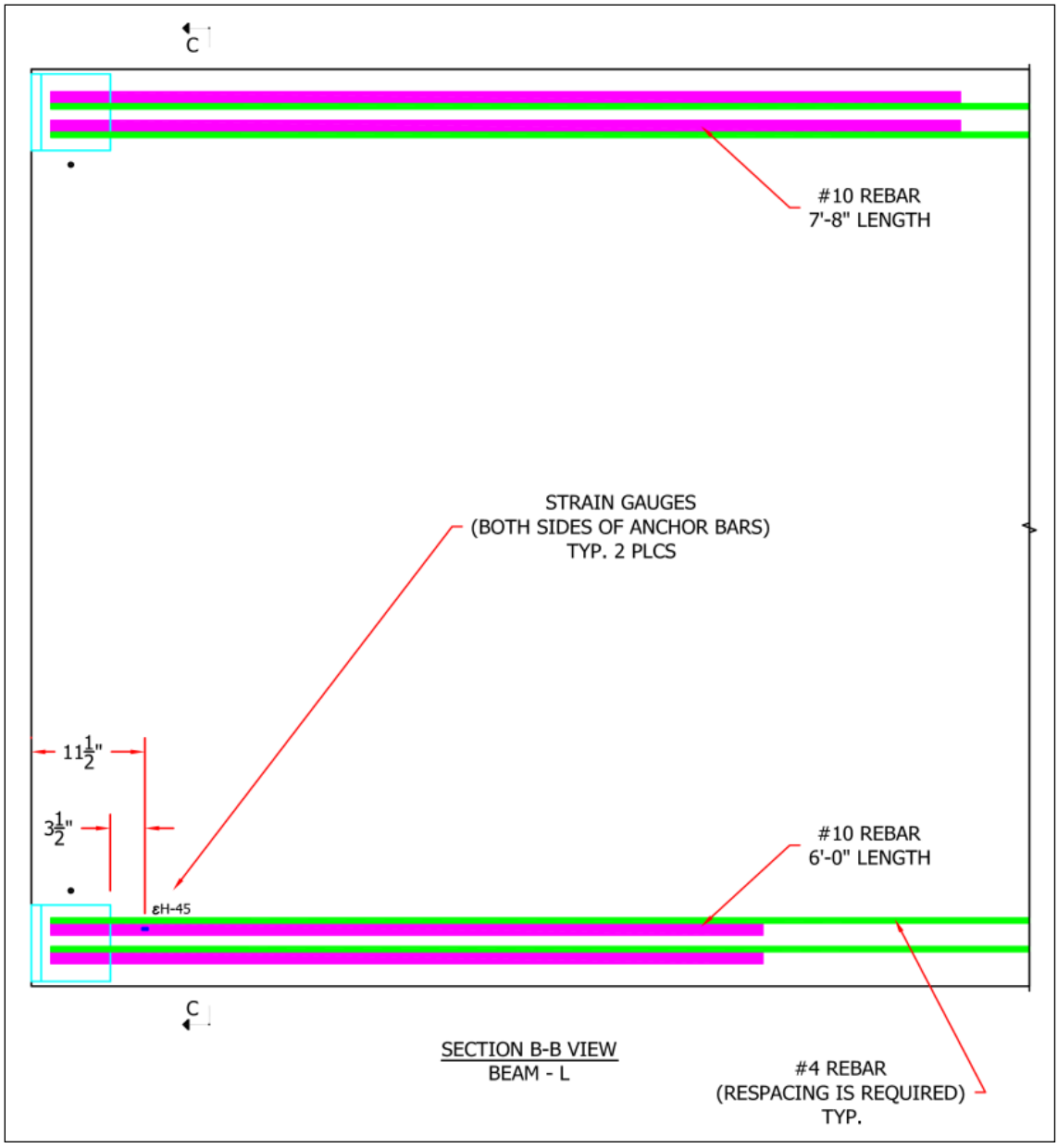

Figure C.3 Section B-B of SDC-B overview layout

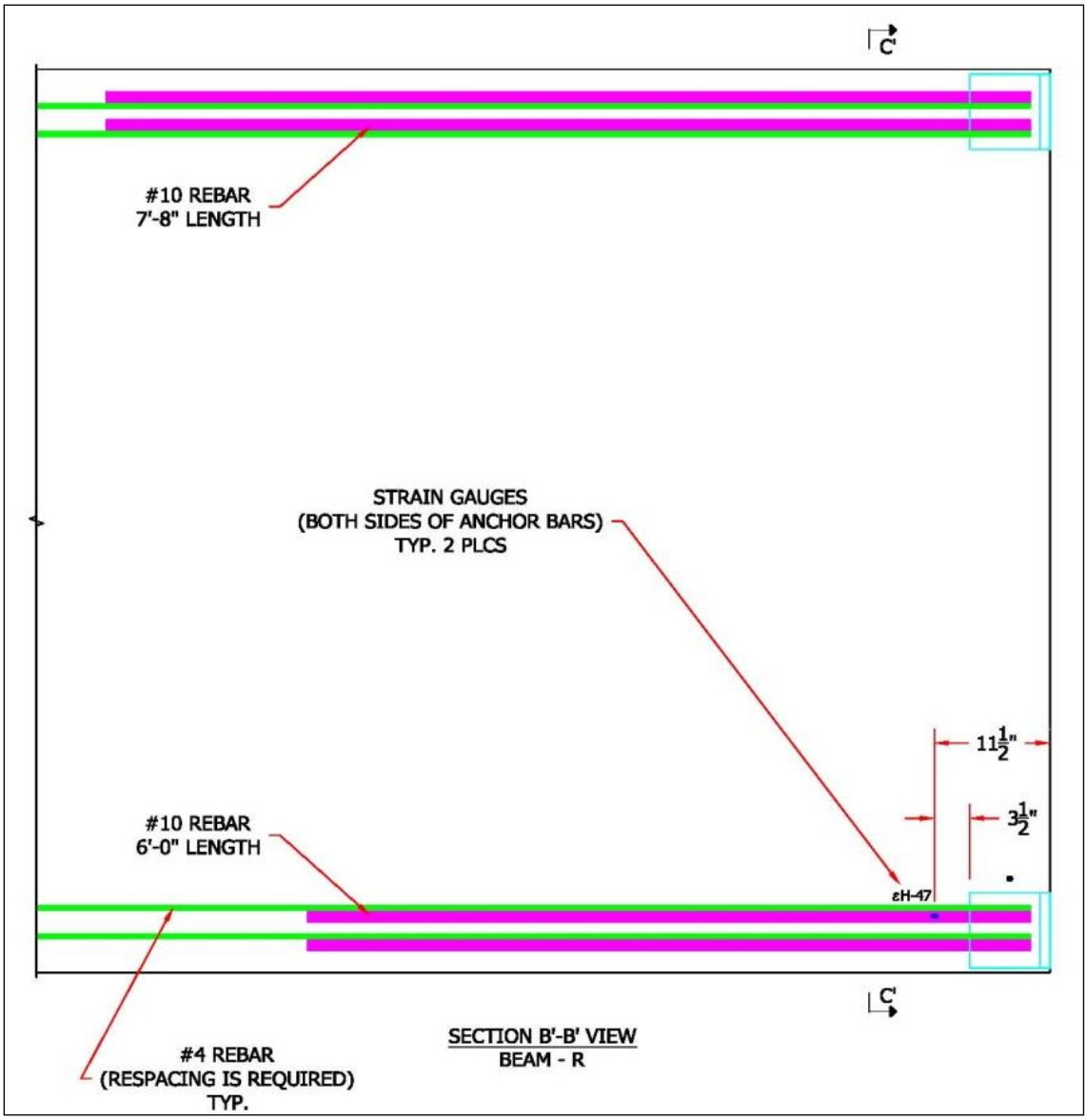

Figure C.4 Section B'-B' of SDC-B overview layout

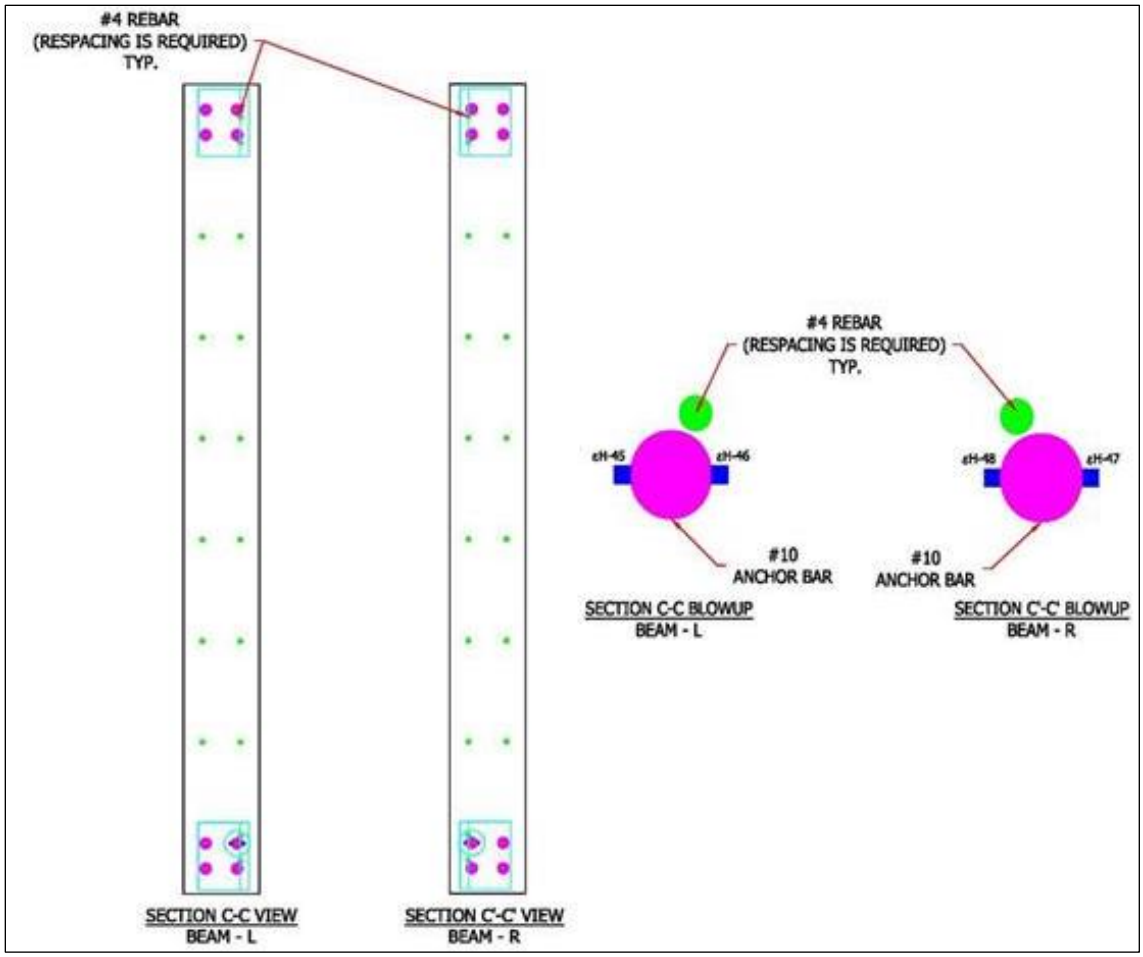

Figure C.5 C-C and C'-C' of SDC-B overview layout

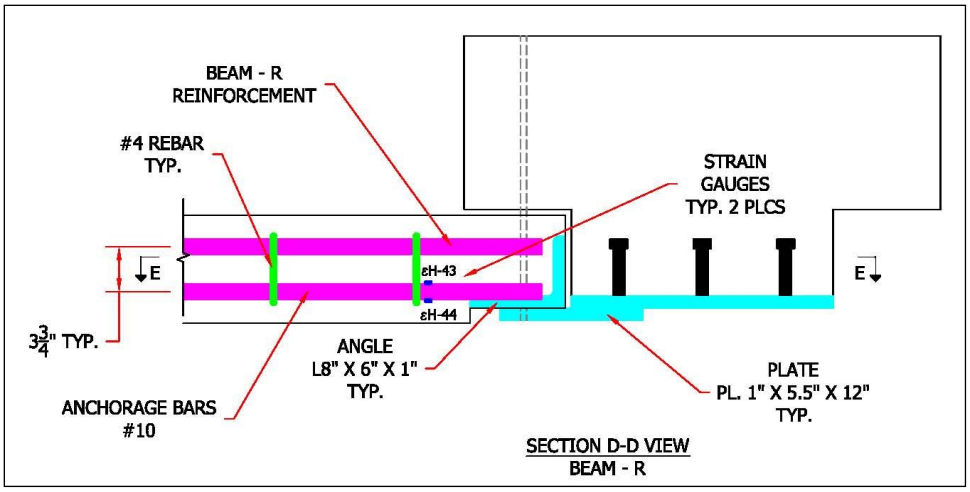

Figure C.6 Section D-D of SCD-B overview layout

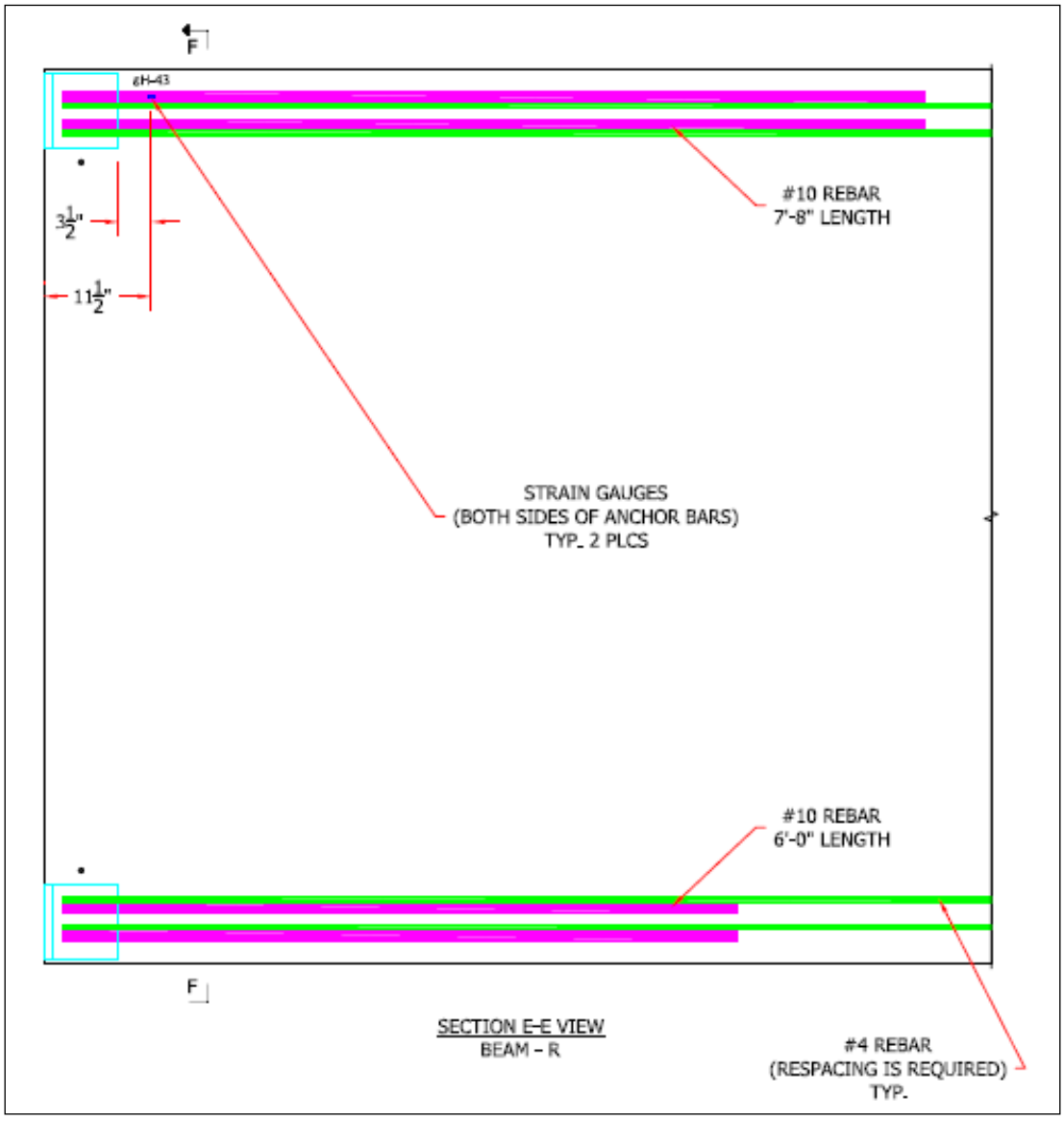

Figure C.7 Section E-E of SDC-B overview layout

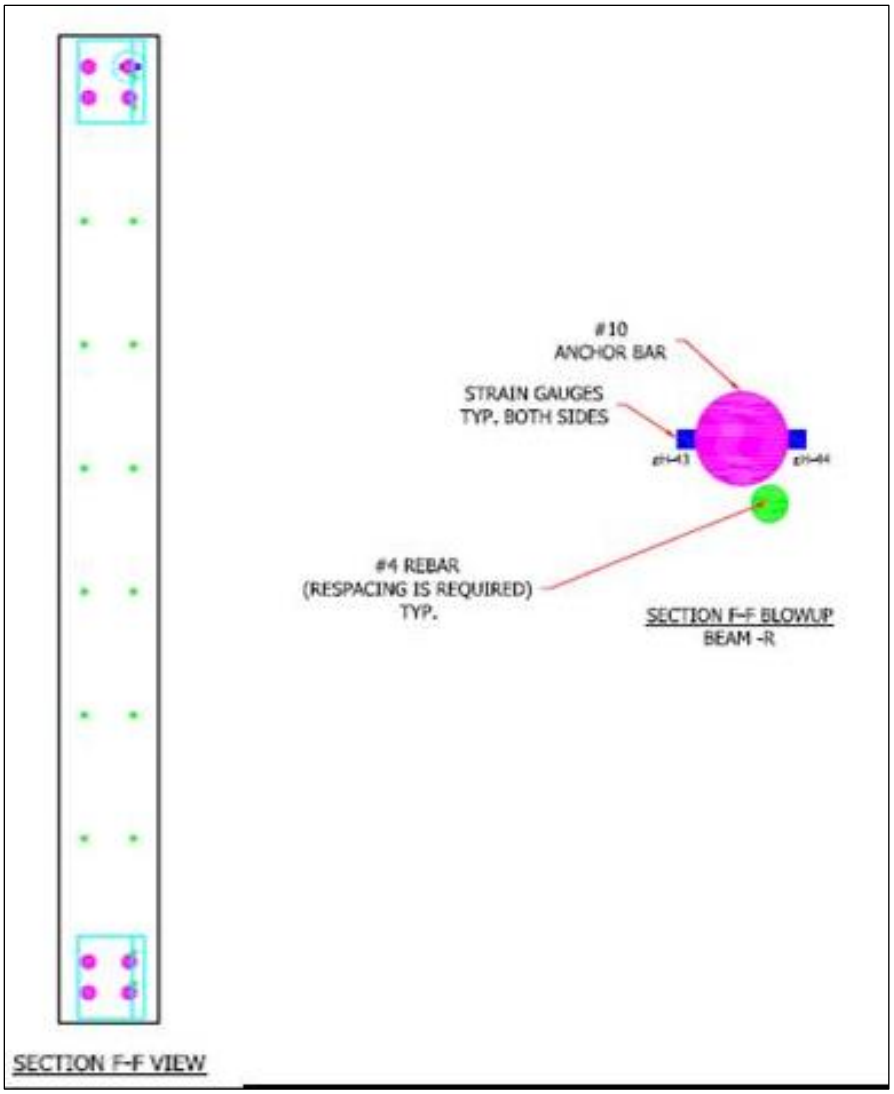

Figure C.8 Section F-F of SDC-B overview layout

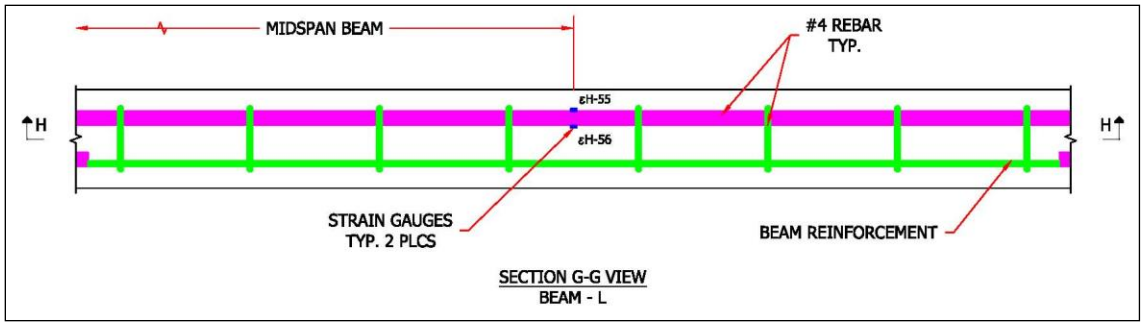

Figure C.9 Section G-G of SDC-B overview layout

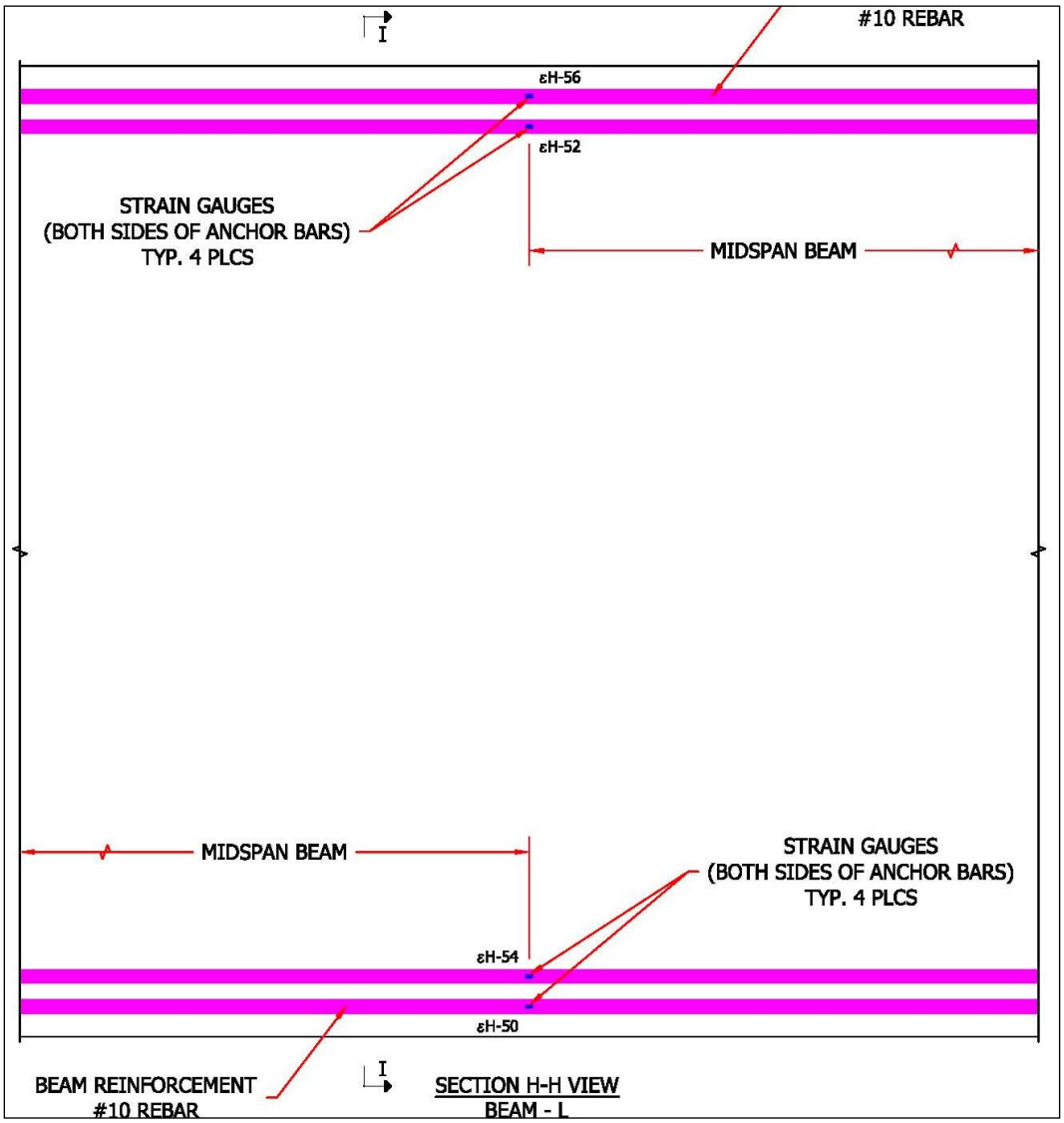

Figure C.10 Section H-H of SDC-B overview layout

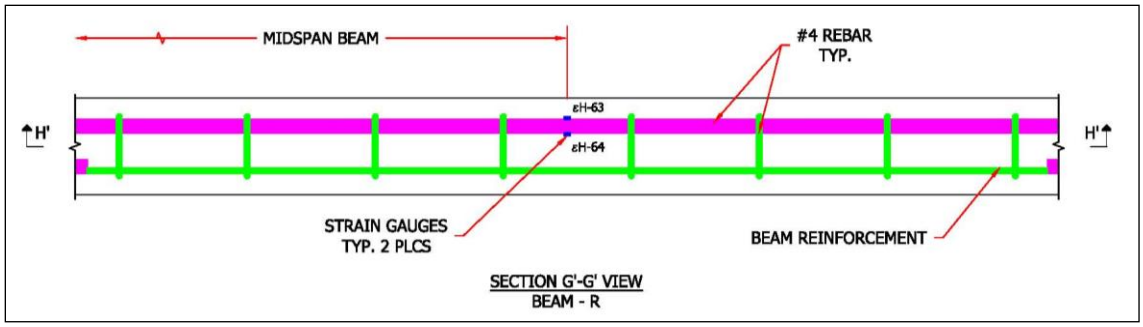

Figure C.11 Section G'-G' of SDC-B overview layout

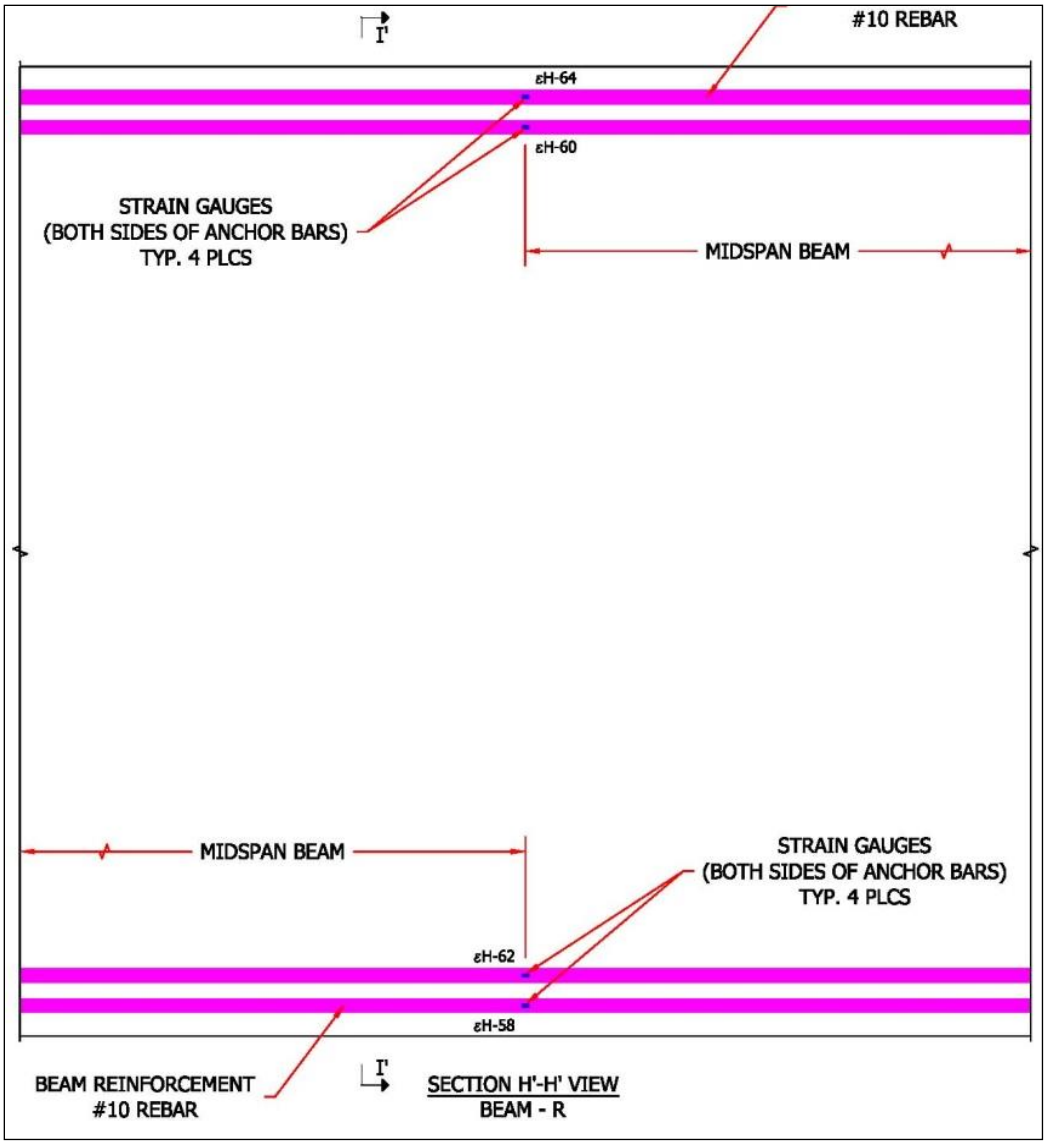

Figure C.12 Section H'-H' of SDC-B overview layout

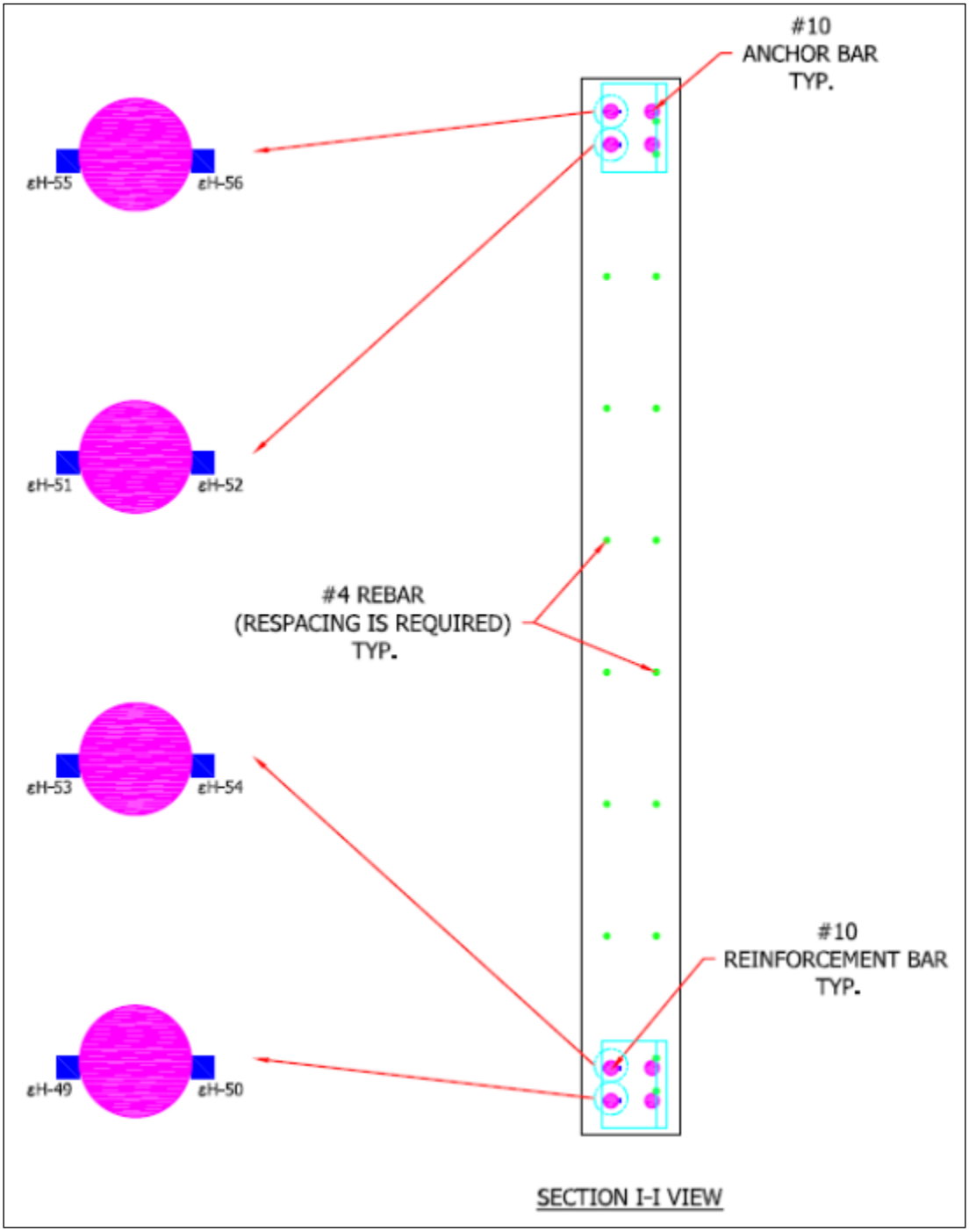

Figure C.13 Section I-I of SDC-B overview layout

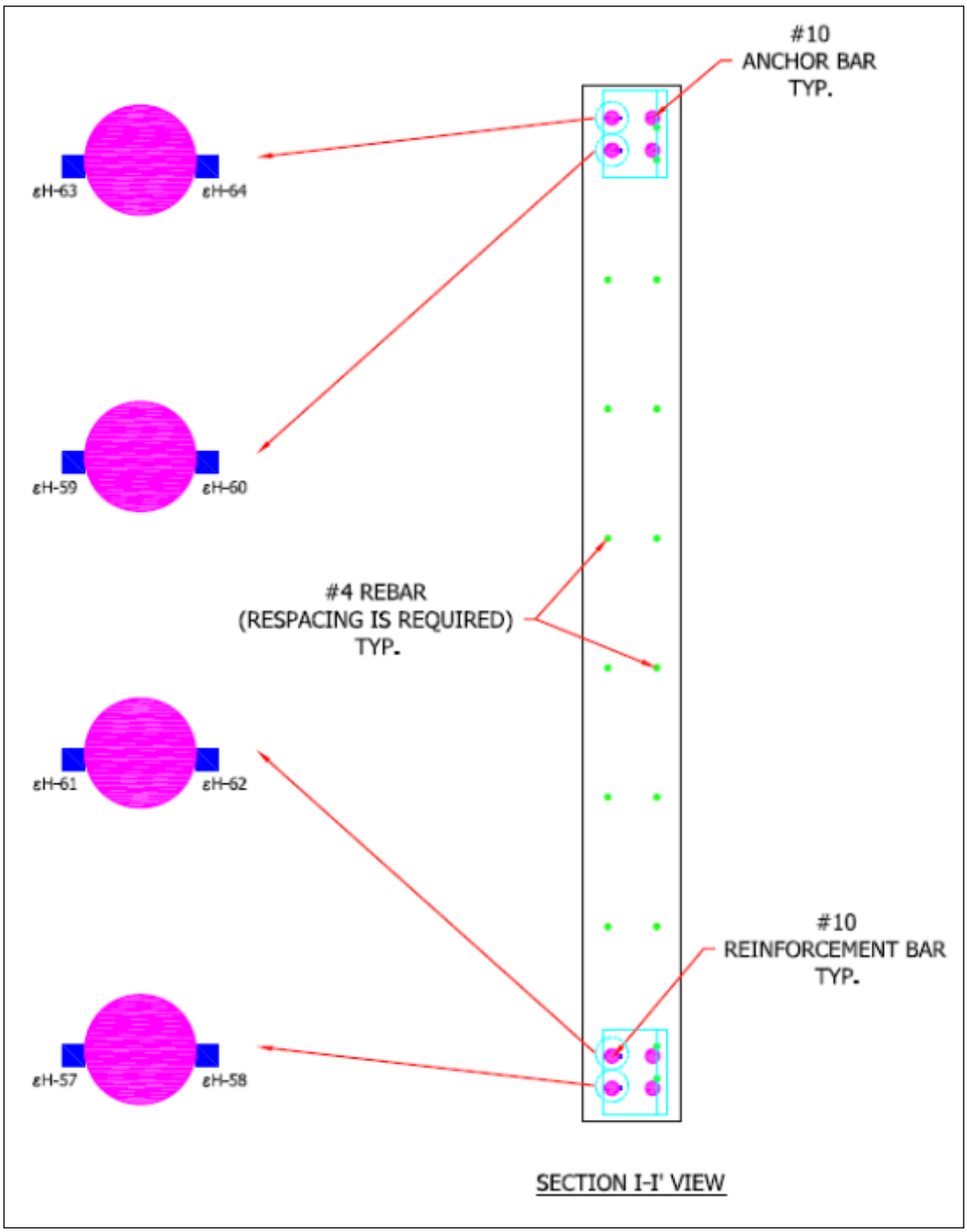

Figure C.14 Section I-I’ of SDC-B overview layout

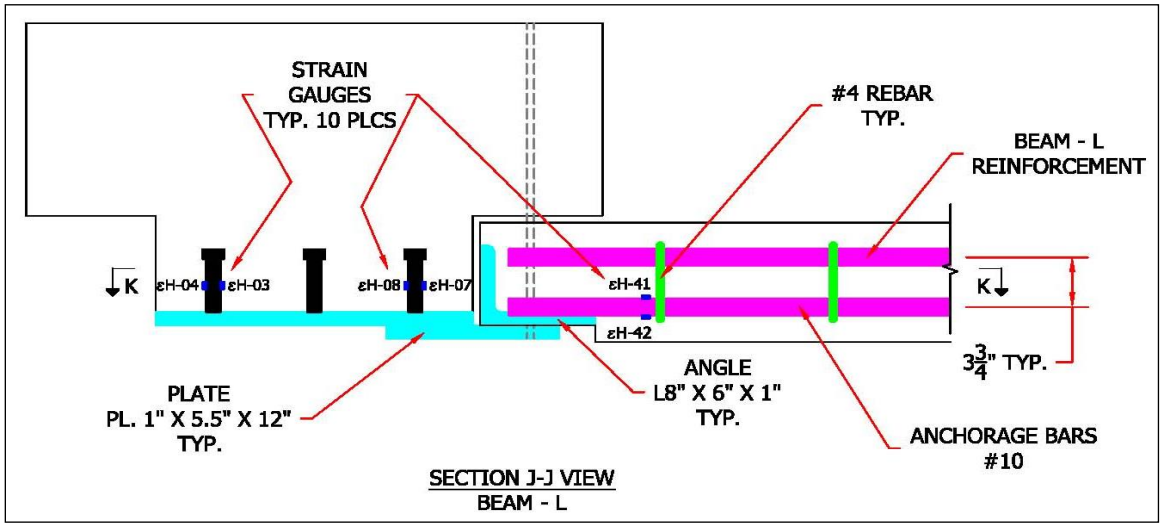

Figure C.15 Section J-J of SDC-B overview layout

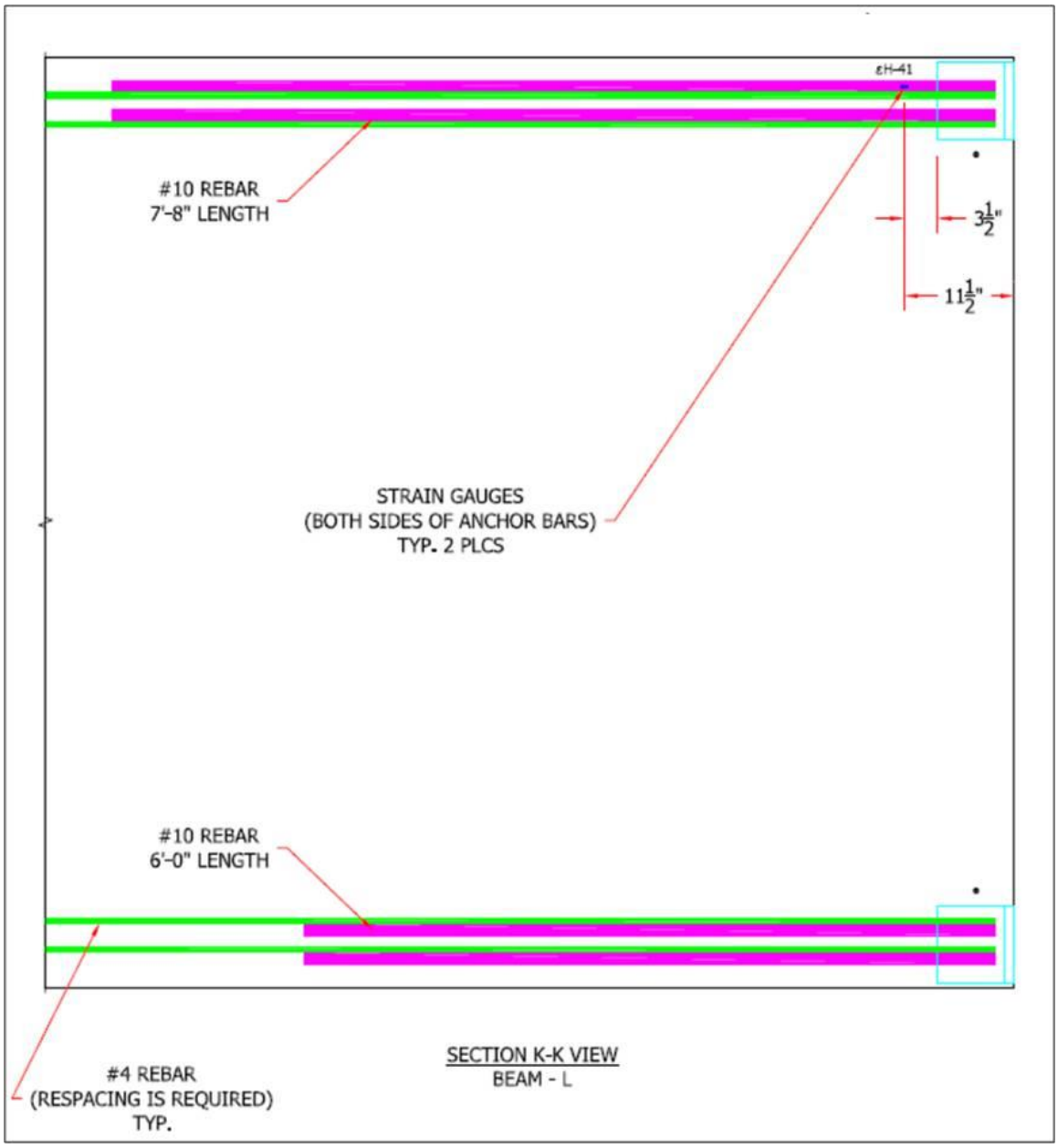

Figure C.16 Section K-K of SDC-B overview layout

APPENDIX D

EXPERIMENT PROCEDURE

D.1 Experimental Testing Procedure

1. Place spacers between top loading plate and ram.
2. Place plywood over the windows of the instrumentation building that is located in front of the reaction frame.
3. Move all nonessential personnel from the testing floor before starting the test.
4. Begin recording of instrumentation data and digital video.
5. Remove angle supports from bottom of stub column.
6. Remove all essential personnel from test floor.
7. Place people at each entrance to the test floor to prevent people from walking on test floor during the experiment. The people watching the doors will be out of the line of sight of the reaction frame and specimen.
8. Initiate hydraulic ram and load in displacement control mode at 0.02-in./min. (0.51 mm/min) using displacement increments as described in the next page; *make pauses of 10 minutes between some increments until failure or the hydraulic ram runs out of stroke.
9. Unload the hydraulic ram.
10. Allow all nonessential personnel on test floor.
11. Obtain posttest measurements and photographs.
12. Secure test specimen and rope off area around reaction frame.

* During each pause, only authorized personnel will be obtaining data from the cracking patterns on the specimen. Once all the data are obtained, the Project Engineer will give the call to proceed loading.

Experiment Name: OMRF Specimen (SDC-B)

Test Day: October 5, 2012

Test Time: 1053 to 1509 CT

Displacement and Loading Increments:

Table D.1 SDC-B Experiment Procedure

Start Time (hr)	Center Ram Displacement (in.)	Load (kips)	Time Finished (hr)	Pause (min.)
1053	0.10	8	10:55	
1057	0.20	25	10:59	02:00
1102	0.30	43	11:05	03:00
1108	0.40	61	11:12	03:00
1115	0.50	60	11:18	03:00
1119	0.70	76	11:21	01:00
1131	0.80	86	11:37	10:00
1140	0.90	96	11:42	03:00
1146	1.00	106	11:50	04:00
1152	1.20	101	11:56	02:00
1158	1.40	124	12:03	02:00
1213	1.60	127	12:21	10:00
1222	1.80	131	12:31	01:00
1233	2.00	121	12:39	02:00
1249	2.40	128	13:00	10:00
1302	2.80	123	13:09	02:00
1312	3.20	127	13:18	03:00
1320	3.60	129	13:23	02:00
1325	4.00	117	13:30	02:00
1340	5.00	127	13:52	10:00
1354	5.84	47	13:59	02:00
1407	7.00	100	14:15	08:00
1422	8.00	100	14:31	07:00
1432	9.00	105	14:46	01:00
1448	10.00	112	14:54	02:00
1456	12.00	106	15:03	02:00
1504	15.00	71	15:08	01:00
1509	18.25	53	15:13	01:00

D.2 Test safety procedures

During the execution of the OMRF Experiment (SDC-B), all personnel around the test frame and specimen must be wearing appropriate safety equipment such as hard hats, safety glasses, and steel toe shoes. The yellow painted line on the test floor will serve as the boundary where safety equipment must be worn. Also, the yellow caution lines indicated the boundary where personnel access is allowed during the test. No personnel are allowed to cross the caution lines during the test.

The static test will encompass applying a load to the top of the stub column using a hydraulic ram that is mounted overhead. The condition of the test specimen will be monitored while it is being loaded, and the testing will stop if the specimen reaches a point where loading it further would pose a safety concern. All employees occupying the upstairs offices and downstairs offices will be required to evacuate their offices 15 min. before the test or stay in their offices. All employees on the lab floor must be evacuated 15 min. before the test. The following procedures will be taken leading up to, during, and following the testing:

1. Move all nonessential personnel from the testing floor before starting the test,
2. Place people at each entrance to the test floor to prevent people from walking on test floor during the experiment. The people watching the doors will be out of the line of sight of the reaction frame and specimen,
3. Plywood will cover the windows of the instrumentation building that is located in front of the reaction frame, Only the instrumentation personnel will have access to the inside of the instrumentation building,

4. The specimen will be loaded at increments of 25,000 lb, making a pause of 10 to 15 minutes between each increment until failure or the maximum stroke of the hydraulic ram is reached. If the specimen has not reached failure, then a spacer will be placed between the specimen and the ram, and the test will continue until failure,

5. Non-essential personnel are not allowed on the test floor until the project engineer on site gives the all clear after all testing has been done on the test specimen,

6. After the testing ends, personnel will be allow adjacent to the test specimen to examine the specimen, but not inside the reaction frame,

7. The load will removed from the stub column, and the specimen will be braced to keep it stable.